THREE-DIMENSIONAL SEISMIC MODELING

: VELOCITY ANALYSIS AND INTERPRETATION

A Dissertation

Presented To

the Faculty of the Department of Geology

University of Houston

In Partial Fulfillment

of the Requirements for the Degree

Doctor of Philosophy

---

by

Luh-Cheng Liang

December, 1981

ACKNOWLEDGEMENT

Sincere appreciation is extended to my research advisor, Dr. Fred J. Hilterman, for his guidance and friendship. Without his help this work would not have been possible.

I also wishes to thank the Seismic Acoustics Laboratory for funding the thesis research and those who have made my experience at SAL more enjoyable. They are too many to name but all of them should be acknowledged.

This thesis is dedicated to my parents and to my wife Meifei, whose love and support made this study possible.

THREE-DIMENSIONAL SEISMIC MODELING
: VELOCITY ANALYSIS AND INTERPRETATION

An Abstract of a Dissertation

Presented To

the Faculty of the Department of Geology

University of Houston

In Partial Fulfillment

of the Requirements for the Degree

Doctor of Philosophy

---

by

Luh-Cheng Liang

December, 1981

ABSTRACT

In this research, interpretations based on theoretical and physical modeling data are given in the hope that they can be useful to the seismic interpreter for discerning pitfalls in real data. Recognition of these pitfalls could be an additional aid in the area of seismic interpretation.

As for the theoretical modeling, several interpretational pitfalls were identified when a systematic analysis was carried out with respect to three basic geological structures: basins, domes and partial reflectors. The pitfalls identified include: apparent pinchouts and grabens which were related to the profile line direction; extra reflection layers related to the depth of the model and the areal size of the structure; cross-stratifications related to the profile line direction and the areal size of the structure; faults or extra events related to the data acquisition schemes; weak events related to the processing flow; apparent "ambient noise" related to structural dip change; etc.

As for physical modeling, both the lateral and vertical velocity variations in a 3-D environment were evaluated and several pitfalls were identified. These pitfalls include: a dim spot which was related to an overlying high-velocity lens; a bright spot related to an overlying low velocity lens; an apparent velocity pullup where actually a velocity pushdown should be observed; a low frequency disturbed zone under the lens having a high velocity contrast; the

"thick lens" effect which distorted the appearance of the true structure; the wave conversion within sharply curved 3-D structures which is yet an unsolved problem of converted wave; ghost events which result from wavelet processing; etc.

Also in this research, three different velocity analysis algorithms were developed and evaluated for areally gathered seismic data. The first velocity algorithm was designed for data gathered by closely spaced conventional CDP lines. An optimum stacking velocity along with the apparent dip were obtained. The second velocity algorithm was designed for areal common-mid-point data. A migration velocity along with strike and dip were obtained. The third velocity algorithm was designed for multi-midpoint data such as would be gathered in a crooked-line survey. An optimum stacking velocity as a function of dip and strike and a final migration velocity were obtained.

These velocity algorithms offered a new processing flow which was applied on the crooked-line data using the output parameters derived from the third velocity algorithm. A satisfactory depth reconstruction was obtained and it proved that the processing flow and velocity algorithm were correct.

TABLE OF CONTENTS

TABLE OF CONTENTS (Cont'd)

TABLE OF CONTENTS (Cont'd)

LIST OF FIGURES

LIST OF FIGURES (Cont'd)

LIST OF FIGURES (Cont'd)

LIST OF FIGURES (Cont'd)

LIST OF FIGURES (Cont'd)

LIST OF FIGURES (Cont'd)

LIST OF FIGURES (Cont'd)

LIST OF FIGURES (Cont'd)

LIST OF FIGURES (Cont'd)

LIST OF FIGURES (Cont'd)

LIST OF TABLES

ABBREVIATIONS

AGC : Automatic gain control.

ASR : Arbitrary source-receiver.

CDP : Common-depth-point.

CMP : Common-mid-point.

dB : Decibel.

fk : Frequency (f) and wavenumber (k).

Hz : Hertz; cycles/sec.

NMO : Normal moveout.

RTV : Room temperature vulcanized silicone rubber.

S/N : Signal-to-noise ratio.

SR : Source-receiver.

VA : Velocity analysis.

ZSR : Zero source-receiver.

2-D : Two-dimensional.

3-D : Three-dimensional.

I. INTRODUCTION

The seismic reflection method has been the most widely used technique in petroleum exploration since the early 1930s (Weatherby, 1940). Along with the greatly improved data acquisitional and processing techniques over the years, seismic modeling has been an important aid in interpretation. While the interpretational aspect and theoretical modeling verification are still the prime use of modeling today, the use of modeling to study the data acquisition parameters and processing algorithms has grown as well in the past few years.

Many theoretical and physical modeling systems for reflection exploration seismology have been developed and reported in literature, but all these systems have had limitations. For example, in the area of theoretical modeling, most of the systems -- Peterson et al (1955), Wuenschel (1960), Goupillaud (1961), Trorey (1962), Darby and Neidell (1966), Taner et al (1970), Gangi and Yang (1976) -- have simulated the 2-D planar or curved universe. Some of those models have included multiples and absorption. Hilterman (1970) used the Kirchhoff integral approach and Dunkin and Levin (1971) used ray geometry to synthesize 3-D reflection models but for one layer only. Dobecki (1973) produced 3-D models for arbitrary velocity distributions but was limited to planar reflectors.

Along with the theoretical modeling system, many physical modeling systems have been studied to test the original theoretical assumption. For example, Levin and Hibbard (1955), Hall (1956), Bennett (1962), Berckhemer and Ansorge (1963), Hilterman (1970) and Woods (1975) have all reported on physical modeling. Most of them, however, were concerned with some specific problems. Two separate laboratory modeling systems which were suitable for 3-D purposes and research studies were designed by Yu and Telford (1974) and French (1974). Both systems consisted of a water tank and used ultrasonic transducers to simulate the source and receiver. The basic design of the physical modeling system at Seismic Acoustics Laboratory, where data for this research were collected, was based upon French's system.

The objective of this research is to investigate both the theoretical and physical model data which simulate time sections gathered by conventional 2-D seismic lines over 3-D geological structures. Both theoretical and physical models are incorporated to produce the synthetic time sections. In order to produce a correct interpretation and recognize potential interpretational pitfalls, the velocity-analysis algorithms and data processing procedures are studied and documented in a systematic fashion. When necessary for an interpretational comparison , 3-D (areal) coverage over the same geological structures are collected and analyzed.

This investigation starts by modeling theoretically time sections gathered across three basic structures, namely, domes, basins and partial reflectors. More complicated geologic models are assumed to be synthesized from these basic structures. On the resulting time sections, only a first surface interpretation is conducted. From this interpretation, the problems of viewing spherical wave propagation with a 2-D "cross-section" are illustrated.

For the evaluation of both lateral and vertical velocity variations in a 3-D environment, physical models are classified into two categories, structural and stratigraphic. Interpreted results from these scaled models along with known controlled conditions are catalogued and hopefully provide general criteria for spotting velocity pitfalls.

When appropriate, both 2-D and 3-D velocity analyses are evaluated with respect to the earth parameters of dip, strike, and interval velocity. From this portion of the study, the relationship between 2-D stacking velocity , 3-D stacking velocity and migration velocity is determined.

II. DESCRIPTION OF PHYSICAL MODELING SYSTEM

2.1 PHYSICAL SYSTEM

The block diagram of the total physical modeling system is shown in Figure 2-1. The physical system has been continuously updated and the discussion within represents the setup when the majority of data were collected. The dotted lines represent the command flow and the solid lines represent the data flow. The dotted lines indicate that the control block receives programmed instructions from the CPU and steers the scanning mechanism, triggers the source energizer and the recording system. The solid lines indicate that the signal from the receiver in the water tank is amplified, filtered and converted into a digital code before transferring the signal into the CPU through the DIO interface (SAL Progress Review, Volume 2, 1978 and Volume 4,1979).

A simplified schematic of the mechanical system is shown in Figure 2-2. The fiberglass water tank, manufactured by NECO in Houston, has inner dimensions of 6 x 8 ft by 5 ft deep and is set in a 3 ft pit. The tank was designed so that no spurious events, such as those from the water surface, side wall or bottom of the tank, would return during the time that the desired reflection signal is being collected. The four plexiglas windows on the side of the tank are for quality control when the initial positioning is being conducted (SAL Progress Review, Volume 2, 1978).

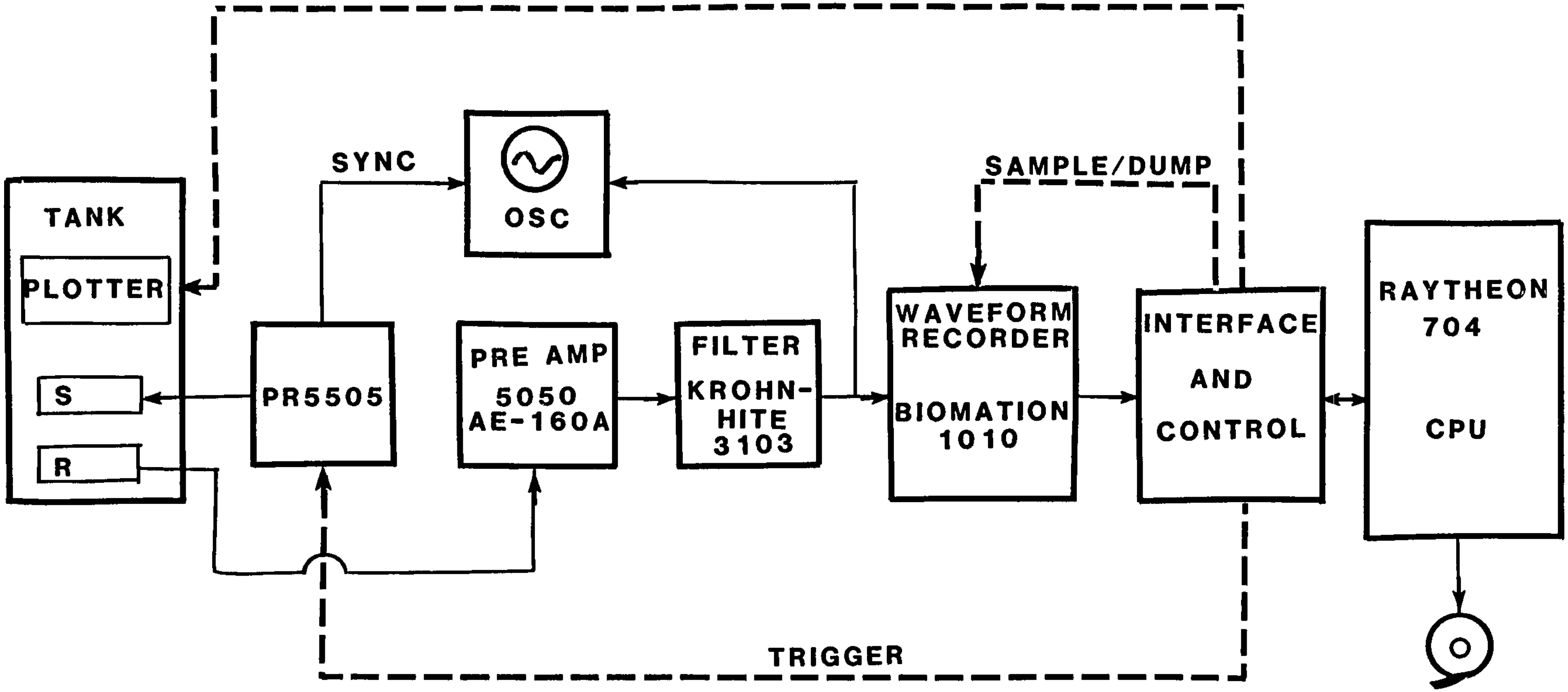

Figure 2-1 Block diagram of physical modeling system.

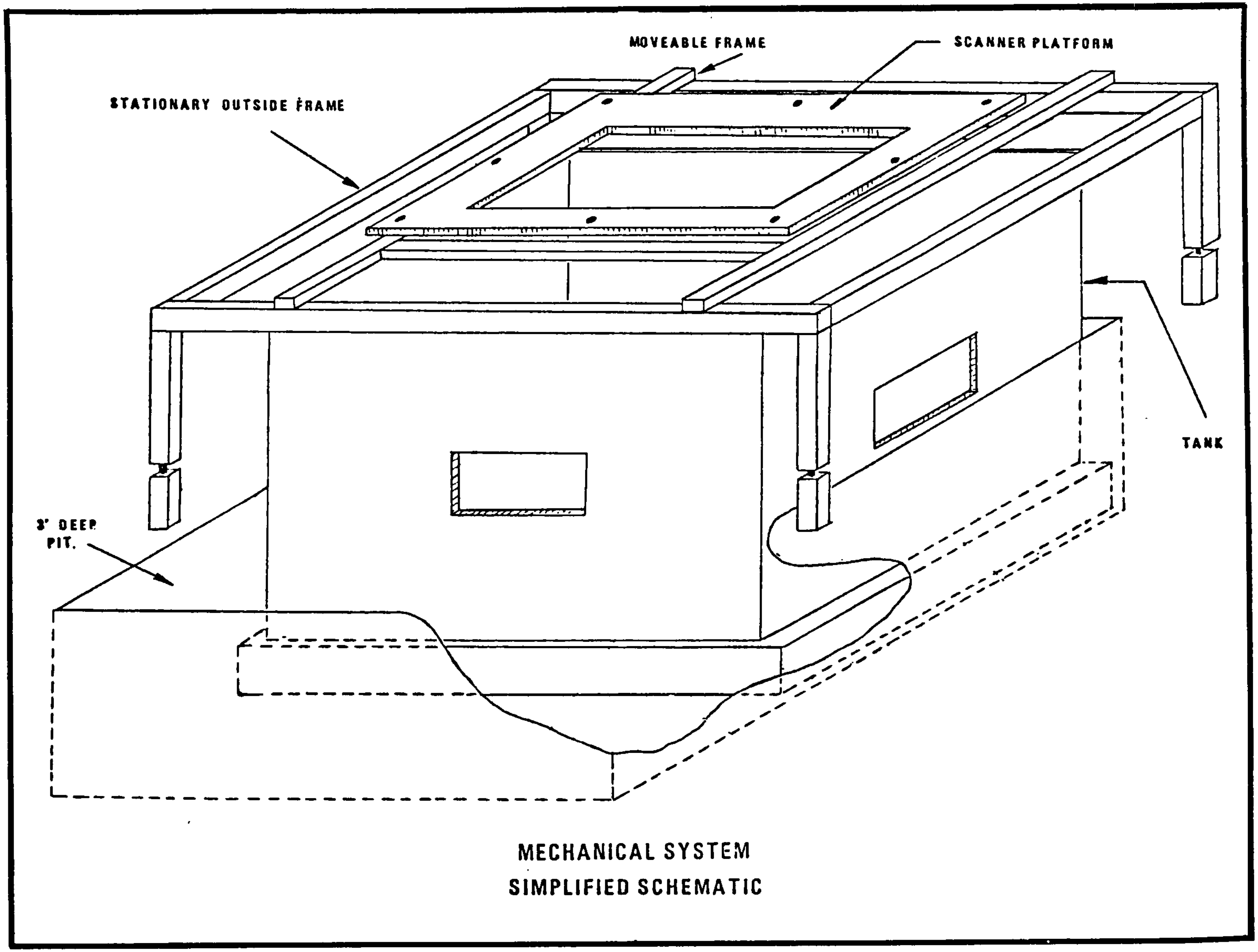

Figure 2-2 Simplified isometric of mechanical system.

The two Wang plotters which move the source and receiver transducer assemblies are mounted on a frame external to the tank to reduce positioning noise in the tank. The water in the tank is continuously circulated through two de-ionization tanks, two 25-micron filter assemblies and an ultraviolet light to remove the pollutants and destroy the micro organisms (SAL Progress Review, Volume 2, 1978).

The model source consisted of a Panametrics V3034, flat surface transducer with a diameter of 2-1/2 in and a central frequency of 250 KHz. A polystyrene acoustic lens is attatched to the source to decrease the directivity and increase the spatial bandwidth. An additional styrofoam "coffee" cup with an aperture opening of 3/16 in (about a wavelength) is fitted to the bottom of the source (Figure 2-3). The aperature is located slightly below the focal plane of the source and shapes both the temporal and spatial response of the pulse. That is, the aperature acts as a point source. The cup also successfully attenuates the direct transmition between the source and the receiver. The receiver is an ITC 1089 spherical transducer, 1/8" active transducer diameter, with a central frequency slightly higher than 250 KHz. The beam directivity pattern of the source-receiver pair is about 104 degree at -10 dB amplitude points (SAL Progress Review, Volume 2, 1978 and Volume 4, 1979).

The Panametrics model 5055 Pulser-Receiver activizes the source

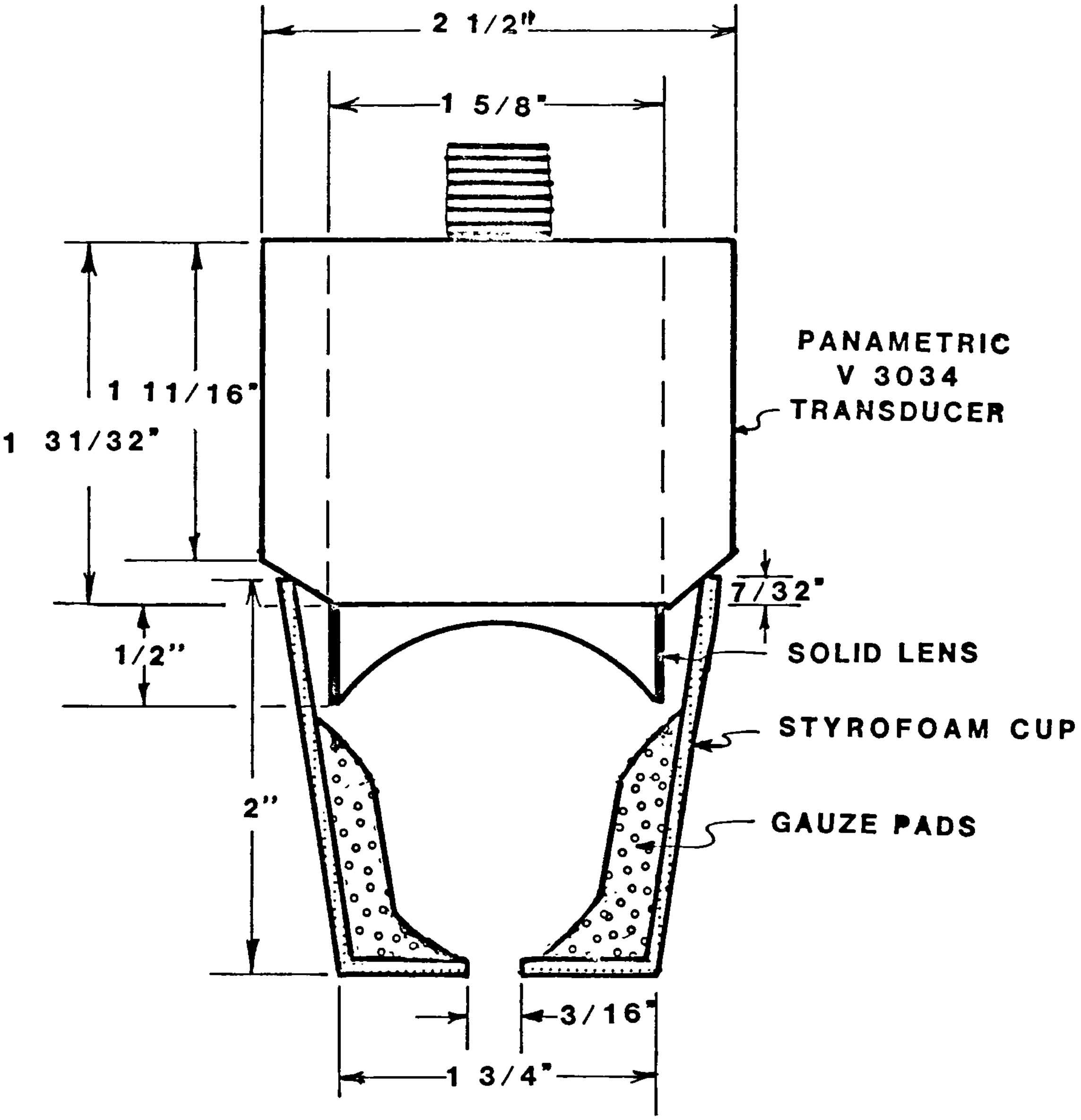

Figure 2-3 Focused source transducer with noise attenuating coffee cup.

transducer with a 200 V, 10 ns boxcar signal. The receiver signal then goes through the Panametrics model 5050 AE-160A preamplifier (60 dB) and then through the Krohn-Hite model 3103 variable bandpass filter (normal setting of 90-400 KHz). The output from the filter is simultaneously fed to a Biomation 1010 waveform recorder for digitization and to a Hewlett-Packard 1741A oscilloscope for quality control. The entire system is controlled by a Raytheon 704 computer and driven by the software package HARDWA (SAL Progress Review, Volume 2, 1978) which can accommodate shooting geometries from simple CDP profile lines to sophisticated multi-fold areal surveys. The final digitized data are recorded on 1/2 in magnetic tape in 16 bit integer format (SAL Progress Review, Volume 2, 1978).

2.2 SCALE FACTORS AND MODEL MATERIAL

To study the earth prototype through scale modeling, it is necessary to establish a relationship of similarity between the physical model and the prototype system (Hubbert, 1937). The three fundamental dimensions to specify this relationship are length, time and mass. All physical parameters contain only ratios of length, time and mass and thus can be uniquely determined if the scale factors in these fundamental dimensions are defined.

The two most important physical parameters to consider for the purpose of seismic reflection modeling are velocity and density. It was determined that a length scale factor of 1 in to 1000 ft for the model-prototype ratio would be pratical and convenient. The time scale factor was set at 1:5000 (model: prototype); and consequently, the velocity and frequency scaling become 1:2.4 and 5000:1 (model:prototype) respectively. Table 2-1 summarizes the scale factors for the fundamental dimensions and derived parameters (SAL Progress Review, Volume 2,1978).

The candidate material that is most suitable for the construction of physical model would be either solids that could be readily shaped, formed and hardened; or liquids that could be cured in prefabricated molds. Desired physical properties would be: low attenuation, density not lower than that of water and acoustic velocity comparable to that of water. The materials thus chosen were; RTV* 170, RTV 184, RTV 3110, RTV 3120, Resin 1266 and plexiglas.

Some characteristics of the model materials are given in Table 2-2. The calculated normal incidence reflection coefficients between the model materials are listed in Table 2-3. The curing compatability and bonding characteristics of the RTV compounds are listed in Table 2-4.

---

*Room Temperature Vulcanized Silicone Rubber.

DIMENSIONLESS

	PROTOTYPE	MODEL
Length	12000	1
Time	5000	1
Velocity	2.4	1
Frequency	1	5000

COMMON DIMENSIONS

	PROTOTYPE	MODEL
Length	1000 ft.	1 in.
Time	1 ms.	.2 usec.
Velocity	12000 ft/s	5000 ft/s
Frequency	50 Hz	250 KHz

Table 2-1. Scale factors for physical models

Sample No.	ρ(gm/cc)	V(ft/sec)*	ρV	Color
RTV 170	1.29	3115	4018	Black
RTV 184	1.04	3600	3744	Clear
RTV 3110	1.17	3300	3861	White
RTV 3120	1.37	2944	4033	Red
Plexiglas	1.17	9000	10575	Clear
Resin 1266	1.18	7889	9309	Amber
Water	1	5000	5000	Clear

*P-wave velocity.
The shear wave velocity is 4452 ft/sec for plexiglas and 3766 ft/sec for Resin 1266.

Table 2-2. Characteristics of Model Materials

-- TOP MATERIAL --

BOTTOM MATERIAL	Water	RTV 170	RTV 184	RTV 3110	RTV 3120	Resin 1266	Plexi- glas
Water		.206	.239	.129	.107	-.301	-.358
RTV 170	-.206		.035	-.081	-.101	-.397	-.449
RTV 184	-.239	-.035		-.114	-.136	-.426	-.477
RTV 3110	-.129	.081	.114		-.022	-.414	-.465
RTV 3120	-.107	.101	.136	.022		-.395	-.448
Resin 1266	.301	.397	.426	.414	.395		-.064
Plexiglas	.358	.449	.477	.465	.448	.064	

Table 2-3. Normal reflection coefficients between model materials

BOTTOM MATERIAL	TOP MATERIAL: 170	184	3110	3120
170		Yes	Yes	Yes
184	No		Yes	Yes
3110	No	No		Yes
3120	No	No	Yes	

Table 2-4. Bonding characteristics of the RTV. 'Yes' means top material will cure and bond with the bottom material.

2.3 CALIBRATION AND WAVELET PROCESSING

In order to accurately time the reflection data collected over the physical model, the mechanical-electrical delay has to be determined properly. To accomplish this,the source and the receiver are mounted on an aluminum rod and aligned axially. The transmission time from the source to the receiver is recorded on magnetic tape and checked against the oscilloscope display, and the varied distances between source and receiver are measured with a .001 in dial indicator. The water velocity is derived from the least-squares fit time-distance slope and the system time delay from a linear extrapolation to distance equals zero. A water velocity of 4970 ft/sec (prototype = 11928 ft/sec) is adopted from this measurement. A static delay of 9.2 μsec is extrapolated to the plane of the edge of the lens. The datum for the actual model data collection is leveled at the plane of the source aperature stop, which introduces an additional delay of 28.6 μsec. The total static correction would be:

Biomation delay - (9.2 + 28.6) μs.

A frequency-domain inverse filter was designed to shape the recorded source wavelet. The basic procedure is as follows:

Desired wavelet d equals the basic wavelet b convolved with the inverse filter f, that is

$$d = b * f.$$

Taking the Fourier transforms yields ,

$$\begin{aligned} F &= D/B \\ &= D\bar{B} / |B|^2 \\ &\approx D\bar{B} / (|B|^2 + c|B|_{max}) \\ &= \bar{F} \end{aligned}$$

where c is a stability factor and $\bar{F}$ is an approximation of F . The inverse Fourier transform of $\bar{F}$ yields $\bar{f}$, which is then truncated by a Bartlett window (Bath, 1973).

A basic wavelet taken from the direct transmission between the source and the receiver is shown in Figure 2-4. Note that dimensions in this research will be converted to the prototype scale when it is appropriate. Also shown is the desired wavelet. The corresponding spectra are shown in Figure 2-5. The inverse filter and the filtered output are shown in Figure 2-6 (SAL Progress Review, Volume 3, 1979).

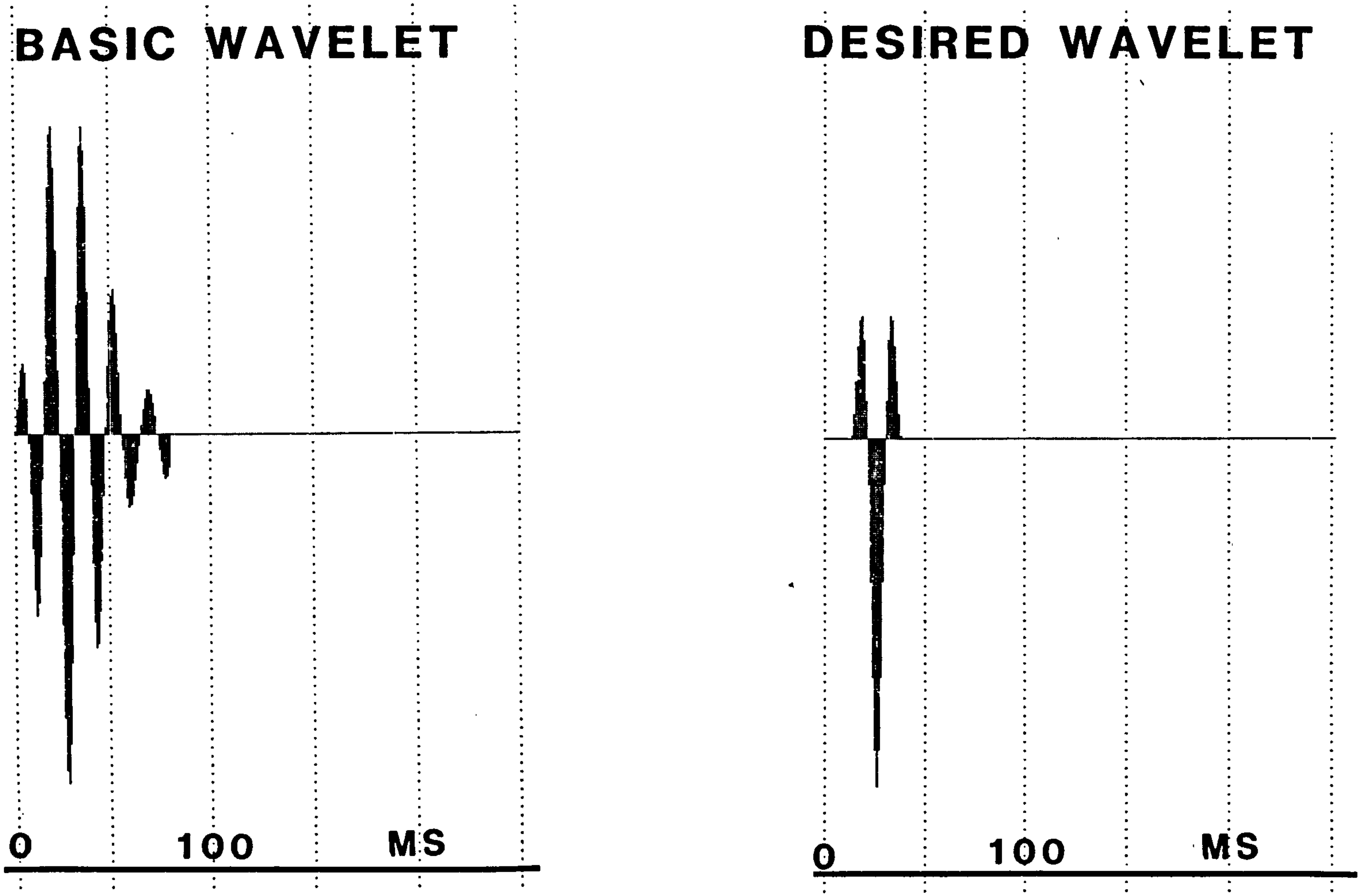

Figure 2-4 Basic source wavelet and desired wavelet in prototype scale.

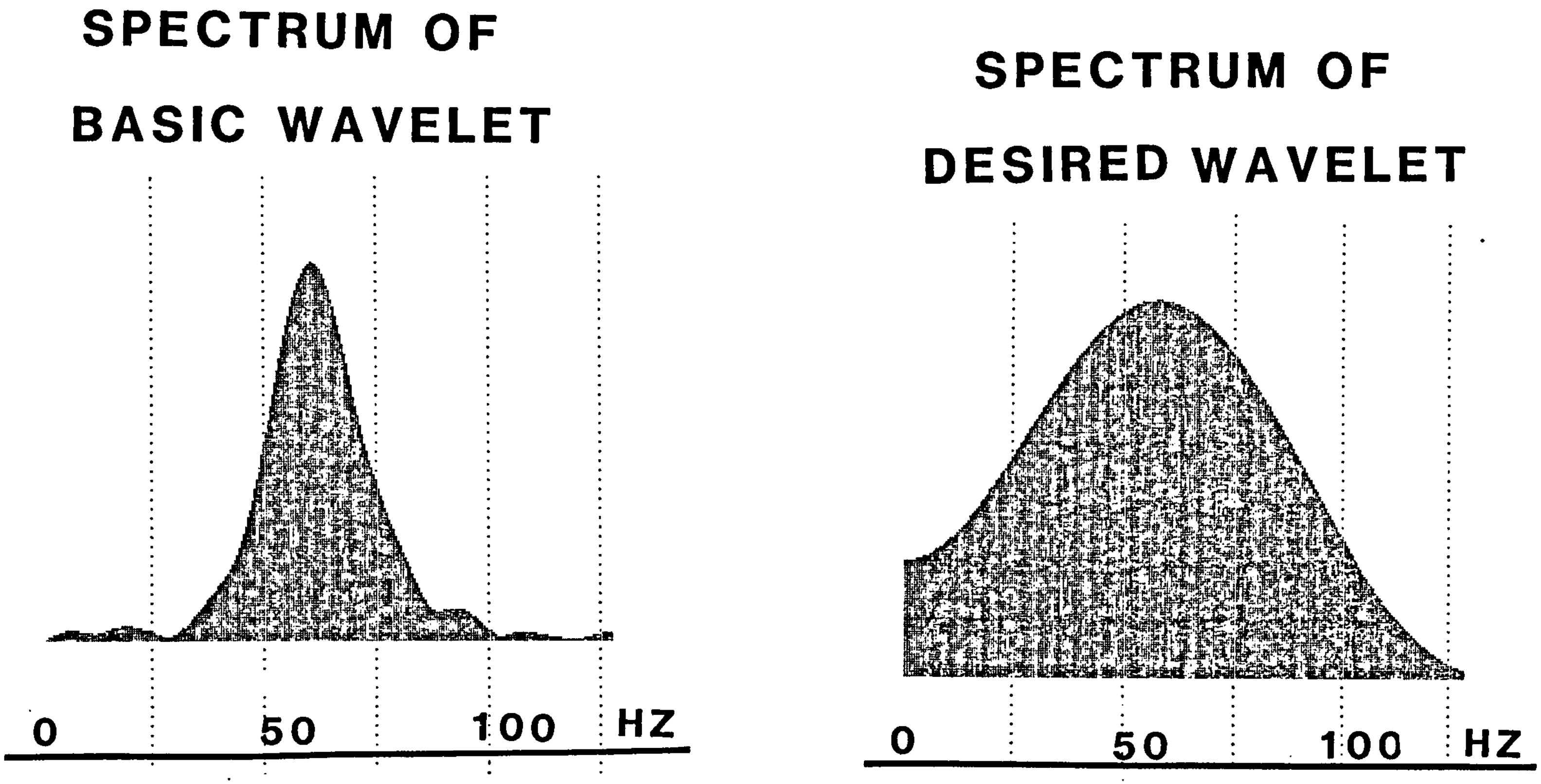

Figure 2-5 Spectra of basic wavelet and desired wavelet.

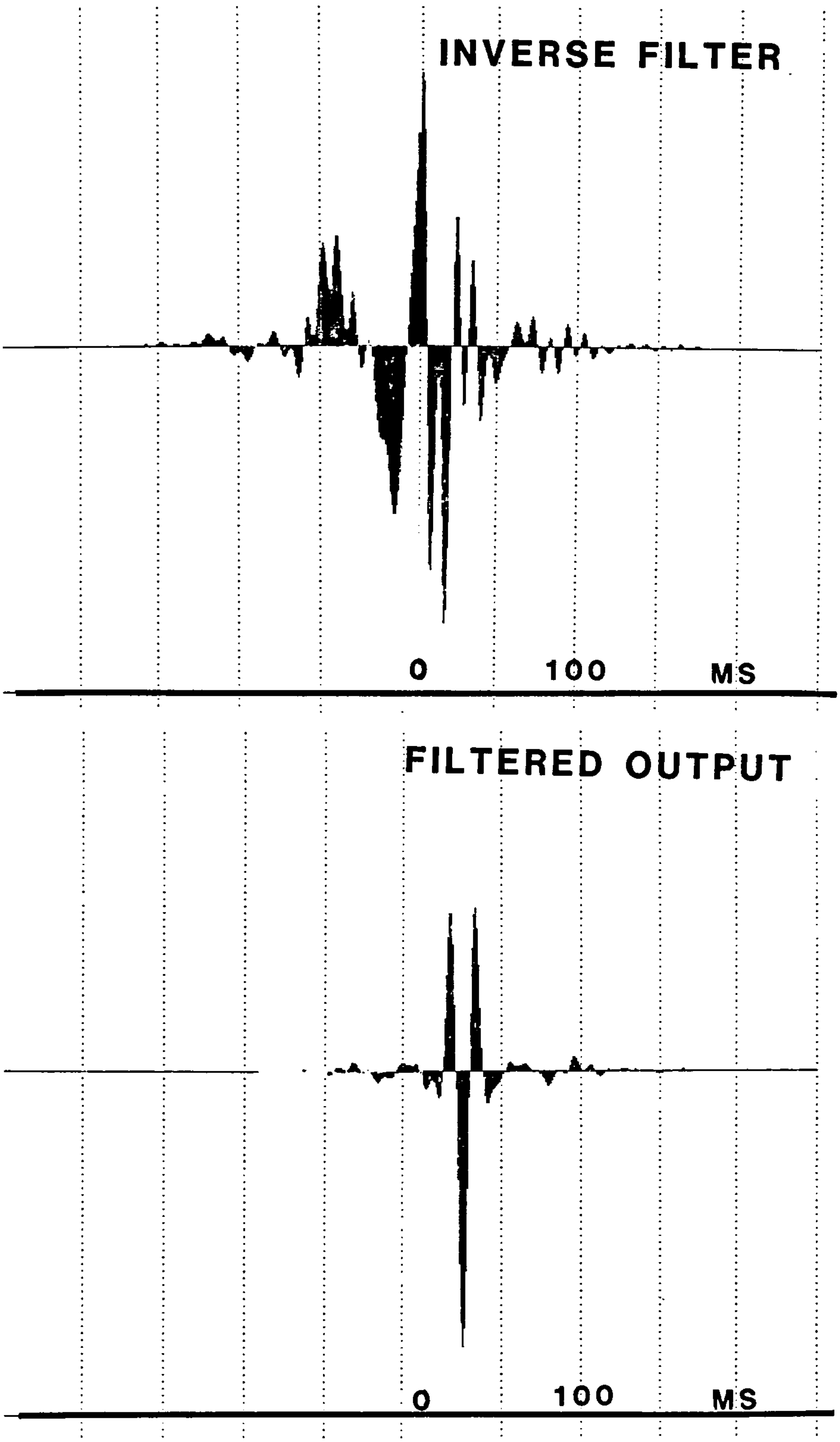

Figure 2-6 Inverse filter and filtered output.

An additional calibration test was performed periodically to insure that the spatial and temporal response of the total system was not changing. As outlined in Figure 2-7, a direct transmission experiment was conducted to document the source-receiver angular response. The receiver is fixed 14.05" below the source point. Two perpendicular profile lines were obtained by first scanning the source in the x-direction and then in the y-direction. Each profile line had 151 traces and a typical profile line in the x-direction is shown in Figure 2-8. Both the near offset and far offset data were windowed and enlarged as shown in Figure 2-9. Also shown are the deconvolved data. They illustrate remarkable similarity in waveshape from the near traces to the far traces. This desirable feature allows us to measure one seismic pulse for future wavelet processing of the physical model data. This also assures that the migration programs, which assume a consistent pulse shape in all directions, will operate correctly (SAL Progress Review, Volume 4,1979).

2.4 SUMMARY

The water velocity 4970 ft/sec (prototype=11928 ft/sec) obtained from the calibration test is used for further processing such as normal moveout (NMO) corrections and migration. The system delay 37.8 μsec is equivalent to 179 samples for the conventional .2 μsec sampling interval. The V3034-ITC 1089 assembly has a broad-band, near symmetrical spatial response and a well defined temporal

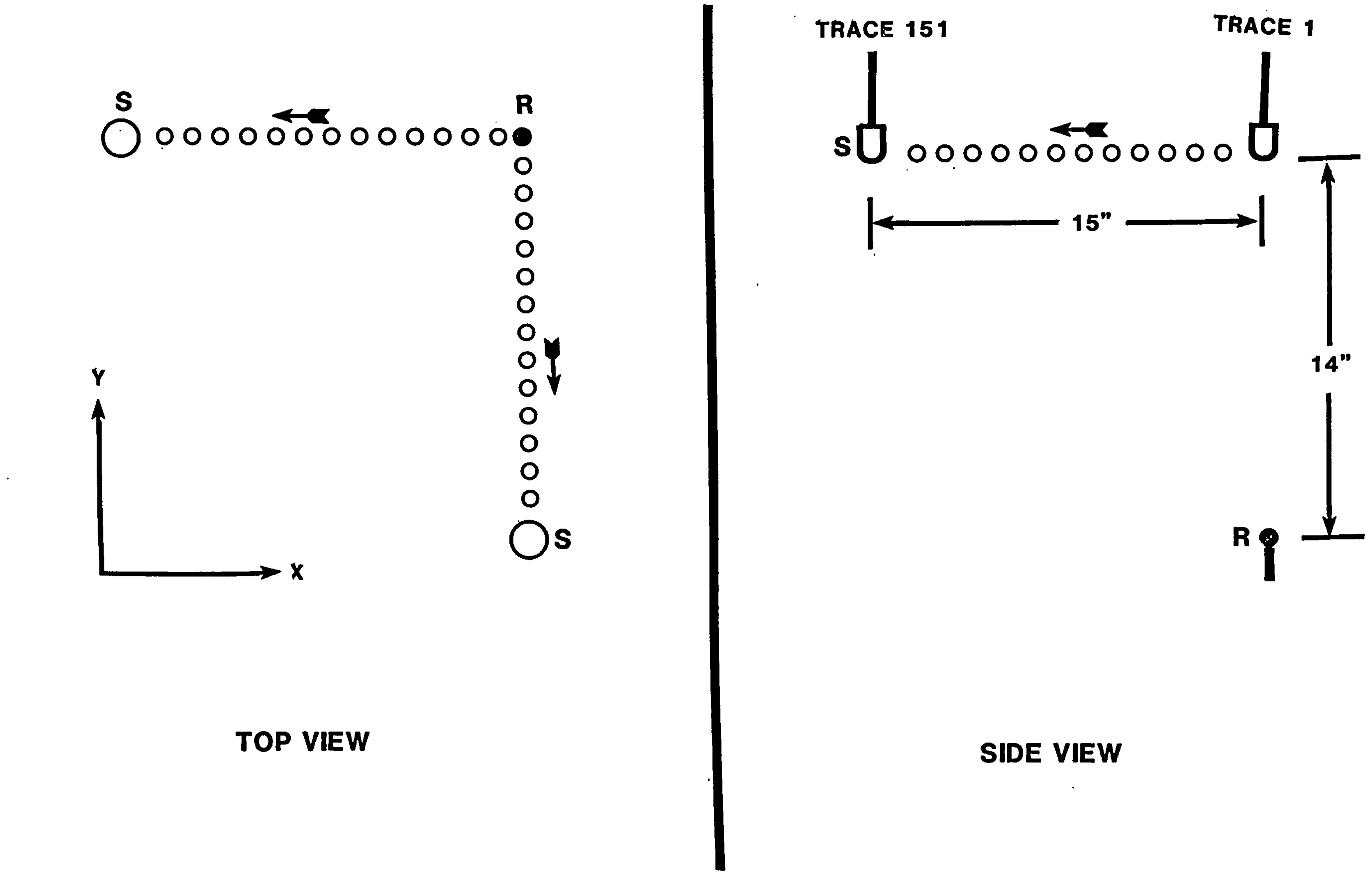

Figure 2-7 Source-receiver characterization setup.

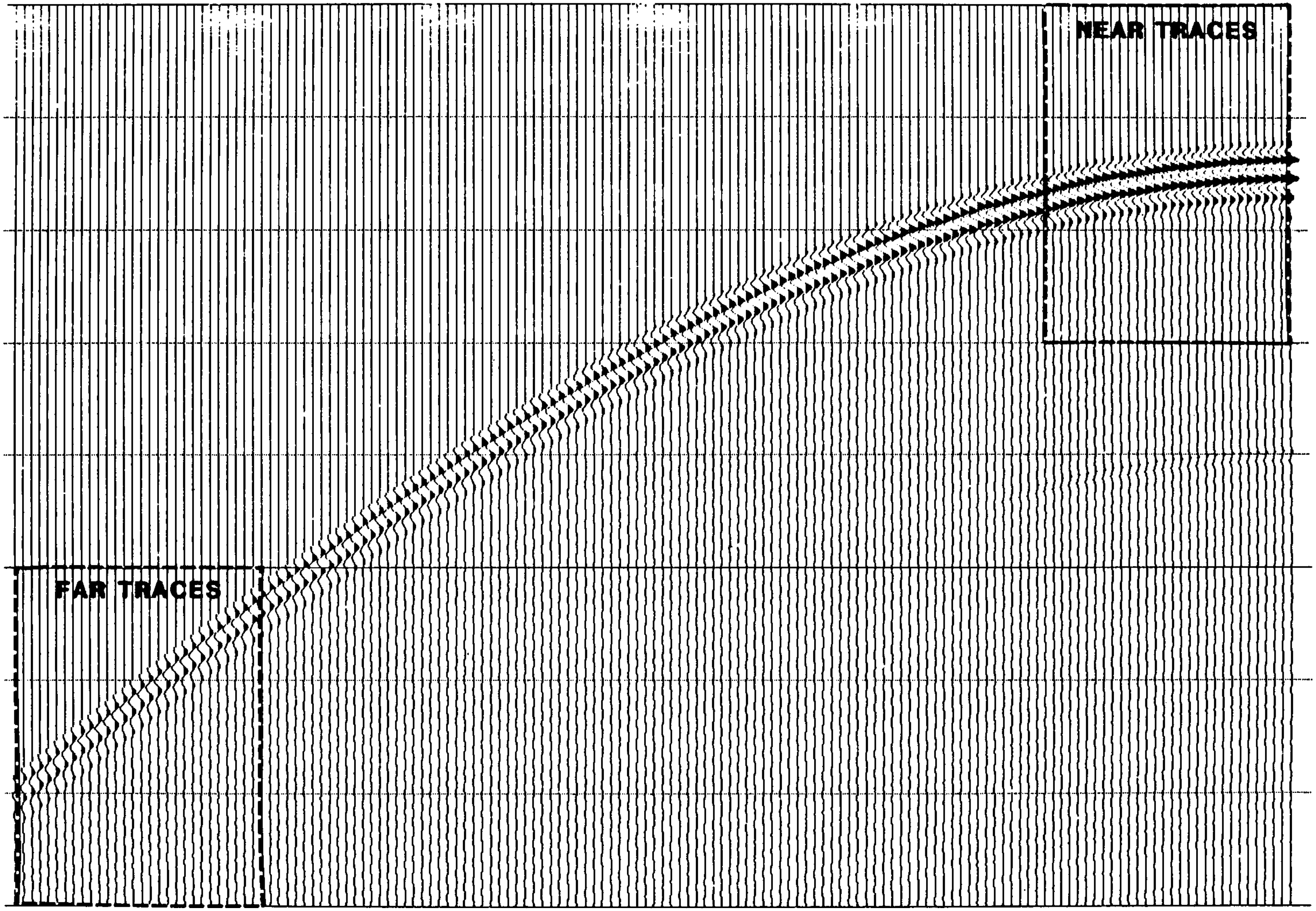

Figure 2-8 Profile line in the x-direction.

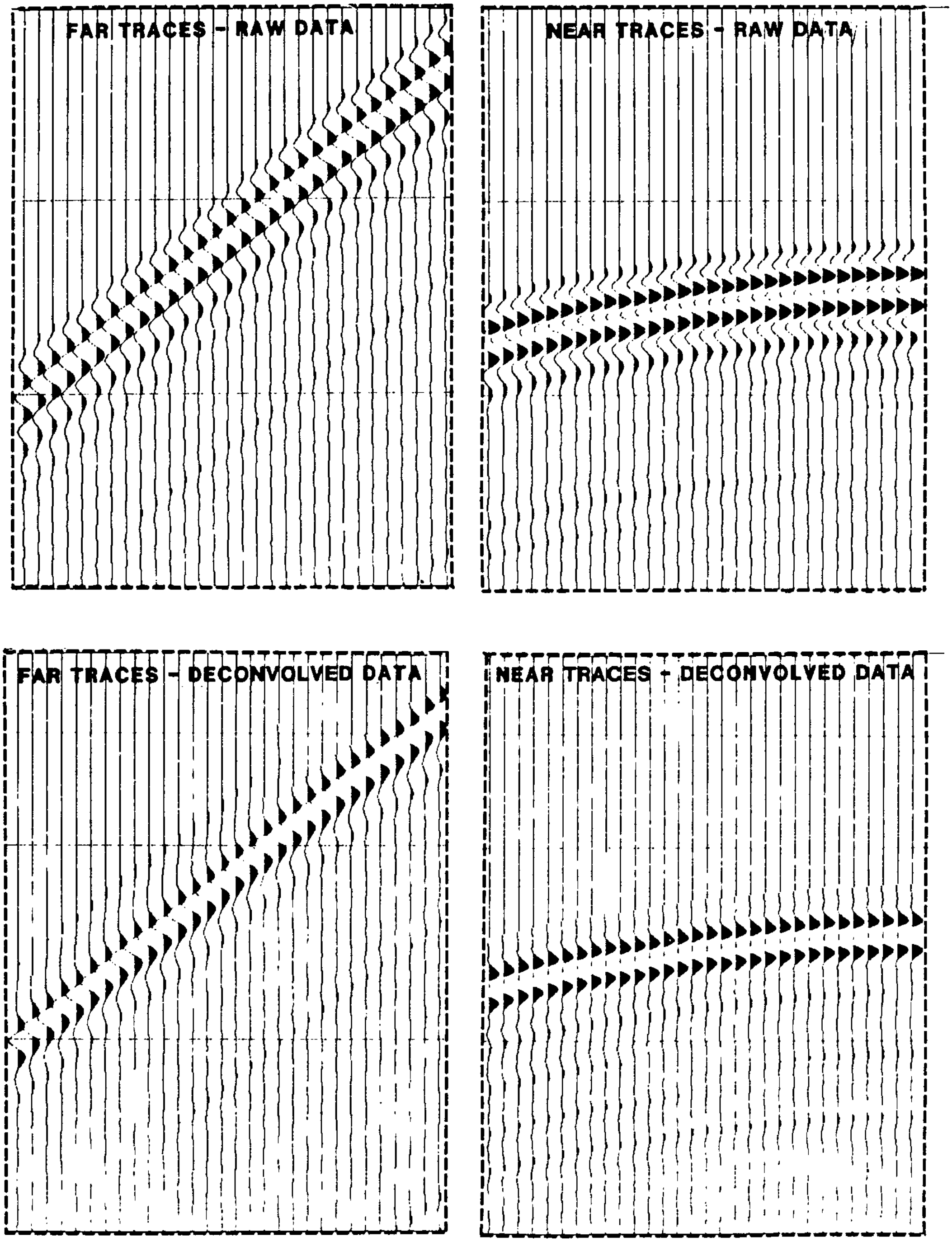

Figure 2-9 Enlarged segments of the profile line in the x-direction -- raw and deconvolved data.

response, which allows us to collect wide angle reflection data and pulse shape the downgoing wavelet. However, the physical size of the source dictates the minimum offset to be 1500 ft. The two plotters, which drive the source and the receiver independently, can simulate most of the data acquisition schemes. The only restriction is that the source and the receiver can not cross each other.

III. NUMERICAL MODELING

3.1 INTRODUCTION

Sideswipe and other seimic events from 3-D structures which appear on conventional 2-D time sections are investigated through numerical modeling in this chapter. The algorithm for generating 3-D Kirchhoff models basically follows the development given by Hilterman (1976). Modifications to this algorithm have been incorporated to allow for arbitrary source-receiver (ASR) offsets (Smith, 1981).

When using the Kirchhoff 3-D wave equation to generate seismic time sections, a slowly varying velocity assumption is necessary. This assumption allows one to ignore double reflections, refracted-reflections, shear wave propagation and abnormal transmission losses.

Another assumption made is that all geological structures could be analyzed with a few elementary "building blocks". These building blocks are basins, domes, half-plane faults and partial reflectors. Then more complicated structures are composites of the time sections from these "building blocks". Seismic sections across each model were evaluated with respect to several parameters: namely, the 2-D profile location, the areal size of the model and the depth and dip of the model.

Also, the assumption that the stacked seismic section represents a normal incident time section was tested for 3-D structures by gathering single-fold, 12-fold and crooked-line surveys across the same structure. The resulting sections were then stacked, 2-D migrated and where appropriate 3-D migrated to illustrate where and why the normal incident assumption is not always valid.

3.2 CHARACTERIZATION OF NUMERICAL MODEL SURFACE

The basic reflection surfaces of the numerical model were constructed with triangular plates. The similarity between the digitized description of the model and the prototype of the geological structure will depend mainly upon the sampling density and the depth of the structure. The finer the sampling density is, the better the description of the geological structure will be. For numerical forward modeling, the shallow structures must be sampled more densely than deeper structures. This comes from the fact that the shallower a geological structure is, the more the seismic time section looks like the geological cross-section.

To illustrate the concept of the sampling density, a circular basin is sampled four different ways as shown in Figure 3-1. The tiles were purposely coded to be symmetrical with respect to the four quadrants so that diffraction energy due to improper sampling would be in-phase. Basin A has the least number of tiles at 104 while B

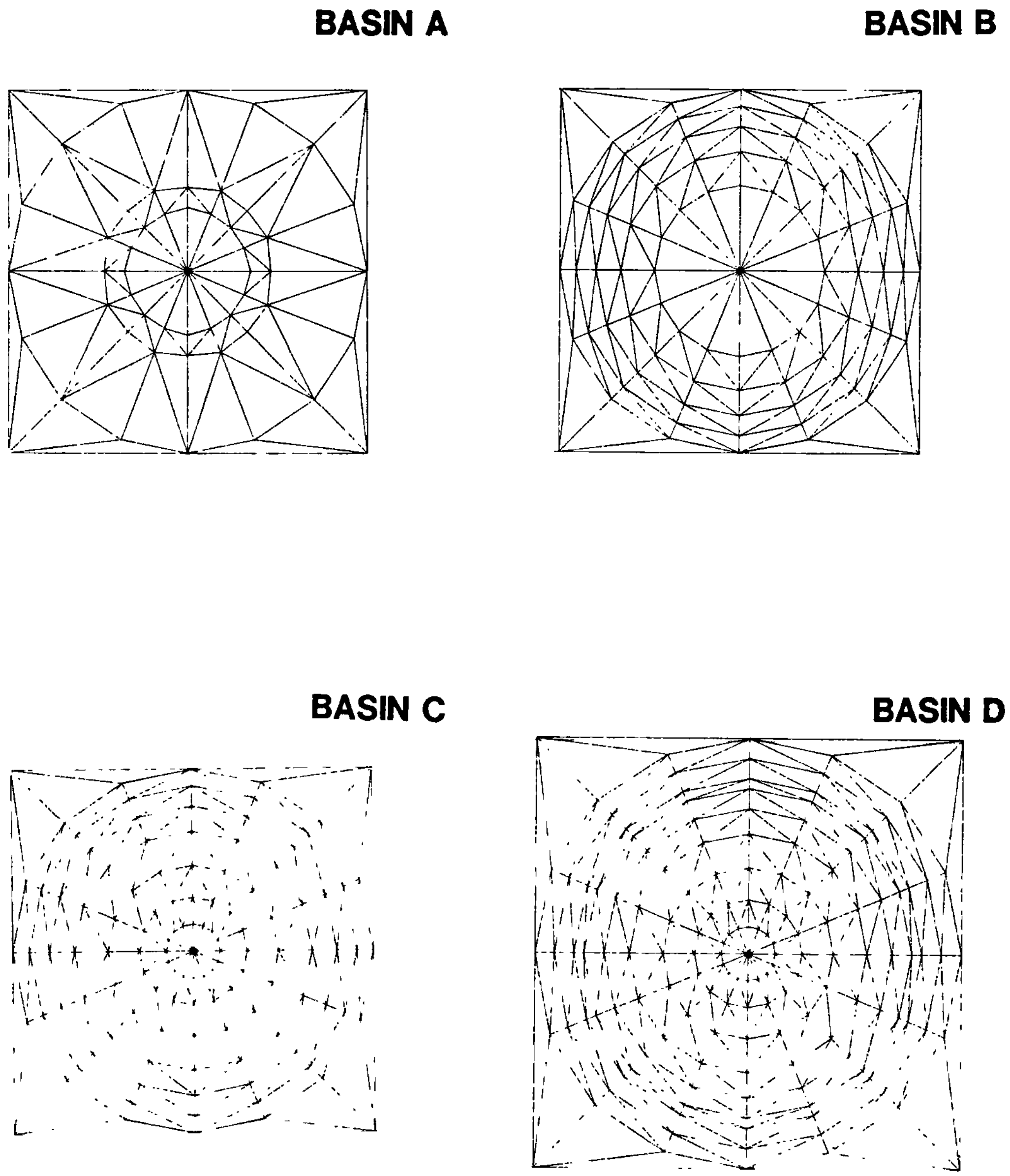

Figure 3-1 Triangular plates of circular basins.

and C have 168 and 232 respectively. Basin D is similar to C in the middle portion but has additional tiles (total 296) on the outside of the structure to yield a smooth curvature at the lip.

The isometrics and contour maps of the four differently sampled basins are shown in Figure 3-2. At first glance there does not appear to be any difference in the isometrics of the four basins, but notice the deepest part of Basin A with respect to C or D. Basin C and D are more continuous. Also, the lip of Basin D is much smoother when one compares it to the sharp edges of Basin A, B or C. The continuity in the middle portion of the basins is not obvious on the 100-ft contour maps, while the gradient at the basin lip is. For Basin A, the gradient of the contour remains constant over a large portion of the model. The isometrics provide a good quality control when one interprets a seismic time section over a 3-D structure and tries to determine from where the energy might be scattering.

The sections in Figure 3-3 are profile lines taken 1500 ft above the flat portion of the circular basin models and taken across the center of the models. These are zero source-receiver (ZSR) offset models with a trace spacing of 60 ft. In the left portion of Figure 3-3, there are noise events (diffractions) near the middle of the basin which are caused by sampling too sparsely. The noise events are not as evident, however, on the corresponding migrated sections in the right portion of the figure.

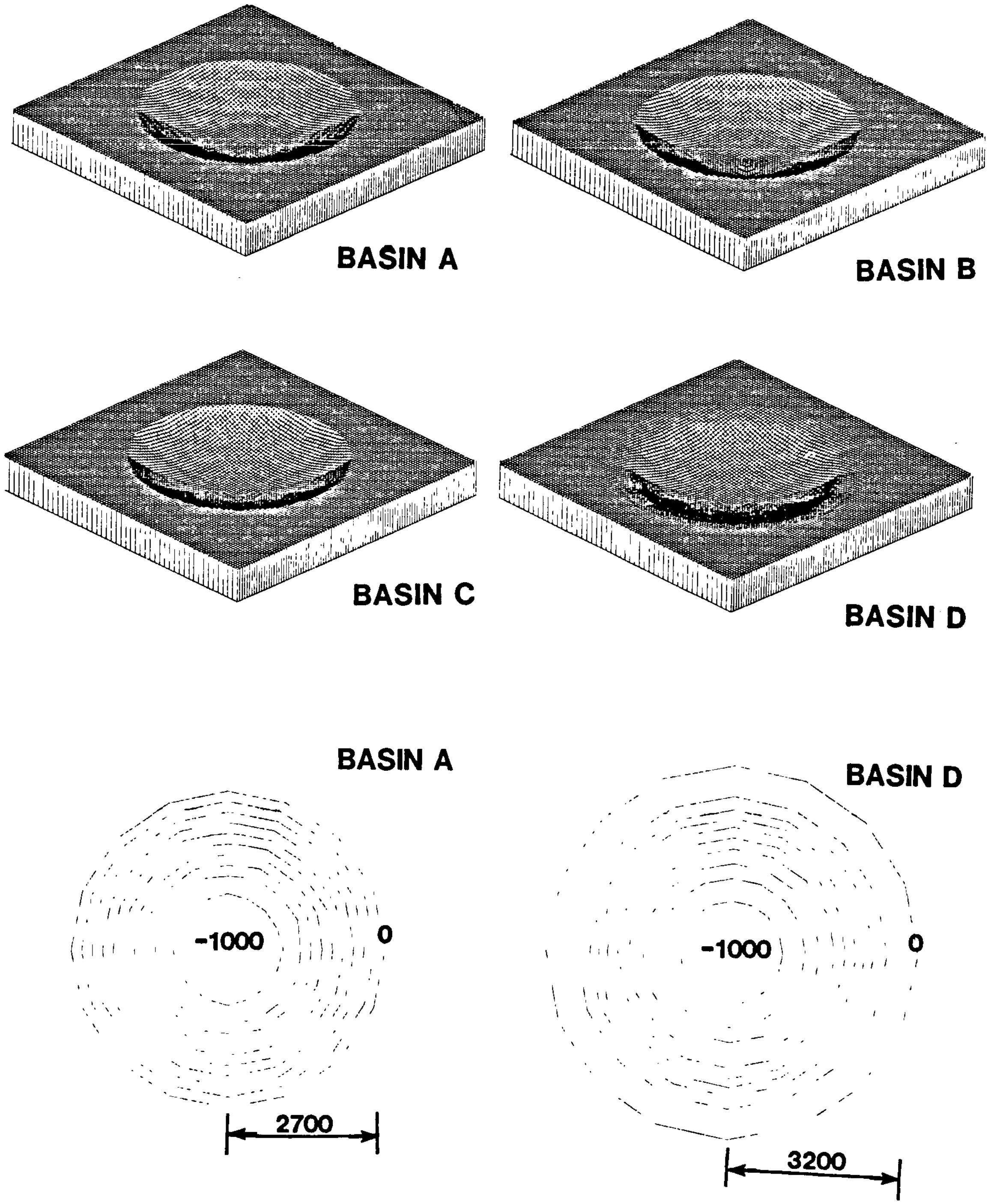

Figure 3-2 Isometrics and contours of circular basins.

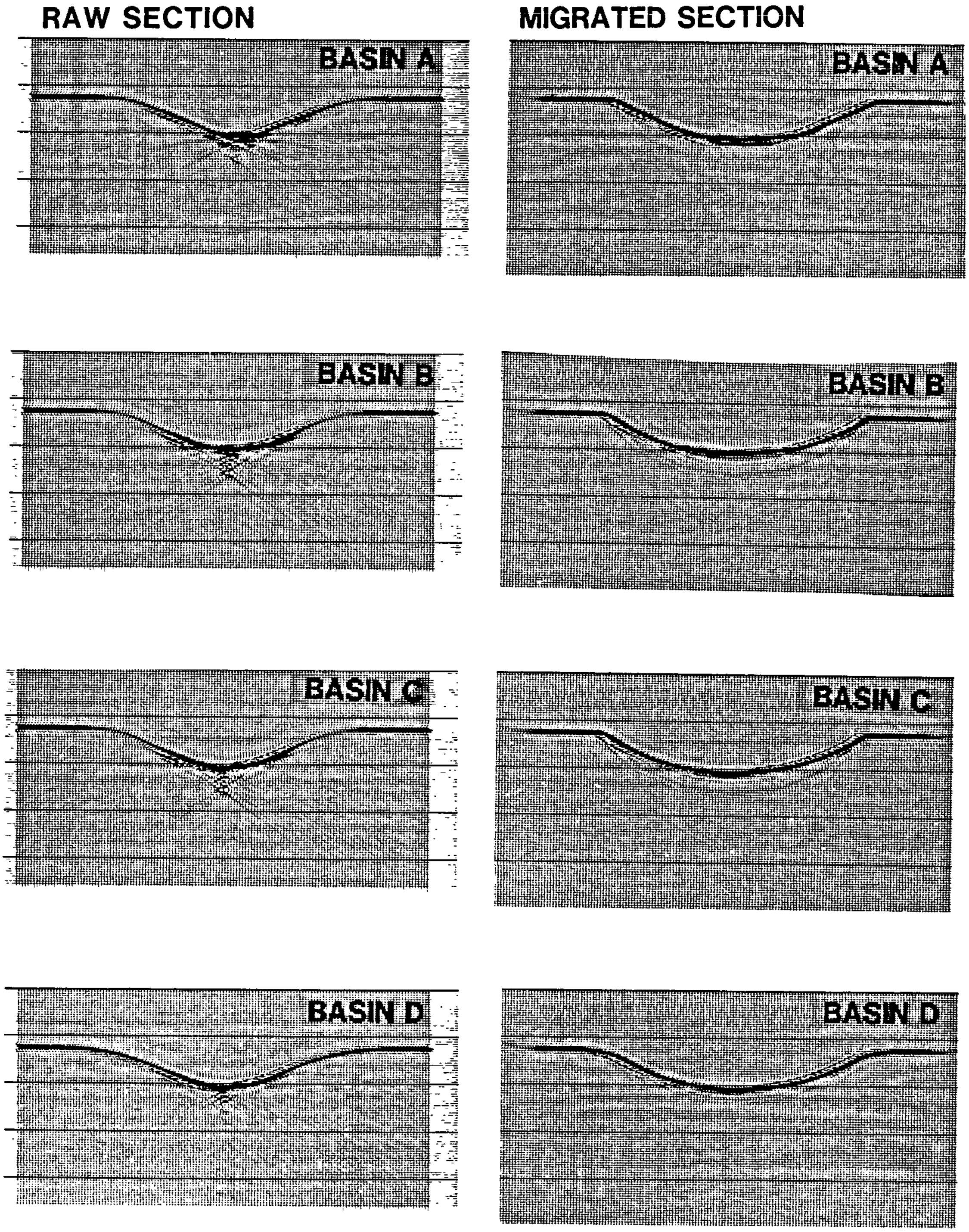

Figure 3-3 Raw and migrated sections of 1500 ft depth circular basins.

Basin A which has the least number of reflection tiles appears to have the most difficult raw seismic section to interpret. The radius of curvature at the bottom of the basin is 4145 ft so the basin does not have a buried focus with respect to the surface at this point. However, sharp edges from the out-of-plane boundaries focus energy beneath the source-receiver location and produce a distorted version of the classical bow-tie event. We will discuss this bow-tie phenomenon later. The events which are similar to "bow-tie" events in the Basin A raw section are once again caused by abrupt changes in the slope of the input model. They are simple diffractions, like those generated when a profile line crosses a half-plane. Notice also that as the slope of the model becomes smoother (the smoothest is Basin D) the "noise" under the middle part of the basin decreases on the raw sections.

On the 2-D migrated section, Basin A has an apparent reversed polarity event in the bottom of the anomaly. It is really two events that are superimposed, one from the bottom of the basin and the other from the coarsely sampled out-of-plane sides. On the migrated sections for Basin B and C beneath the main event there are circular reflection events, which are caused by 3-D curvature near the basin lip.

Because there is focusing due to boundary curvature in two directions, we are not surprised to see that the amplitude in the basin is not correct on the 2-D migrated sections.

The sequence of sections in Figure 3-4 is similar to that in Figure 3-3 except now the depth to the flat portion of the model is 5500 feet. Notice the similarity of these raw time sections from corresponding models which are sampled differently. It indicates the deeper the model is, the coarser the boundary sampling interval can be. At this depth there are wo buried foci, one in the plane of the profile line and one perpendicular to it. Notice the 180° phase change on the event from the deepest part of the basin (raw sections). It is not surprising that this same event has a 90° phase change on the 2-D migrated section. Remember that 2-D migration of a buried focus event removes a 90° phase shift.

3.3 BASIN

Basin D which is the most densely sampled one and has the smooth curvature at the lips is investigated in this section. Therefore, the name "Basin" will refer to Basin D from now on. Several items with respect to the basin are studied; these are: (A) circular basin, (B) synclinal versus circular basin, (C) oblong basin, (D) small and large basin and (E) tilted basin.

A. CIRCULAR BASIN

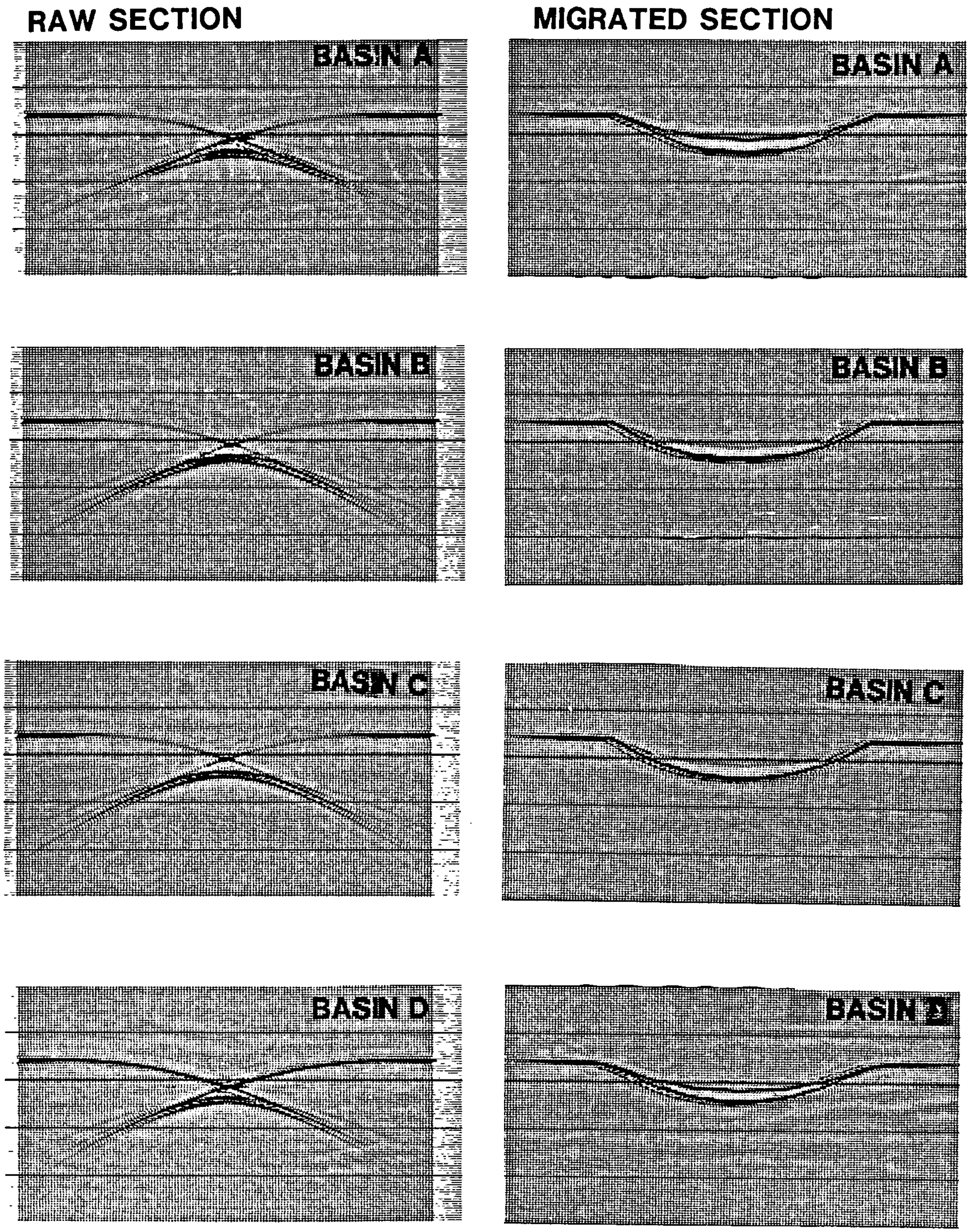

Figure 3-4 Raw and migrated sections of 5500 ft depth circular basins.

The Basin (circular) model was profiled at various depths to evaluate the raw and migrated 3-D effects. Since the radius of curvature at the bottom of the basin was 4100 ft and the basin relief was 1000 ft we can expect a buried focus (foci) effect on the 3100 ft depth profile line. Examining the raw sections in Figure 3-5 at the 2500 and 3500 ft depths, we notice that the section amplitude was so large that on playback the peaks wrapped around and the tops of the peaks appear to the left of the high amplitude (this is a function of our particular section display program). The amplitude of this event is 10 to 15 times larger than any other event on the section.

The diffraction events on the 3500 ft section are once again due to the geometry of the basin and the coarseness of the boundary sampling. They disappear with depth.

The 7500 ft profile section appears to be the classical example of a 2-D buried focus but the migrated version on the next figure does not show this. The migrated version of Figure 3-5 is shown in Figure 3-6. At 500 ft the migrated basin appears to be a 2-D structure while at 7500 ft we notice the extra layer produced by the out-of-plane geometry. As the extra layer gets thinner, we approach the buried focus depth and the two events superimpose to yield the abnormal amplitude in the migrated sections. The large amplitude event in the 2500 ft and 3500 ft sections is a giveaway to 3-D effects.

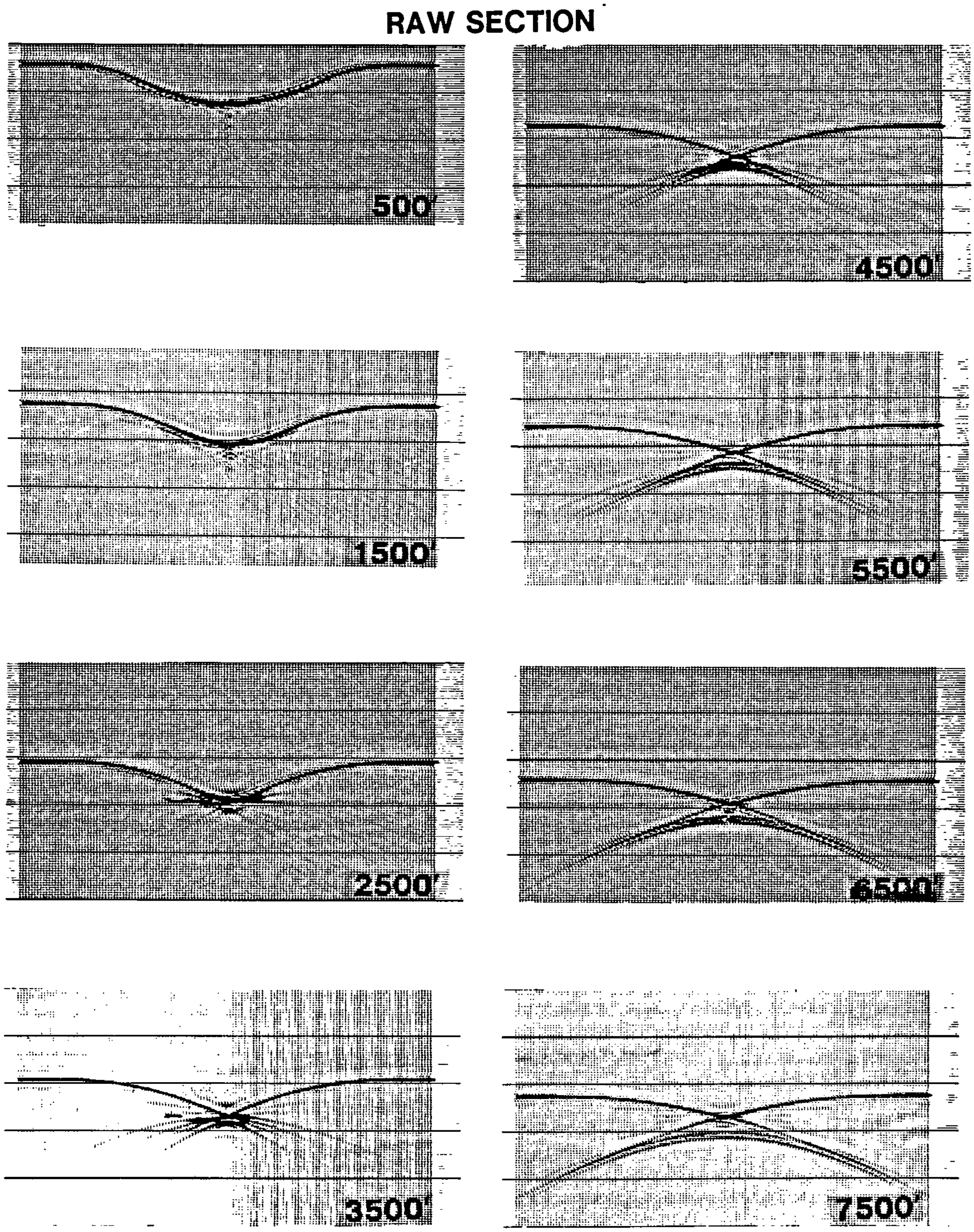

Figure 3-5 Depth effect of circular basin -- raw sections.

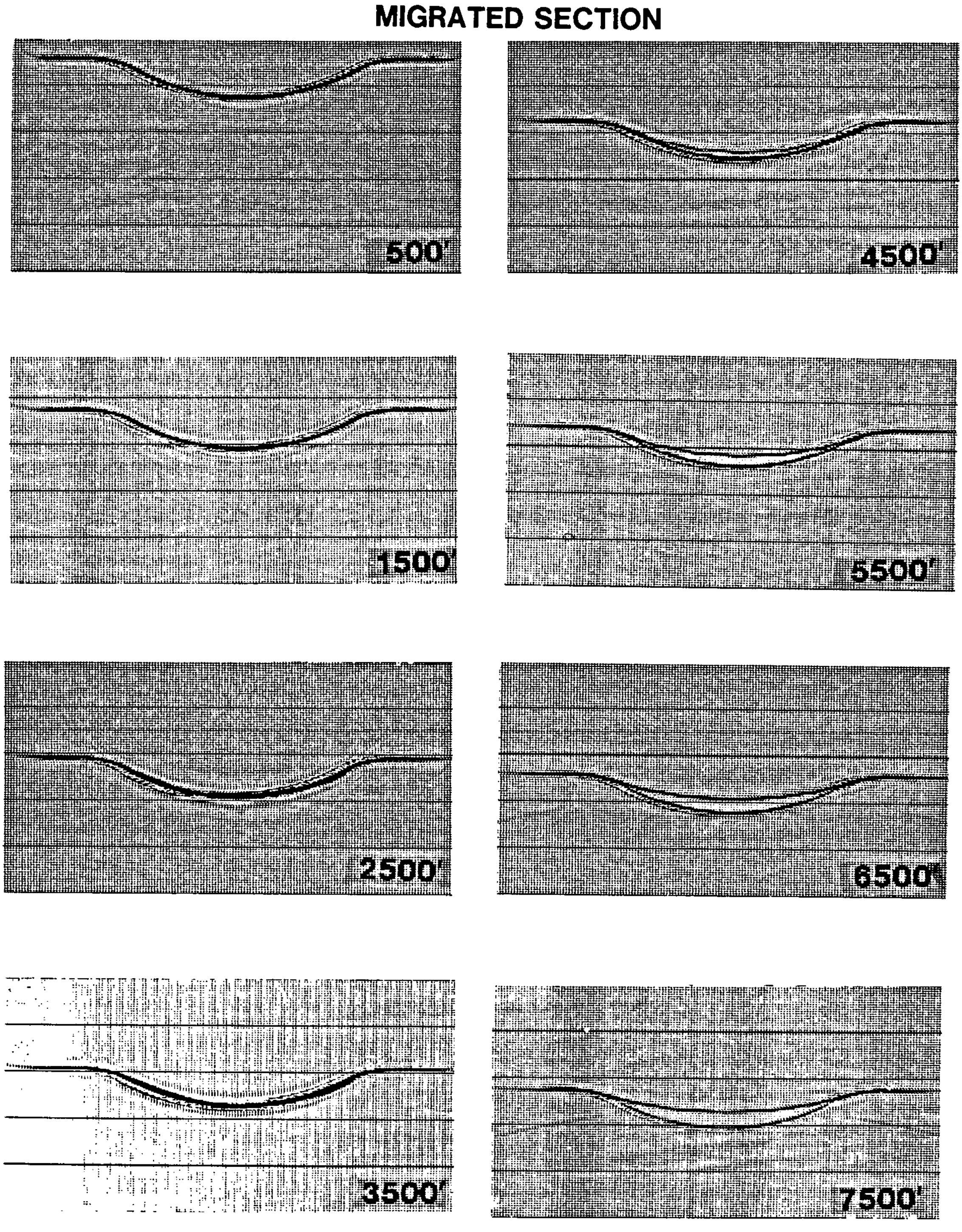

Figure 3-6 Depth effect of circular basin -- migrated sections.

The extra layer is not evident on the raw section because of the exact symmetry of the model. The extra layer event arrives at the cross-over time on the raw sections.

This interpretational pitfall of the "extra layer" of sediment in the basin is not easily avoided. The 90^{o} phase shift, even if recognized could have been introduced by the reflectivity function if the layering was transitional. Basically one relies on questioning the probability of having a geological setting that would give this type of thinning.

If the extra layer is recognized then a rough estimate of the areal size of the model can be made by mapping the upper event in the 7500 ft section out of the plane of the profile line.

From this figure we would expect deeper structures to be more susceptible to 3-D false interpretations. However if the total size of the basin decreases, then at 500 ft it can have a 3-D effect also.

B. SYNCLINE VERSUS CIRCULAR BASIN

Shown in Figure 3-7 are the raw time sections from a 2-D syncline and a 3-D circular basin. The most evident features in this comparison of 2-D structures versus 3-D structures is that the differences are hard to find except for the 90^{o} phase shift in the

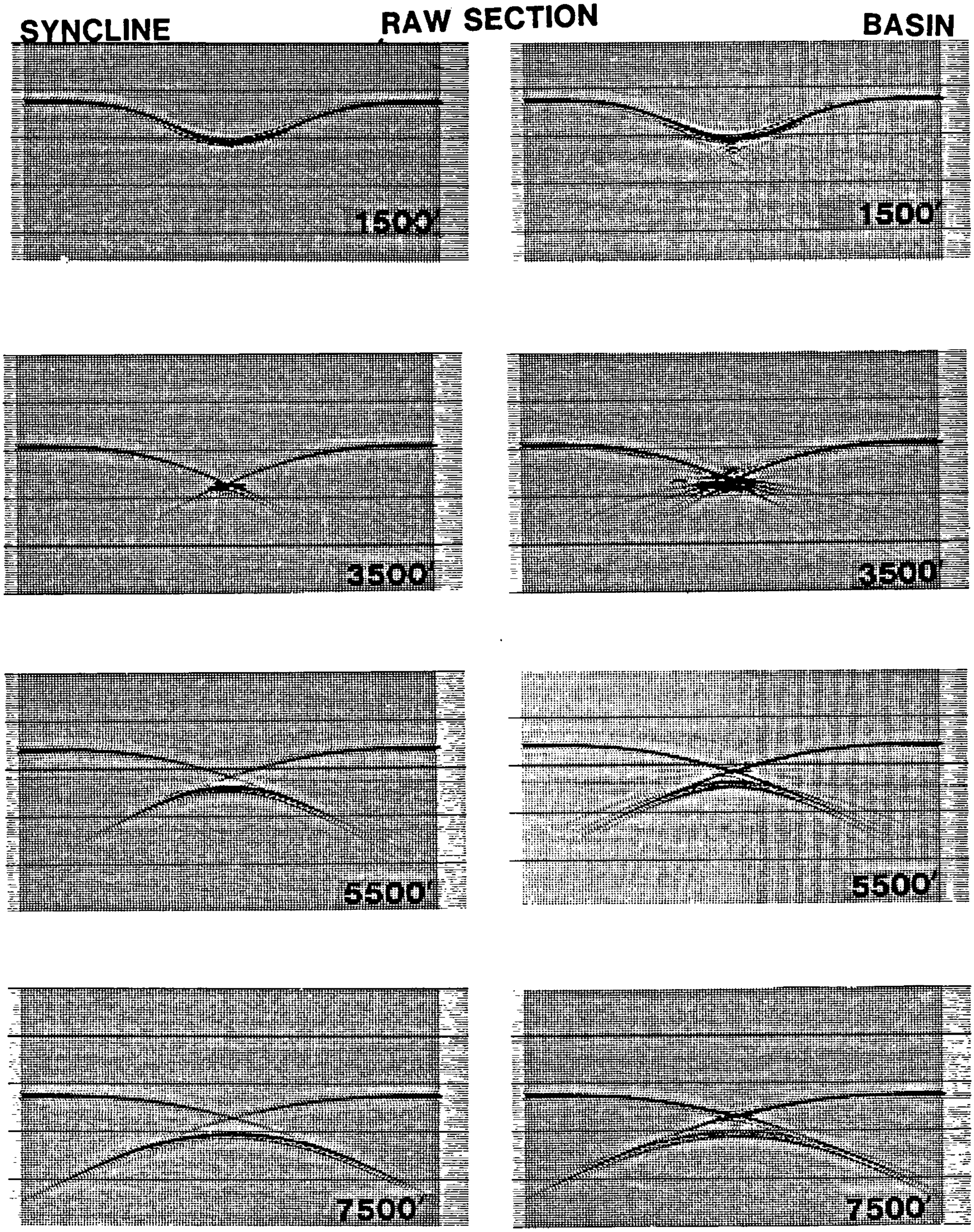

Figure 3-7 Two-dimensional syncline versus 3-D basin
-- raw sections.

syncline section as opposed to the 180° phase shift in the basin section. The similarity between these two sets of raw time sections occurs because the seismic lines were shot directly over the center of the 3-D basin and along the "dip" profile of the 2-D syncline. The migrated version of Figure 3-7 is shown in Figure 3-8. Once again, the existence of the extra "layer of sediment" is evident on the basin models while the 2-D synclines are a duplicate of the geological cross-section. Note that the amplitude in the migrated sections remains about the same for the 2-D synclines but changes for the 3-D basins as a function of depth. It is surprising how similar the raw (unmigrated) sections appear after viewing the migrated sections.

C. OBLONG BASIN

It is unrealistic to have a perfectly symmetrical basin, so the coordinates of the tiles were linearly stretched and compressed with respect to the xyz-coordinates to yield the equivalent models A and D as illustrated in Figure 3-9. The major-to-minor axis ratio was 1.16/0.86 which then gives the prototype scales of 6264 ft and 4644 ft respectively with a relief of 750 ft. This corresponds to the physical model shown in SAL Catalog No. 1, (p. 28).

The eight profile lines illustrated formed the standard grid which was shot over the various geologic models. Lines 5 and 6 are

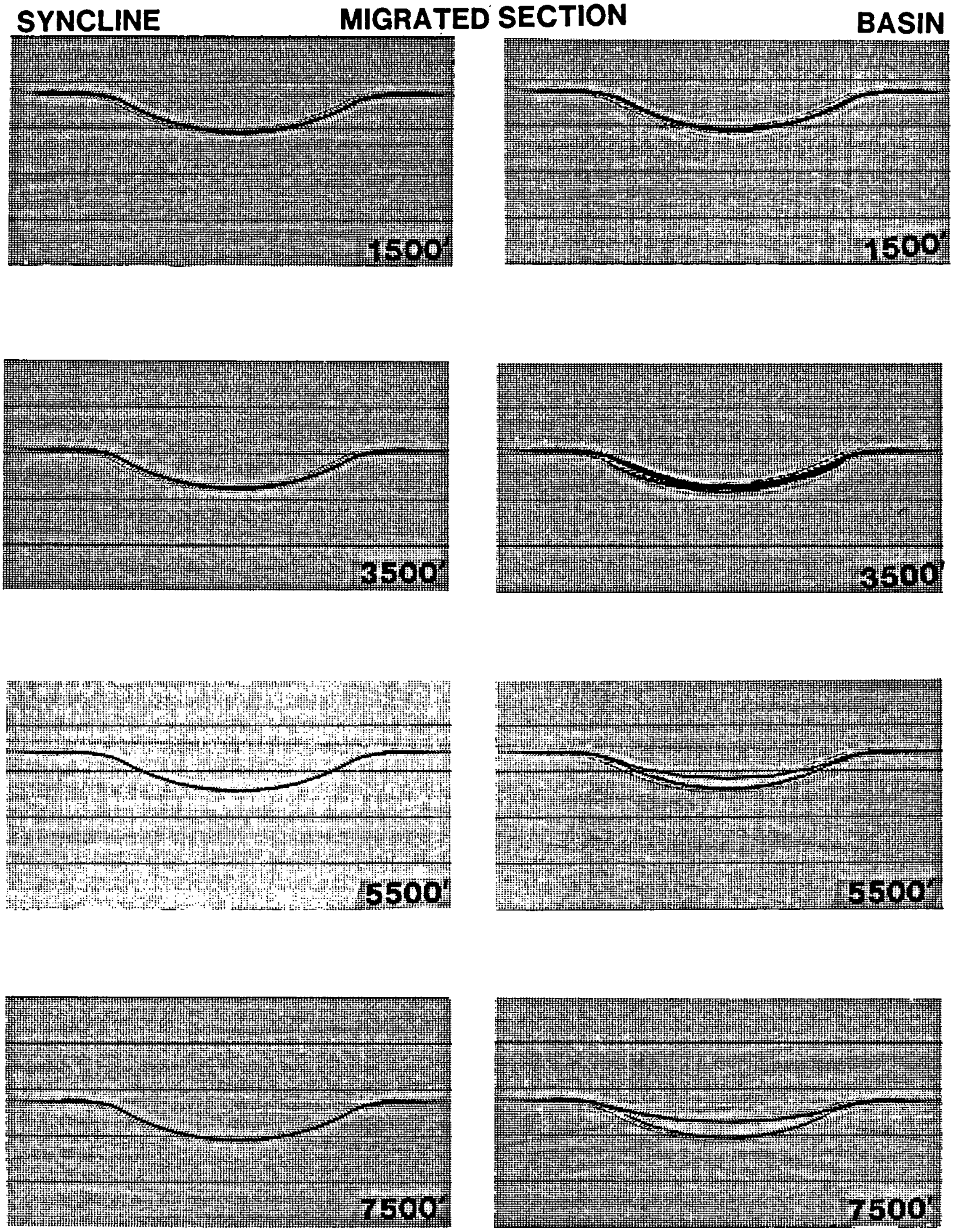

Figure 3-8 Two-dimensional syncline versus 3-D basin
-- migrated sections.

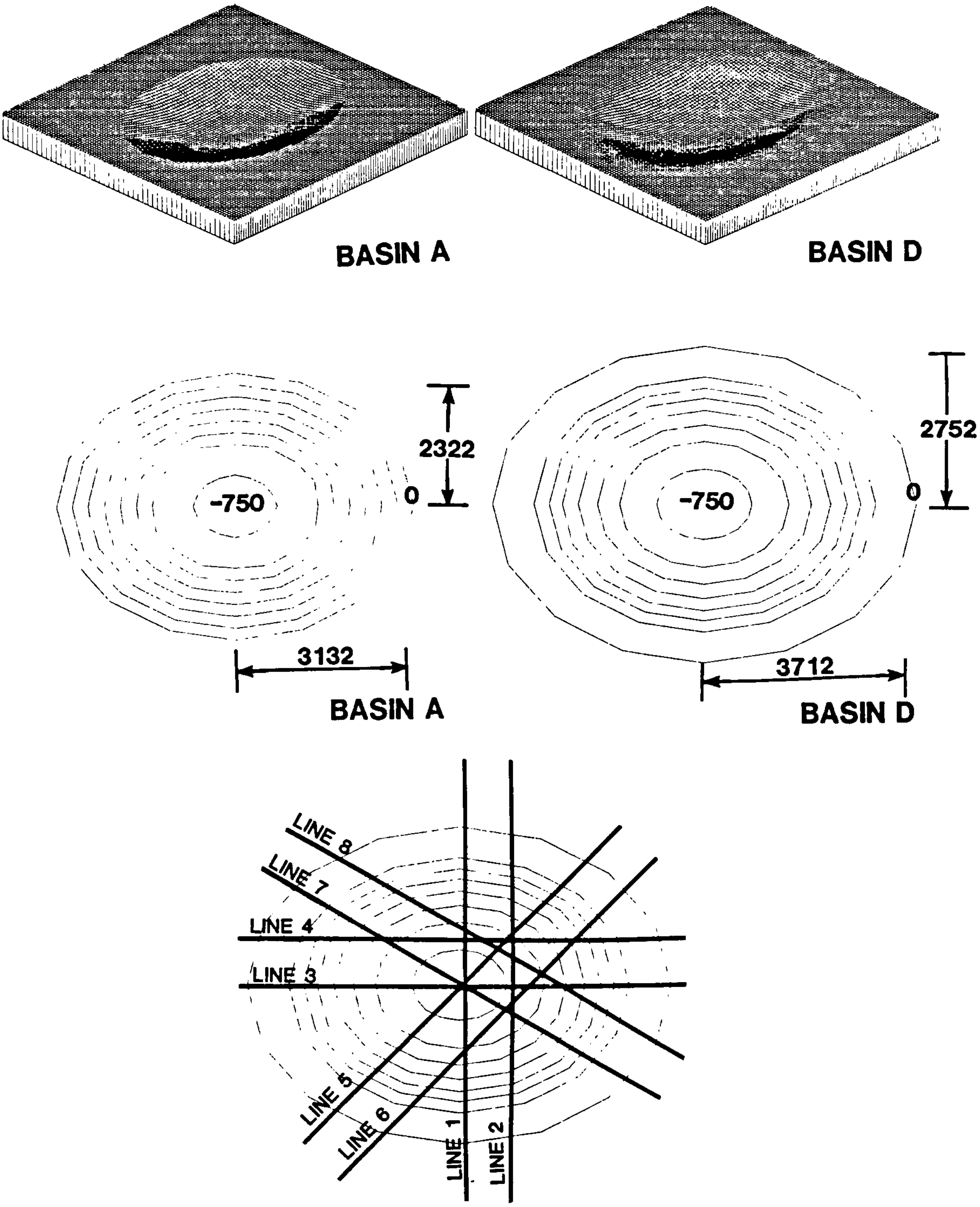

Figure 3-9 Isometric, contours and profile lines of oblong basin.

at an angle of 45° with respect to the EW direction while Lines 7 and 8 are at 30°. Lines 1, 3, 5 and 7 pass through the center of the basin and also through the center of the other models. The trace spacing on the time sections which will be shown later is 60 ft for the basin and 100 ft for the dome.

The oblong basin model was profiled in one principal plane, Line 1, at various depths and the resulting raw time sections are shown in Figure 3-10. Referring to Figure 3-9, notice that Line 1 crosses the oblong basin in the principal plane which has a radius of curvature of 4000 ft while the perpendicular principal plane has a radius of curvature of 6900 ft along Line 3. The depth of burial is the variation parameter for this set of sections.

The extra layer in the 9500 ft migrated section can now be found on the corresponding raw time section. The reason it does not have as large an amplitude as it did on the migrated circular basin in Figure 3-6 is because the oblong basin does not have the perfect symmetry and, thus, in-phase tuning results.

The apparent migration noise on the 9500 ft section (series of reversed "smiles" through the bottom of the basin) is caused by a linear interpolation of the complex frequency value in the FK migration program. Had the geometric interpolation been used (that is the linear interpolation of the phase and a geometric average of

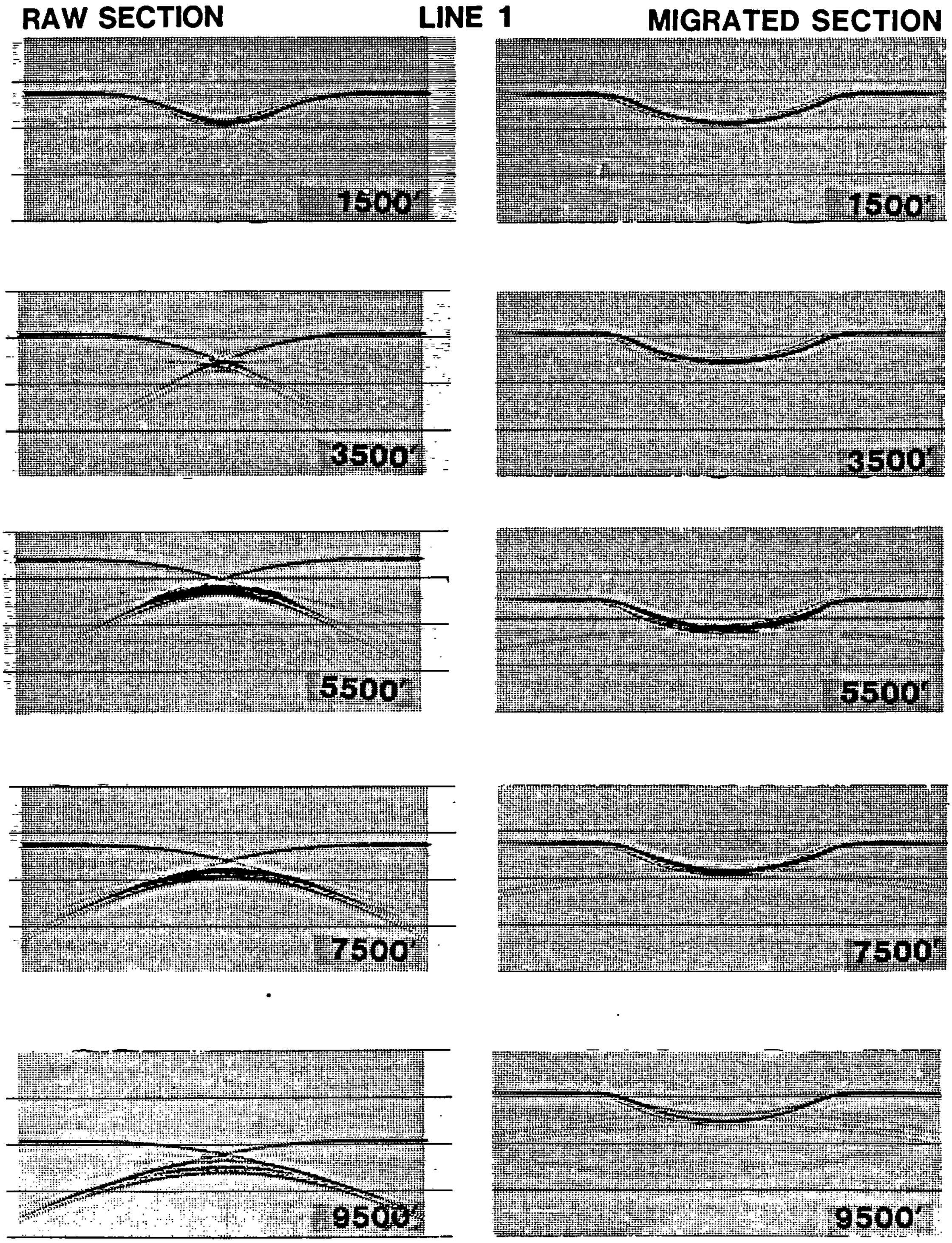

Figure 3-10 Depth effect of oblong basin
-- principal plane Line 1.

the amplitude), this noise would have been reduced.

Five different depths were examined for a line (Line 8) that does not cross the center of the basin. Both the raw time sections and the migrated sections are shown in Figure 3-11. For depths below 5500 ft the migrated sections erroneously depict an active fault with sediment contemporaneously filling the basin. Once again the "smiles" on the 9500 ft migrated section are interpolation errors.

The raw time sections for the eight profile lines illustrated in Figure 3-9 are shown in Figure 3-12. Notice in Line 4 that the lower events are not connected to the continuous upper horizon. This 3-D effect is observed when profiling tight curvature structures (basins) that are not in the plane of the seismic profile line. It is a focused event from the far flank of the structure.

The 2-D migrated version of Figure 3-12 is shown in Figure 3-13. The "active" fault that was misinterpreted before now becomes a false graben as shown on Lines 5 and 7. Because of the symmetry, a double fault is exhibited. This is a common situation that geophysicists see on field data that have been migrated.

Up to now, all the time sections were generated for a zero-offset distance between the source and receiver. To illustrate the problems of stacking before migration, several previous lines

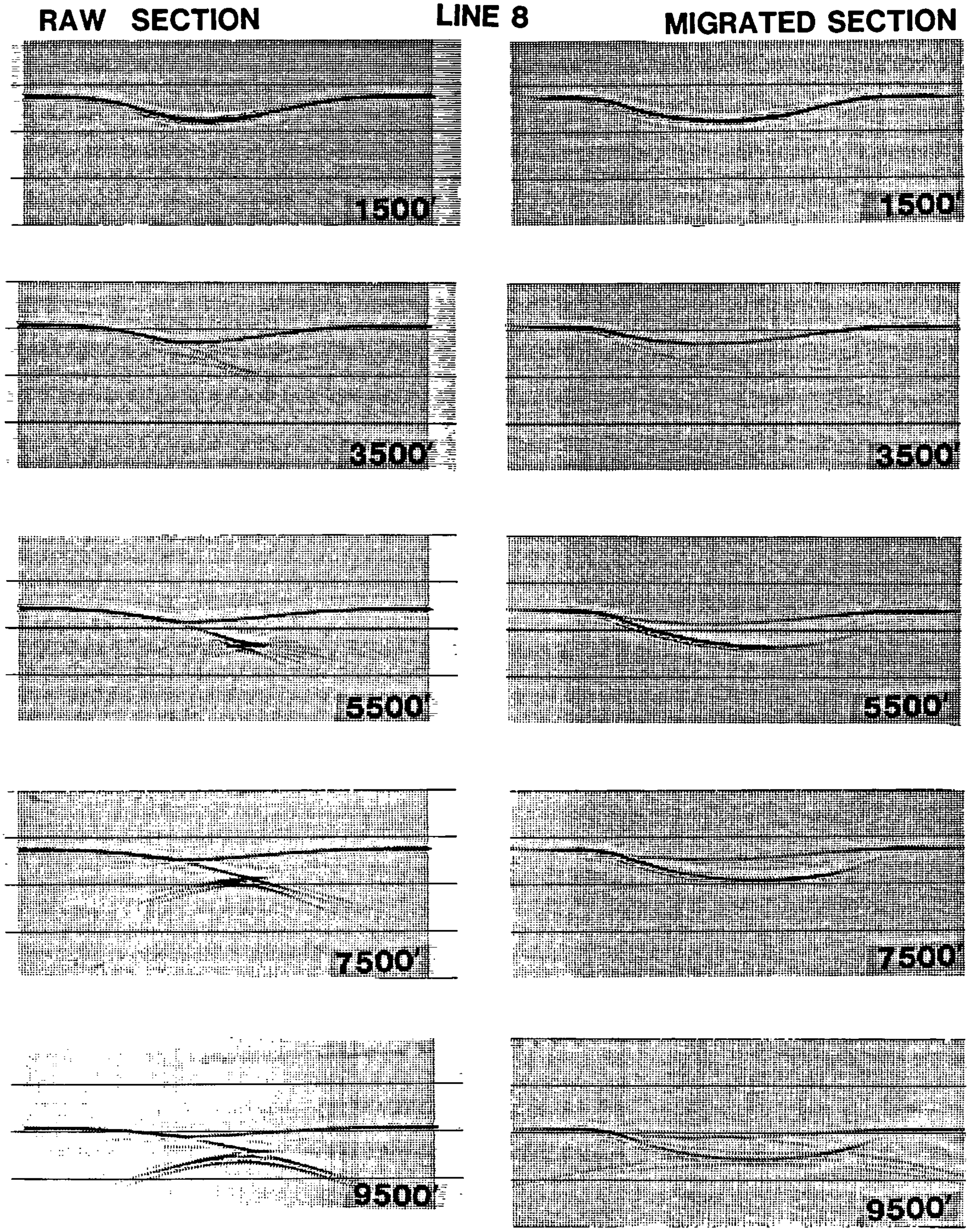

Figure 3-11 Depth effect of oblong basin -- oblique Line 8.

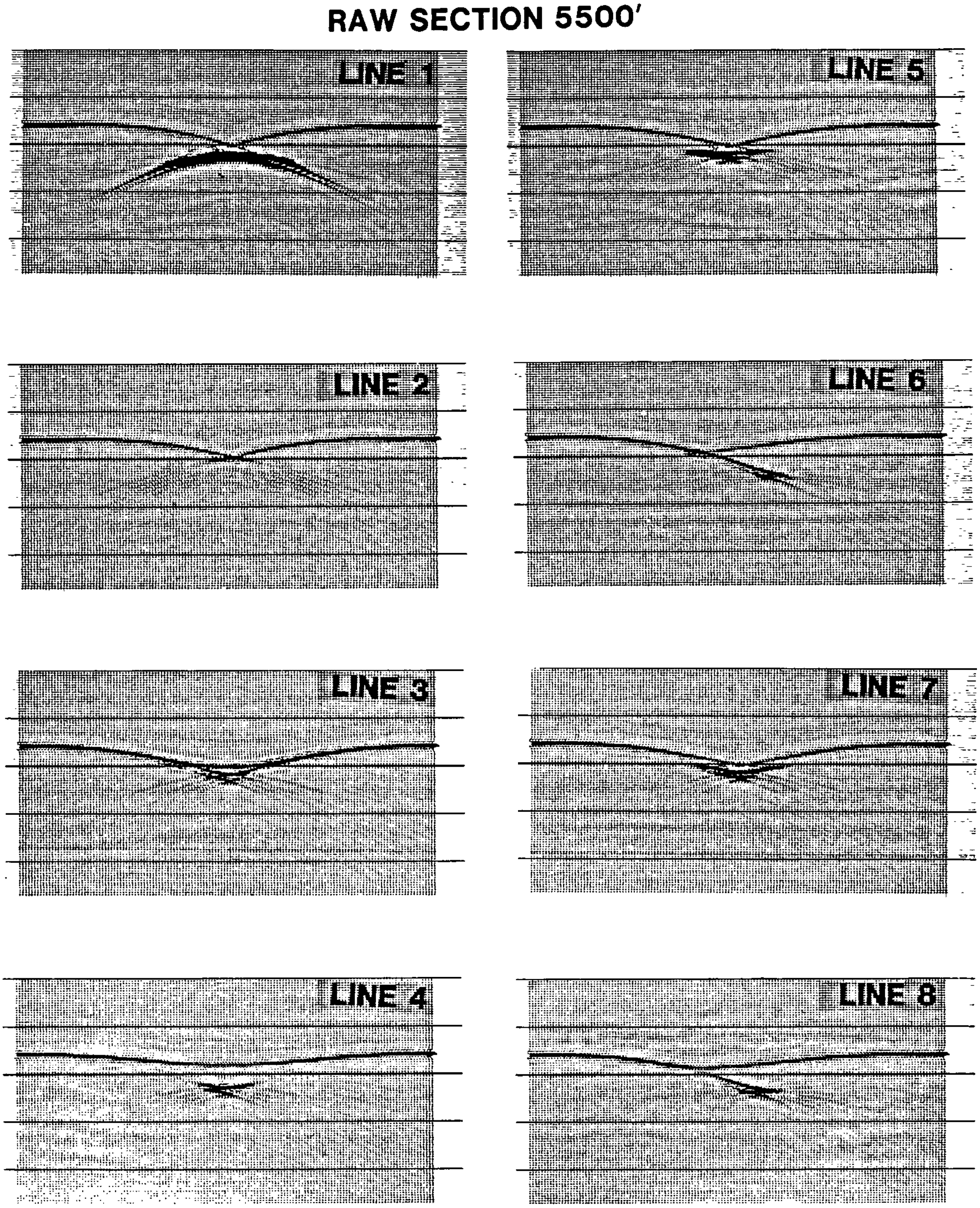

Figure 3-12 Profile direction variation across 5500 ft depth oblong basin -- raw sections.

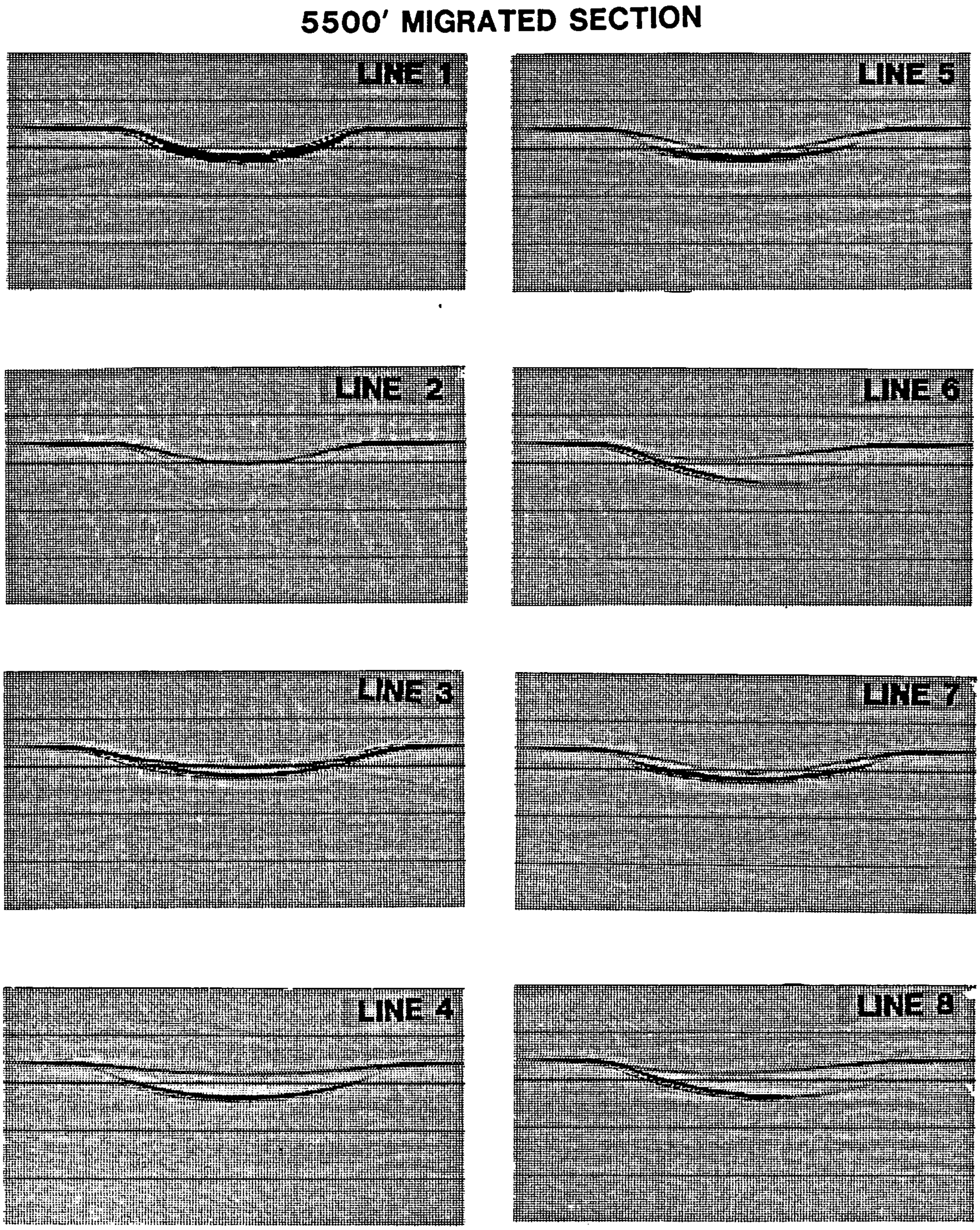

Figure 3-13 Profile direction variation across 5500 ft depth oblong basin -- migrated sections.

will be examined in a 12-fold CDP format. Both single-fold data and 12-fold data were collected across the oblong basin which was at a constant depth of 5500 ft and are shown in Figure 3-14. The CDP data with the CDP spacing of 60 ft have a near-trace offset of 800 ft and a far-trace offset of 9600 ft. The CDP gathers were stacked with a constant velocity of 12000 ft/s. Only three profile lines are shown here, namely Lines 1, 3, and 8.

It is usually assumed that the stacked section represents a zero-offset section and this is not always the case. The main problem is the deterioration of the stacked diffraction tails. In Figure 3-14 all the diffraction tails were suppressed except for those in Line 1 where one diffraction event was enhanced after stacking. On the 12-fold migrated sections, the edge portions of the basin have weaker energy than on the corresponding single-fold migrated sections, because an incorrect "stacking" velocity was used.

Another feature that was tested across the basin was crooked-line processing. A 12-fold crooked-line with the CDP spacing of 60 ft and lateral-offset variations to 8 CDP spacings was gathered and the resulting time sections are shown in Figure 3-15. The common mid-points (CMP) are shown in map view of Figure 3-15. This line is a variation of Line 8 in Figure 3-9. Data were stacked and migrated two-dimensionally and three-dimensionally.

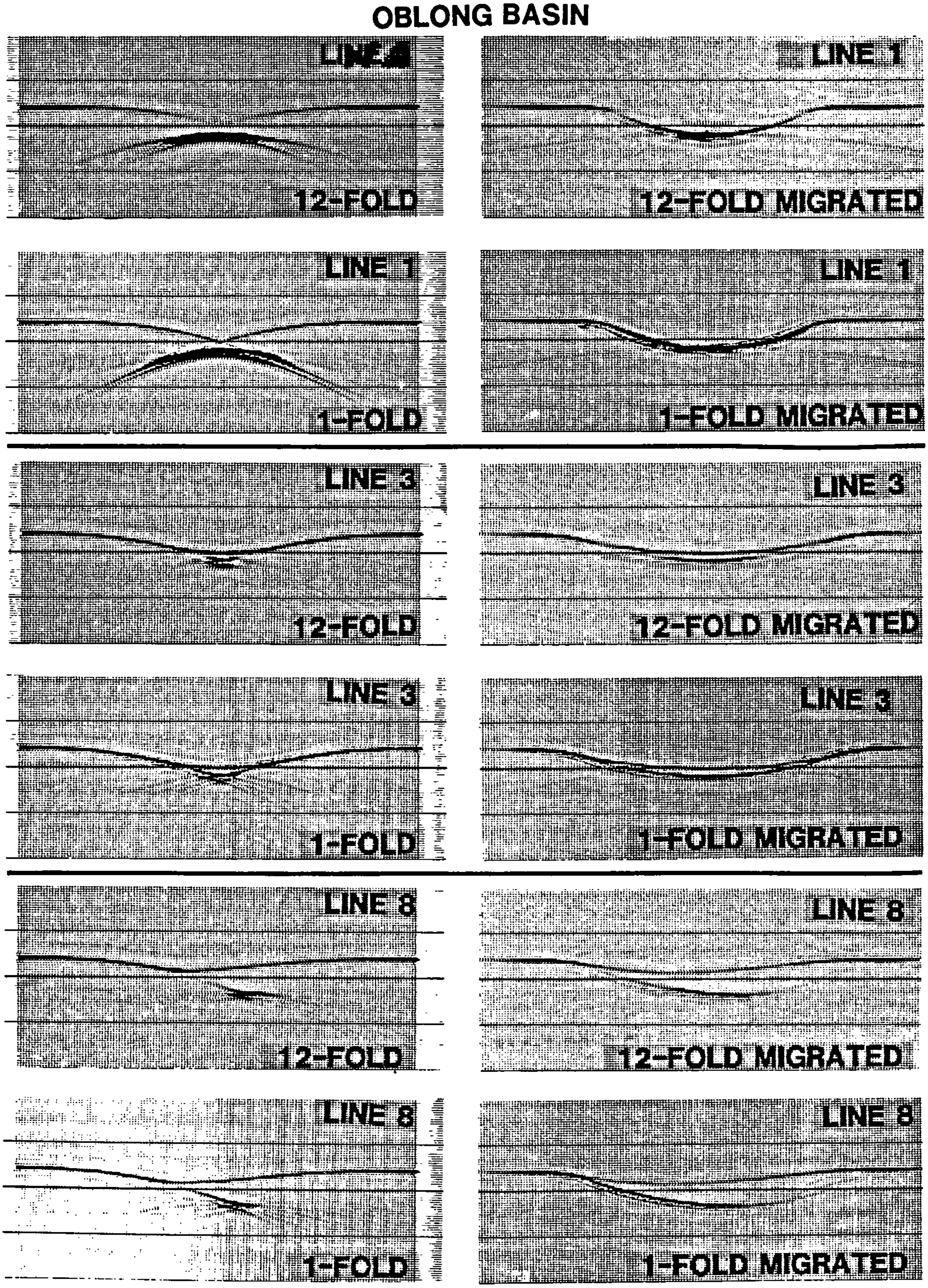

Figure 3-14 Single fold versus 12-fold -- oblong basin.

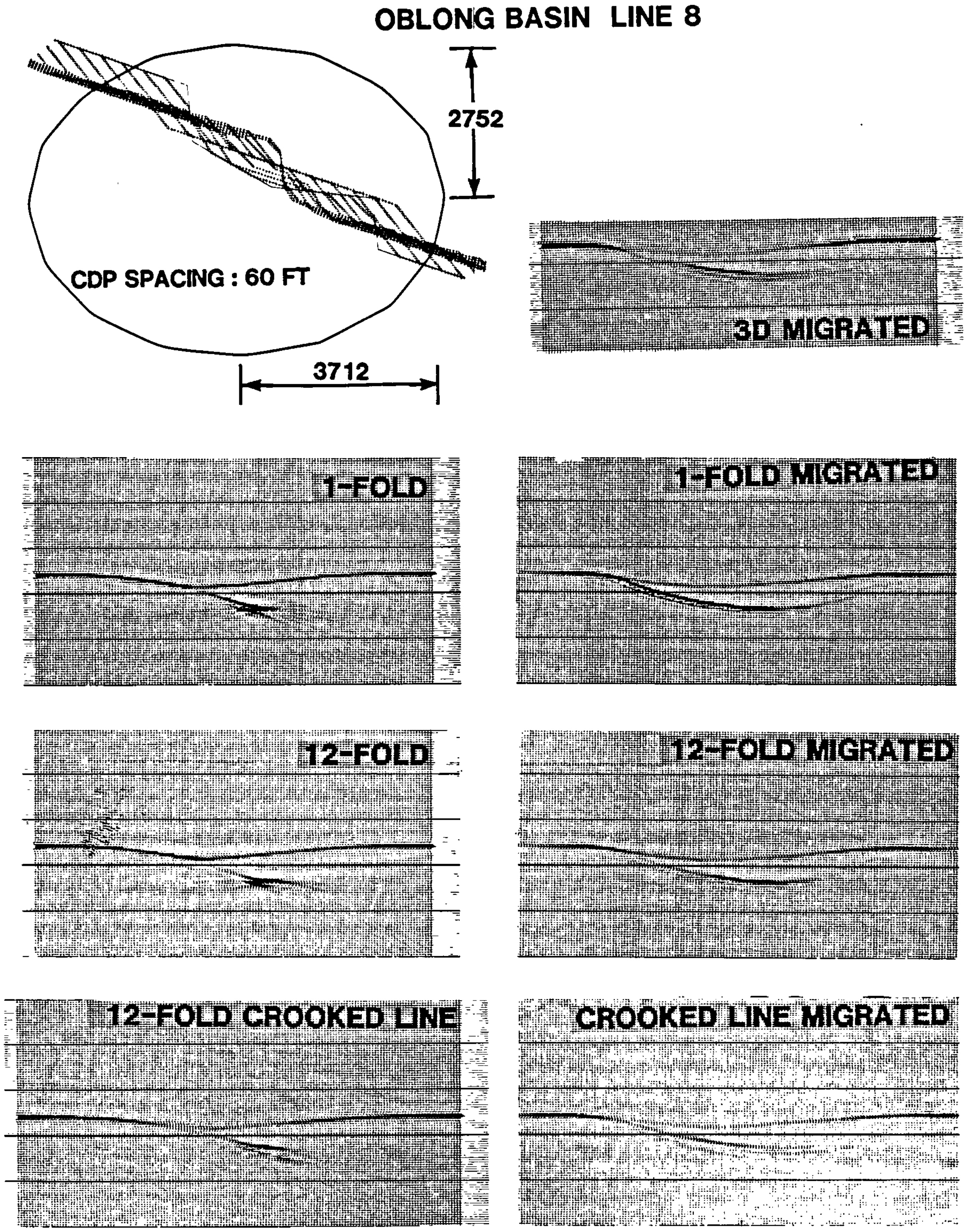

Figure 3-15 Crooked-line across oblong basin.

The 2-D processing (labeled 12-fold) made no corrections for the CMP mislocation. The data were brute stacked and migrated. The 3-D processing, however, applied a variation of the 2-step Kirchhoff migration algorithm. The original Line 8 (straight line) falls in the densely plotted portion of the CMPs. This line was processed by the 2-step Kirchhoff program (Hu, 1980) and the traces (un-NMOed) were projected, based on the CMP, onto the straight profile line. This was migrated and is shown as 3-D migrated. It is not a total 3-D migration though, but an attempt to correct for the CMP mislocation. A new velocity and stacking algorithm will be discussed in Chapter VI which will improve the S/N of the crooked-line data.

Notice the similarity between the 1-fold, 12-fold and 12-fold crooked-line sections. Numerical modeling allows one to test the severity of the bends in the crooked line data to determine if it can be processed as if it were straight-line data.

The results of 3-D 2-step migration for three lines (1, 3 and 8) are shown in Figure 3-16. Also shown are the first-step migrated sections with the 2-step 3-D migration process. Notice that the amplitude in the middle of the basin in the first-step migrated sections is lower than that in the corresponding unmigrated 1-fold sections. This tells us that the out-of-plane diffractions were reduced by the first step process.

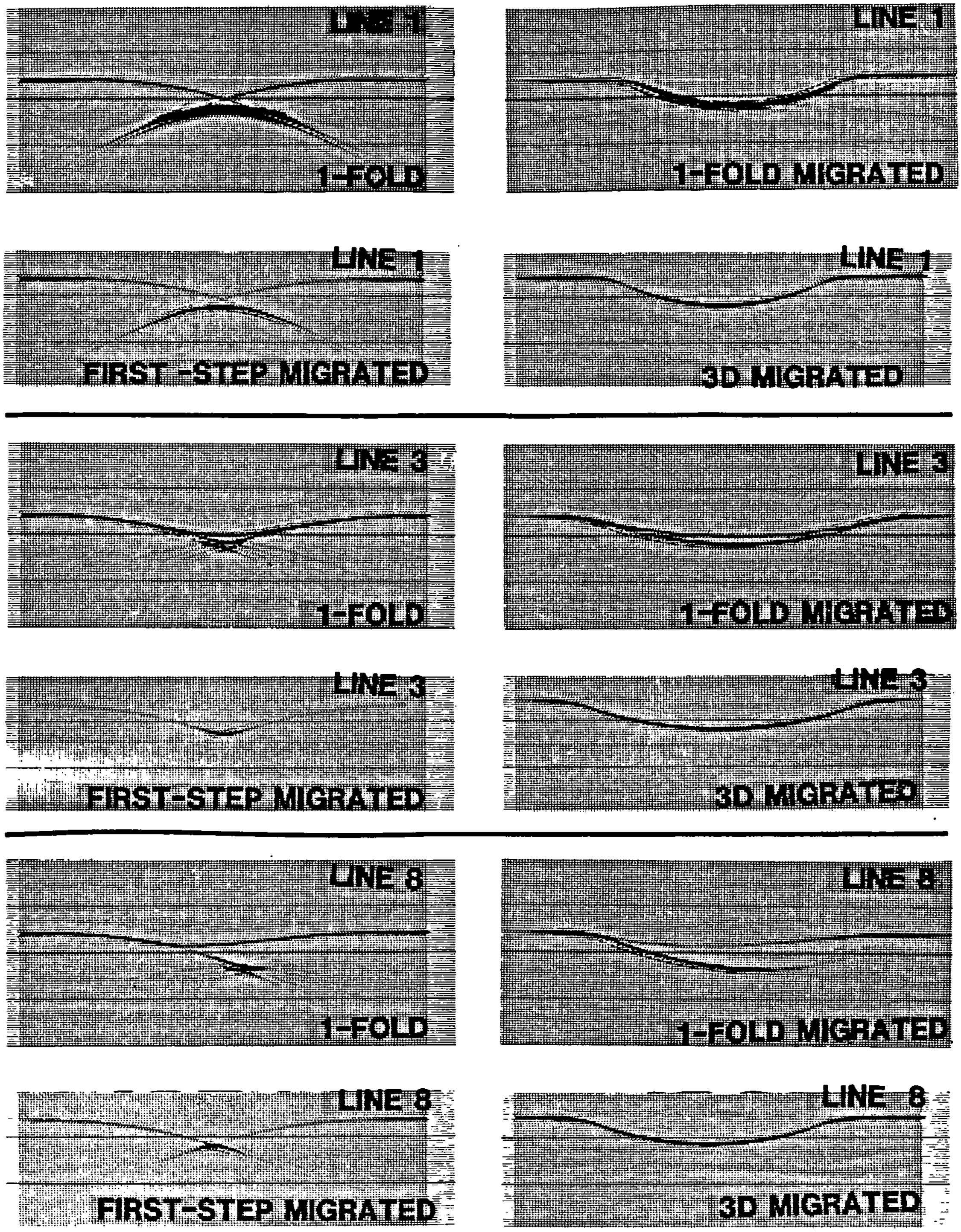

Figure 3-16 Two-dimensional migration versus 3-D migration -- oblong basin.

On Line 3 several extra diffraction events are obvious on the 1-fold raw section which then disappears after the first-step migration. On Line 8, the out-of-plane event after the first-step migration moved beneath the major negative anomaly. The first step migration, even though it is a perpendicular projection, has the apparent capability of moving the seismic energy laterally along the line.

The buried focus event in all the raw sections was phase shifted 90° after the data were first-step migrated. When data were finally 3-D migrated, all the sideswipe events were removed and structures were delineated accurately.

D. SMALL AND LARGE BASINS

When investigating the seismic effect of structural size, little information would be obtained if all dimensions were equally changed. This is because variation of depth would handle these cases if velocity is scaled inversely. Thus, the dip of the theoretical model must change significantly to evaluate the effect of varying size. The contour map and profile line positions of both the small and large basins are shown in Figure 3-17. They will remain the same in the following examples except that the contour values are reversed for small and large domes, as will be discussed later.

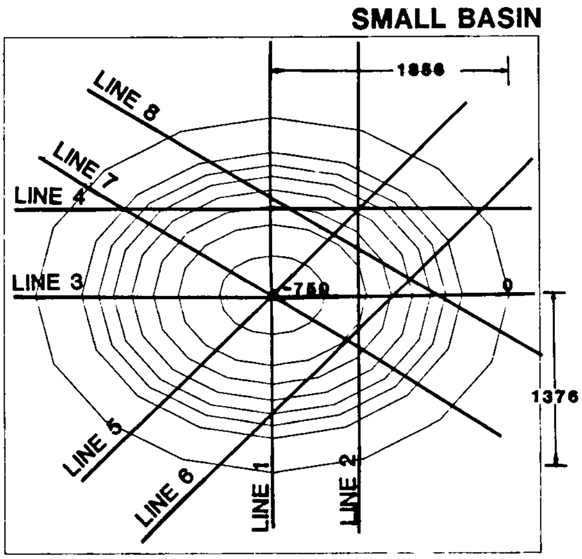

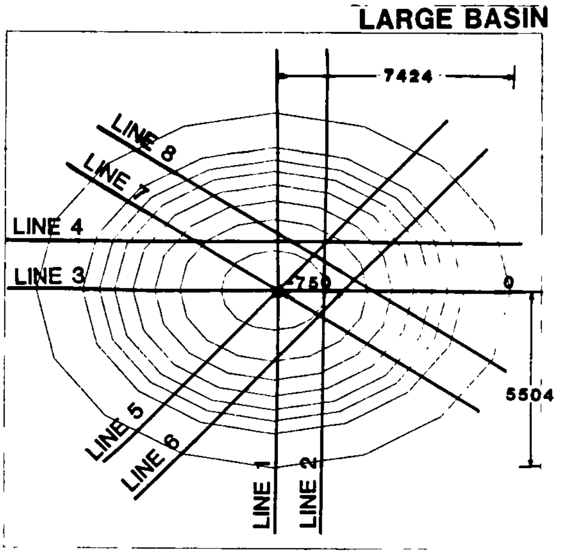

Figure 3-17 Profile line positions of small and large basins.

Shown in Figure 3-18 are raw time sections across a small oblong basin. In this numerical model the x,y dimensions were scaled by 0.5, while the total relief of the basin was held constant with respect to Basin D in Figure 3-9. This does, however, make a rather unrealistic geologic model because of the steep dip.

The trace spacing (60 ft) for these sections remains the same as those of Figure 3-12. As one might anticipate the hole at the top of the basin has healed itself as depicted in all the raw time sections. Also the reflected-diffracted energy from out of the plane is once again not touching the upper event.

The 2-D migrated sections shown in Figure 3-19 which correspond to the raw time sections shown in Figure 3-18 have an additional extra event that the larger basin sections did not have. In fact the interpretation would be a "buried channel" on almost all of the sections. In fact, if one is doing seismic stratigraphy, an apparent "cross-stratification" is evident in a few of the channels. Slightly different interpretational pitfalls have occurred on the small basin in Figure 3-19 that were not obvious in the larger basin shown in Figure 3-13.

The effectiveness of 3-D migration versus 2-D migration for interpretational purposes is illustrated in Figure 3-20. Again, all the buried-foci events with 180° phase changes have been shifted 90°

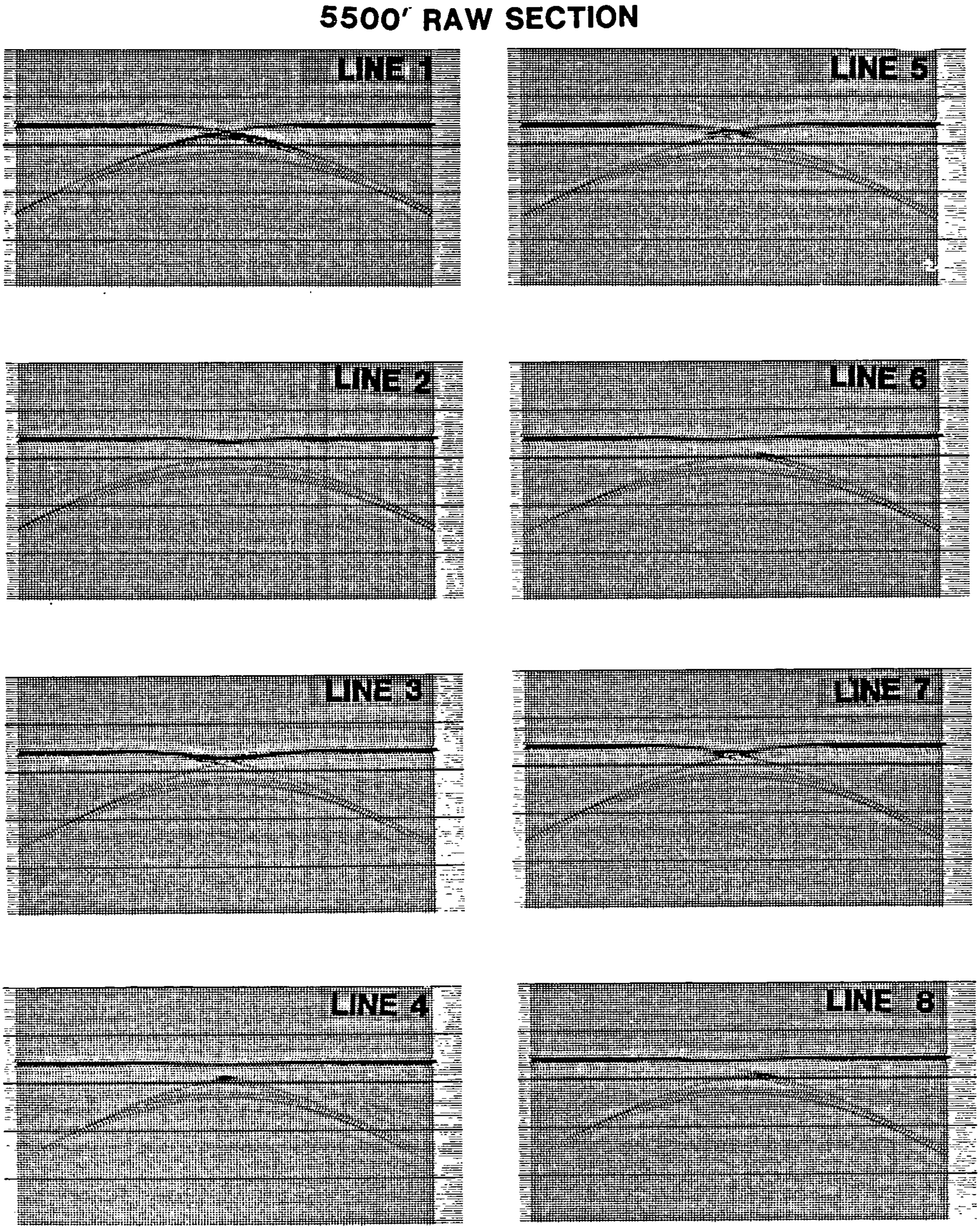

Figure 3-18 Profile direction variation across 5500 ft depth small oblong basin -- raw sections.

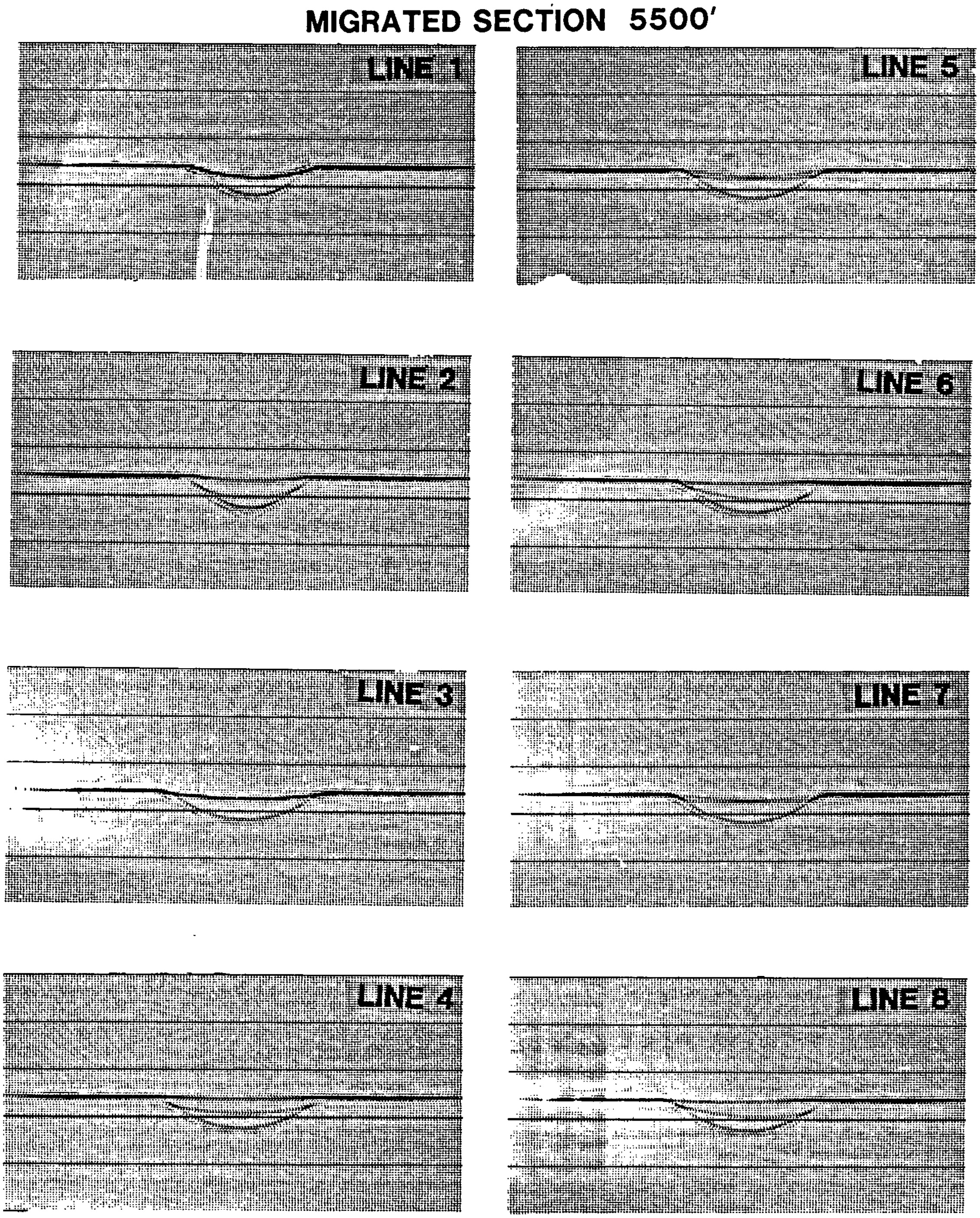

Figure 3-19 Profile direction variation across 5500 ft depth small oblong basin -- migrated sections.

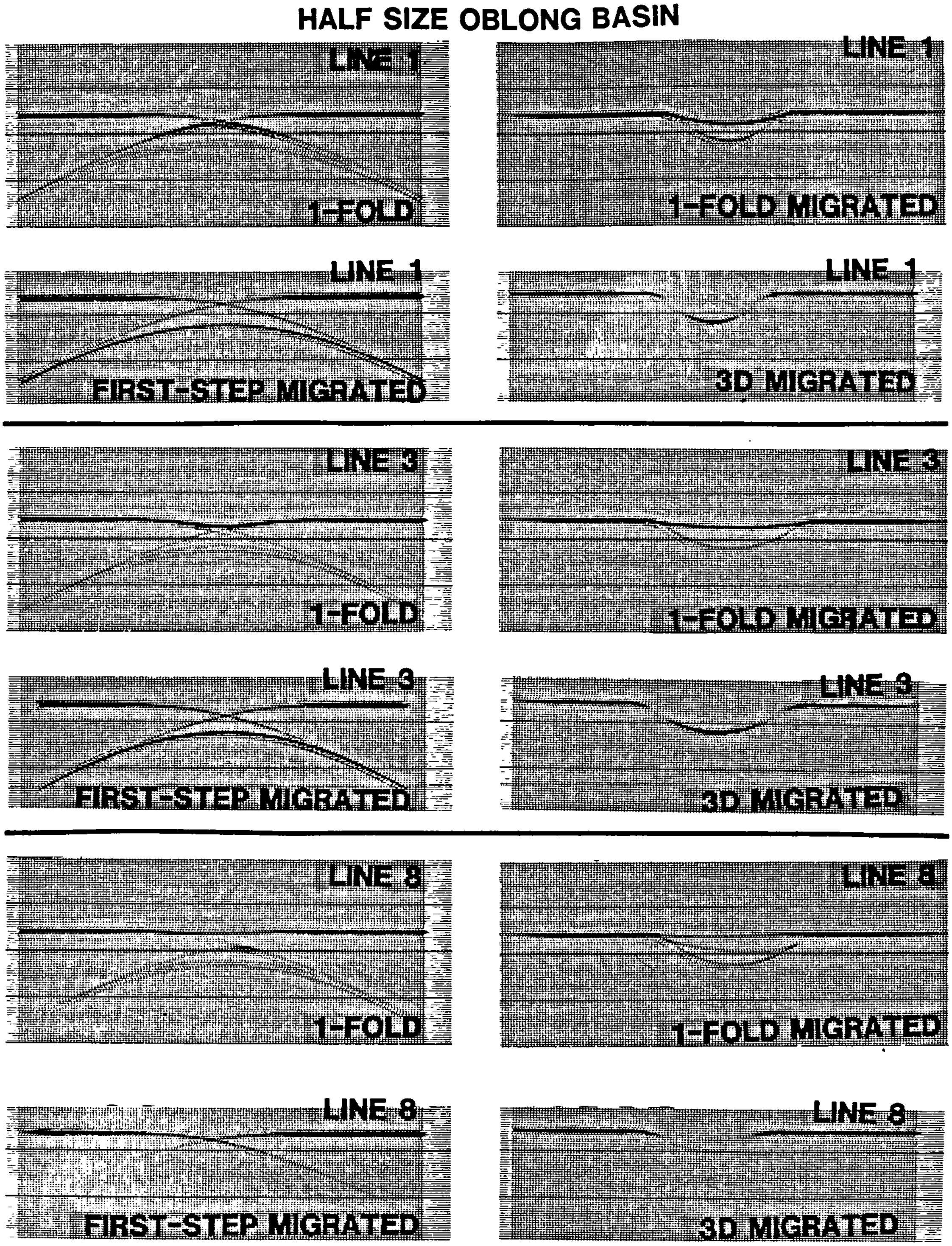

Figure 3-20 Two-dimensional migration versus 3-D migration -- small oblong basin.

after first-step migration. The cross-sections of the basin along the three discussed lines were well defined and the extra events were removed after 3-D migration. The weak energy at the steep portion of the basin in the 3-D migrated section is caused by an insufficient aperture size when the data were collected. Likewise, the uneven amplitude on the first-step migrated section and the loss of energy on the 3-D migrated section of Line 8 was caused by insufficient data collection. The need for areally gathered data and 3-D migration is dramatically illustrated by these results.

Increasing the x,y dimensions of the oblong basin model by a factor of 2 and retaining the same total relief yielded a gently dipping structure. The resulting time sections along the eight profile lines are shown in Figure 3-21. In order to see the entire basin, the length of the lines were increased while the trace spacing remained the same (60 ft). The raw time sections showed no unexpected events and thus these sections were not even migrated.

E. TILTED BASIN

In order to test the seismic effect of dip on 3-D structures, the previous eight profile lines were also taken over tilted models of the basin and dome. The isometrics and the contour maps of the tilted basin and dome are shown in Figure 3-22. Locations of the eight profile lines across the tilted basin and dome are shown in

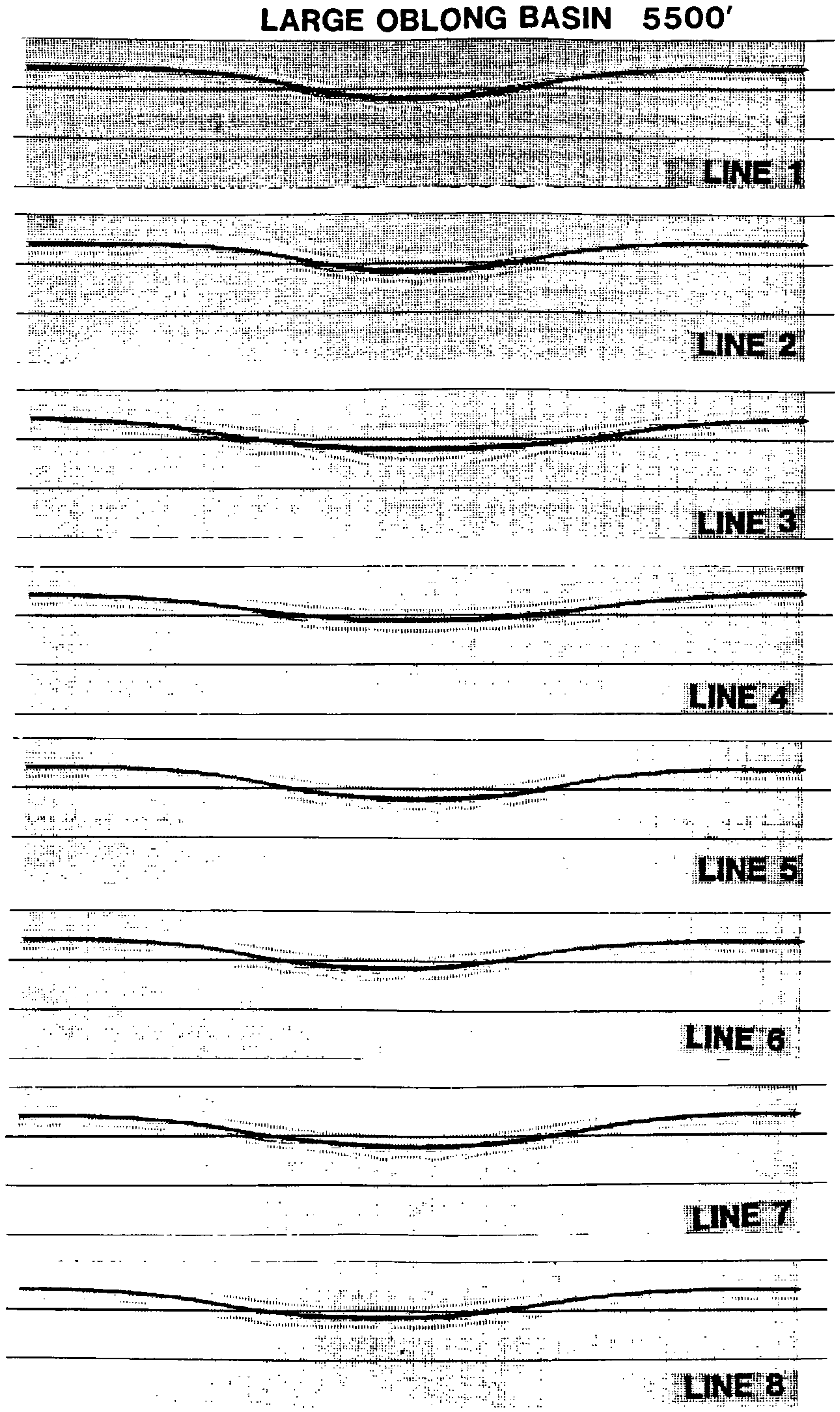

Figure 3-21 Profile direction variation across 5500 ft depth large oblong basin -- raw sections.

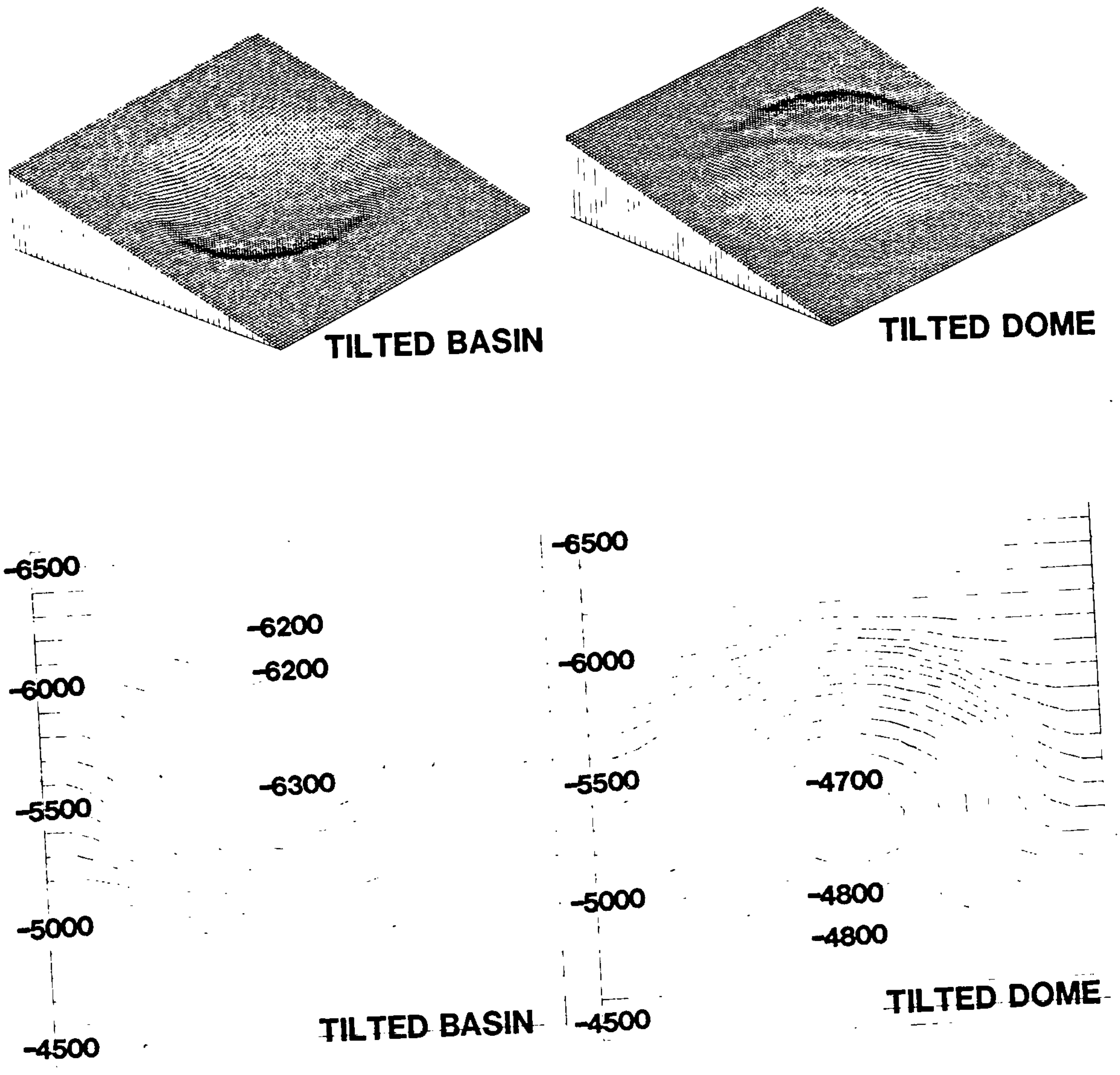

Figure 3-22 Isometrics and contours of tilted basin and dome.

Figure 3-23. Basically, the oblong basin and dome shown in Figure 3-9 were tilted down to the north direction by 15° (see Figure 3-22).

The time sections along the eight profile lines across the tilted basin are shown in Figure 3-24. The crossing events in Line 2 could be interpreted as a fault while the "spike" energy in the middle of Lines 3 and 7 could be interpreted as ambient noise. The monoclinal event on Line 6 gives no indication of the basin.

The migrated version of Figure 3-24 is shown in Figure 3-25. The "spike" noise events on Lines 3 and 7 migrate into the classical "smile" which now forms a well-defined synclinal structure with a false upper layer. Obviously, dip degrades one's ability to interpret the basin's true structure or, worse, even recognize that it exists.

3.4 DOME

A. OBLONG DOME

Data corresponding to the profile lines shown in Figure 3-9 were collected over a dome (Figure 3-26). The dome has the same geometry as the basin with the sign of the z-coordinate changed. In order to collect all diffraction tails, a trace spacing of 100 ft was used in the data collection over the dome. The raw time sections (Figure

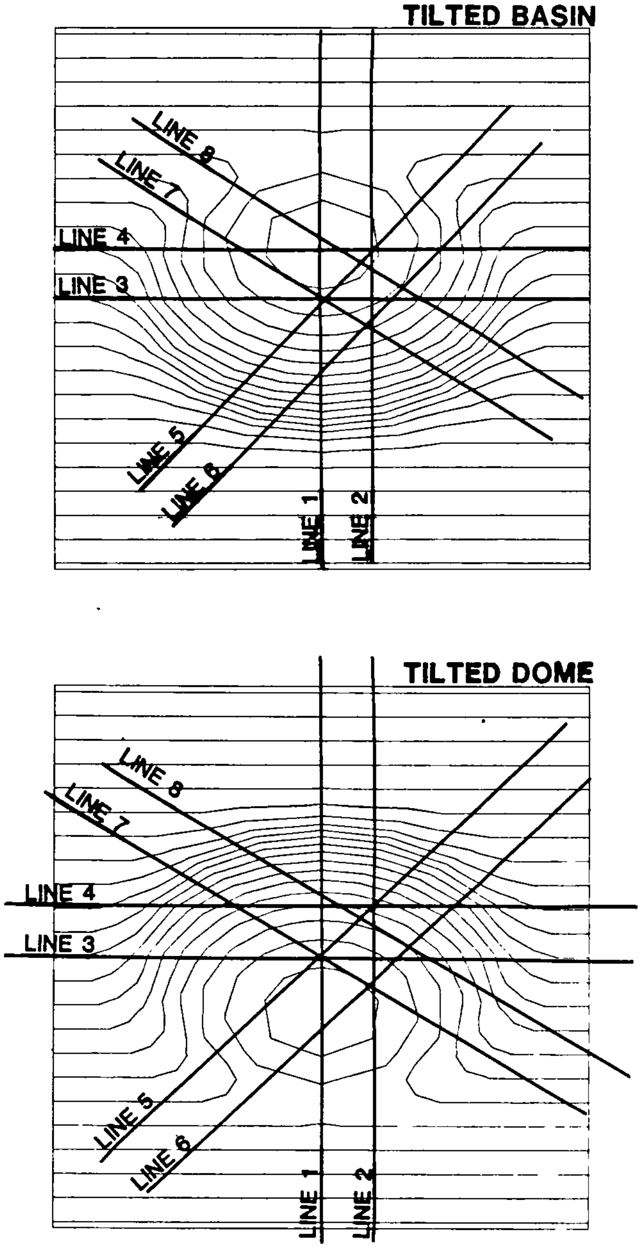

Figure 3-23 Profile line positions of tilted basin and dome.

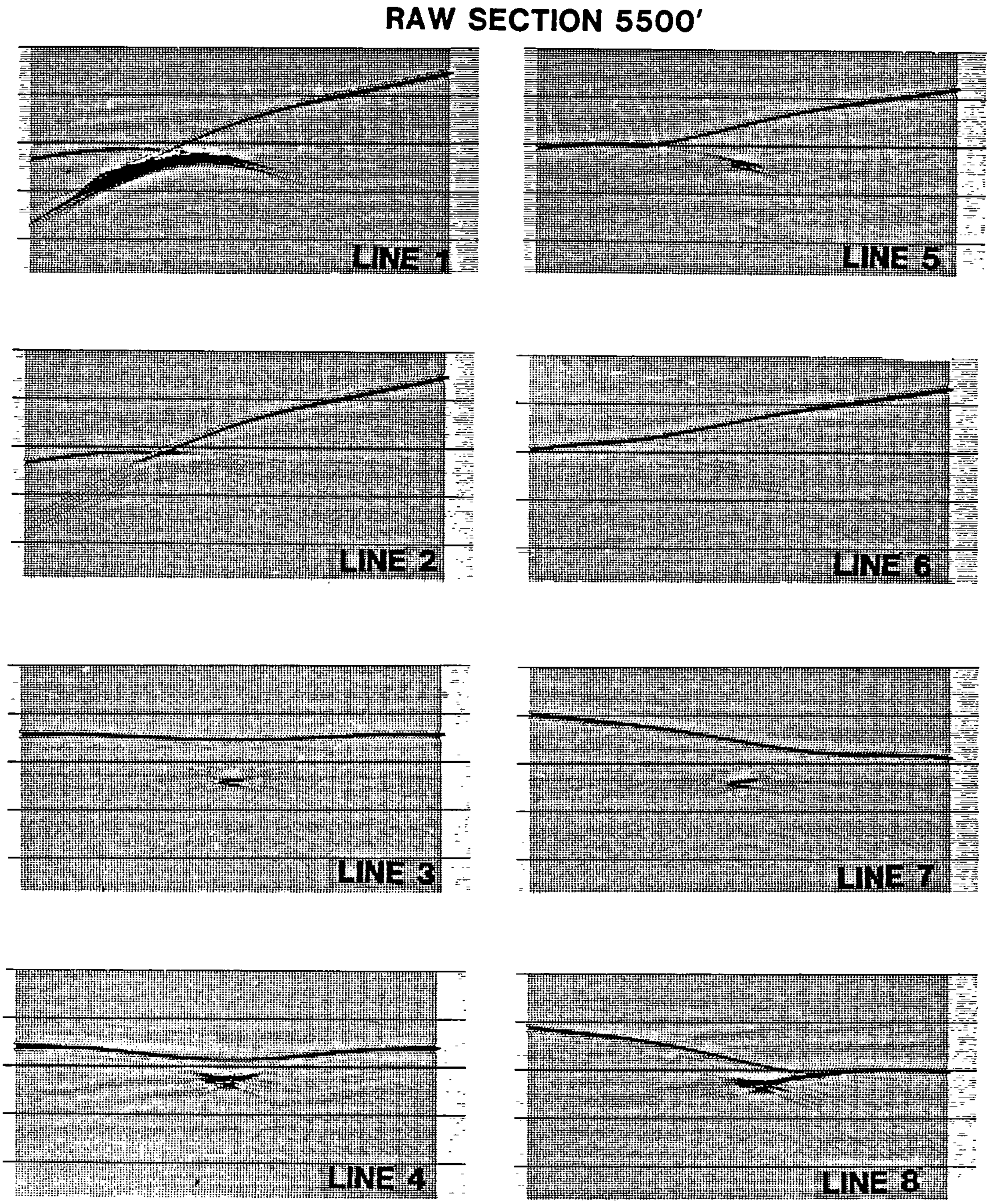

Figure 3-24 Profile direction variation across tilted oblong basin -- raw sections.

5500' MIGRATED SECTION

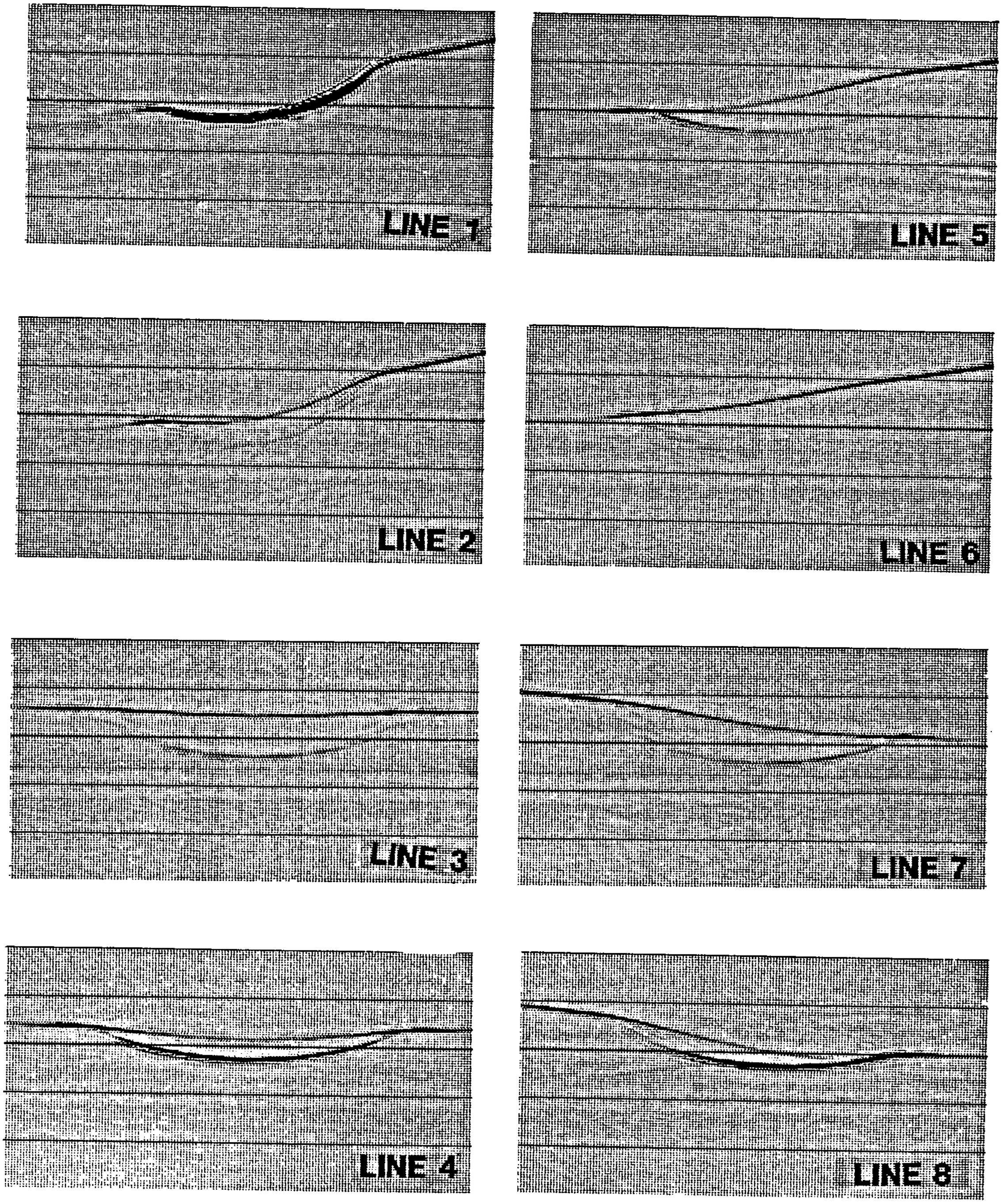

Figure 3-25 Profile direction variation across tilted oblong basin -- migrated sections.

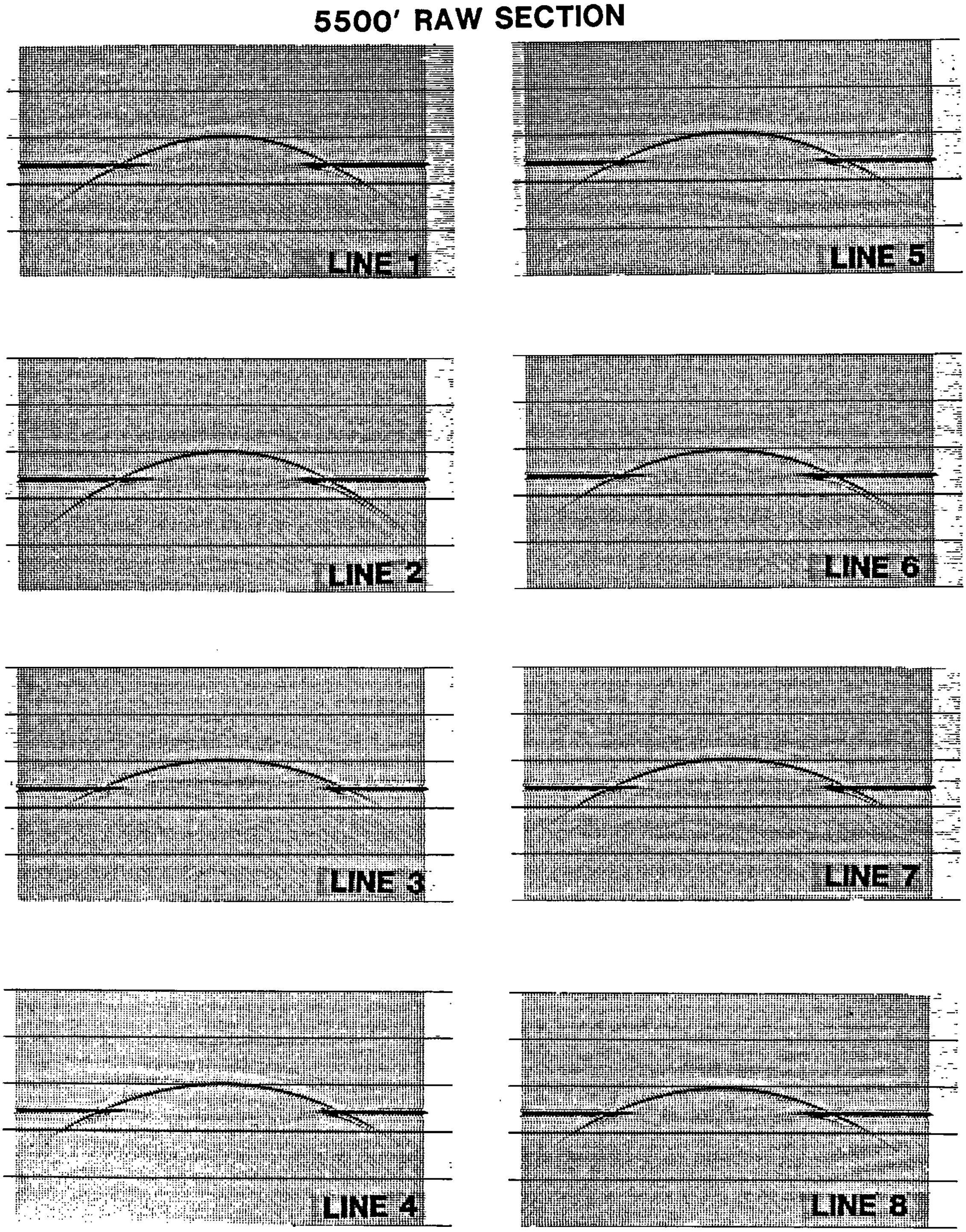

Figure 3-26 Profile direction variation across 5500 ft depth dome -- raw sections.

3-26) have very similar features. Because of the similarity no migration was performed.

Similar to the tests conducted across the basin, single-fold data were compared to 12-fold data across the dome (Figure 3-27). Data from the 12-fold CDP gathers were stacked with a constant velocity, and thus the diffraction events from the flanks of the dome were not stacked coherently and weak amplitude spots on the flanks resulted in the 12-fold migrated sections.

A crooked-line was generated and processed similar to the basin crooked-line discussed for Figure 3-15. Figure 3-28 illustrates a 12-fold crooked-line with CMP offset variations of 20 CDP spacings (2000 ft) when compared to an equivalent line which has the same two end points as Line 8. After the crooked-line data were brute stacked with a constant velocity, segmented events were depicted because of the severity of the crooked survey. The crooked-line 2-D migrated section shows a three-lobed domal structure which has a larger lateral extent than the true dome. This lateral extent is diminished when the crooked line is 2-step Kirchhoff processed at intervals equivalent to the CDP spacing of the straight line data along Line 8. The 3-D migrated section at the top of the figure depicts more accurately the shape of the dome but still has pitfalls, namely an apparent fault near the top of the dome and an apparent gap at the right edge of the dome. Methods to improve the continuity of these

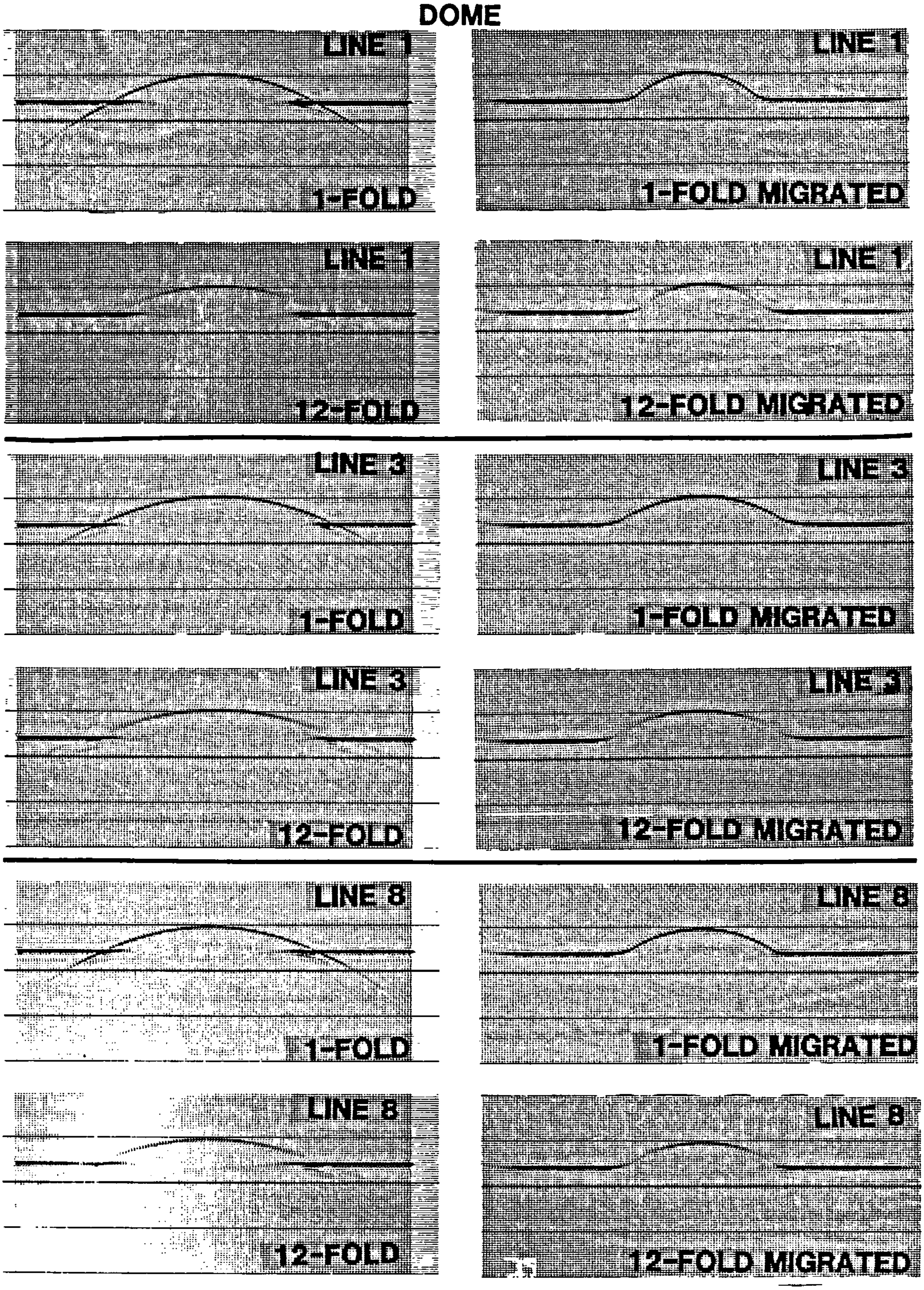

Figure 3-27 Single fold versus 12-fold -- dome.

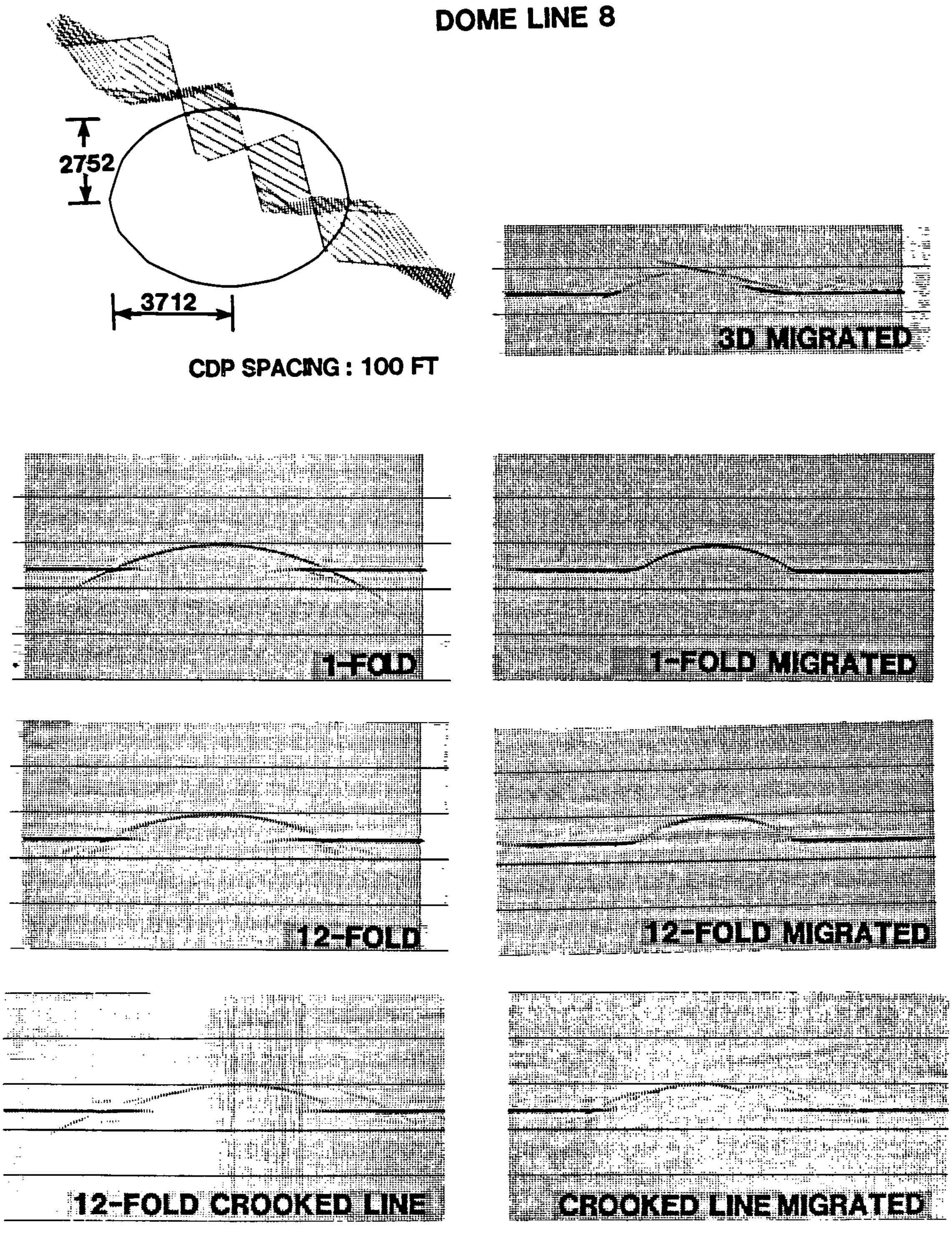

Figure 3-28 Crooked-line across dome.

events will be once again illustrated in Chapter VI with the 3-D NMO equation and projection algorithm.

B. SMALL AND LARGE DOME

The previous dome was scaled down as the basin was scaled down (see Figure 3-17). The corresponding sections are shown in Figure 3-29. Notice the healing diffractions under the main events in the center of the section, especially on Lines 3, 4, 6 and 8. This healing effect is similar to that of the small basin.

Figure 3-30 contains the migrated sections across the half-size dome. On the 2-D migrated sections, the domal shape was delineated adequately except for an extra horizontal event under the major domal structure on Lines 3, 4, 6 and 8. These false events are caused by out-of-plane diffractions from the domal edge.

The dome was scaled laterally by a factor of two while retaining the same vertical relief. The length of the lines was increased while the trace spacing remained the same (100 ft). The corresponding sections shown in Figure 3-31 display the shape of the dome and do not pose any interpretational problems.

C. TILTED DOME

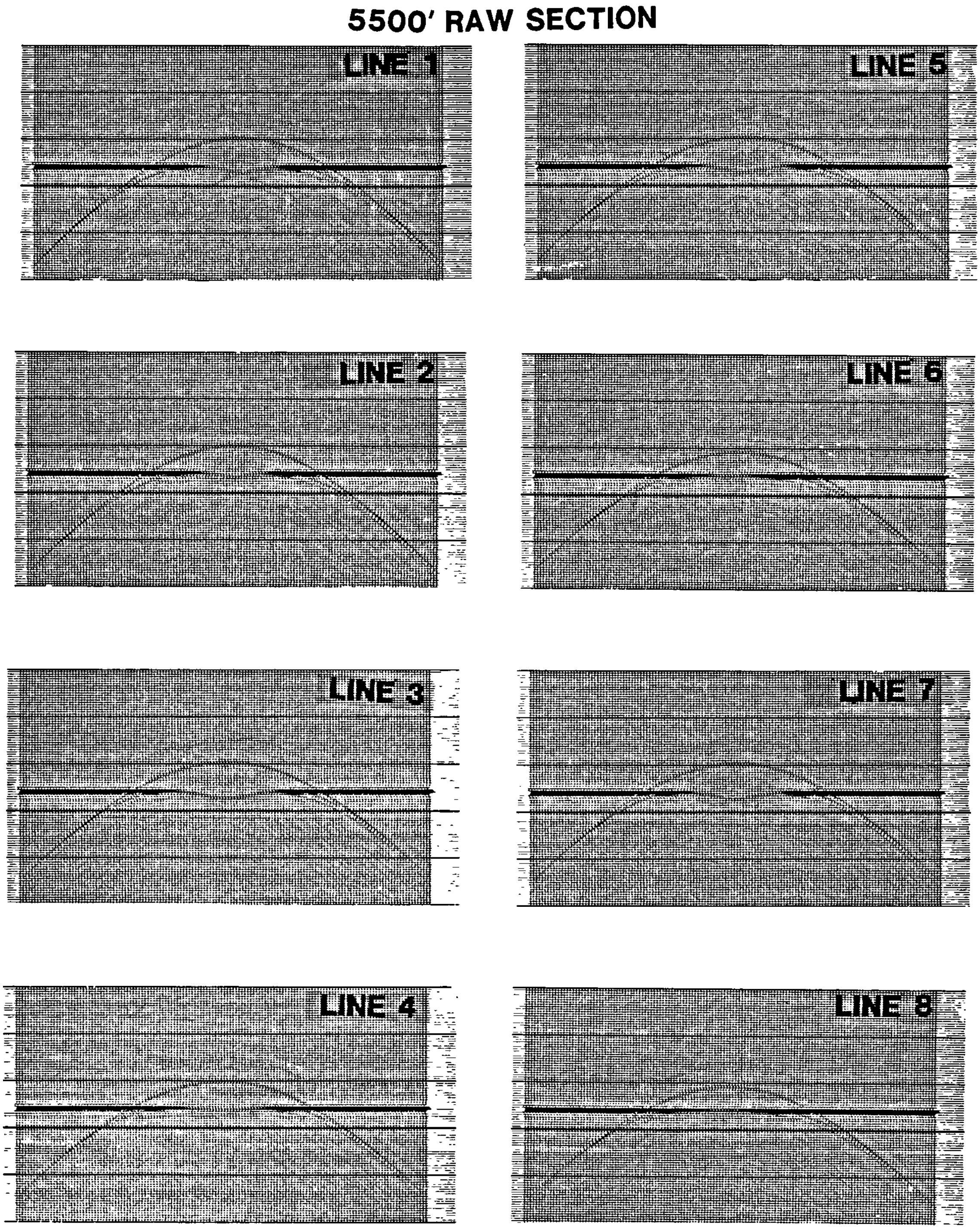

Figure 3-29 Profile direction variation across 5500 ft depth small dome -- raw sections.

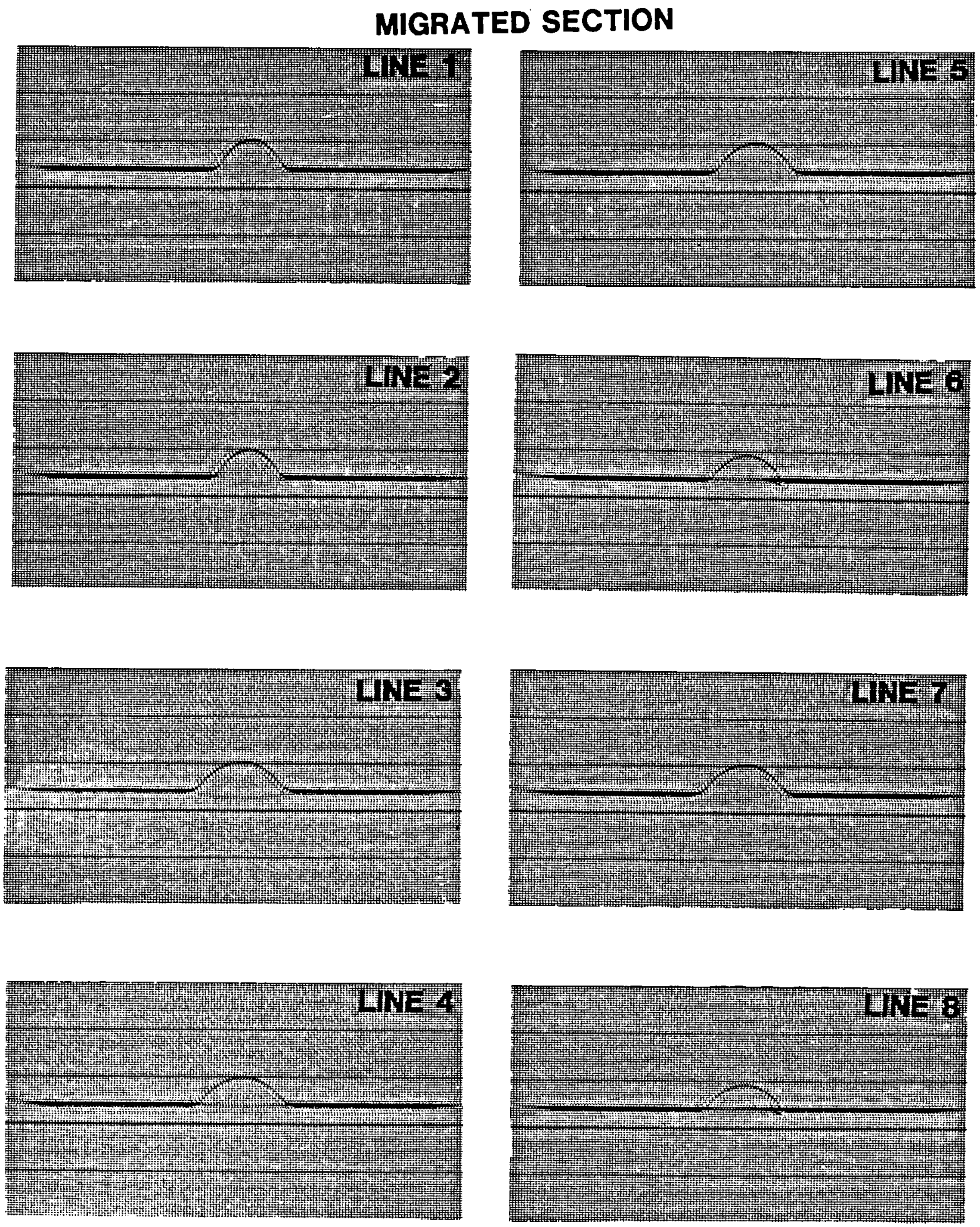

Figure 3-30 Profile direction variation across 5500 ft depth small dome -- migrated sections.

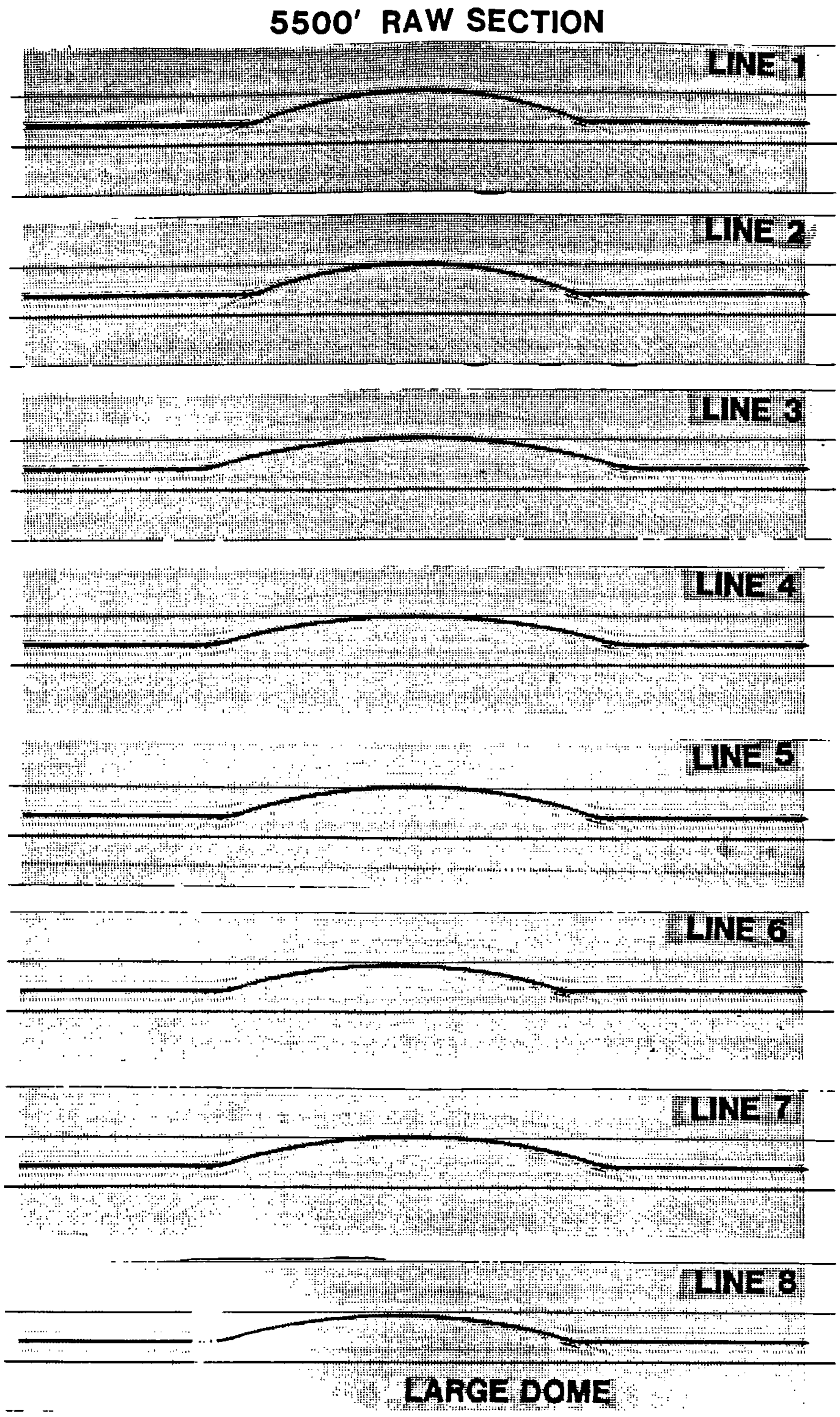

Figure 3-31 Profile direction variation across 5500 ft depth large dome -- raw sections.

The dome was tilted down to the north by 15° and profiled with a ZSR configuration (Figures 3-22 and 3-23). The raw time sections presented here are easy to interpret (Figure 3-32). The truncated diffraction tails at the left-hand side of the sections in Line 1 and 2 are caused by an insufficent time window used when generating the synthetic data.

The migrated version of Figure 3-32 is shown in Figure 3-33. Once again 2-D migration is doing a good job even when the dome is tilted. The weak energy at the left edge of the dome in the first two lines is caused by the window truncation. Also the domal shapes in the sections are slightly skE-Wed except for the two E-W lines (3 and 4).

3.5 PARTIAL REFLECTORS

An irregularly shaped disc with an approximate size of 2800 ft by 2000 ft (about a half-wavelength Fresnel zone) was ZSR modeled at a depth of 5500 ft(Figure 3-34). Line 0 was collected over a single layer to test the healing effect due to out-of-plane diffraction energy. Lines 1 through 4 were collected over thin layers of thicknesses 25 ft, 50 ft and 100 ft to examine the tuning effects of both areal size and thickness. A bottom reflection coefficient opposite to the top reflection coefficient was used on Lines 1-4.

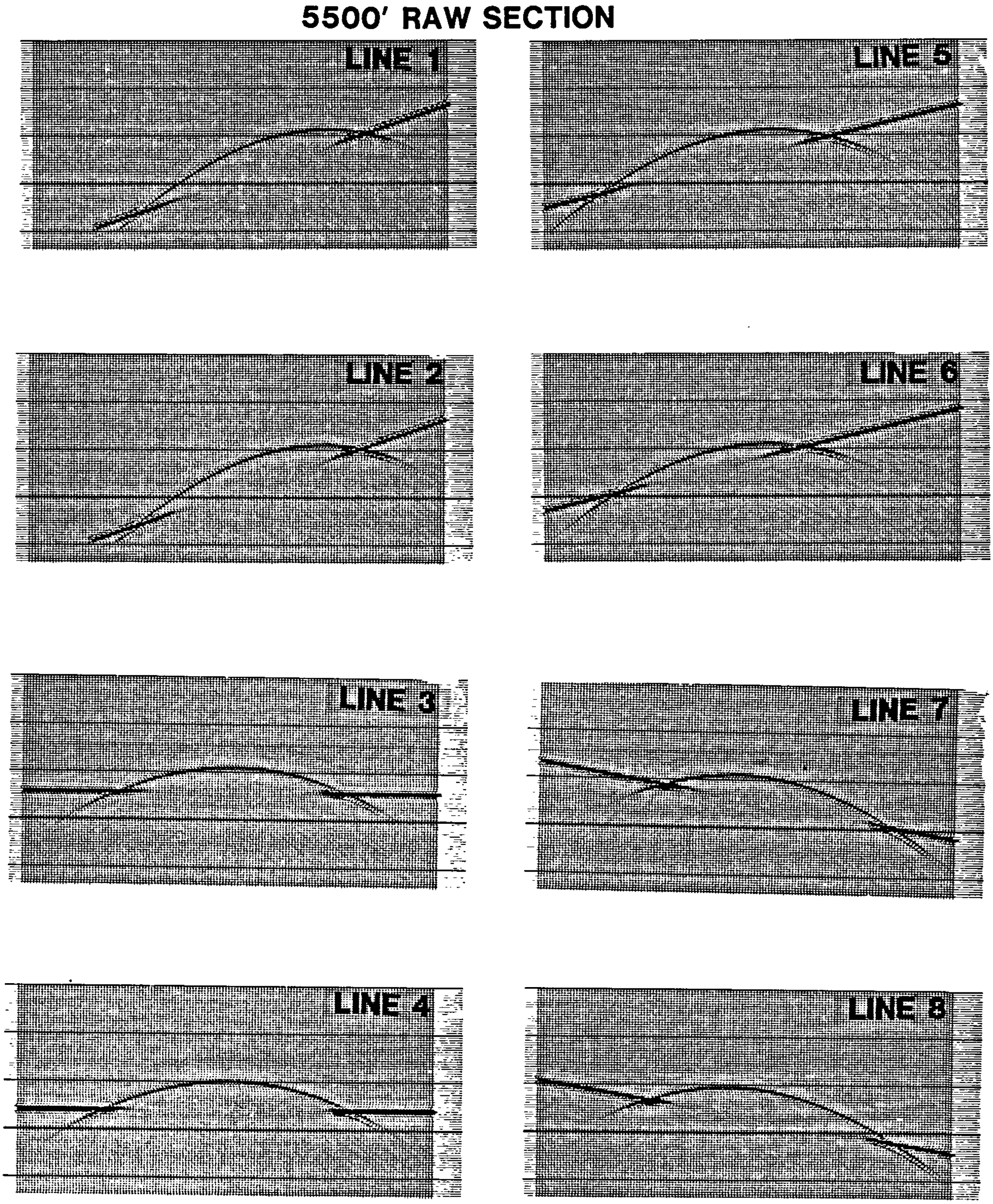

Figure 3-32 Profile direction variation across tilted dome -- raw sections.

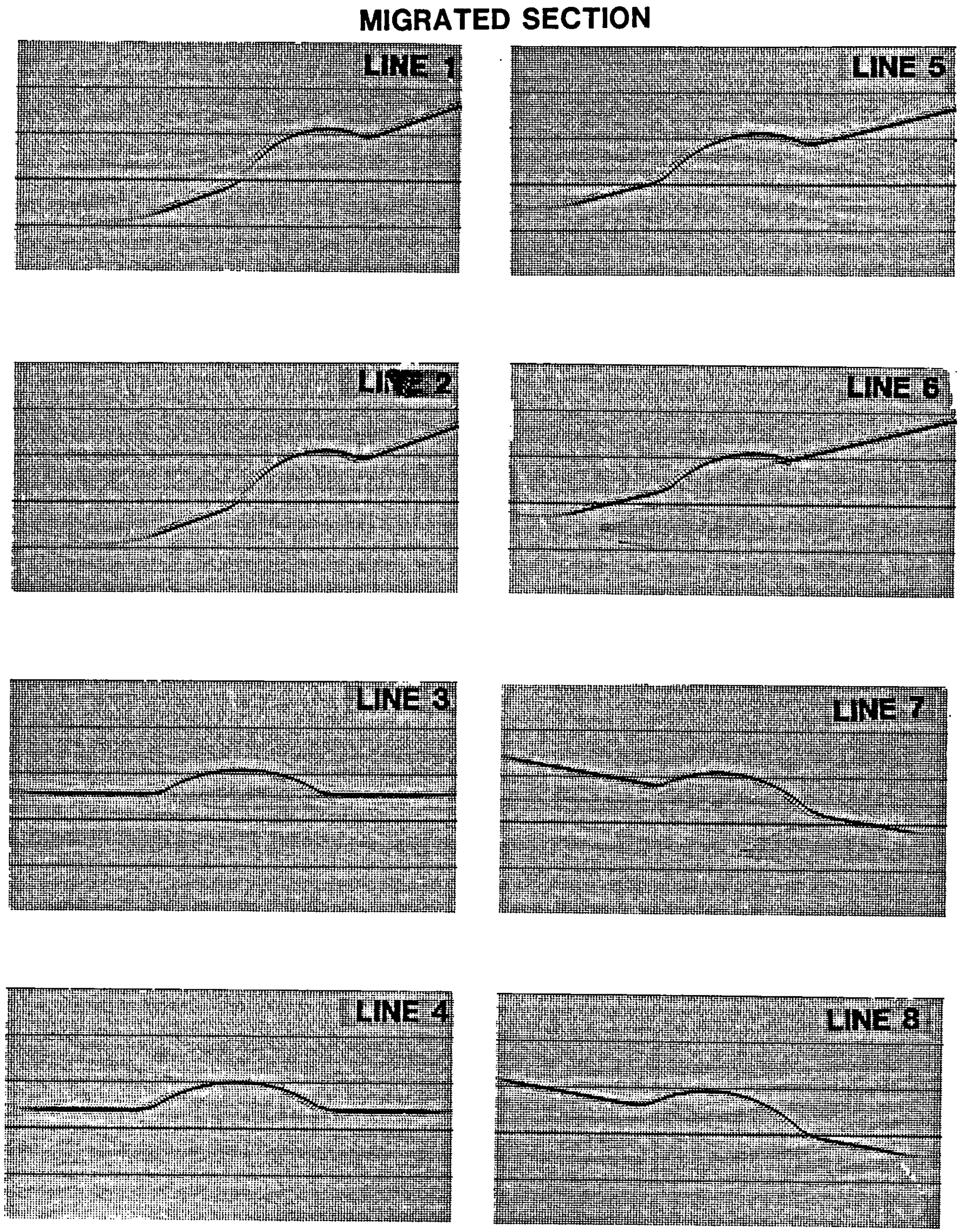

Figure 3-33 Profile direction variation across tilted dome -- migrated sections.

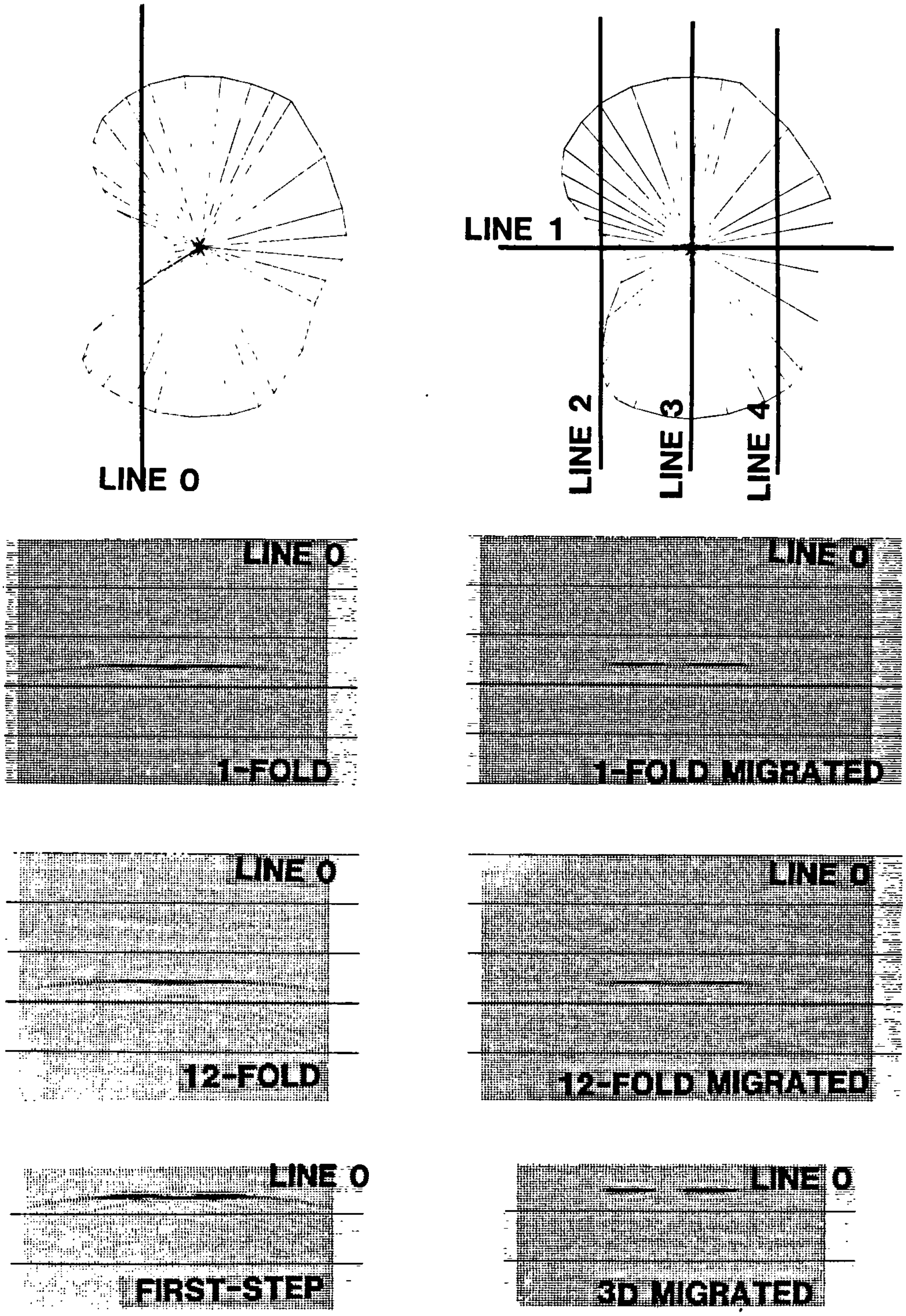

Figure 3-34 Two-D migration versus 3-D migration over disc.

For Line 0, a continuous event was shown on the 1-fold section with little evidence of a gap along the profile line. The 12-fold stacked section illustrates a greater healing effect over the 1-fold data. Two-dimensional migration of both the 1-fold and the 12-fold data was not able to totally delineate the gap which was healed by out-of-plane diffractions. Notice though that on the first-step migrated sections, a push-down is obvious where the gap exists. The 2-step 3-D migrated section shows two distinct segments. Also the wavelet on the 3-D migrated section is similar to the seismic wavelet.

When a small areal reflector is combined with a thin bed, the wavelet on the raw time section is not the same as the initial seismic wavelet. Widess (1973) noted that for a thin bed, constructive interference occurred when the thickness of the thin bed is equivalent to a quarter of the predominent wavelength. This tuning thickness would be around 75 ft for our model. However, the amplitude and shape of the reflection wavelet from a disc also depend upon the areal size. A detailed discussion on this appears in Duffy's work (1980). For the half-wavelength disc we used, it is anticipated that the reflection event will tune at a thickness of 75 ft with a total 180° phase change.

Figure 3-35 contains time sections collected over a thin layer. This model consists of two identical discs with the second disc 25 ft

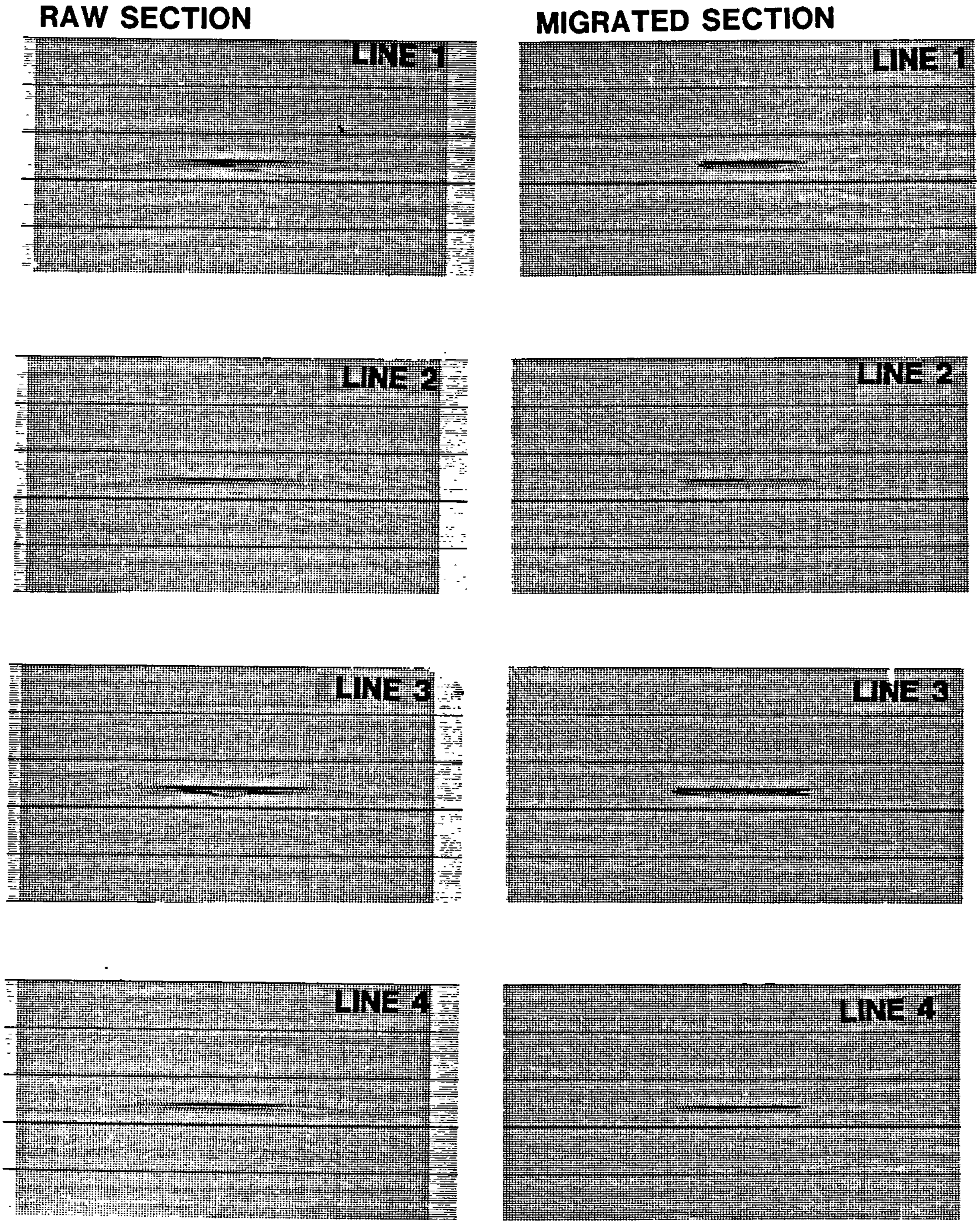

Figure 3-35 Raw and migrated sections over 25 ft disc layer.

below the first one. There is an event difference in the raw sections of Lines 1 and 3 which are perpendicular to each other at the midpoint. The diffraction-like event in the raw section of Line 1 comes from the sides of the discs which gave rise to the third interface in the migrated section. Also note the variation of amplitude across the migrated section of Line 2. The dim portion is again from the side diffraction.

Similar time sections for a 50 ft thick disc are shown in Figure 3-36. The diffraction features in the sections for the 50 ft layer are almost the same as those for the 25 ft layer except the amplitudes are higher because of tuning effects.

Shown in Figure 3-37 are the sections from the disc of thickness 100 ft. The same event on Line 1 (raw section) mentioned in Figure 3-35 now forms an apparent fault with the event from the bottom interface of the disc. The necessity of 2-D migration even for flat 3-D structures is illustrated by this last set of examples.

3.6 SUMMARY

The similarity between the digitized description of the model and the prototype of the geological structure depends upon the sampling density and the depth of the structure. A finer sampling density is need for shallow geological structures so that the seismic

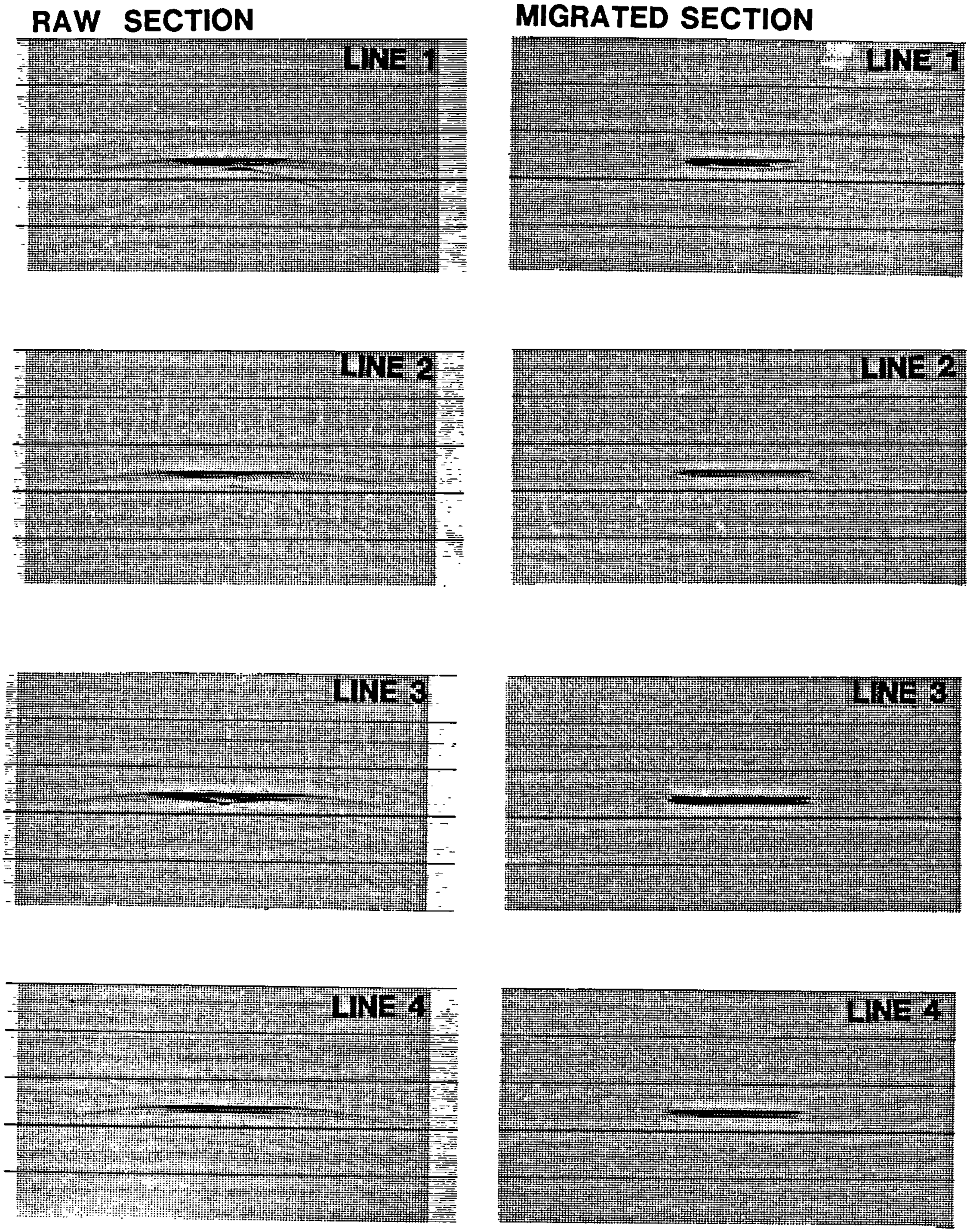

Figure 3-36 Raw and migrated sections over 50 ft disc layer.

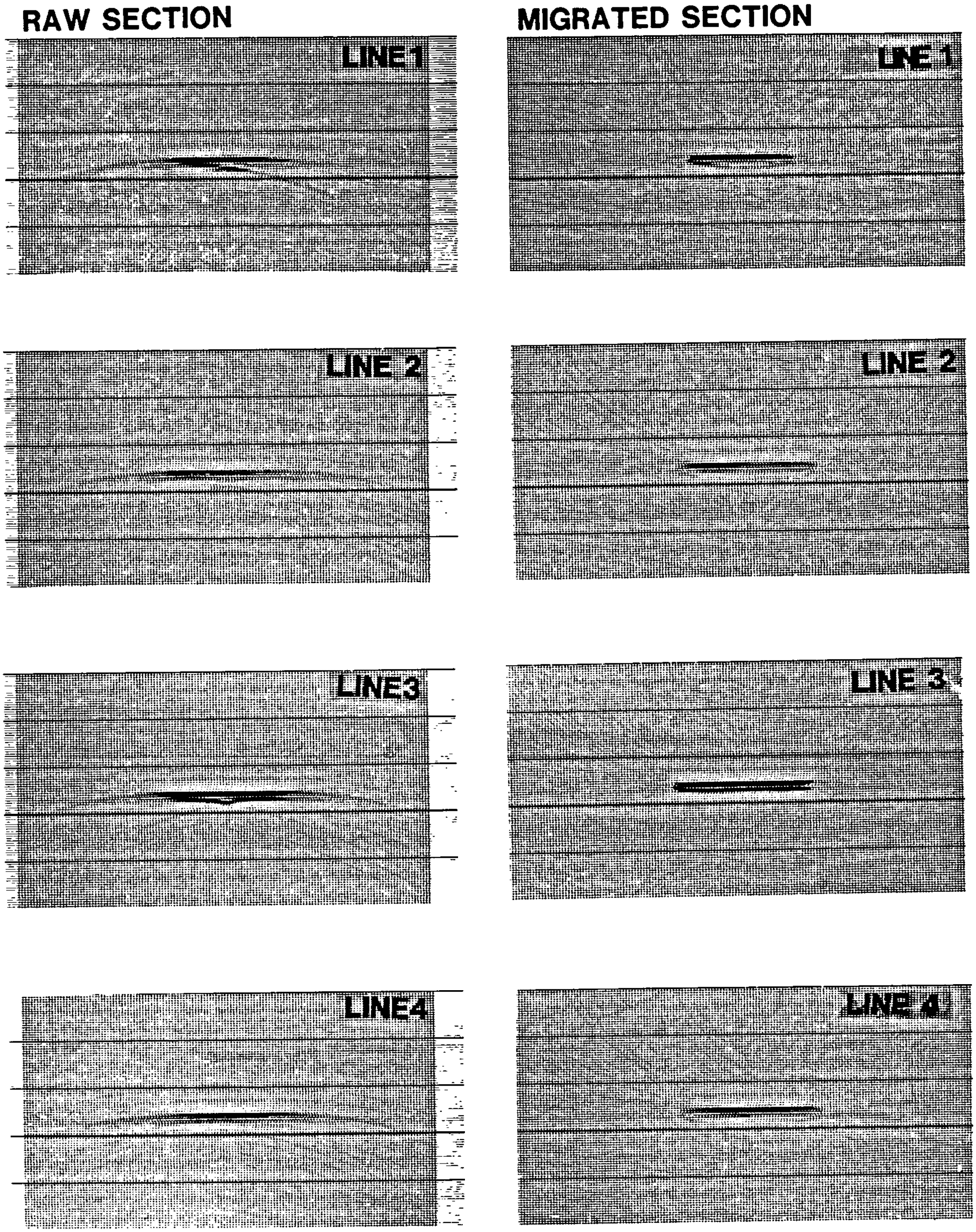

Figure 3-37 Raw and migrated sections over 100 ft disc layer.

time sections are not affected by spurious diffractions. False events such as extra reversed polarity events can exist if the surface sampling is not fine enough.

For near-circular basins, the 2-D migrated section can have an extra layer which is not evident on the raw time section. This interpretational pitfall of the "extra layer" of sedminent in the basin is not easily avoided. The 90° phase shift, even if recognized on the migrated section could have been introduced by the reflectivity function if the layering was transitional. If the extra layer is recognized then a rough estimate of the areal size of the basin can be made by mapping the extra event out of the plane of the profile line.

To discern a 2-D syncline from a 3-D basin, the 2-D migrated section is more diagnostic than the raw section. The raw time sections were similar except for the 90° phase shift in the syncline section as opposed to the 180° phase shift in the basin section. However, there is a high amplitude event on the basin's 2-D migrated section which one can attribute to the 3-D effect of the basin, while the syncline's migrated section has a uniform amplitude after migration.

Sometimes, data processing generates additional events which can not be easily explained if the processing algorithm is not thoroughly understood. A reversed "smile" was obvious on the basin model after 2-D fk migration with linear frequency interpolation was performed. The geometrical frequency interpolation method canceled this noise. In addition, the multi-fold stacked section is not always a good representation of the zero-offset section as one would think. This occurs bacause diffraction tails or dipping events are stacked destructively in most cases.

For oblong basins, a skewed buried focus event is obvious on the raw time sections if the profile line obliquely crosses a portion of the basin. When 2-D migrated, a variety of false events can emerge such as active faults, grabens, ambient noise, cross-stratification, infill sediment, and buried channels. Of course these pitfalls are related to the structure size, depth and profile direction. Also, dip degrades one's ability to interpret the basin's true structure or, worse, even recognize that it exists.

When the size of the basin is increased, the large basins pose no interpretational problems.

For domal structures, the interpretational pitfalls are usually related to data processing procedures. Inadequately stacked dipping and diffraction events from the flanks of the dome result in weak amplitude spots in the migrated stack section.

When domal structures were tilted or increased in size, no interpretational pitfalls were evident. That is to say, the dome is much easier to interpret than that of the basin.

For an irregular thin layer, false structures such as faults were generated on the raw time sections. Two-D migration of these data helps to relieve the problem. However, in order to delineate the true shape of the structure, 3-D migration is necessary.

IV. PHYSICAL MODELING

4.1 INTRODUCTION

Physical modeling experiments serve multi-fold purposes with respect to the seismic exploration program. Physical experiments have been designed to verify theoretical modeling results, such as the 3-D Kirchhoff modeling (Hilterman,1981); to assist in evaluating new field acquisition programs(Hu and Gardner,1981); to provide unbiased input for new processing algorithms; and, to aid in the seismic interpretation of both subtle and complex geological structures. In this research, the theoretical, acquisitional, processing and interpretational modes have been related to physical modeling. In this chapter we are concerned mainly with the interpretational aspects of physical modeling.

The interpretational purpose of this area of physical modeling was to evaluate both lateral and vertical velocity variations in a 3-D environment. The previous section on numerical modeling provided one with first-surface analysis in a 3-D environment but the numerical model was not sophisticated enough to handle multi-velocity media.

Conventional 2-D data acquisition and data processing are applied to the physical model data; these include the constant-offset data collection, CDP data collection, wavelet processing, static correction , CDP stacking and 2-D migration.

The physical models are classified into the two broad categories of structural models and stratigraphic models. Before any structural or stratigraphic aids in interpretations are obtained from the physical models, non-conventional events such as those from model corners must be identified.

4.2 EVENT IDENTIFICATION

The interpretation of major events on the raw time sections collected from physical models can sometimes be quite confusing, especially when the major events are juxtaposed with refracted-reflection events from model corners. At times, it is extremely difficult to identify all the events we see on the reflection profiles, even though we know exactly the geometry and elastic parameters of the physical model. As was reported by Baysal et al (1981), at times we have to rely on more sophisicated theoretical modeling to identify events on the physical model time sections.

Since the propagation velocity of RTV, from which most of the models were made, is much slower than that of water, a significant portion of refracted energy will be trapped in the lower corners of the model and this energy will be returned to the receiver. If a series of parallel line profiles with small line spacing are used, such as would be gathered in a 3-D survey, these spurious events can be identified and separated from major events without the need for further data processing (SAL Progress Review, Volume 5,1980).

An example using a plunging syncline model will be given to illustrate this simple method. In all the time sections presented here, the gain is quite high and therefore because of clipping, several events appear to ring quite a bit. If the gain is reduced, the events would have almost symmetrical wavelets. The earth prototype dimensions of the plunging syncline model are shown in Figure 4-1. The four model edges at the base are labeled as A, B, C, and D and the four model corners at the base are labeled as I, J, K and L respectively. These letters will be used to distinguish corresponding events on the seismic sections. The two defining edges on the top of the syncline are labeled as E and F.

Figures 4-2 through 4-5 are the respective sections selected from a series of parallel profile lines. First, let's examine Event C which is the reflected-reflection event from the lower corner of model edge C. Because the velocity of the surrounding water is higher than that of the model material, event C can be thought of as a composite of ray paths that are critically reflected twice from the two surfaces that make the edge. In Figure 4-2, the illustrated profile line is the farthest profile line of the included four from

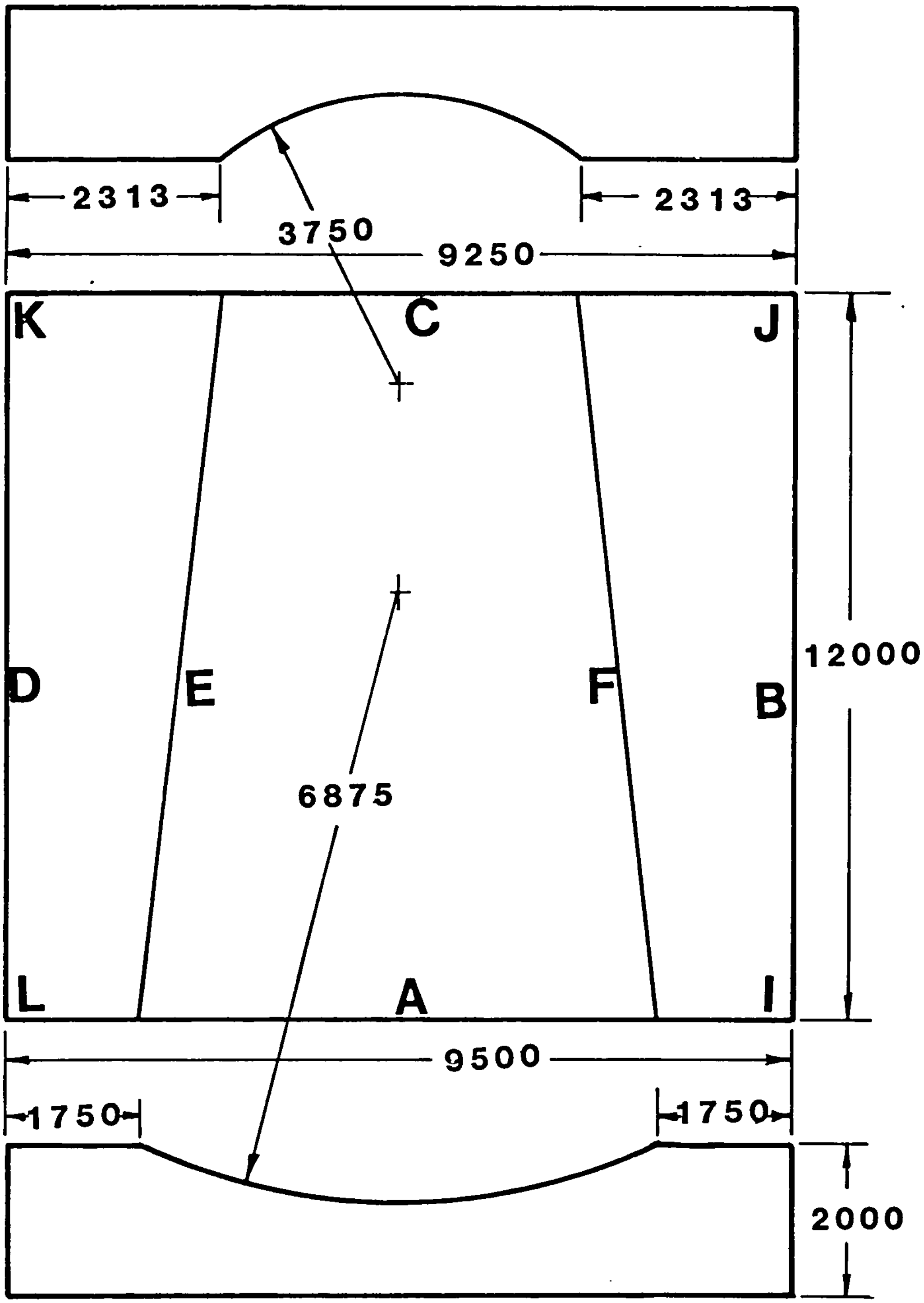

Figure 4-1 Dimensions of plunging syncline.

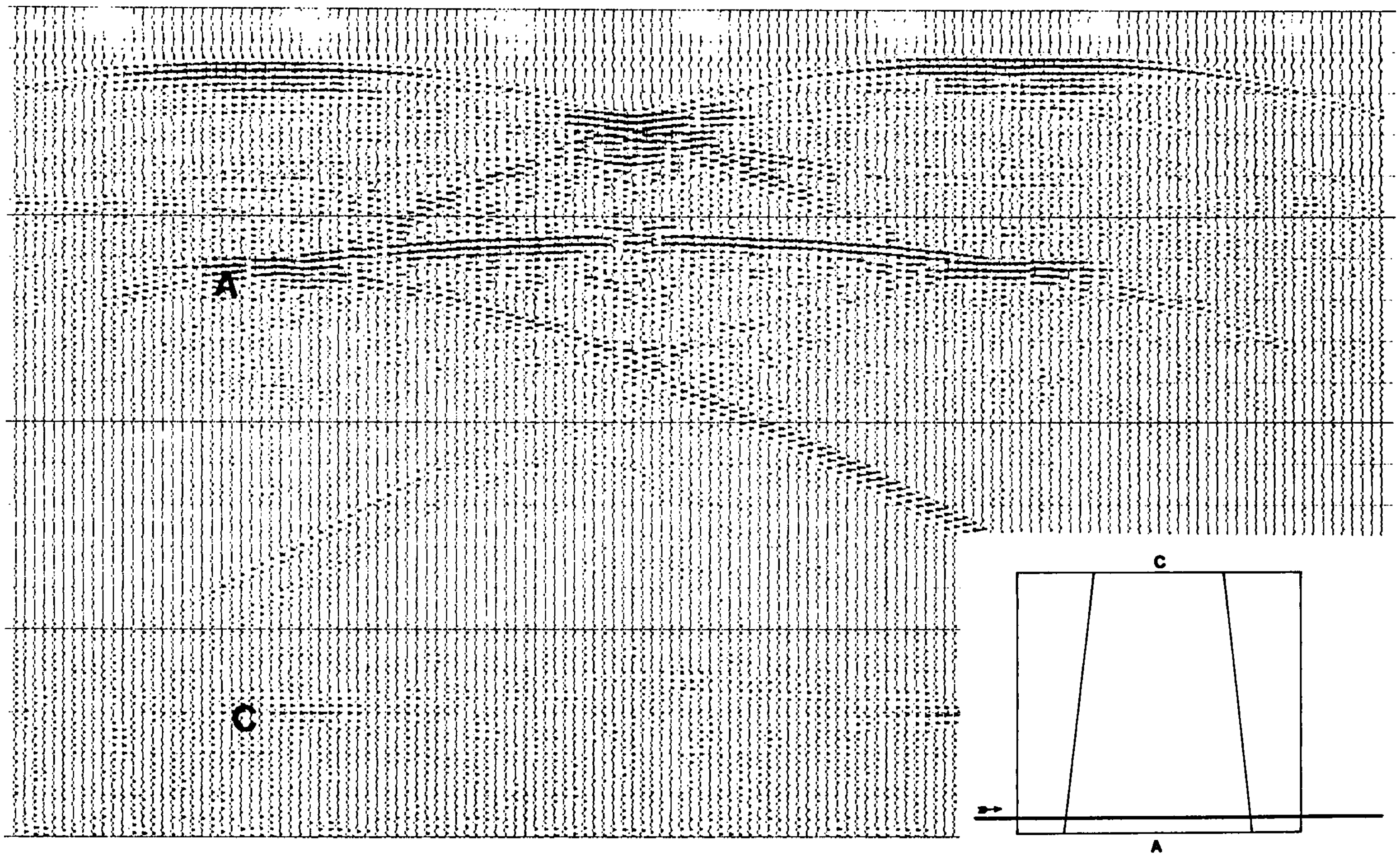

Figure 4-2 Line 1 across plunging syncline.

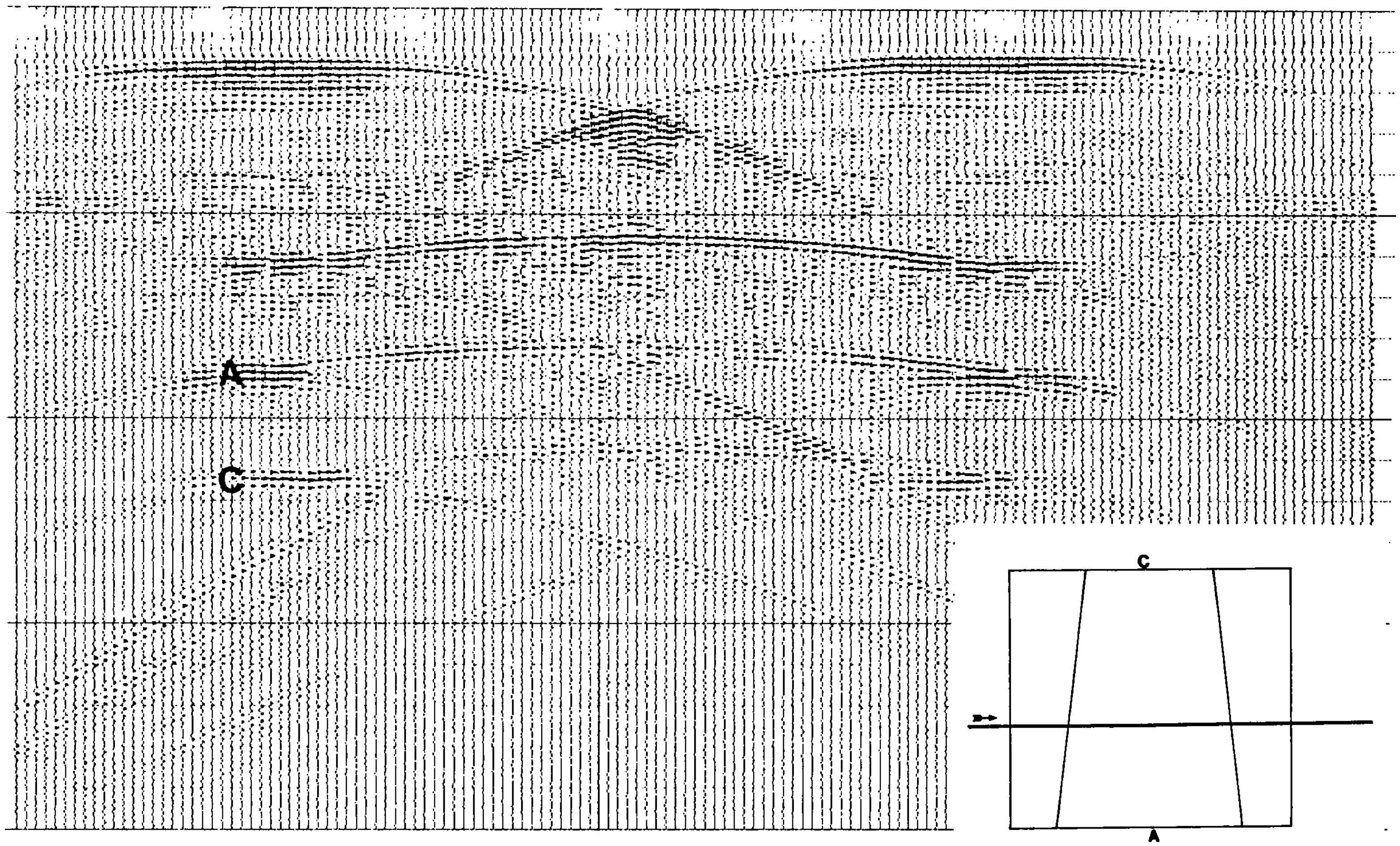

Figure 4-3 Line 2 across plunging syncline.

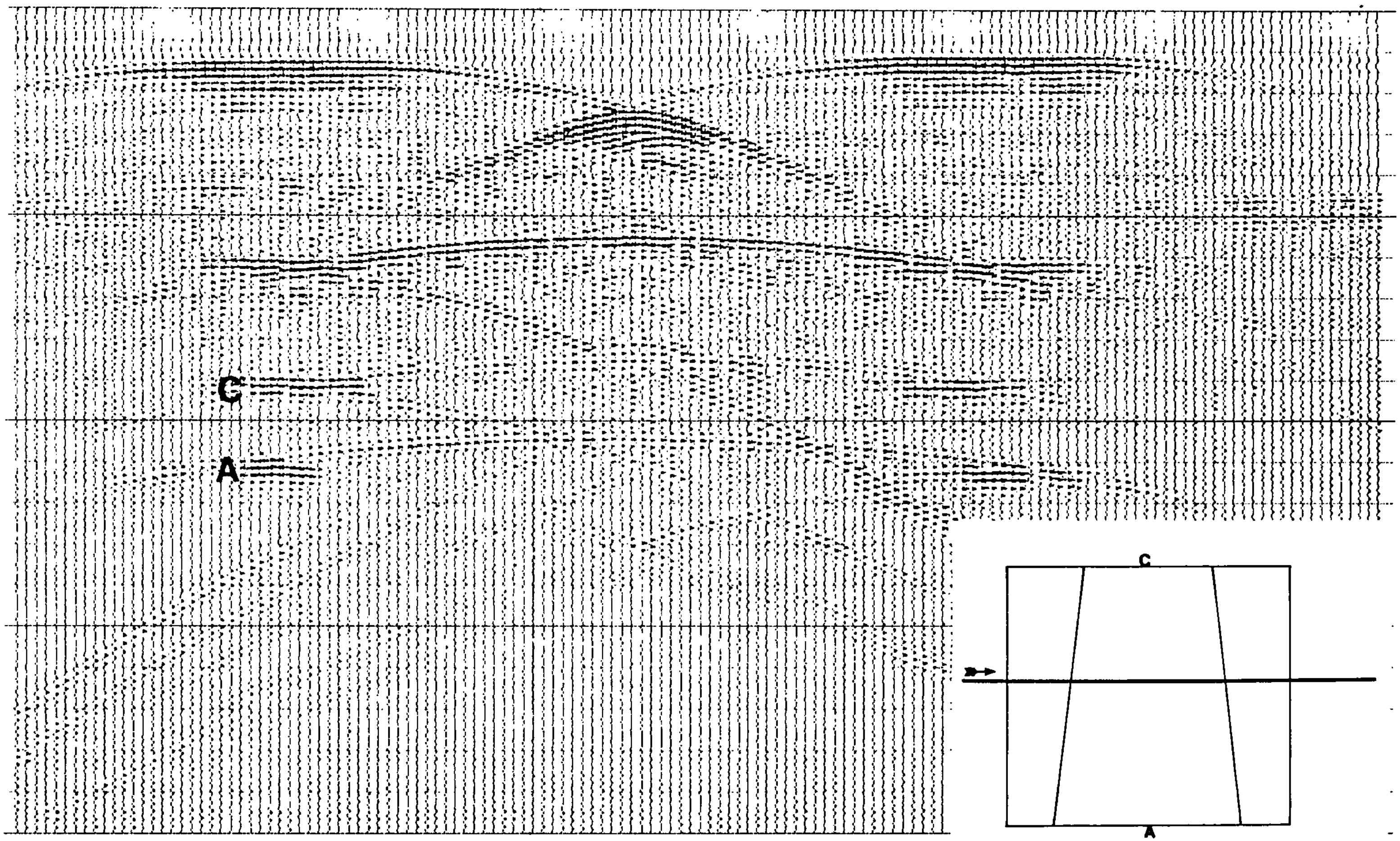

Figure 4-4 Line 3 across plunging syncline.

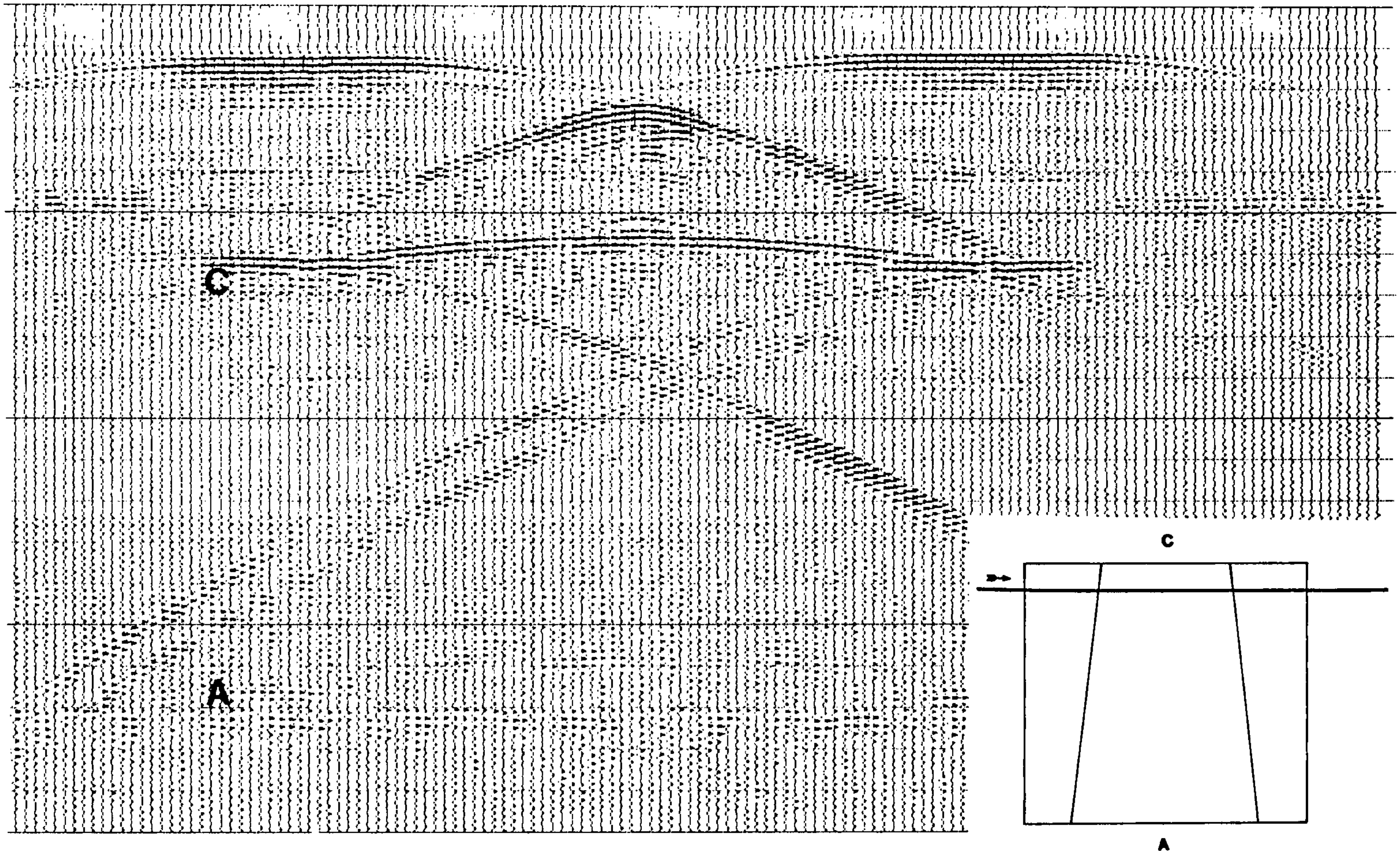

Figure 4-5 Line 4 across plunging syncline.

model edge C. Thus, the Event C which appears near the bottom of the section is at its "deepest" position. When the line position is moved closer to the model edge C, the Event C moves up the section as is shown in Figures 4-2 through 4-5. On the other hand, Event A moves down in the section as one progresses from Figure 4-2 to Figure 4-5. Also observe that in Figure 4-3 the position of Event A is higher in the section than that of Event C, while in Figure 4-4 the relative positions are reversed.

Using the simple method just described, the interpreted version of Figure 4-3 is shown in Figure 4-6. Event M is the reflection from the top of the model and its shape will depend mainly upon the model relief. The buried focus effect is obvious for Event M because the model depth is larger than the radius of curvature of the plunging syncline along this profile line. Event N is the reflection from the bottom of the model and shows a pullup caused by water replacing the low velocity RTV. The apparent multiple events A and C have been discussed already. Event F is a reflection from the bottom of the model and then a diffraction through the edge F of the syncline. Events B and D are reflected-reflection events from the lower corners of the model side edges B and D. Events I, L, J and K are similar events from the model corners I, L, J and K respectively. The lower edge and corner events appear to be typical fault edge diffraction events, however, one can still discern them from the normal diffraction events by recognizing the extra diffraction legs in the

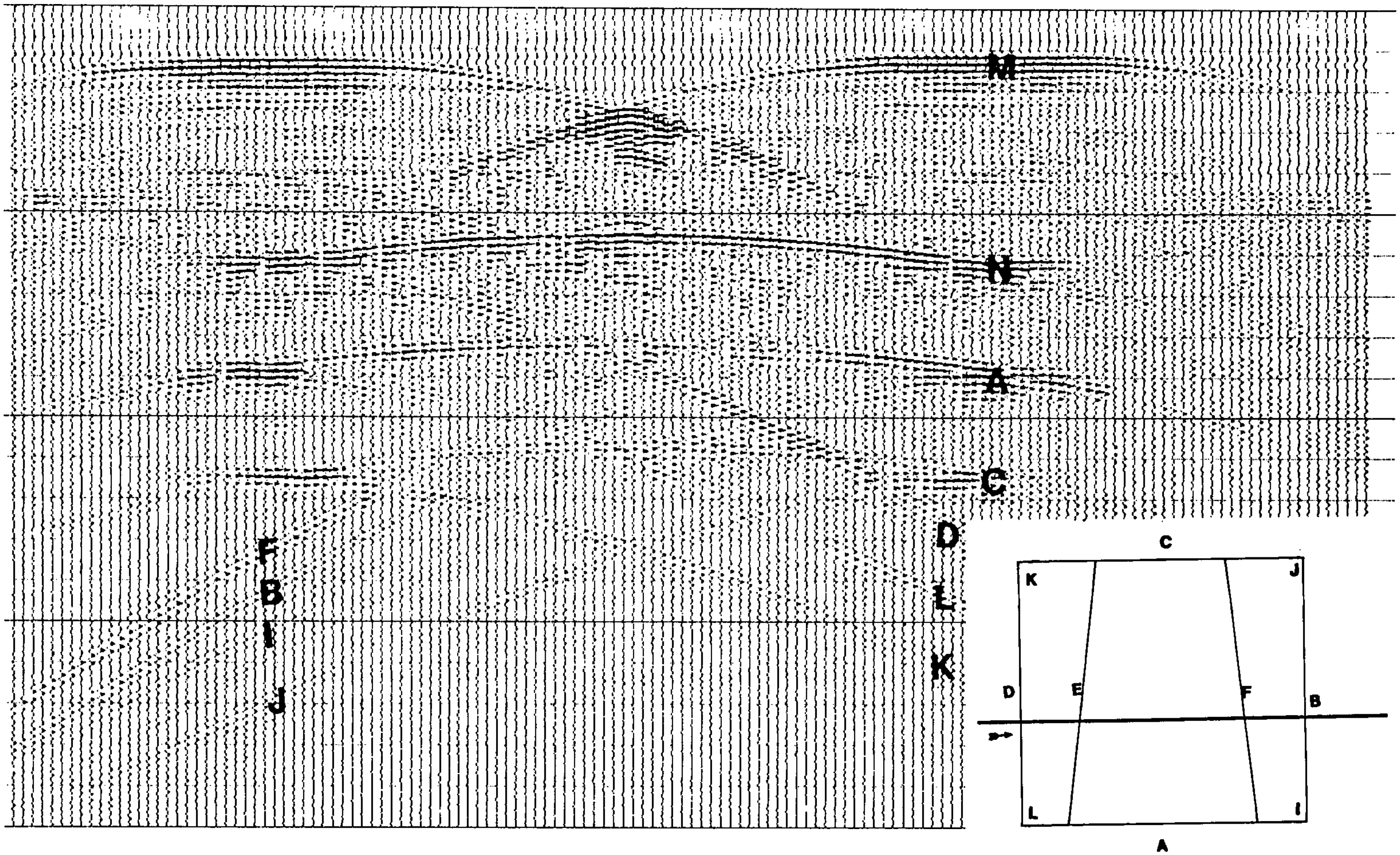

Figure 4-6 Interpreted version of Line 2 across plunging syncline.

events.

4.3 STRATIGRAPHIC MODEL

There are several geological features, which are relatively flat and of limited areal extent, which yield seismic sections with events that are difficult to discern. Such features are igneous sills, low-velocity gas zones, small reefs, and coal deposits. With this in mind, irregular shaped bodies of limited extent were designed and constructed from both high and low velocity materials. When appropriate, the thicknesses of both the high and low velocity materials were also varied.

A. AMORPHOUS BODY - HIGH AND LOW VELOCITY

The model is relatively flat with areal dimensions of 3500 x 2000 ft. The profile lines were approximately 5000 ft above the model. The high velocity material is represented by plexiglas while the low velocity by RTV. The models are positioned in one of two configurations; the model is either suspended on thin threads 1000 ft above a continuous flat plexiglas interface, or placed on the continuous interface. Figure 4-7 is the top view and side view of the suspended model setup. Dashed lines indicate the supporting thin threads. This model has been investigated numerically by Hilterman (1976) and physically by McDonald et al (1981).

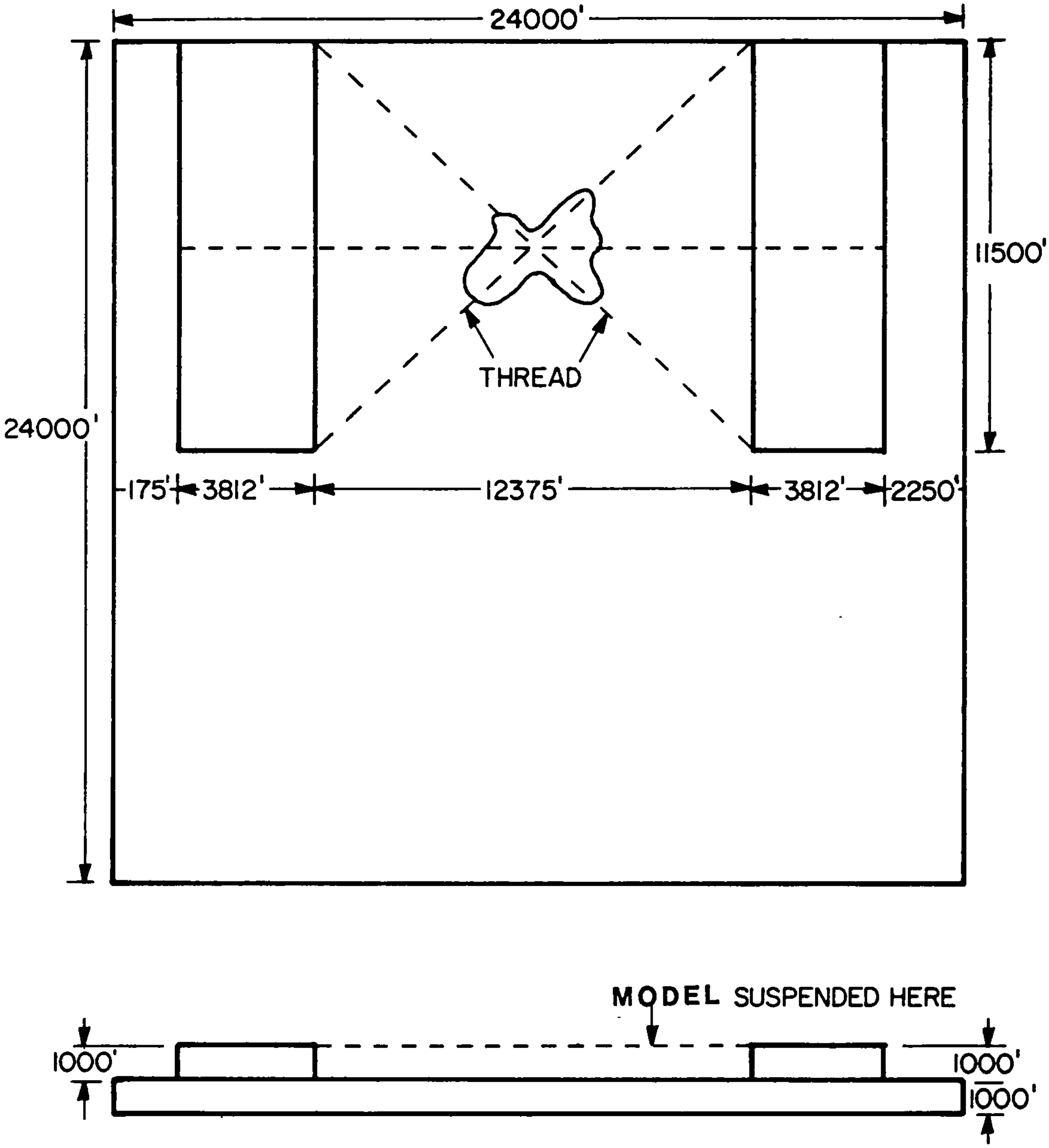

Figure 4-7 Dimensions of amorphous sand body.

Figure 4-8 shows two sections selected from several parallel profile lines across a high velocity plexiglas model with a thickness of 480 ft. The top of the lens is indicated by Event A, the bottom of the lens by Event B, the top of the continuous high velocity reflector by Event C and the bottom of the continuous high velocity reflector by Event D (a positive reflection is a trough). Event E represents the event which travels through the lens and then reflects from the top of the continuous reflector. Because part of this raypath contains the higher velocity lens, the traveltime is less than that of the direct raypath travelling through water to the continuous reflector as indicated by Event G (or C). When part of the wavefront travels around the edges of the lens and reflects from the lower continuous reflector, a diffraction is generated from the continuous reflector as is indicated by Event F.

The raw time sections have been wavelet processed and a better vertical resolution of the lens thus obtained. However, the particular deconvolution operator also introduced a ghost event as indicated by Event 1. Care must be taken to avoid such processing pitfalls especially when deterministic deconvolution is used.

Both Events 3 and 6 result from focused reflected-diffractions from out-of-the plane of the profile. They are not true reflections from the structure itself but are raypaths which are reflected from the concave portion (focused) of the structure and transmitted to the

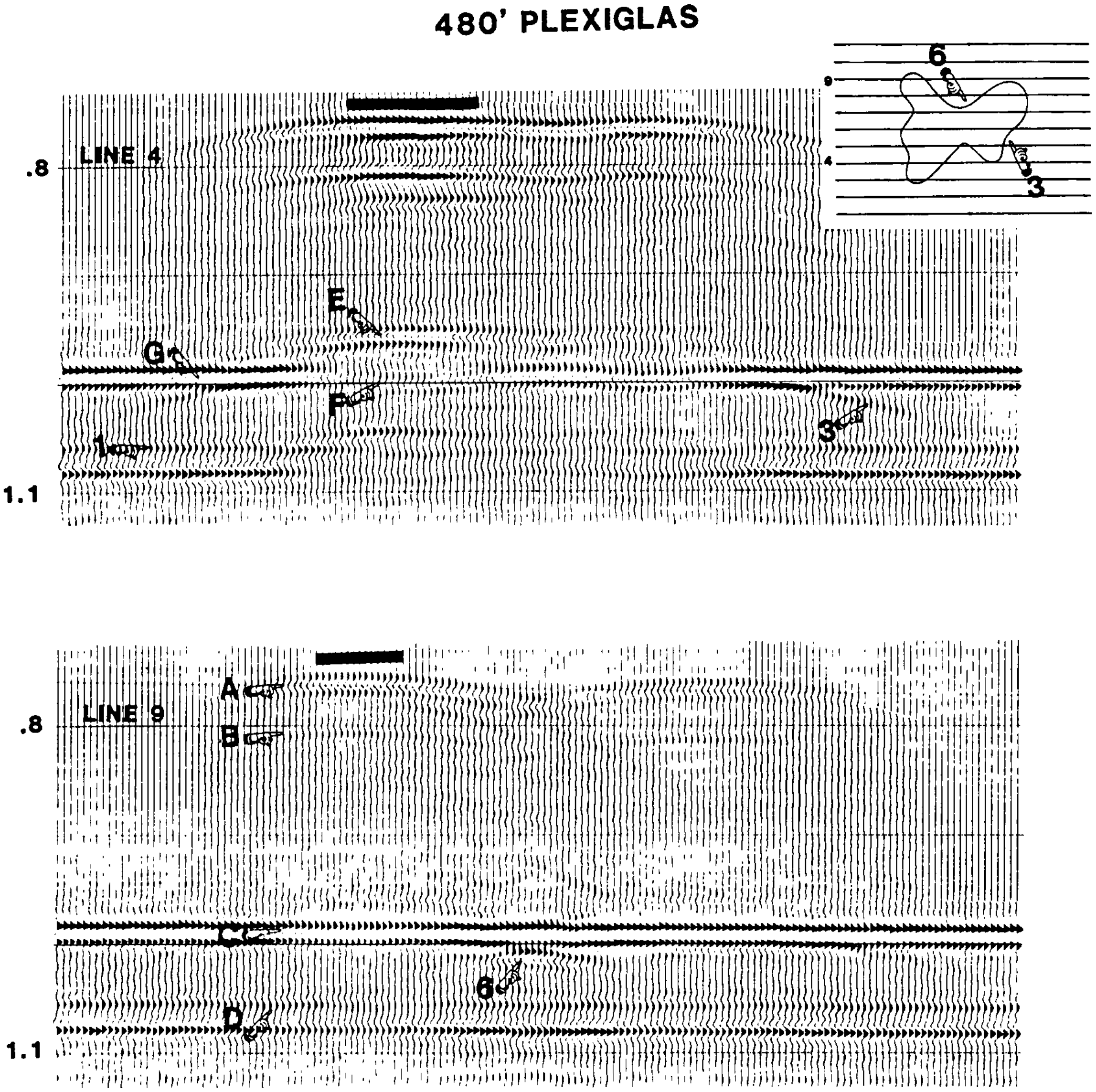

Figure 4-8 Amorphous sand body -- 480 ft high velocity layer.

continuous boundary and return on the same raypath. When these events interfere with the lower reflection events, the possible interpretational pitfalls such as dim spots or deep faults result as shown by Events 3 and 6.

The same recording geometry is carried out over a low velocity RTV lens of thickness 465 ft. The acoustic impedance contrast between RTV and water is much lower than that between plexiglas and water, therefore the RTV reflection amplitudes from the top and bottom surfaces of the lens are relatively low. The Events A, B, C, D, E, F and G in Figure 4-9 correspond to those described for the 480 ft thick plexiglas lens. However, Event E now is a pushdown due to the travelpath through the low velocity lens. When the thickness of the model is reduced, Events E and F, since they are both pushdowns, will coincide to appear as a bright spot. This is depicted in Figure 4-10 on the upper two sections. In contrast, the lower section in Figure 4-10 depicts a dim spot when a high velocity zone is traversed. This is a separation of two events, one a pullup and the other a pushdown diffraction from energy travelling around the lens.

Returning to Figure 4-9, Event 4 on Line 7 indicates an apparent irregular boundary (dotted line) which is caused by the wavefront passing around the lens and reflecting from the continuous boundary. The vertical path reflection from the continuous reflector at these locations is a pushdown as show by Event 5 which is separated from

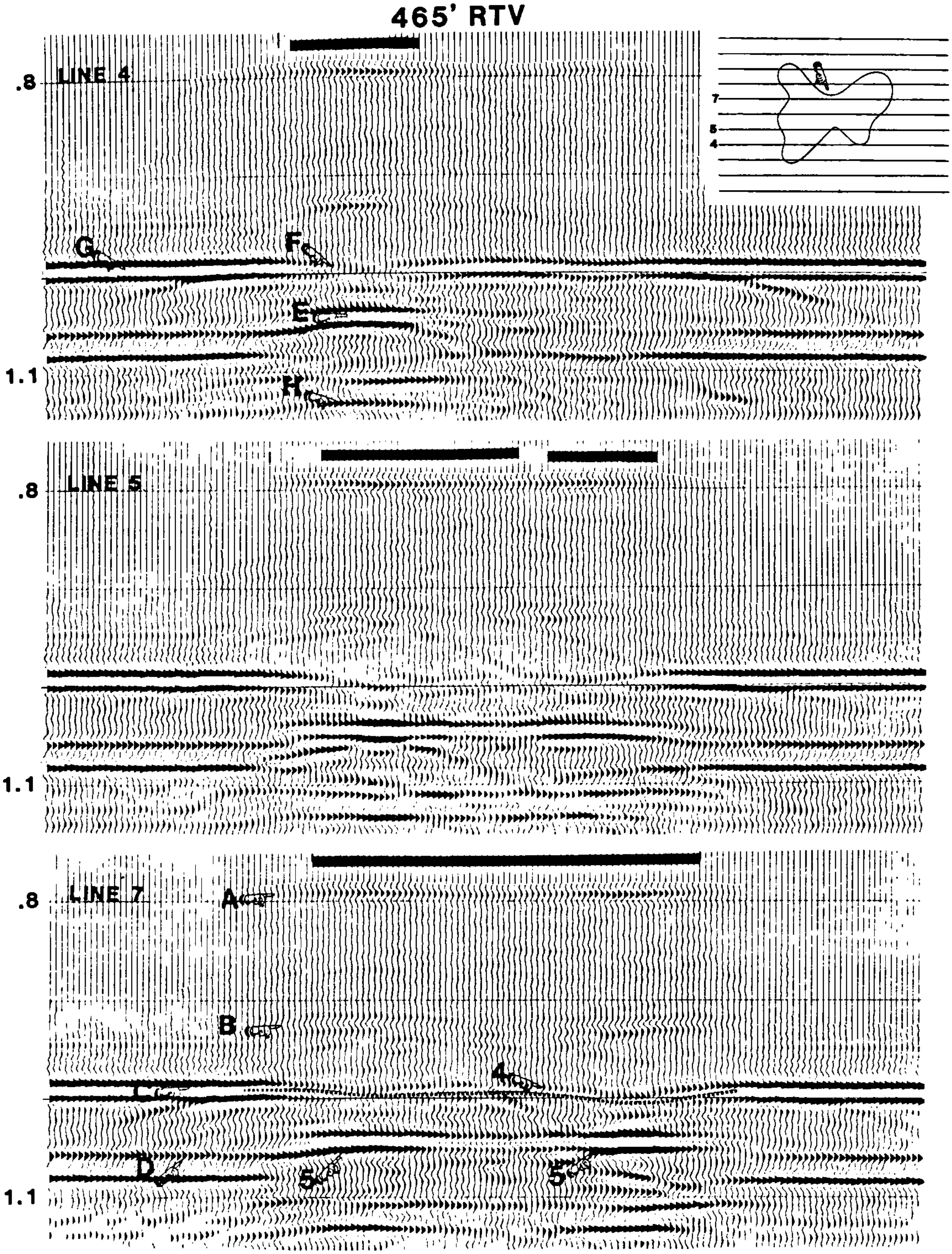

Figure 4-9 Amorphous sand body -- 465 ft low velocity layer.

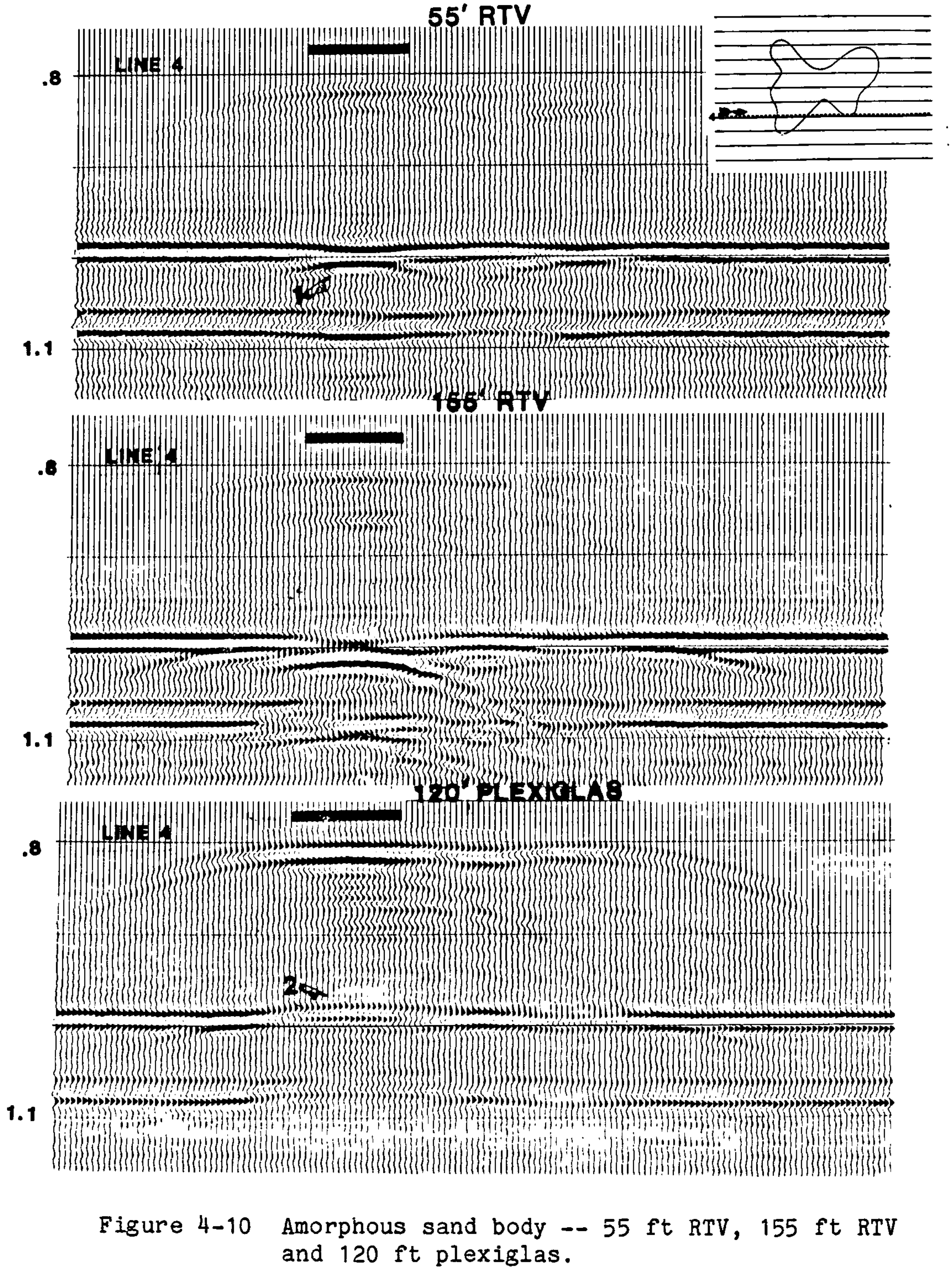

Figure 4-10 Amorphous sand body -- 55 ft RTV, 155 ft RTV and 120 ft plexiglas.

the apparent boundary (Event 4). In Line 7, a high amplitude exists on Event 5 at two places because at these locations a full Fresnel zone of the wavefront is transmitted through the lens, while at the middle portion of the line, only one-half of a Fresnel zone is transmitted.

When a thin plexiglas model of 22 ft thickness is used (Figure 4-11), the thickness of the thin bed can be predicted from the seismic amplitude and waveshape. The approximation $A = A_o 4\pi b/\lambda$ (Widess,1973) relates the thin bed reflection amplitude, A, to that of a thick bed reflection, A_o, where b is the thin bed thickness and λ is the wavelength in the thin bed. Using the lower continuous reflector as a reference, the calculated thickness is 20 ft. The waveform reflected from the thin bed (Event 1) is a good approximation of the derivative of the seismic wavelet reflected from the thick bed, Event 2. Because the lens is thin, the velocity pullup (Event 3) is too small to detect. The reflected-diffractions from the side of the thin lens to the continuous boundary are not as obvious (Event 4) as there were for the thick lens. However, at the upper surface time the out-of-plane diffraction event still is evident (Event 5).

On Event 6 there is a slight loss of amplitude caused by interferring effects of two events, one is a pullup caused by the wave travelling through the high velocity lens and the other is a

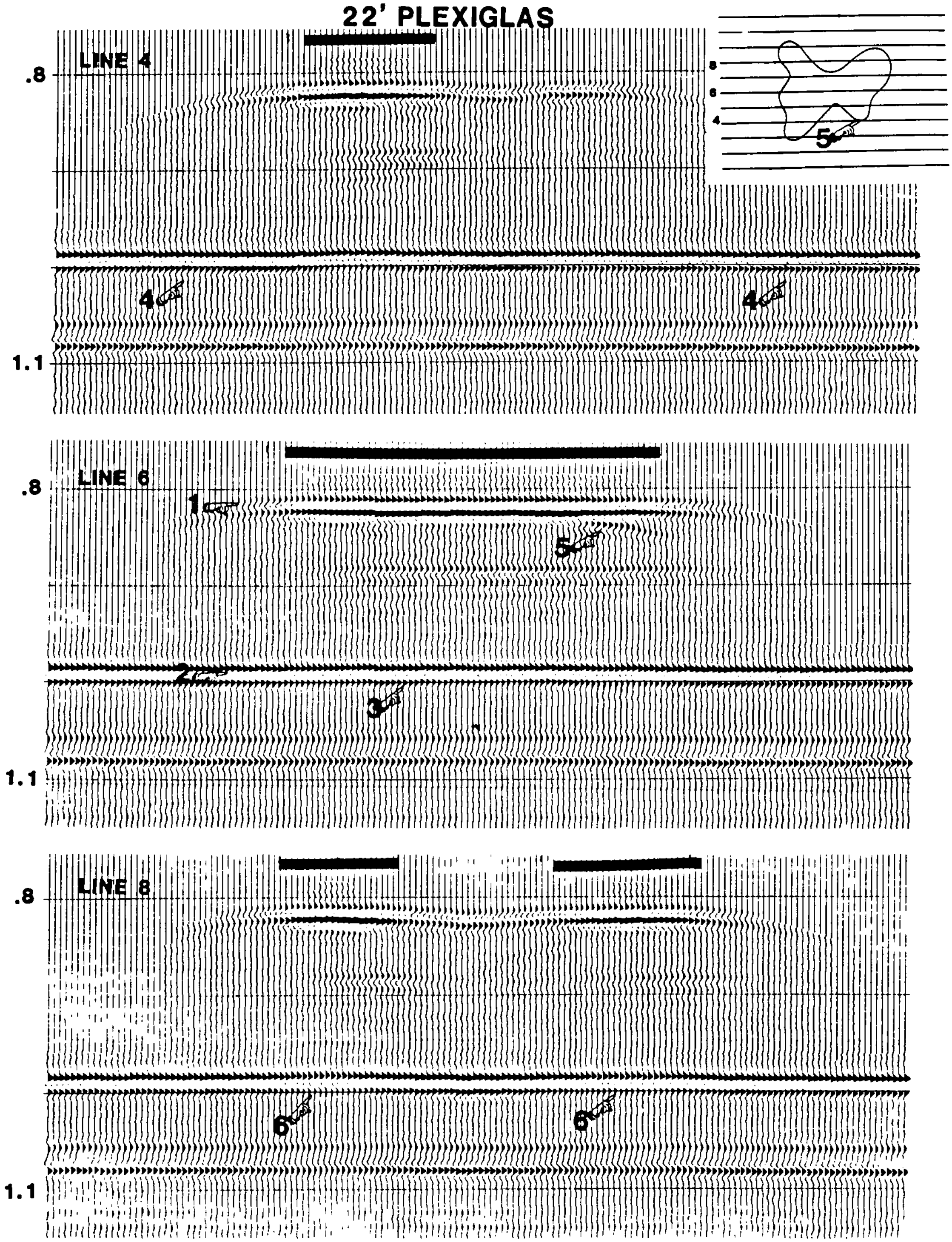

Figure 4-11 Amorphous sand body -- 22 ft high velocity layer.

pushdown caused by the wave travelling around the edges of the lens. Once again, a dim spot is formed under the high velocity lens as compared to a bright spot under a low velocity lens.

The next phase for the lens models was to place them on the continuous reflector to determine characteristic features for identifying a high velocity versus a low velocity stratigraphic trap on a high velocity layer. When a high velocity plexiglas lens of 120 ft is used on top of the high velocity continuous layer (Figure 4-12), there are negligible diffraction events. Likewise when a low velocity lens of 155 ft thickness was placed on the thick high velocity layer (Figure 4-13), the diffractions are only slightly evident. The upper surface of the RTV lens is not easy to detect (Event 1). However, the pushdown due to the low velocity lens is the most diagnostic feature for its recognition. The sections in these last two figures have not been deconvolved.

B. MULTI-SAND BODIES

The isometric and map view of multi-sand bodies are shown at the top portion of Figure 4-14 (Duffy,1980). The lower sand lenses in the geological model are approximately 450 ft above a thick sand body; the upper are 920 ft above the thick sand body. Dimensionally, the map view in Figure 4-14 is 12000 ft on each side and the sand lenses are 125 ft thick. The sand material was

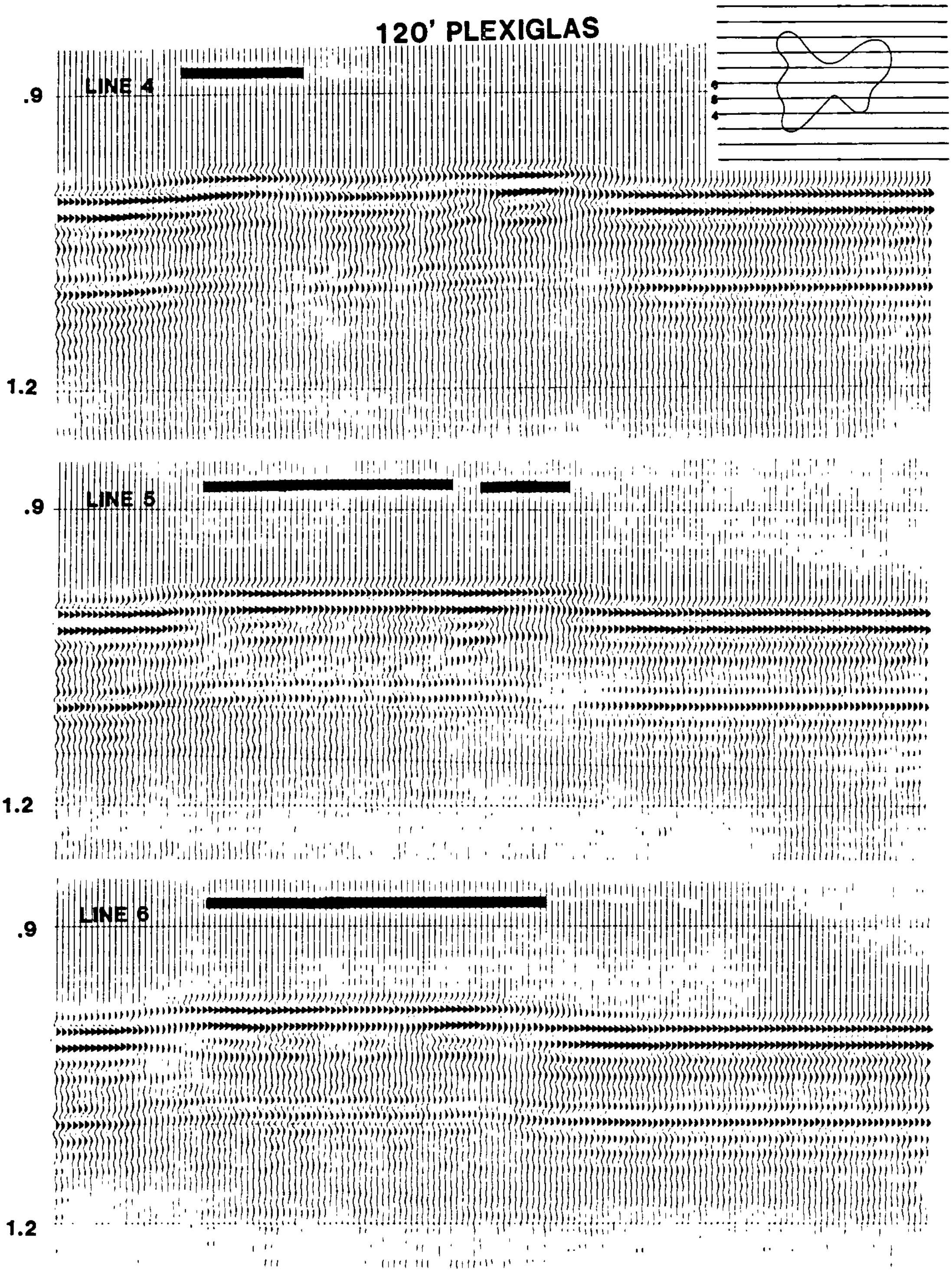

Figure 4-12 Amorphous sand body -- 120 ft high velocity layer.

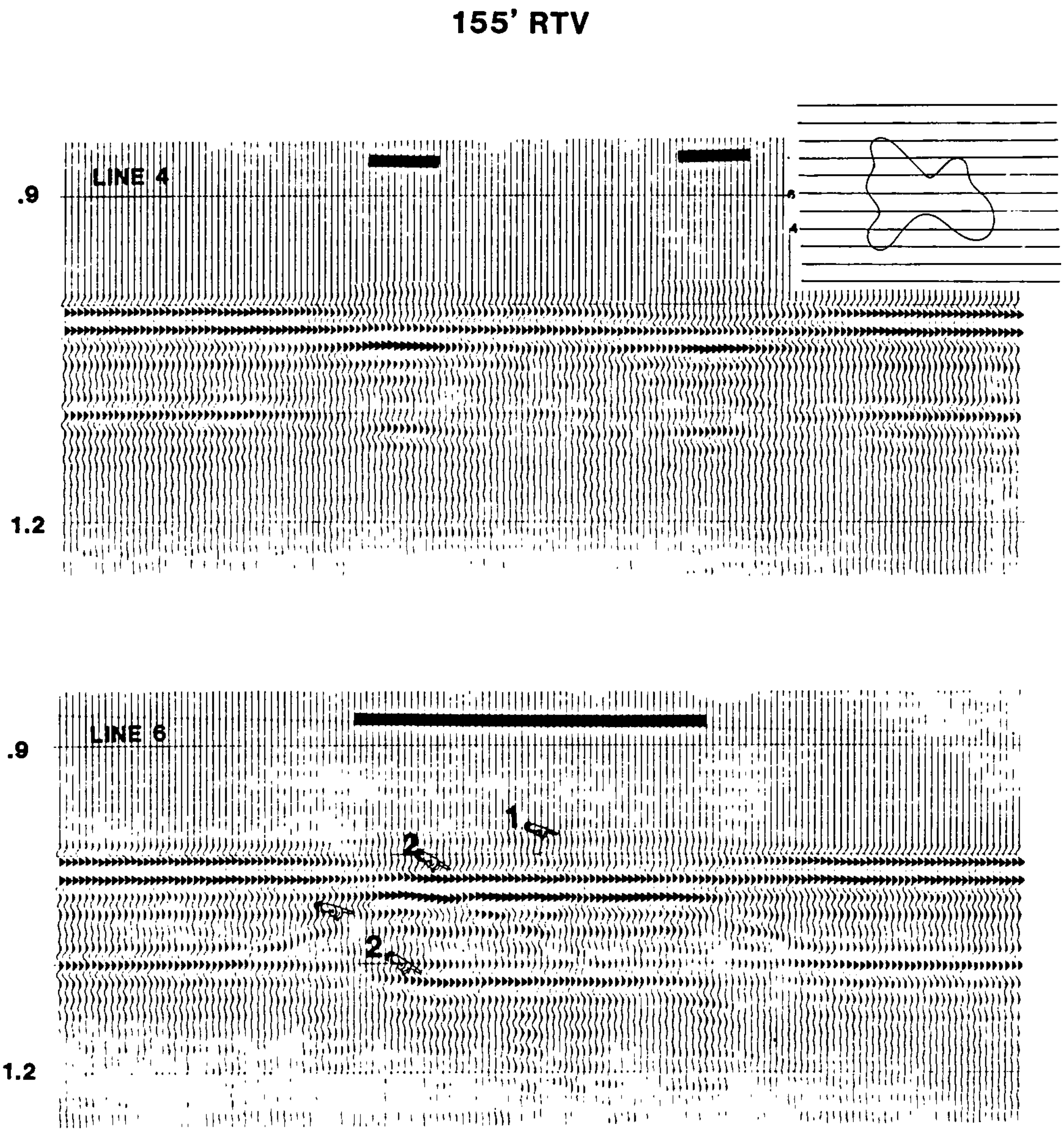

Figure 4-13 Amorphous sand body -- 155 ft low velocity layer.

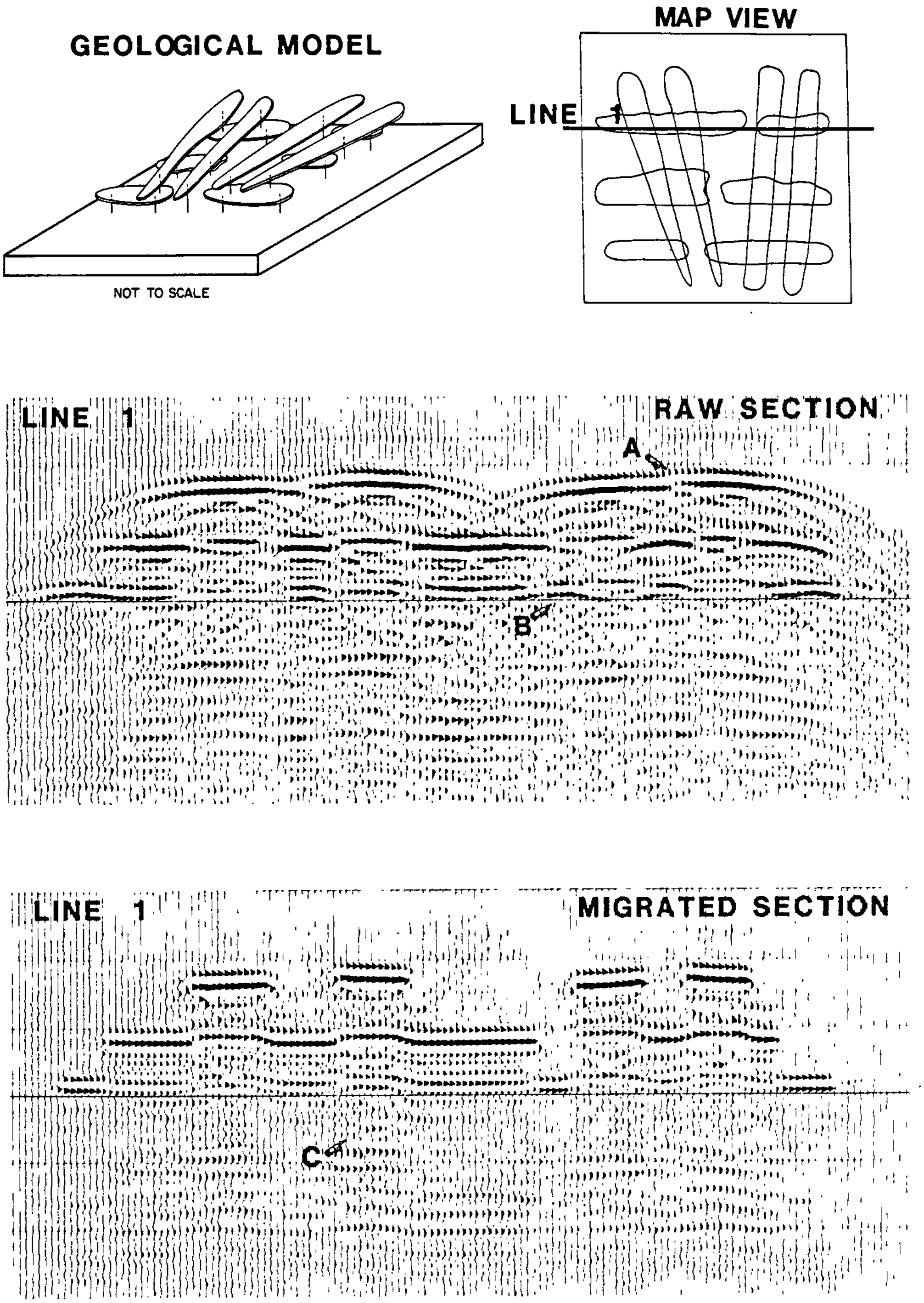

Figure 4-14 Multi-sand bodies -- raw and migrated sections.

represented by plexiglas which has a much higher velocity than that of the surrounding water. Thus we would anticipate velocity pullups under the sand lenses.

The gaps between the sand bodies (Event A) were apparently "healed" by diffraction energy on the raw time section; however, the sand bodies are surprisingly well delineated on the 2-D migrated section. As long as 3-D structures do not have significant dip, the definition of faults or termination of bodies normally are enhanced by 2-D migration.

An apparent velocity pullup occurs on the unmigrated section as indicated by Event B where actually a velocity pushdown should be observed. This paradox occurs for several reasons. First, the wavelet traveling through the sand lenses has had an apparent transfer of energy from the front of the pulse to later legs in the wavelet caused by the high reflection coefficient of the sand lenses. Also, a significant amount of energy travels around the sand lenses and appears later than the water path traveltime.

There are low-frequency disturbed zones indicated by Event C on the migrated sections which might be interpreted as evidence of gas in the upper sand lenses. These disturbed zones are beneath the upper lenses and have the appearance of "rain" falling from the upper lenses. This disturbance is caused by oblique sideswipe from the edges and subsequent diffractions generated by energy travelling around the lenses to lower boundaries.

C. MEANDERING CUT

The meandering cut model (Duffy,1980) as shown in Figure 4-15, is constructed from RTV and it rests on a 380 ft plexiglas sheet. Several small cubes of the same RTV are inserted near the edge between the RTV slab and the plexiglas for additional support.

The profile line in Figure 4-16 crosses the meandering channel three times and in a direction perpendicular to the trend. Events A, B and C are respectively reflections from the top of the RTV, the bottom of the RTV and the top of the plexiglas. The meandering bends on both sides of the profile line are expected to give rise to out-of-plane diffractions as is evidenced by a dome-like sideswipe (Event 3) on the unmigrated section. This sideswipe collapses after migration to form an apparent new reflector, similar to one seen early in the migration of basinal sideswipe.

The "long leg" diffractions (Event 1) on the unmigrated section are properly collapsed after migration is applied. These events have been mentioned in Section 4.1 as the lower corner reflected-reflection. Since the channels are perpendicular to the profile line, the channel geometry is apparently well defined after

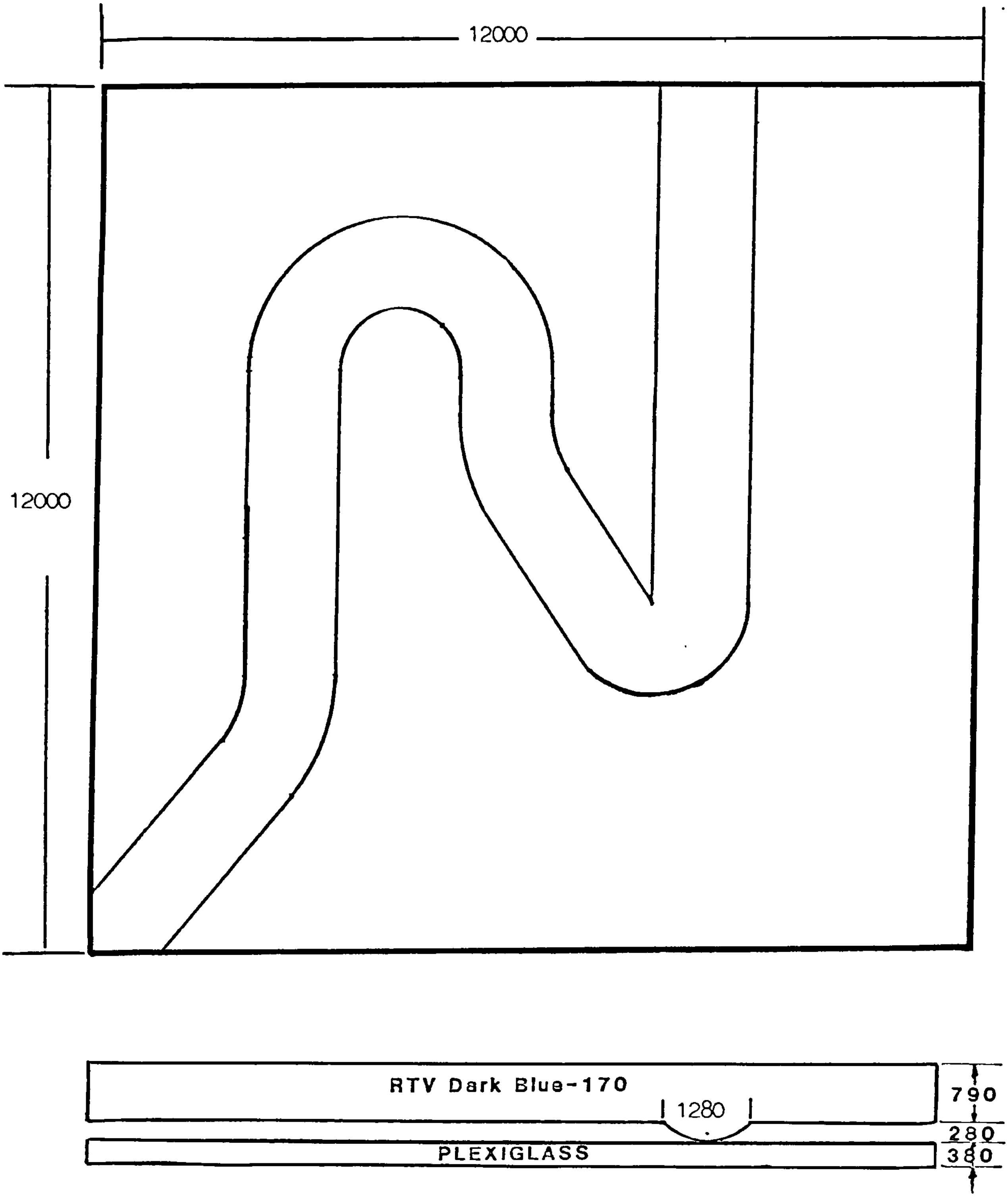

Figure 4-15 Dimensions of meandering cut model.

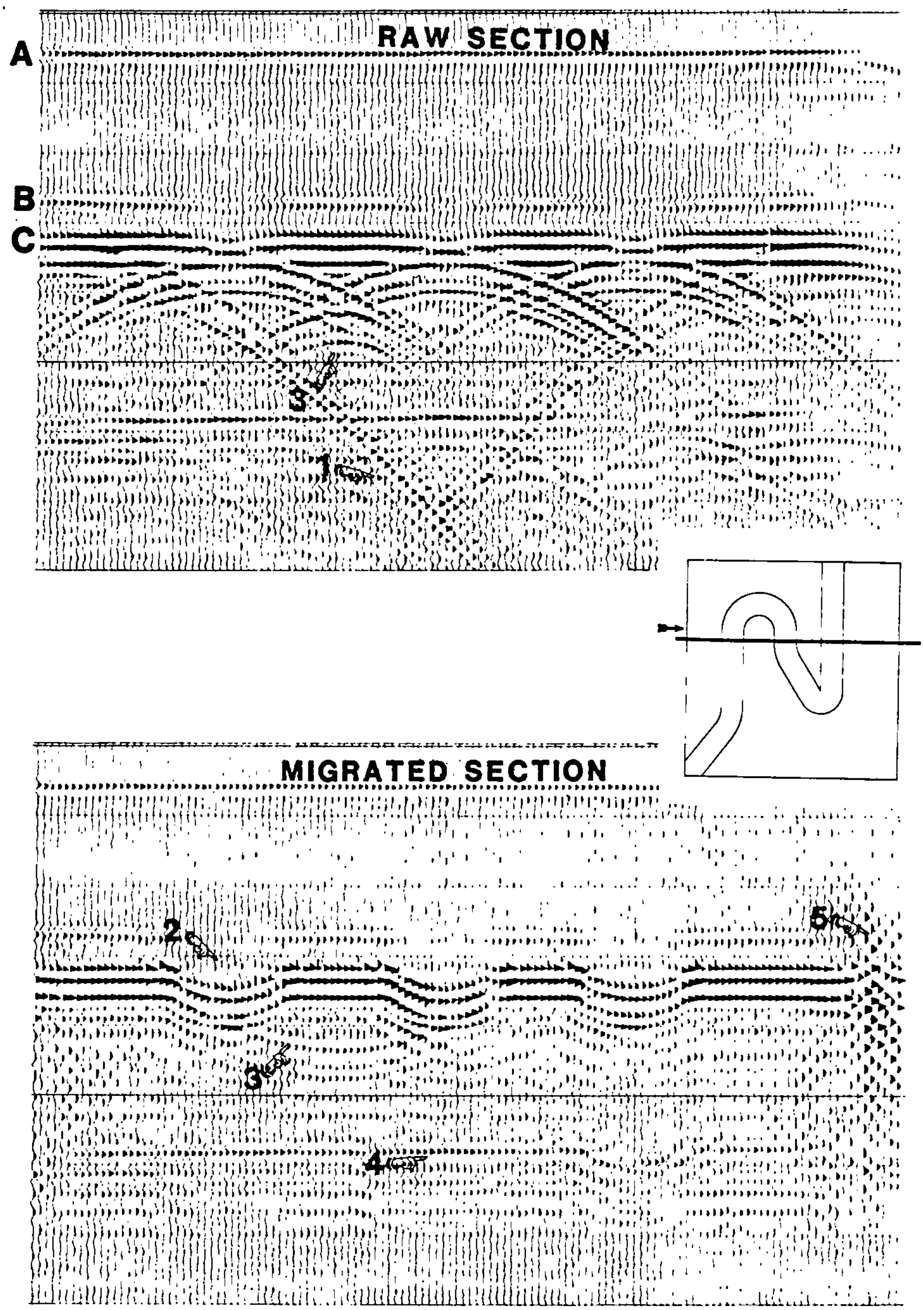

Figure 4-16 Raw and migrated sections across meandering cut model

migration. However, the event pushdown is really the velocity pushdown from the plexiglass-water interface that is defined and not the RTV-water channel interface (Event 2). This occurs for at least two reasons. First, the water-plexiglas interface has a higher reflection coefficient than the RTV-water interface. Secondly, the pushdown dip at the plexiglas-water interface is only one-half that of the true dip on the RTV-water channel and thus is illuminated and migrated much better. This would apply to real channel cuts which are filled with an anomalous velocity.

D. INVERSE MEANDERING CUT

The inverse meandering cut model is basically the previous model (meandering cut) turned upside down and placed on a plexiglas sheet (Figure 4-17). A profile line is chosen as shown in Figure 4-18.

This profile line crosses the channel three times. The middle channel is oblique to the profile line while the two outside channels are orthogonal to the profile line. On the migrated section, the left anticline has weak energy on its left flank because the raw time section should have been extended more to the left to include reflections from this flank. The middle anticline is weak because the profile is oblique to its trend. There are two additional problems that effect the weak anticline amplitude; first the dynamic range of the system is not adequate. Secondly, the reflection angles

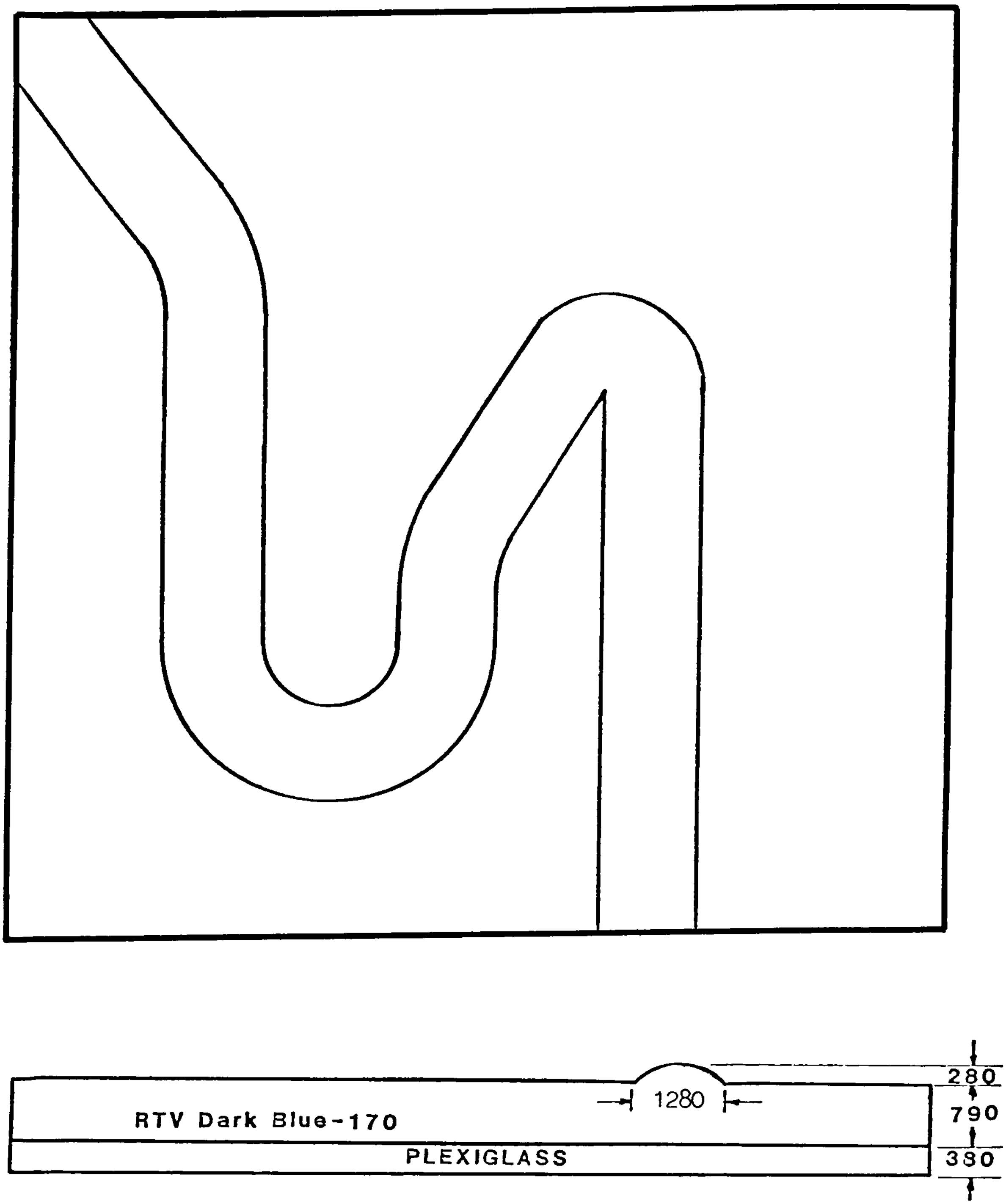

Figure 4-17 Dimensions of inverse meandering cut.

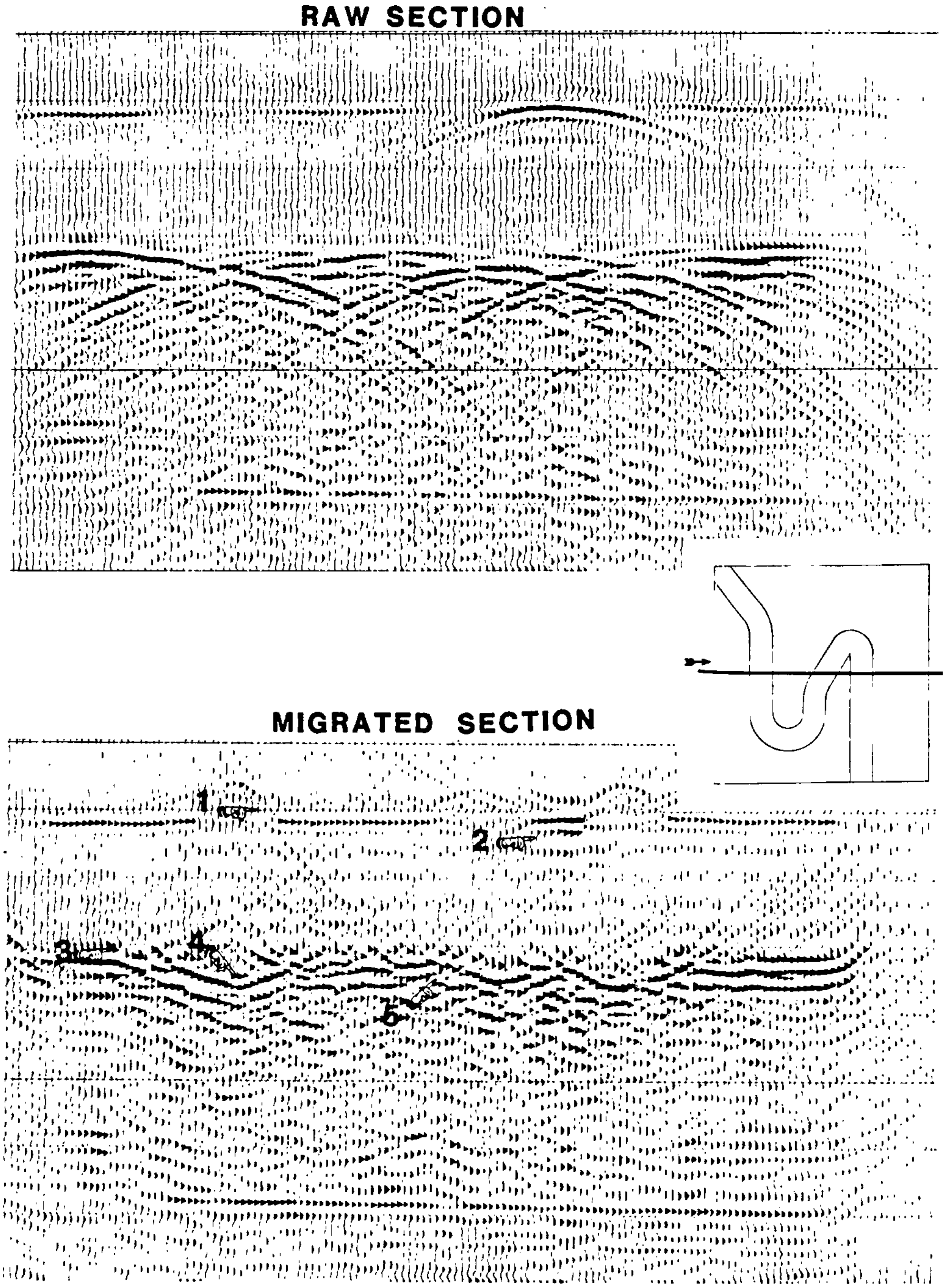

Figure 4-18 Raw and migrated sections across inverse meandering cut.

are too steep to be properly illuminated with our source system. That is, an array source effect is dimming the steep dips.

The bright spot at Event 2, near the middle of the section, is a focused event from the inside edge of the tight meander. There is no lithology change here to give rise to such a strong amplitude.

Events 3, 4 and 5, are poor reconstructions of the lower boundary. This boundary is disturbed more from its true shape of a flat boundary than in the meandering cut model. The meandering cut model is indicative of a thin-lens effect, whereas the inverse meandering cut model illustrates a velocity propagation problem. That is, the wavefront has propagated farther before it hits the next boundary and, thus, static shifts will not correct the distortion. It is impossible to pick the plexiglas reflection.

4.4 STRUCTURAL MODEL

A. OVERTHRUST

Shown in Figure 4-19 is the overthrust model which has an overhang. This RTV overthrust sits on top of a high velocity plexiglas platform. The purpose of this investigation is to identify the reflection-diffraction events which are diagnostic of overthrust surfaces.

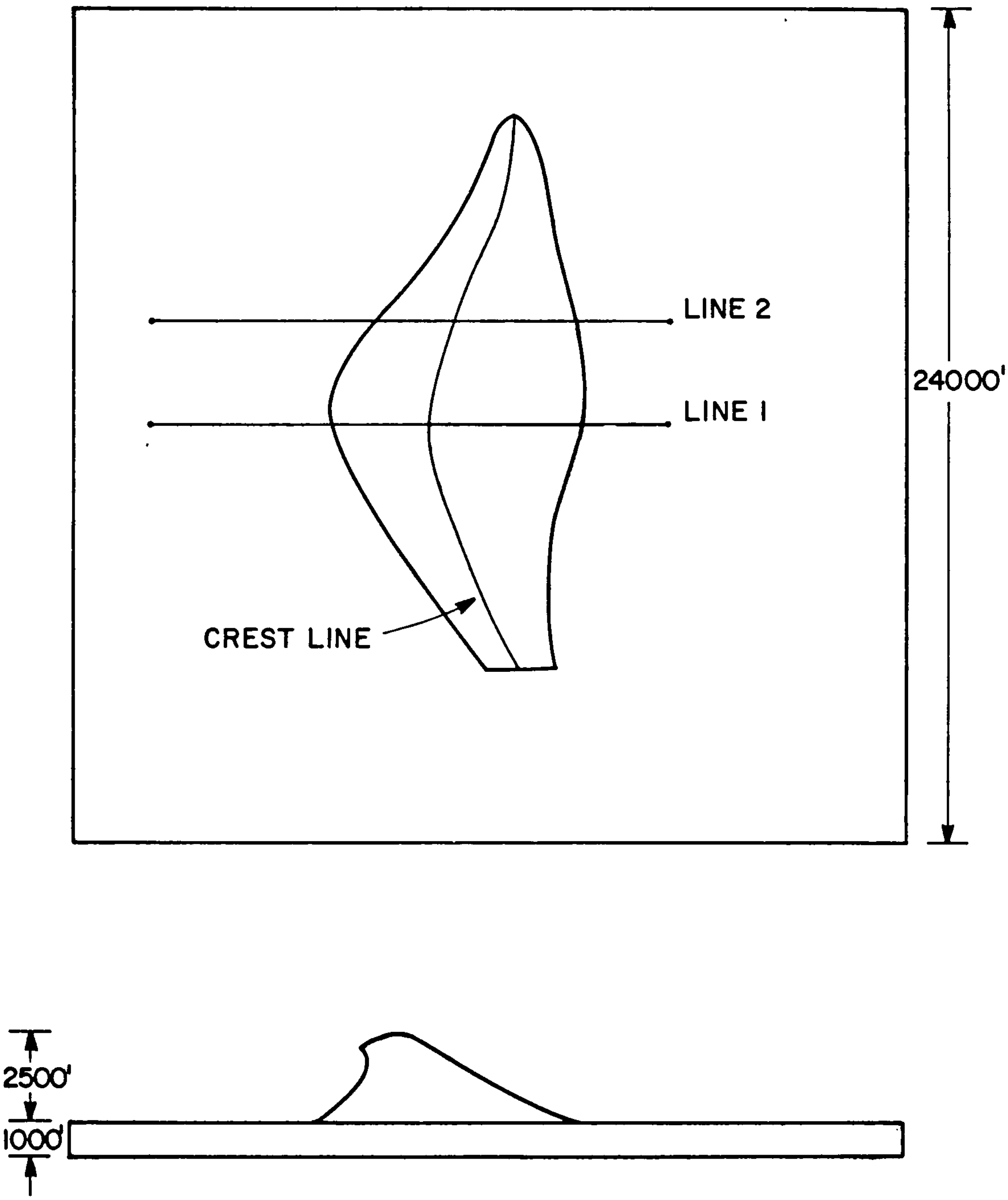

Figure 4-19 Dimensions of overthrust model.

Both the raw time section and the migrated section of Line 1, which crosses the peak of the model, are shown in Figure 4-20. The gain was set high in the raw section in order to see the reflections from the upper surface of the thrust. Because of the high gain, the plexiglas reflections appear ringy.

The maximum time to the reflection from the plexiglas on Line 1 is directly under the top of the structure as indicated by the dashed line. The existence of the "bow-tie" event from the flat plexiglass is related to the low velocity material of the overthrust. The higher amplitude reflection leg (Event 1) is under the gentler dip side of the structure and overrides the reflection leg from the tight curvature side.

Event 2 comes in at the measured time for energy which travels through the gentler dip side and reflects from the tip portion of the overhang. This event disappeared after migration, probably due to the fact that the velocity for migration was grossly off. Event 3 originates from the severe curvature of the boundary under the thrust.

On Line 2 (Figure 4-21), the maximum time to the reflection from the plexiglas reflector is not directly under the top of the structure. This indicates that the 3-D sideswipe effect moves the syncline pushdown from under the apparent top of the structure. If

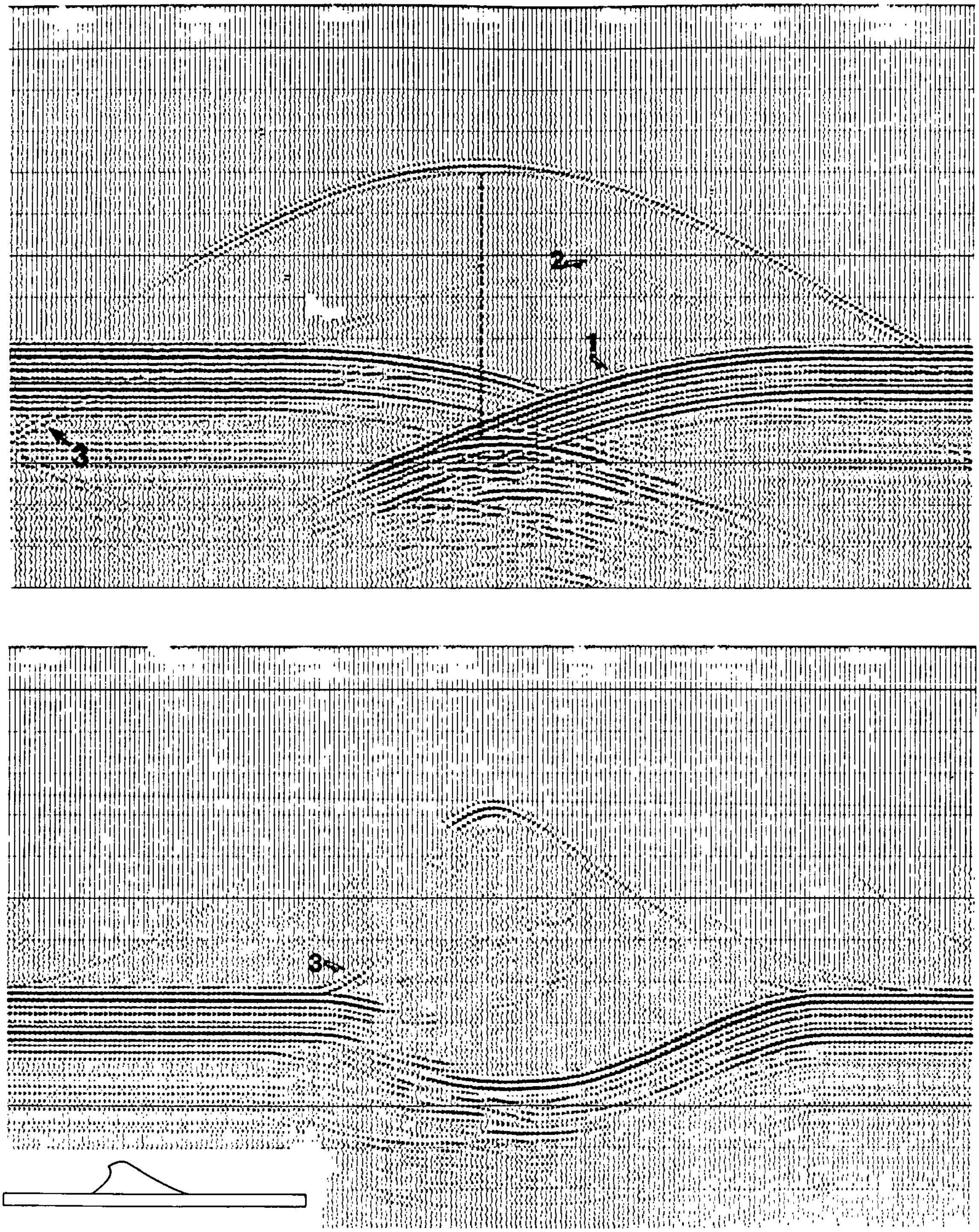

Figure 4-20 Raw and migrated sections across overthrust model -- Line 1.

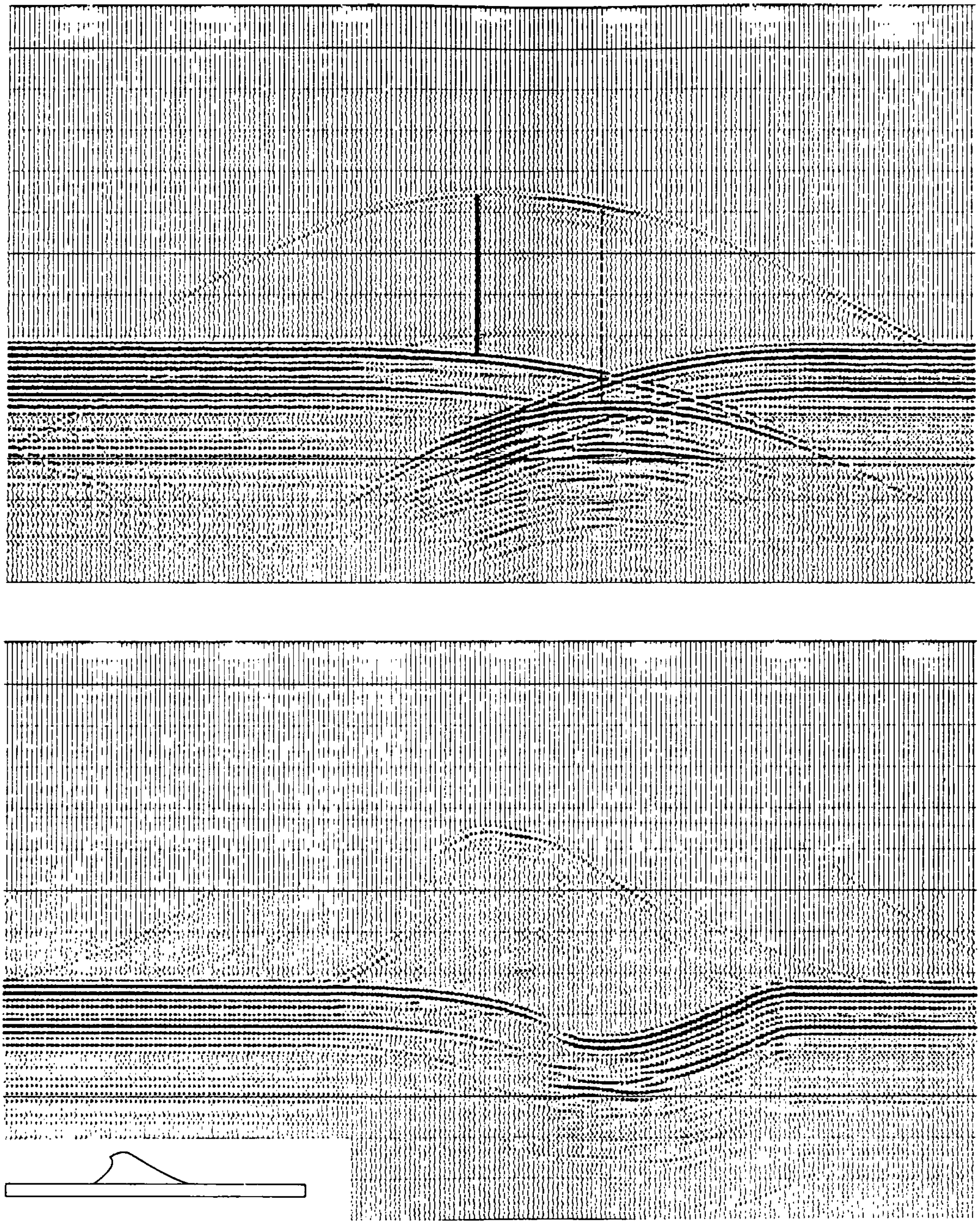

Figure 4-21 Raw and migrated sections across overthrust model -- Line 2.

sideswipe were not suspected, a misleading interpretation would result.

B. REEF MODEL

The map view, side view and contour map of the reef model are shown in Figure 4-22. The reef is supported 1000 ft above a plexiglas platform. This 3-D structure is constructed with three different materials: plexiglas, resin and RTV. The purpose of this study is to investigate the effects of high versus low velocity propagation in tightly curved structures and shear supporting versus non-shear supporting formations that are tightly curved.

A review of the material properties is helpful for interpreting the model data. The velocity in plexiglas is 21082 ft/sec (prototype) for P-wave and 10685 ft/sec for shear wave. The velocity of resin is 18934 ft/sec for P-wave and 9038 ft/sec for shear wave. Neither water nor RTV support shear waves; they have P-wave velocities of 11928 ft/sec and 7920 ft/sec respectively. All three materials have about the same density, which is a little higher than that of water. It was also shown by Smith (1980) that the converted event (PPSP or PSPP) for water over plexiglas has a high amplitude.

Now examine the sections in Figures 4-23, 4-24 and 4-25. The resin model results showed no significant differences from the

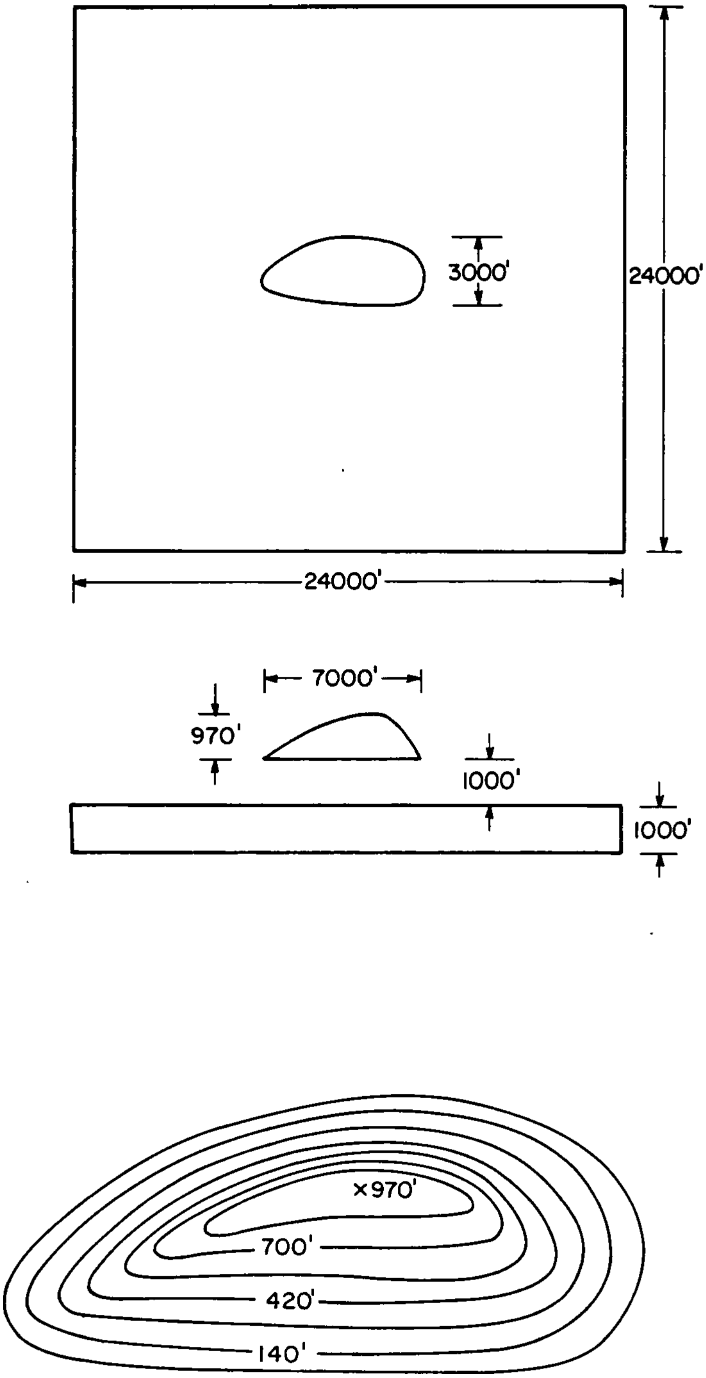

Figure 4-22 Dimensions of reef model.

plexiglas results. However, the RTV lines contained only energy which one would normally predict.

Event 3 is easy to identify as the reflection from the bottom of the reef, which showed a pullup for plexiglas and a pushdown for RTV. For plexiglas and resin, the reflection from the top of the reef has the same polarity as the reflection from the top of the platform. However, it is opposite for RTV. Events 4 and 5 are reflections from the top and bottom of the platform respectively. Again, they showed pullup for the plexiglas and resin reef and pushdown for RTV reef.

Events 1 and 2, which occur on the plexiglas and resin model sections only, were difficult to interpret. Initially, they were thought to be either the direct diffractions from the sharp edges of the reef or peg-leg multiples. However, if Events 1 and 2 are diffractions, it is hard to explain why the diffractions are strong inside the model but weak on the outside. It cannot explain, either, why the amplitude of these two events was weaker for resin than those for plexiglas. Remember the acoustic impedence are approximately the same for both materials. The peg-leg multiple interpretation was not acceptable because the traveltime measurements would not match the events.

Examine now the sections in Figure 4-26 which is the migrated version of Figure 4-23. Events 1 and 2 terminate against the edges

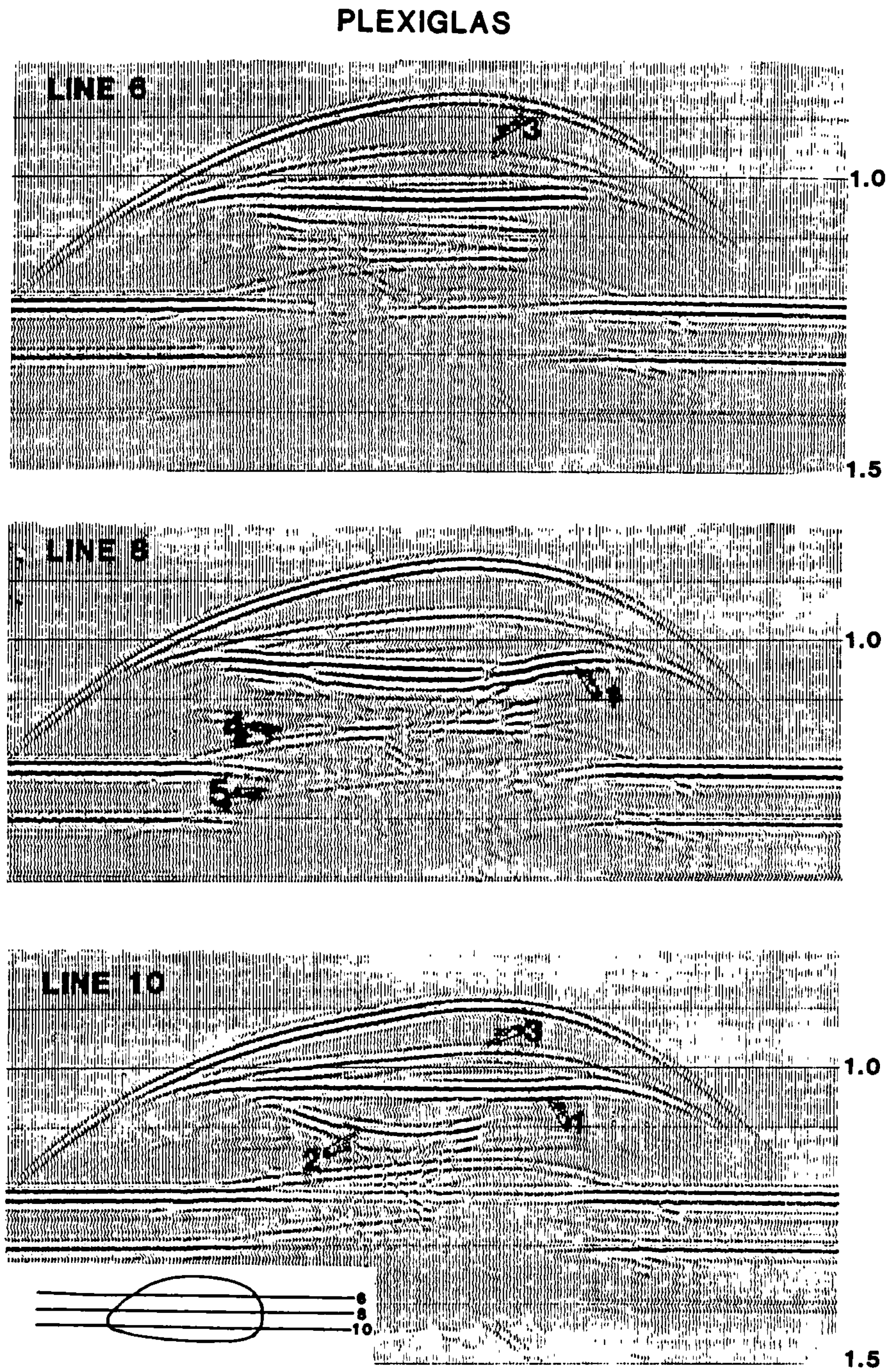

Figure 4-23 Raw sections across plexiglas reef -- trend lines.

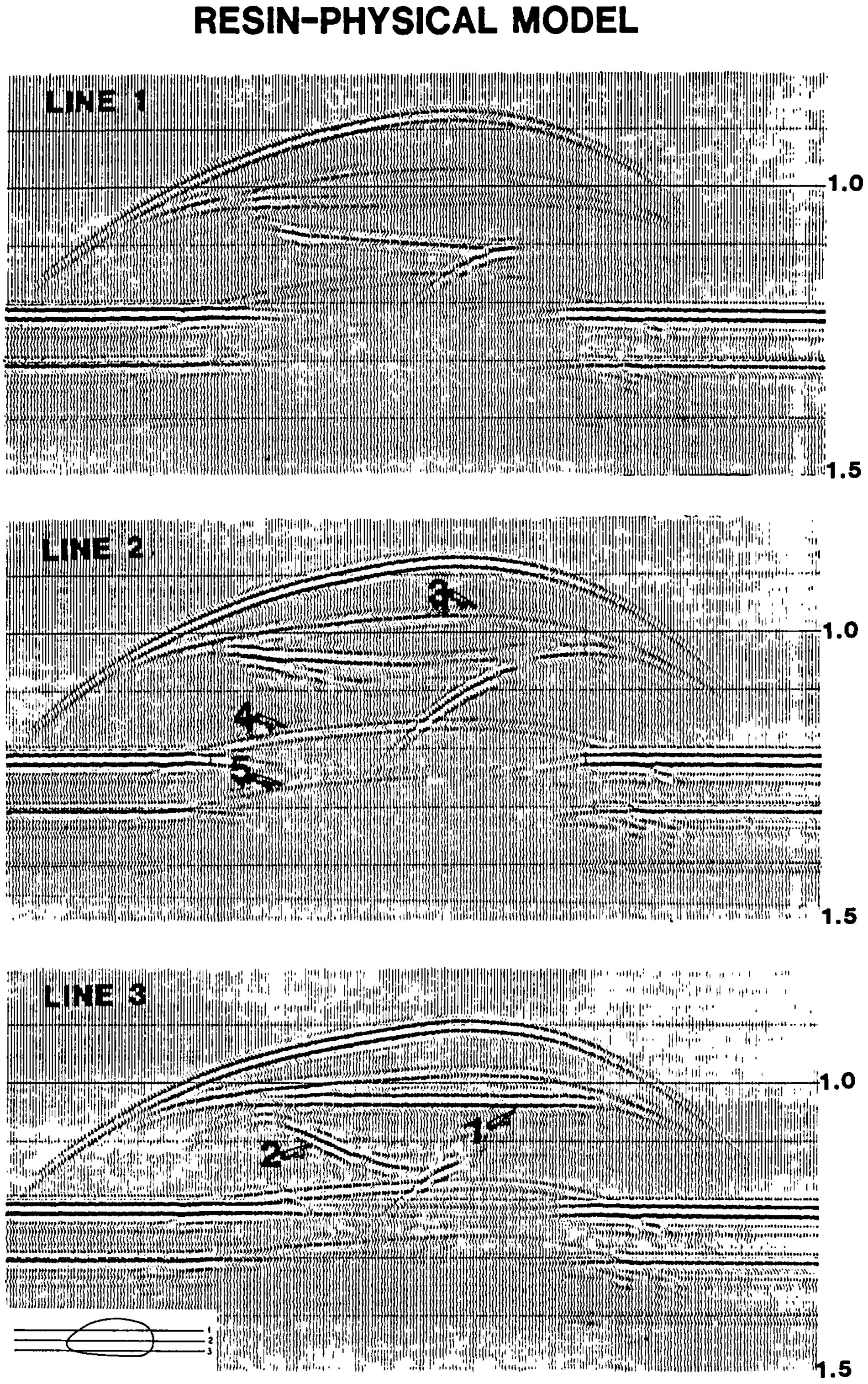

Figure 4-24 Raw sections across resin reef.

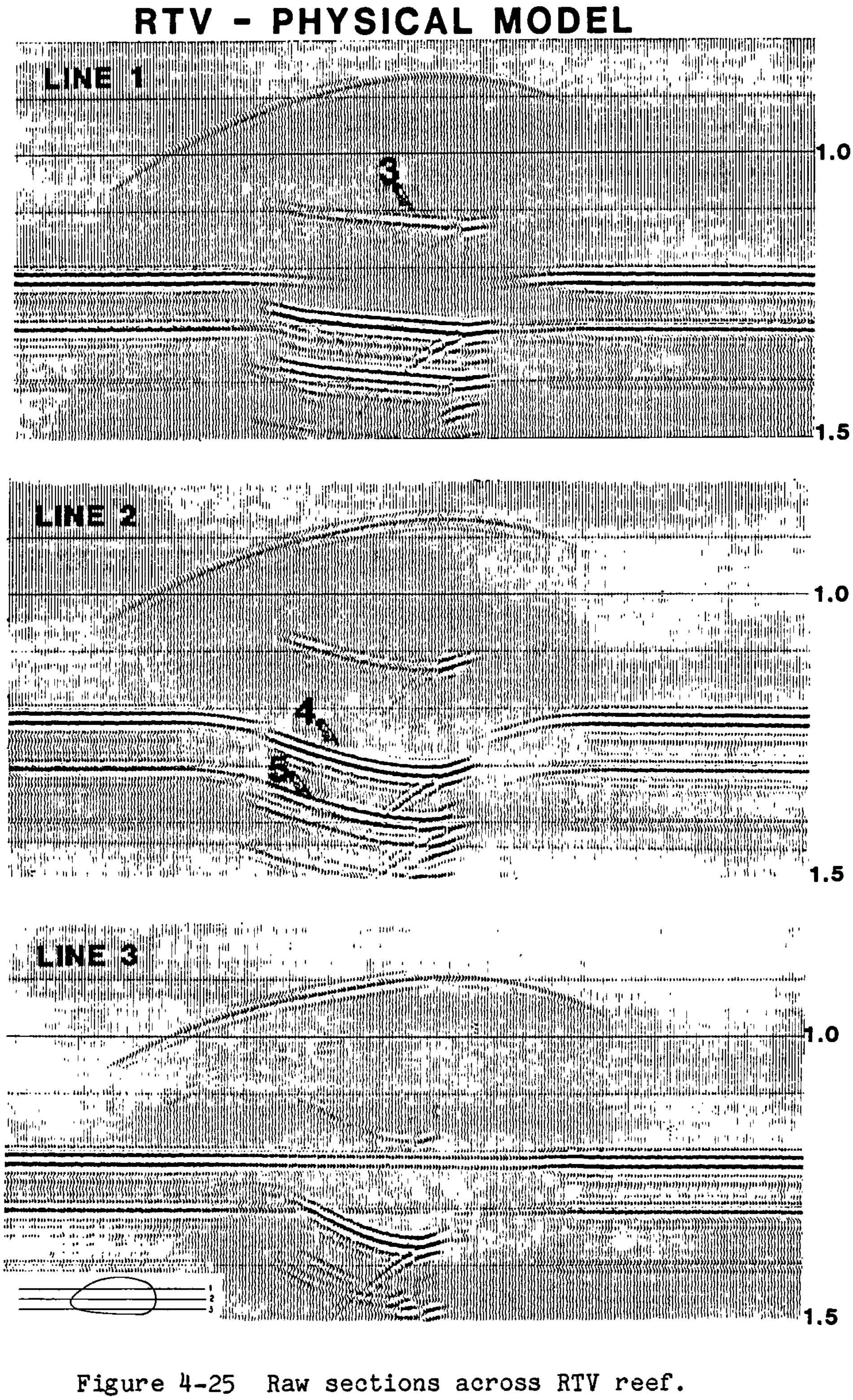

Figure 4-25 Raw sections across RTV reef.

after migration. This indicates that the events are related to the edges paralleling the profile line of the model. After examining Figure 4-27 which were sections collected orthogonally to the trend of the reef, we know the two diffraction-like events in the plexiglas and resin models were corresponding to Events 1 and 2 in Figure 4-23. An aid in this interpretation will be discussed in Chapter V, when the numerical and physical model results are compared.

C. HYDROCARBON MODEL

The geological model shown in the top of Figure 4-28 consists of a domal structure with a relief of 1750 ft. The upper 750 ft consists of RTV, while the lower 1000 ft consists of plexiglas. This domal structure rests on a very thick body.

In Line 5, Event A is sideswipe from the 750 ft RTV and it is "separating" from another sideswipe event B, which comes from the contact between the RTV and the plexiglas. Beneath B is a third sideswipe coming from the base of the plexiglas.

The top and bottom of the plexiglas zone in Line 6 is recognized as the two reflection events right above and below the letter C. This time separation remains the same across a majority of the section.

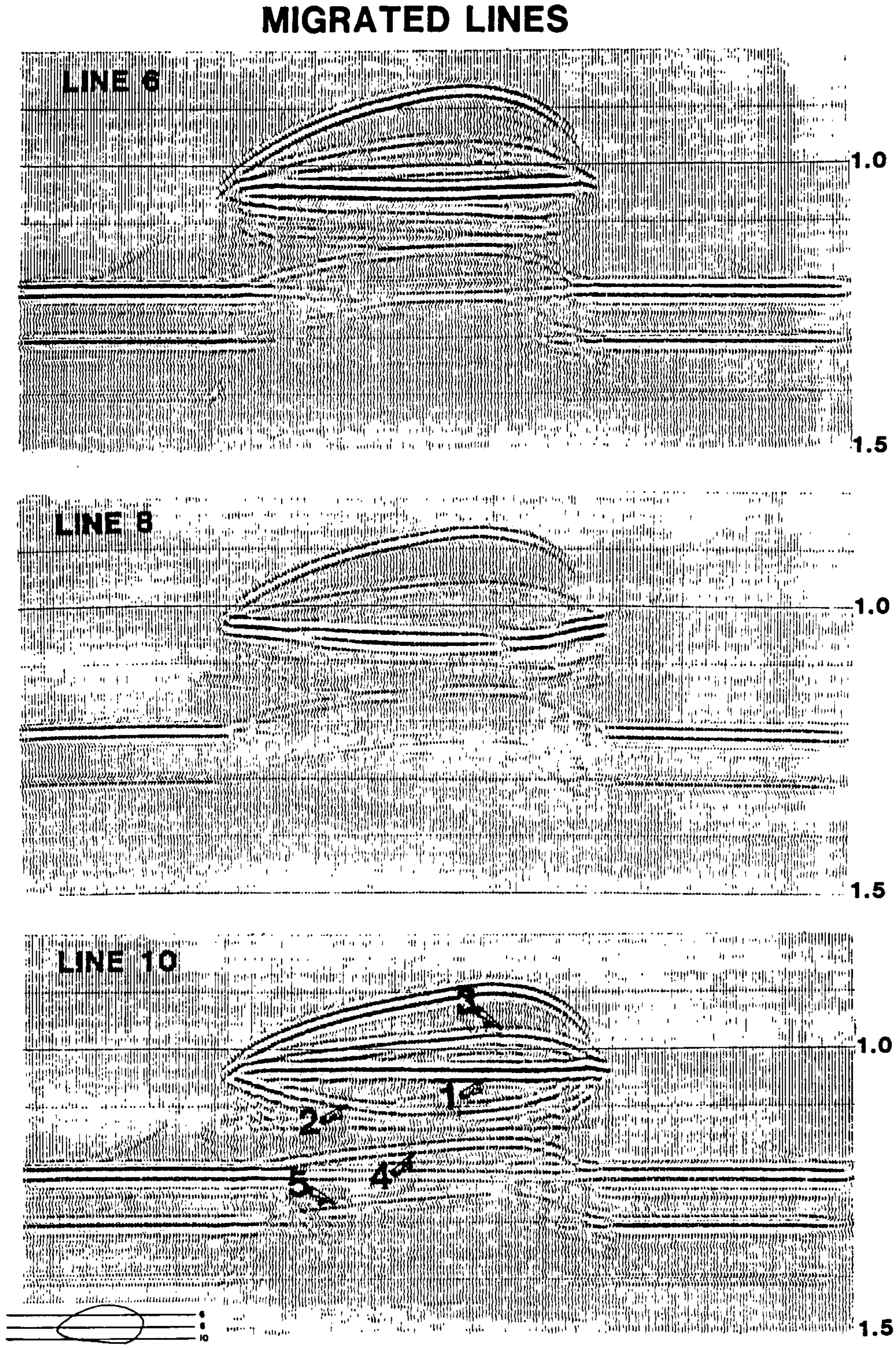

Figure 4-26 Migrated sections across plexiglas reef -- trend lines.

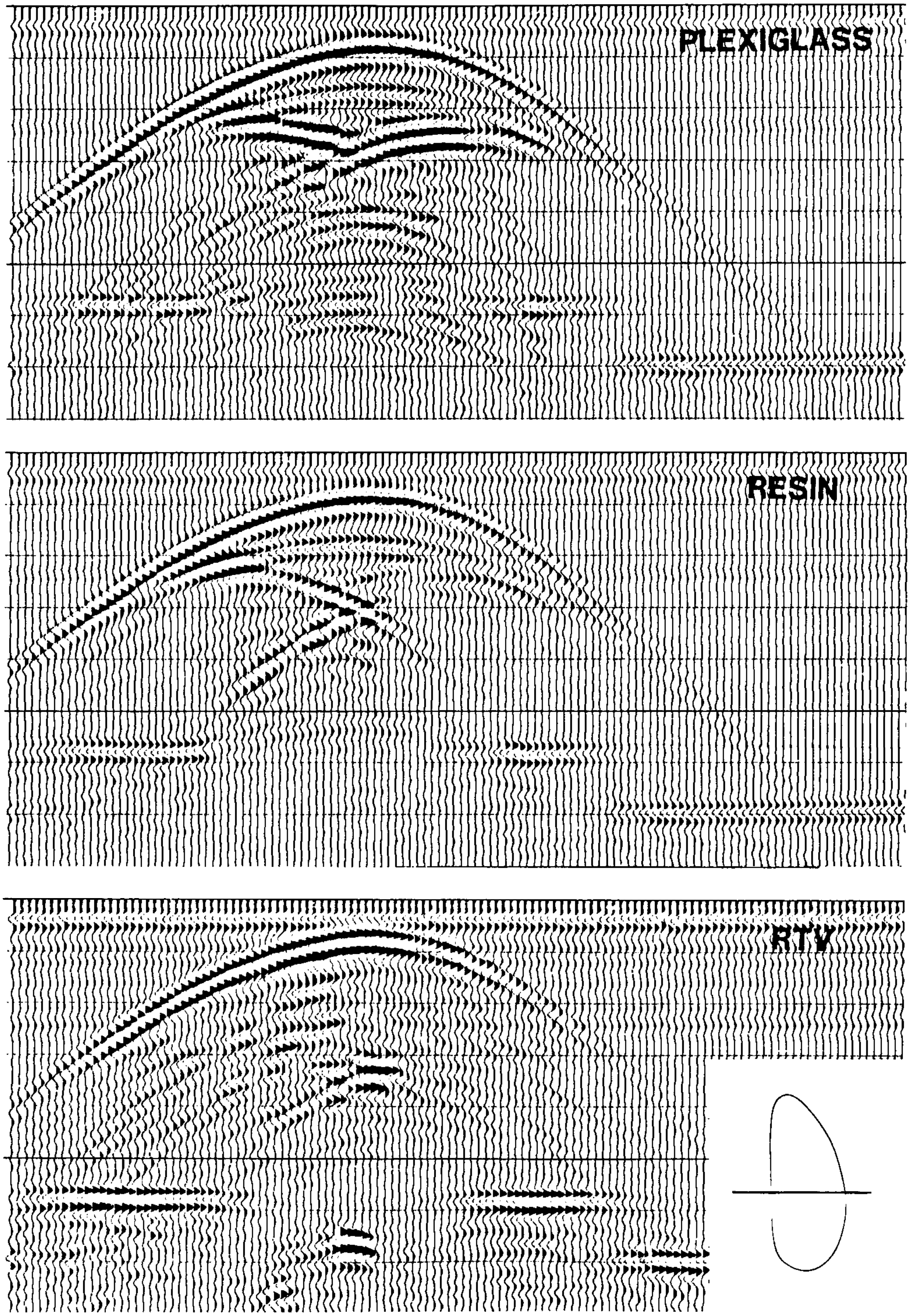

Figure 4-27 Raw sections across plexiglas, resin and RTV reef -- traverse lines.

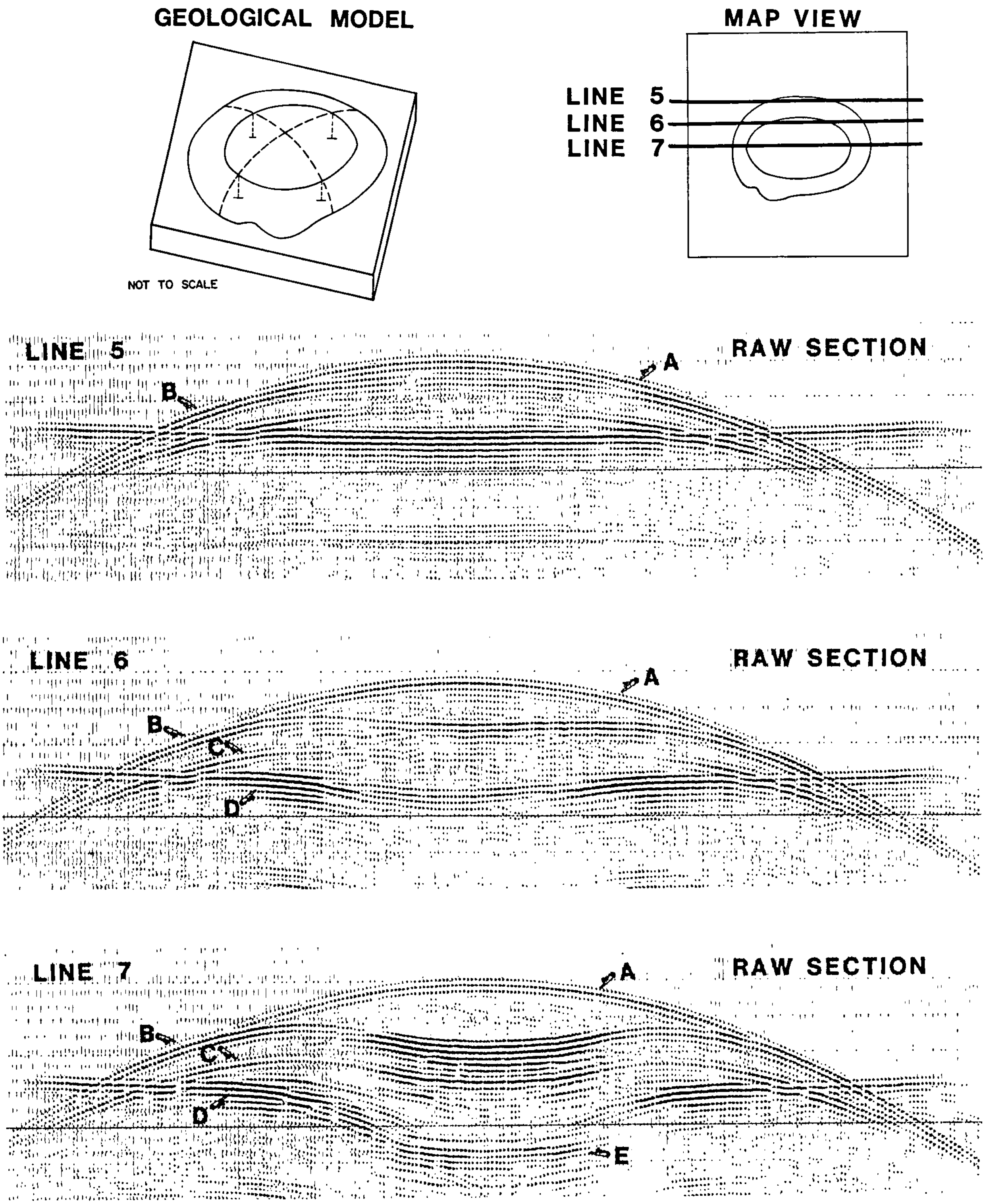

Figure 4-28 Parallel lines across hydrocarbon model.

Line 7 is directly over the center of the model. The strong reflections in the middle are caused by the focusing of energy through the low velocity RTV lens. Event D is a velocity pullup of an edge diffraction. Event E is a source ghost from the strong primary amplitudes in the middle of the section.

Line 8 traverses the trend of the model orthogonally as shown in the top of Figure 4-29. There are four sections in this figure : the single-fold raw section, the migrated single-fold, the six-fold stack and the migrated six-fold stack.

The single-fold section has a better reflection response from the flanks of the model (Event A) than the six-fold stacked section. However, the top and bottom reflections of the plexiglas zone are enhanced on the stacked section because the stacking velocity was set to enhance the flat events. The low velocity pushdown goes through a buried focus on the far traces, as is evident by the bowtie on the stacked section.

Migration of the single-fold data produces a more realistic picture of the model than the six-fold migration (Event B). Event C is anomalous. One possible interpretation is to associate it with a refracted-diffraction which passes through the edge of the high velocity material.

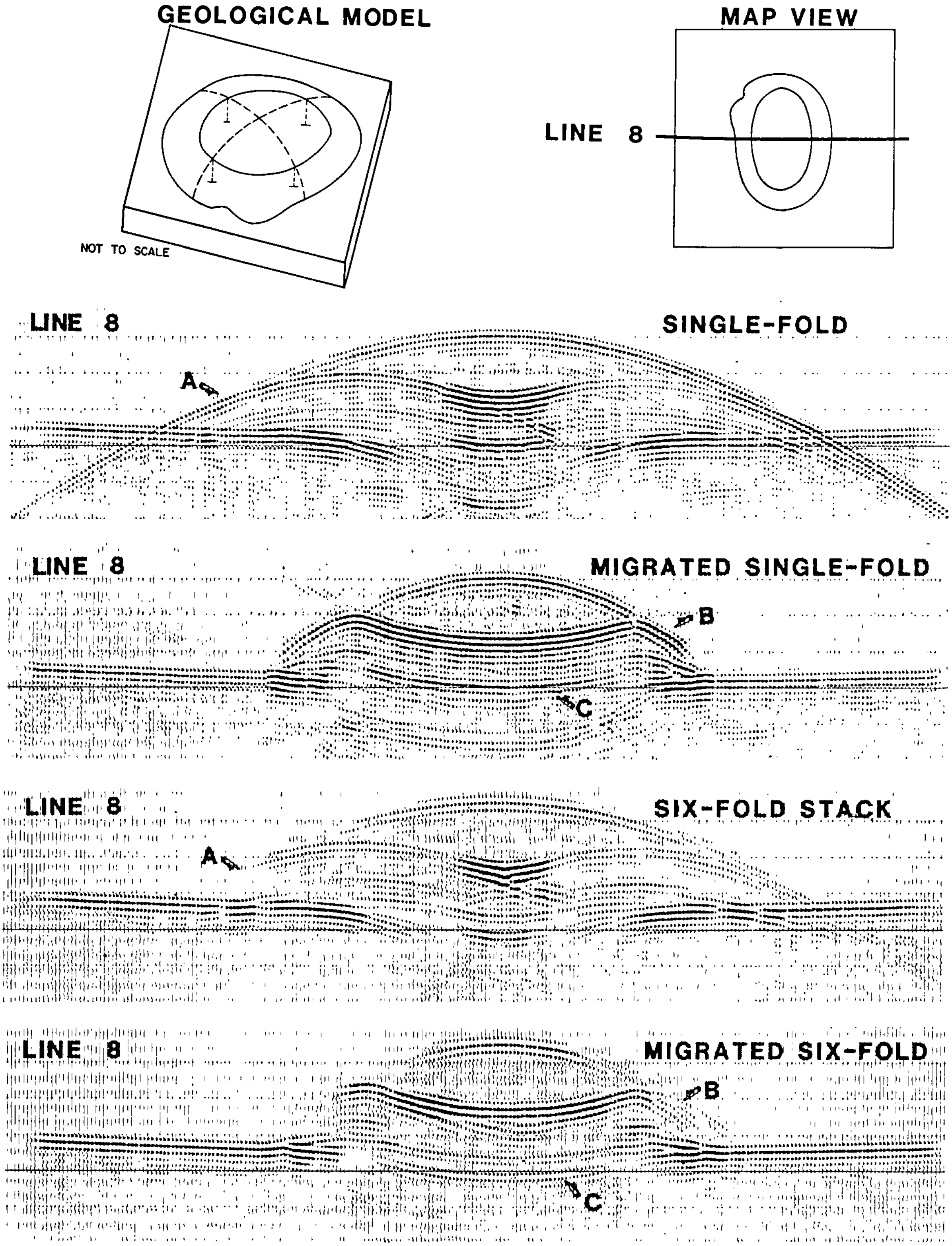

Figure 4-29 Hydrocarbon model -- single fold versus multi-fold.

4.5 SUMMARY

When data are collected over an amorphous body of limited extent, either a bright spot or dim spot can result. A portion of the downgoing wave travels around the edges of the lens and reflect from the lower platform. These out-of-plane events interfere constructively (destructively) with the events travelling directly through the low velocity (high velocity) lens. The dim spot occurs when the high velocity lens is encountered and the bright spot occurs when the low velocity lens is encountered.

For multi-sand bodies with high velocity contrast, out-of-plane edge diffractions cause low-frequency disturbed zones on the migrated sections which might be interpreted as evidence of gas in the upper sand lenses. Three-dimensional migration is needed to collapse these edge diffractions.

For the meandering cut models, both a "thin" lens and "thick" lens propagation effect was observed. The thin lens effect acted as a static shift when the migration was performed. However,the "thick" lens cannot be treated as a static correction.

From the overthrust model, the thickness of the anomalous structure can be misleading when the reflection from the top of the structure is sideswipe. Also the structural shape on the time section becomes skewed.

The 3-D reef model with tight curvature is difficult to interpret when mode conversion is possible. Additional events were generated from these types of models, which can be discerned from the primary events when the non-shear supporting model results are compared. However, no satisfactory explanations have been reached for these additional events.

Even with the model known beforehand, we are constantly surprised on how complicated an interpretation of seismic events can be, especially when multi-velocity 3-D structures such as the hydrocarbon model is used. This is complicated further when stacking is done before migration.

V. COMPARISON OF PHYSICAL AND THEORETICAL MODELS

When doing theoretical modeling, a restricted earth model has to be assumed. The purpose of comparing physical to theoretical model data is to identify the assumptions that fail. Four model results are compared in this work; they are the anticline, dome, basin and reef. All the physical data are collected through the physical modeling system described in Chapter II. Wave theory (with bent rays) and ray theory with diffractions are used to generate the 2-D numerical data over the anticline. The Kirchhoff wave theory with non-refracted rays is used to generate 3-D data over the dome, basin and reef.

5.1 ANTICLINE

The anticline model was constructed from both the high velocity plexiglas and the low velocity RTV materials. Shown in Figure 5-1 are the dimensions of the anticline model. Seismic sections collected over the plexiglas anticline are shown in Figure 5-2. Section A is six-fold stacked physical data, section B is ray-theory numerical data, section C is single-fold physical data and section D is wave theory numerical data.

The results from both wave and ray theory are approximately the same for the plexiglas anticline. The amplitude ratio of the

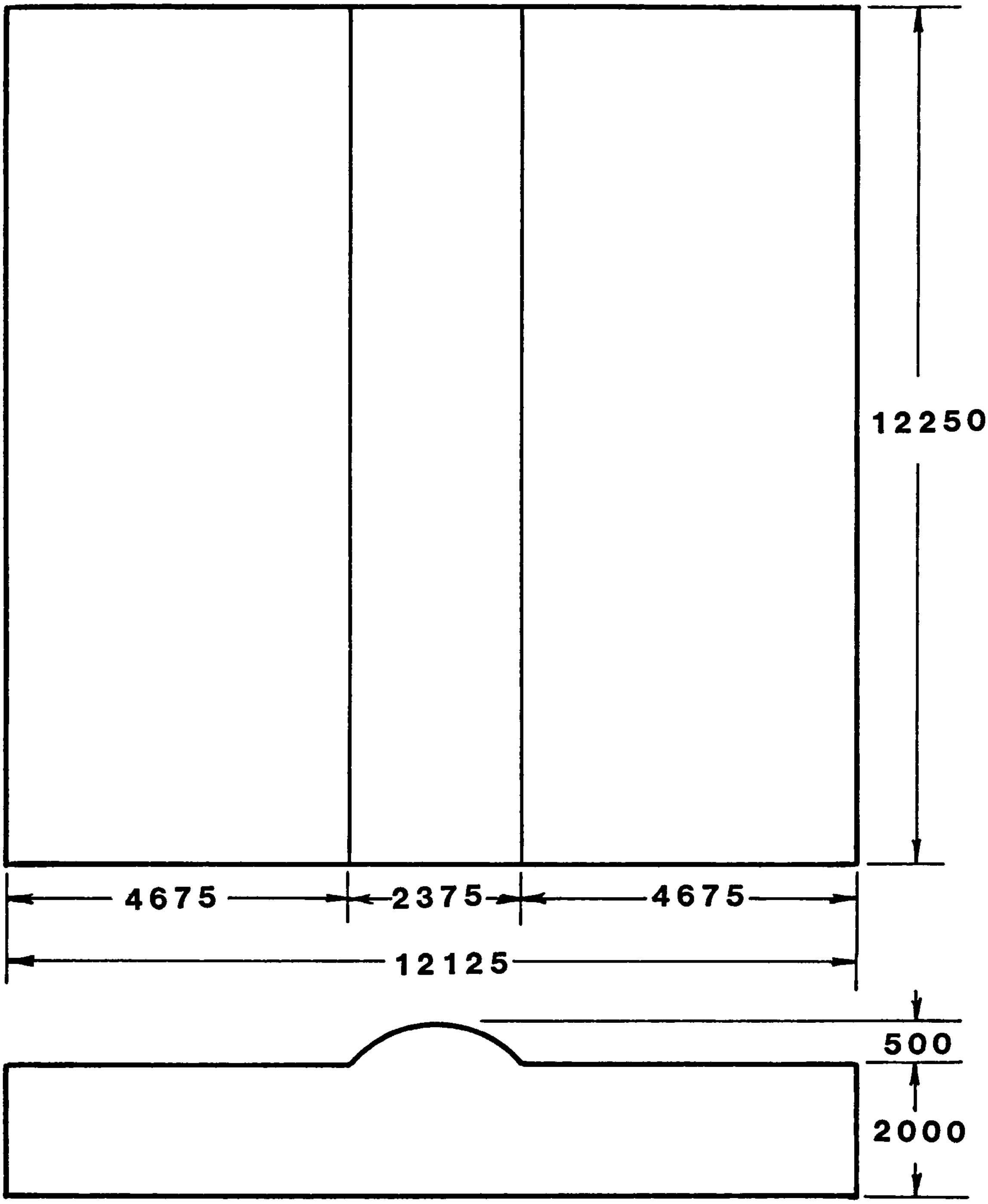

Figure 5-1 Dimensions of anticline.

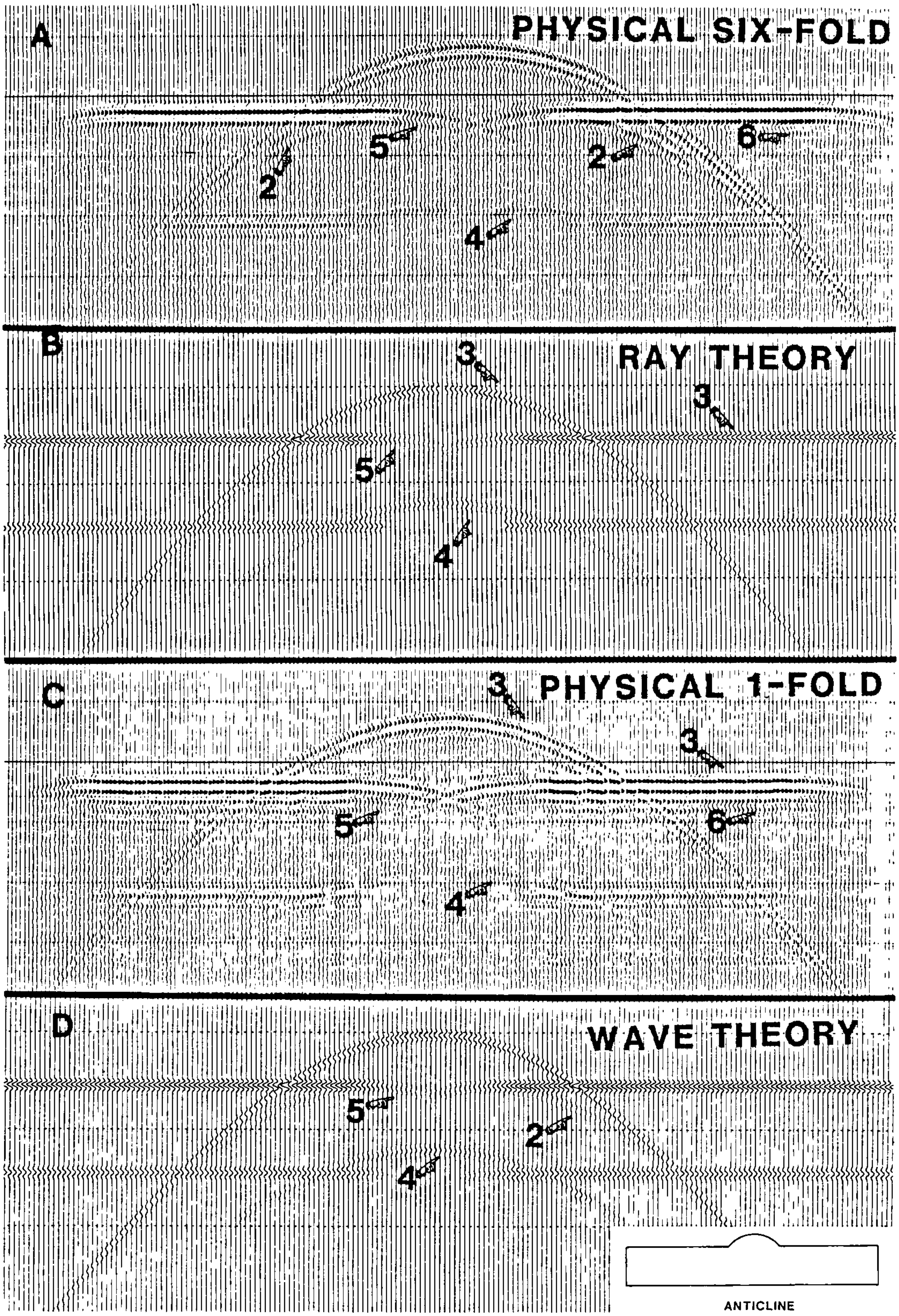

Figure 5-2 Raw sections across plexiglas anticline.
A. Six-fold stacked physical data.
B. Ray theory numerical data.
C. Single-fold physical data.
D. Wave theory numerical data.

reflections from the curved boundary to the flat boundary is approximately the same for both theoretical and physical models (Events 3). The inside diffraction amplitude caused by the sharp edges (Events 5) decays faster on the theoretical data than it does on the physical model data. Also, the outside diffractions on the six-fold section are stronger than on the theoretical model (Events 2). This last additional amplitude is possibly caused by doubly reflected energy at the physical model sharp boundary. Also, both theories predict a larger amplitude on the velocity pullup event than is observed on the physical data.

Shown in Figure 5-3 are sections collected over the RTV anticline. Section A is single-fold physical data, section B is wave theory (bent rays) numerical data and section C is ray theory numerical data. The theoretical wave solution section and the common-offset physical model section are very similar. The diffractions (Events 1), under the anticline, are weak on the physical model time section and the theoretical time section shows this effect also. Remember that the plexiglas physical model diffractions were larger than the theoretical diffractions; this is not the case here. The reflection amplitude for the bright zone in the velocity pushdown (Event 2) is surprisingly similar for the wave theory and the physical model. But the normal-incident ray theory section does not match the physical model data as well in the velocity pushdown zone. The lack of perceivable diffractions (Events

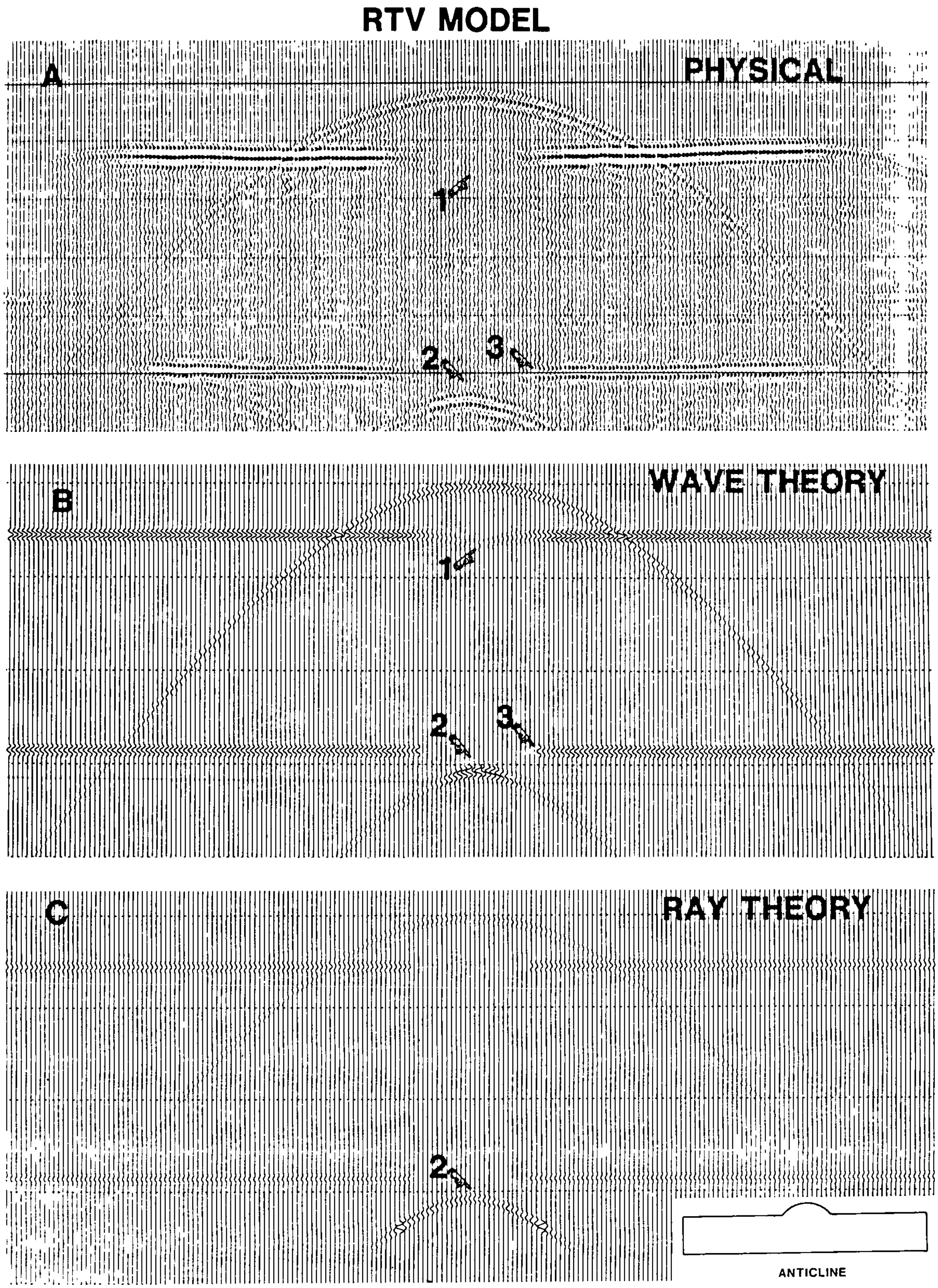

Figure 5-3 Raw sections across RTV anticline.
A. Single-fold physical data.
B. Wave theory numerical data.
C. Ray theory numerical data.

3) on the theoretical model section at the pushdown should not be directly correlated to the wave theory model because we believe this diffraction option was not coded correctly when running the theoretical model.

In Figure 5-4, another theoretical section is compared to the physical model data over the RTV anticline. These numerical data are generated with the same algorithm as was described in Chapter III, with an additional vertical depth adjustment for multi-velocity media. Even thougth the algorithm applied here is wave theory without bending the rays, the results are still a good match.

5.2 TWIN DOME AND FAULT MODEL

Shown in Figure 5-5 is an isometric of the twin dome and fault model which is the duplicate of the French or Gulf model (French,1974). The time sections collected over this model are shown in Figure 5-6. Section A is the theoretical data, section B is the physical resin data and section C is the physical RTV data.

All three sections show similar features from the top reflecion surface of the model. Event 2 on the resin model is much smoother than the similar event on the RTV model because the resin model data were acquired after the source wobble was stablized. RTV data were collected before stabilization.

RTV MODEL

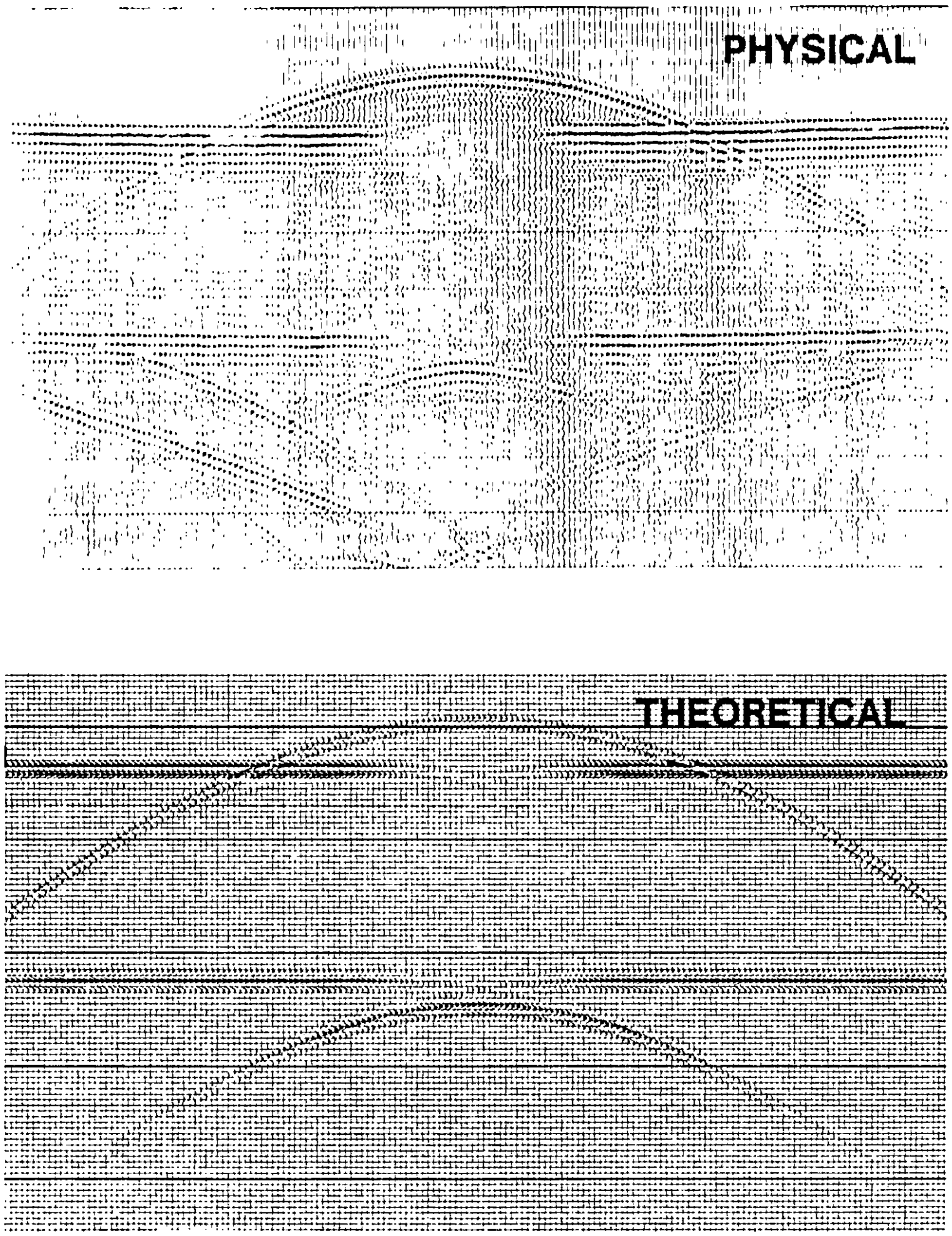

Figure 5-4 Raw sections across RTV anticline
-- Physical versus Kirchhoff theoretical.

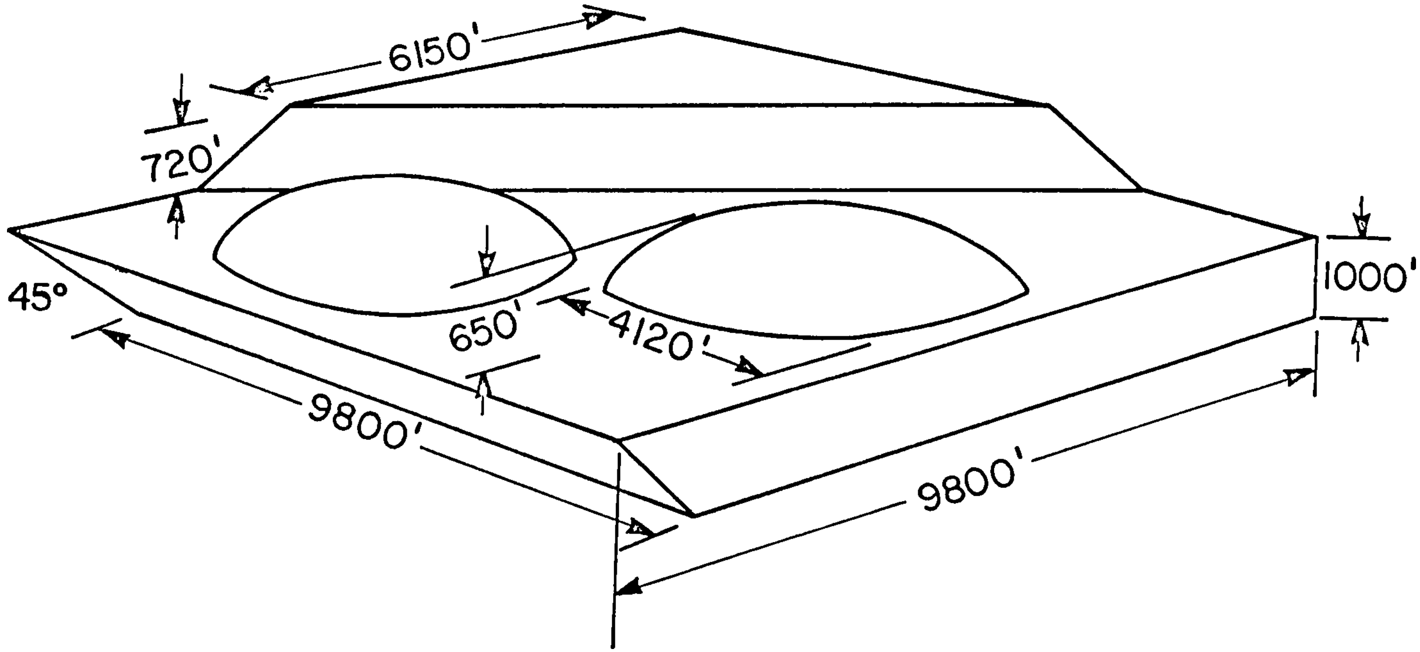

Figure 5-5 Isometric of twin dome and fault model

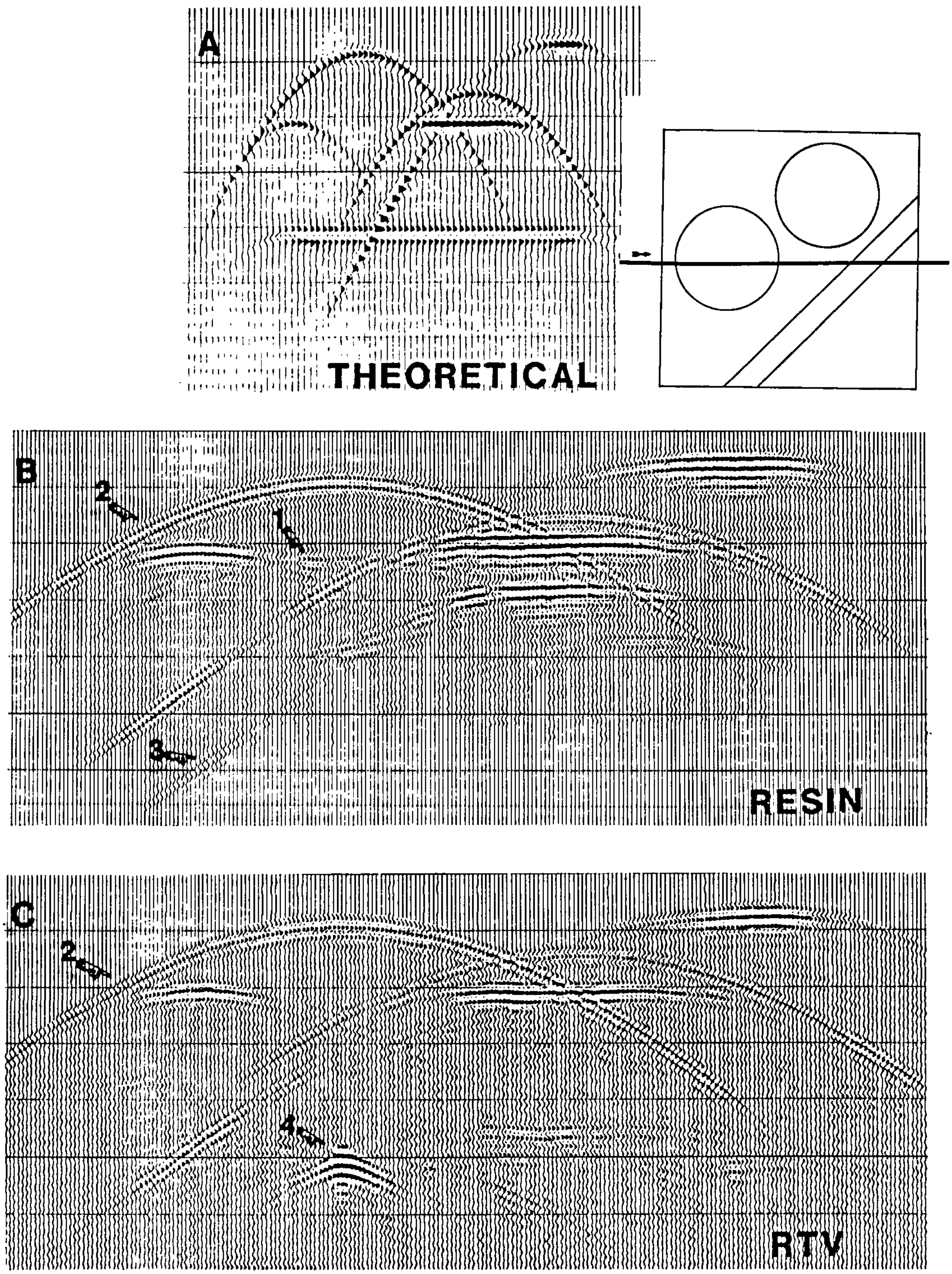

Figure 5-6 Raw sections across twin dome and fault model.
A. Kirchhoff theoretical data.
B. Resin physical data.
C. RTV physical data.

The reflection from the lower boundary is flat on the theoretical section because no vertical velocity adjustment or ray-bending is applied. The low-velocity RTV model generates the buried focus effect under the dome, which is significant only when the profile is directly over the center of the dome.

5.3 BASINS

The physical basin model, as shown in Figure 5-7, has radii of curvature in the two principal planes of 4000 ft and 7000 ft. The basin has 715 ft of relief. The profile lines were 6000 ft above the flat protion of the model, and this places the profile line between the two foci. The model's prototype velocity is 8000 ft/s compared to the surrounding water velocity of 12000 ft/s.

The numerical basin model (Figure 5-8) is very similar to the physical basin model in dimensions except the numerical model has a smooth lip while the physical model has a sharp edge. The numerical basin has 750 ft of relief and the profile lines are 5500 ft above the flat portion of the model. This basin has a single interface with the medium velocity of 12000 ft/s.

Line 2 across the physical basin in Figure 5-7 is equivalent to Line 1 across the numerical model in Figure 5-8. This profile line traversed the model along one of the principal planes of the basin.

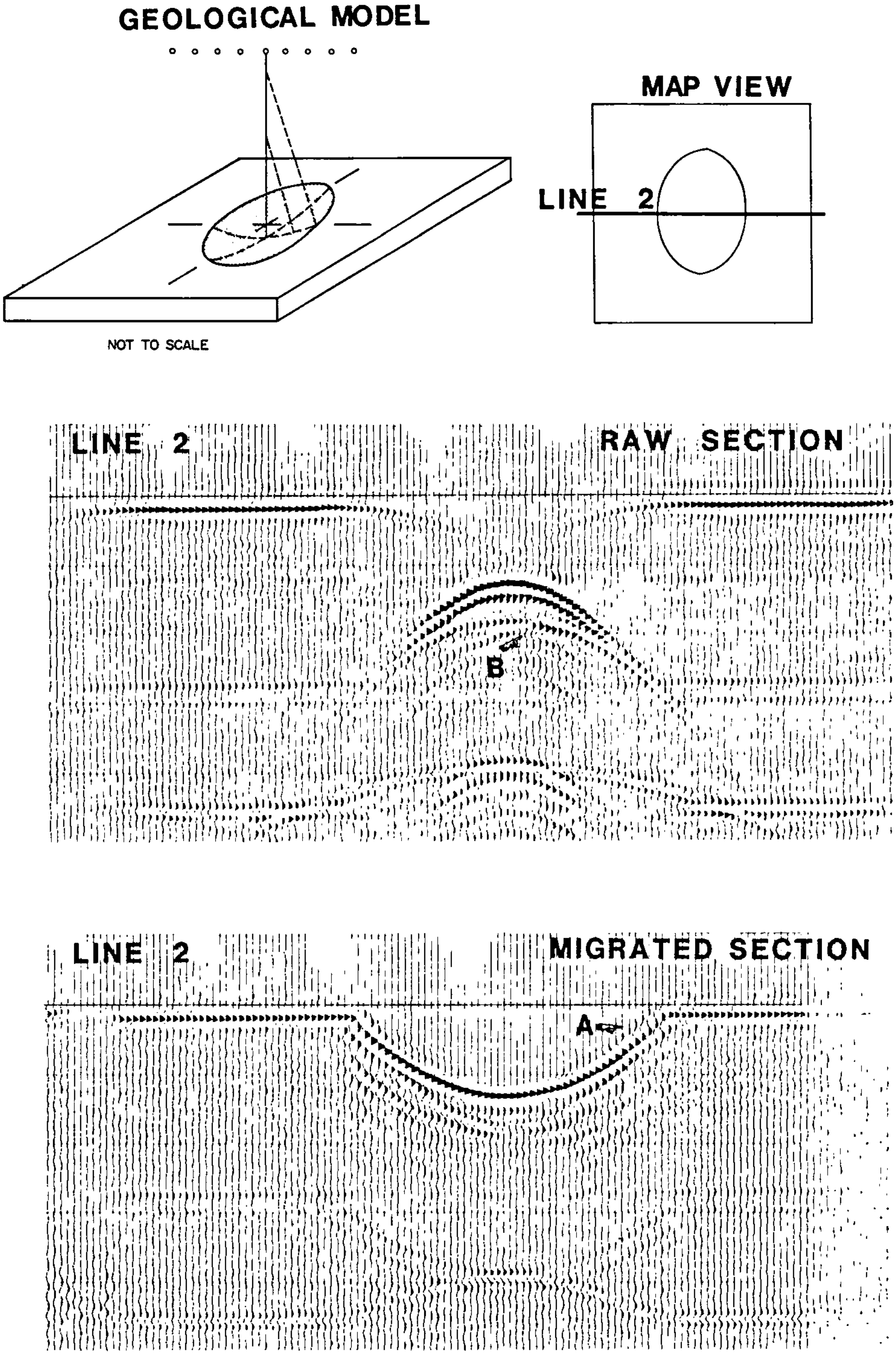

Figure 5-7 Raw and migrated sections across physical basin -- principal plane Line 2.

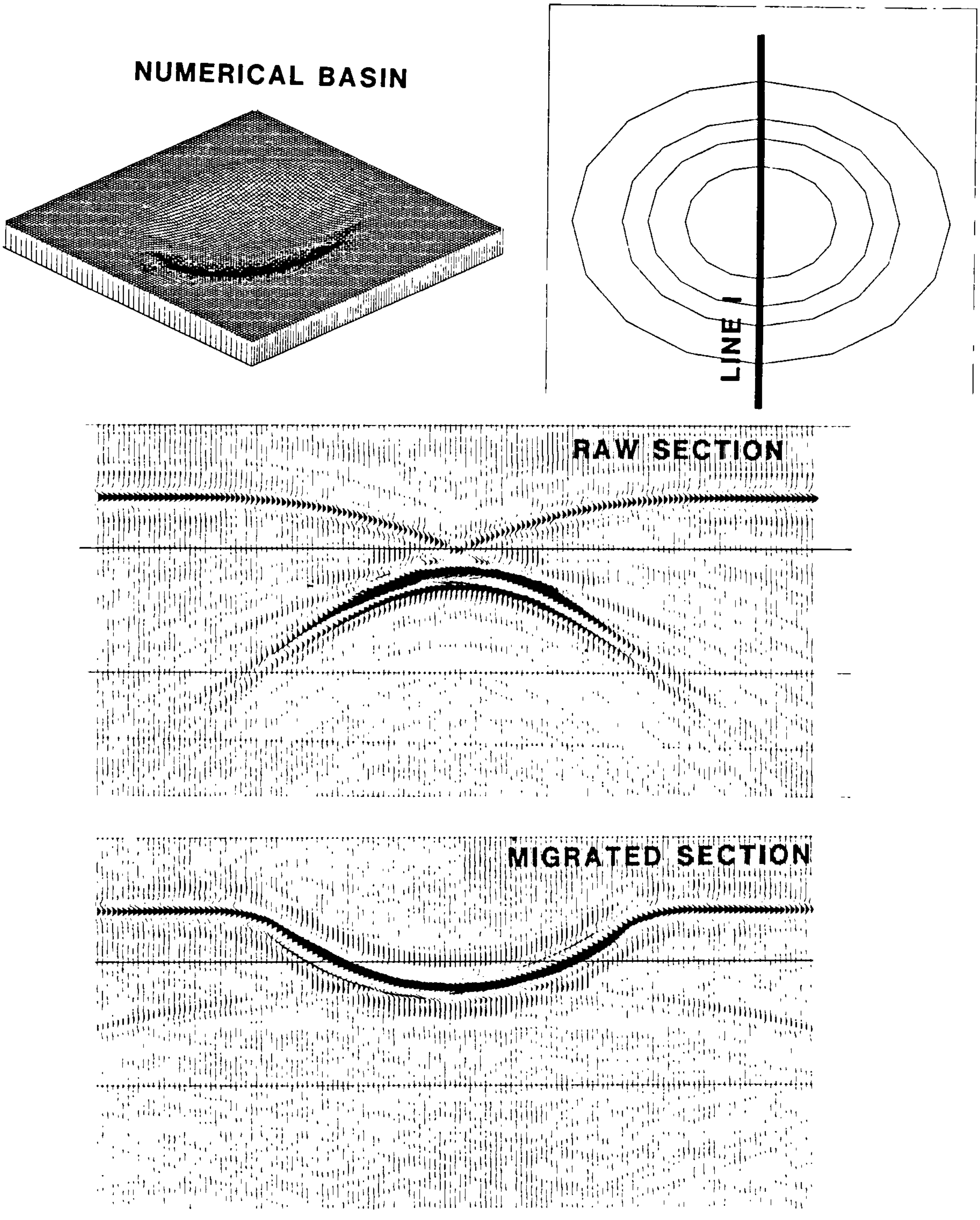

Figure 5-8 Raw and migrated sections across numerical basin
-- principal plane Line 1.

The sections in these two figures have very similar features. Because the profile line traversed the lip of the basin at 90°, a satisfactory migration resulted. Both the high amplitude from the basin and the phase changes, before and after migration, compare very well for the physical and numerical data. The physical model has weaker diffractions caused by the sharp basin edges. Because of the sharp edges and subsequent steeper dip on the physical basin, there is a small frequency broadening at the edge of the basin in the migrated section. Also, the physical basin model shows some out-of-plane events on the migrated section (Event B) from the sharp edge which gives the basin a "dirty" appearance. The velocity pullup due to the low velocity of the physical basin is adequately migrated as well.

Line 3 across the physical basin in Figure 5-9 is equivalent to Line 7 across the numerical model in Figure 5-10. The events on these sections are symmetrical because the profile line still passes through the center of the basin. Both the physical and numerical basin data show similar features;for instance the double fault or graben in the migrated section, which consistently occurs on real field data.

Line 4 across the physical basin in Figure 5-9 is equivalent to Line 8 across the numerical basin in Figure 5-11. This profile line crosses the basin off the center and oblique to the principal plane.

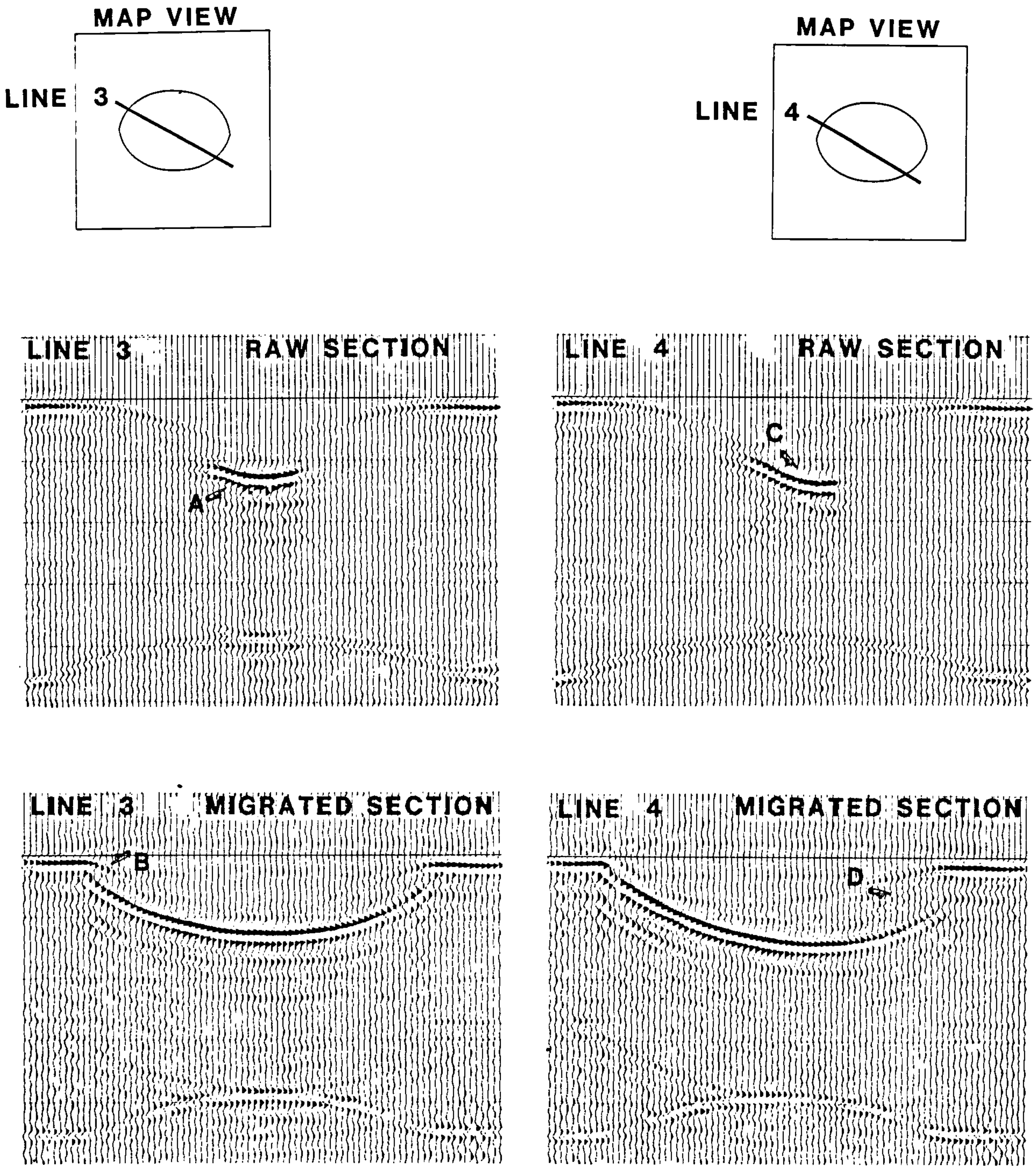

Figure 5-9 Raw and migrated sections across physical basin -- oblique Lines 3 and 4.

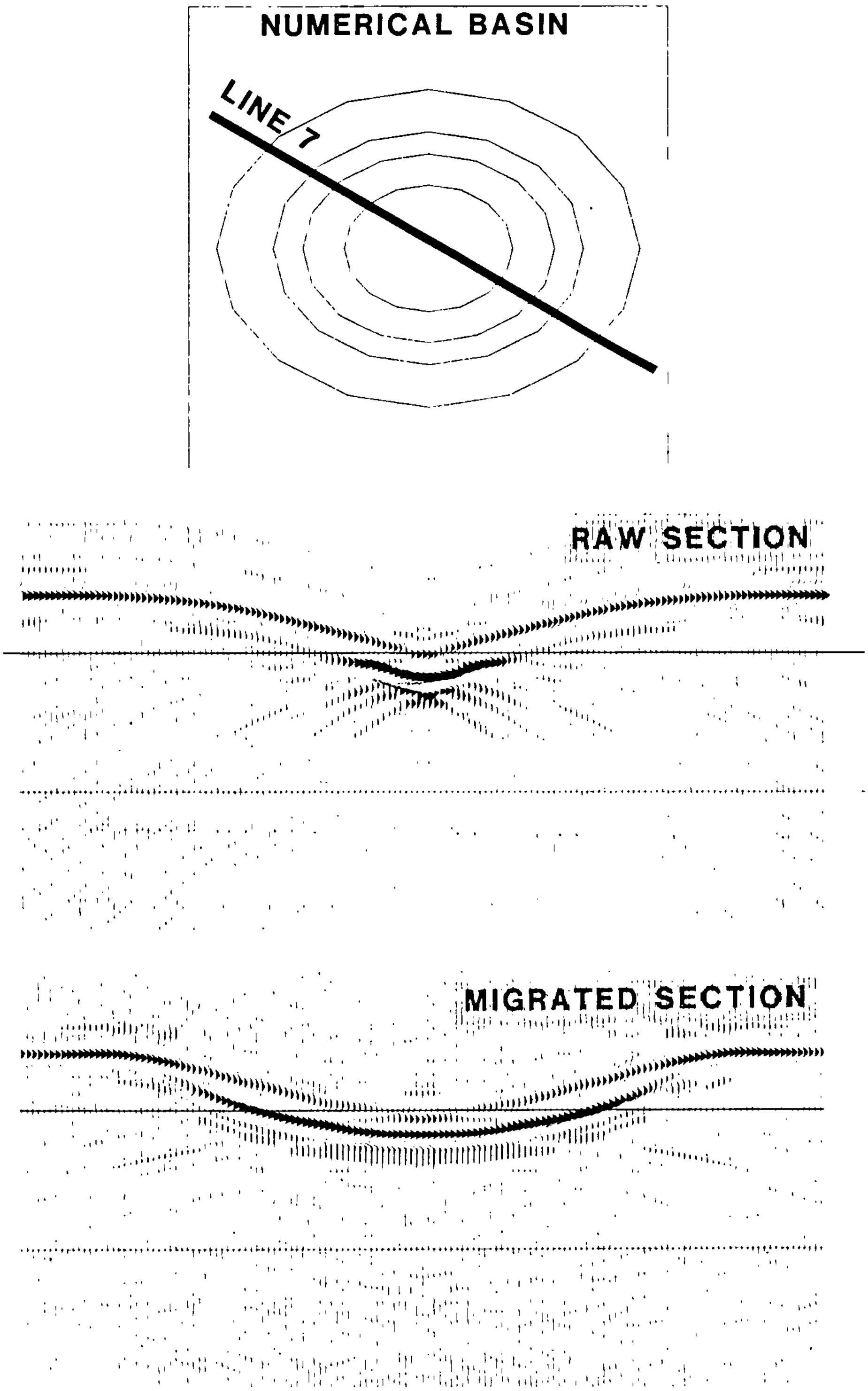

Figure 5-10 Raw and migrated sections across numerical basin -- oblique Line 7.

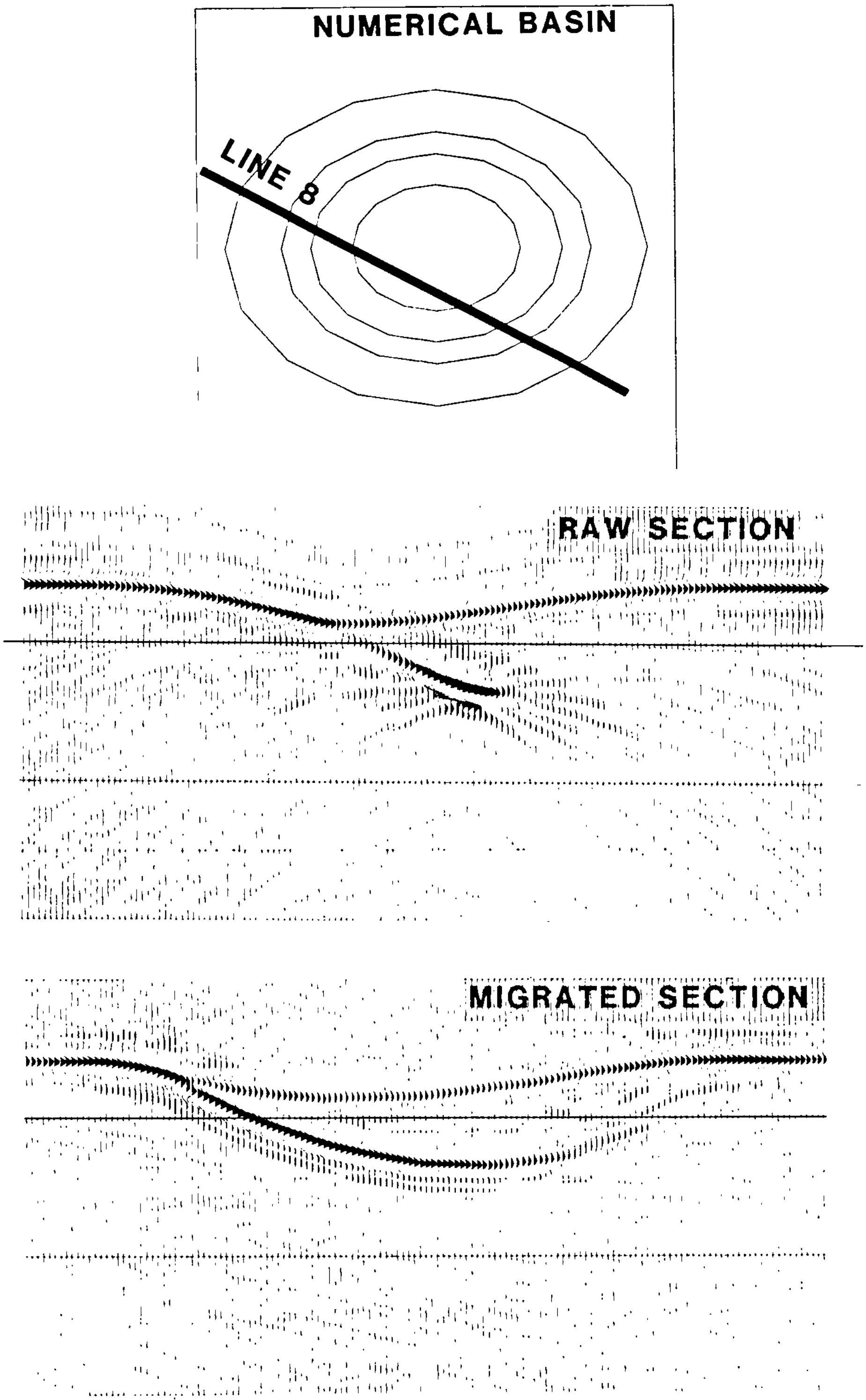

Figure 5-11 Raw and migrated sections across numerical basin -- oblique Line 8.

Again, the numerical basin has stronger edge diffractions due to smoother lips. The diffractions from the buried focus are now skewed on the raw section and show an apparent fault with a pinchout against the base of the basin on the migrated section.

5.4 REEF

The comparison of physical and theoretical reef models was run to try to discern the anomalous wave in the physical model data from the primary events. Both shear supporting resin and non-shearing RTV were modeled. The physical reef models were constructed from plexiglas, resin and RTV. The theoretical data for these models are generated using the Kirchhoff wave theory with a vertical velocity adjustment. This theory, however, does not consider shear waves and multiples.

The theoretical model sections for the RTV reef are shown in Figure 5-12, which correspond to the physical RTV model sections in Figure 4-25. Except for the void of extra lower reflection events in the theoretical model sections because there was no base beneath the theoretical model, the comparisons are good for the RTV model.

The theoretical sections for the resin model shown in Figure 5-13 are rather simple when compared with the physical model sections in Figure 4-24. The high velocity reflection pullup from the base of

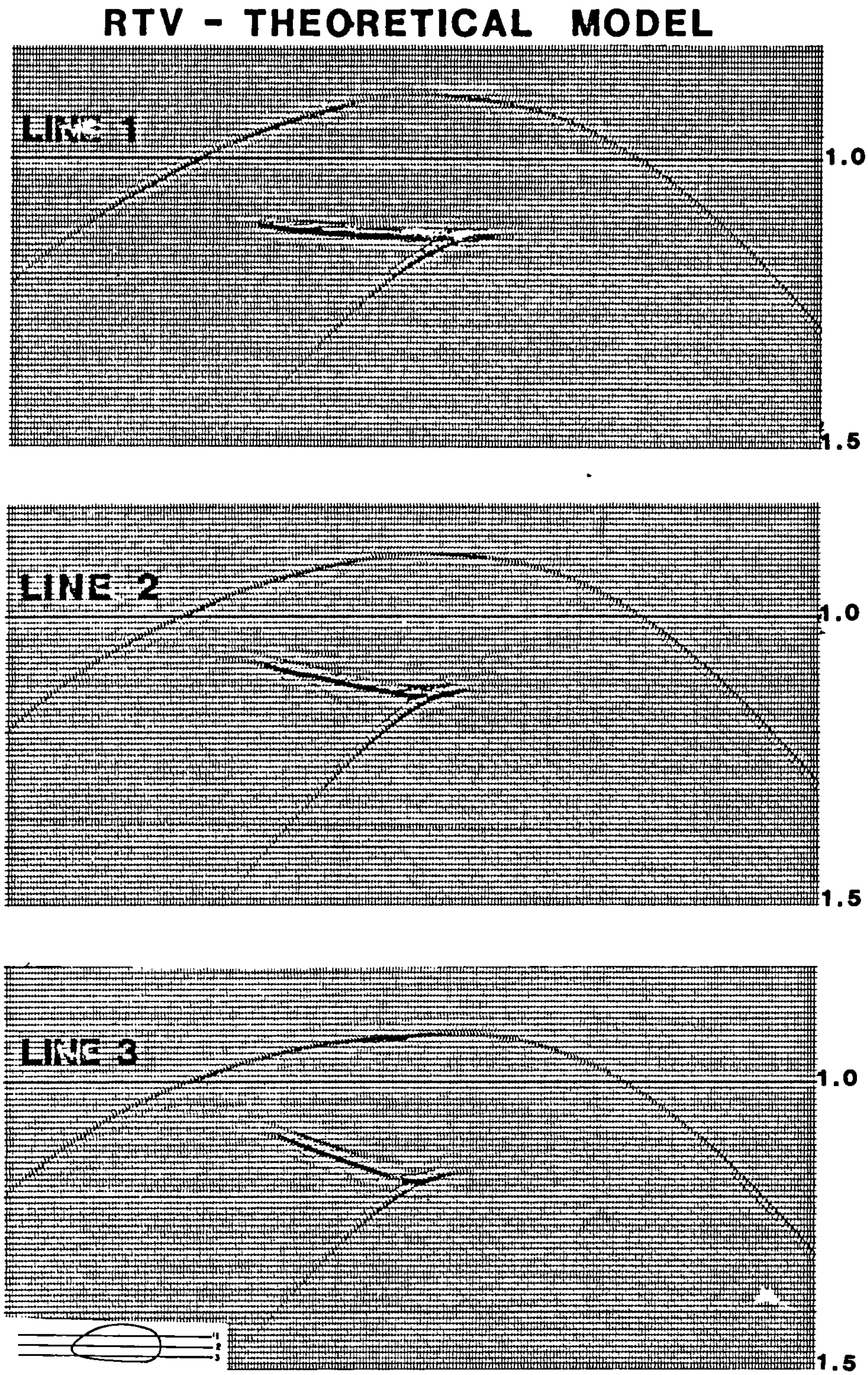

Figure 5-12 Raw sections across theoretical RTV reef -- trend lines.

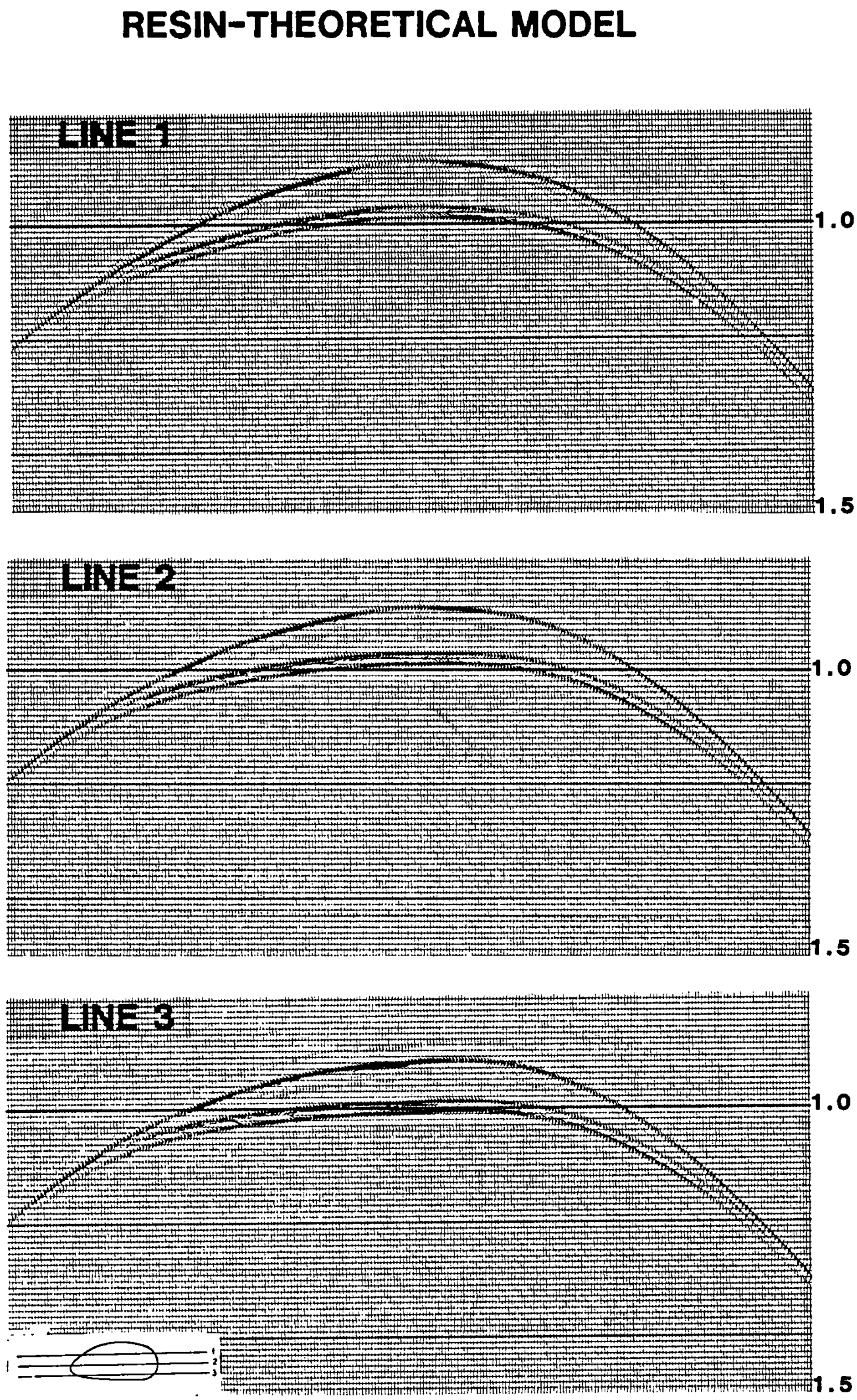

Figure 5-13 Raw sections across theoretical resin reef -- trend lines.

the reef model is obvious on both the physical and theoretical model sections, but the resin model has two additional events. If we refer to the theoretical RTV model sections (Figure 5-12), we can see that one of the additional events in the physical resin model sections (Figure 4-24) has a shape similar to the reflection from the bottom of the RTV reef. This suggest that the event is a converted shear wave to the bottom of the reef.

However, the explanation given above for the presence of the extra events in the resin time sections was not totally supported when we ran a diagonal line as shown in Figure 5-14 and 5-15. The crossing events on line 3 for the physical model did not match the theoretical. It is possible that these extra events could be generated by the incident wave in the water as it wraps around the model (Kosloff and Baysal, 1981). When SAL's 3-D Fourier forward modeling program is available, it will help to identify the events.

5.5 SUMMARY

The comparisons were good between the physical and theoretical data for the four model results except for the following discrepencies:

1. For a high velocity anticline, the diffractions at the edge of the flank are stronger on the physical section than on the theoretical

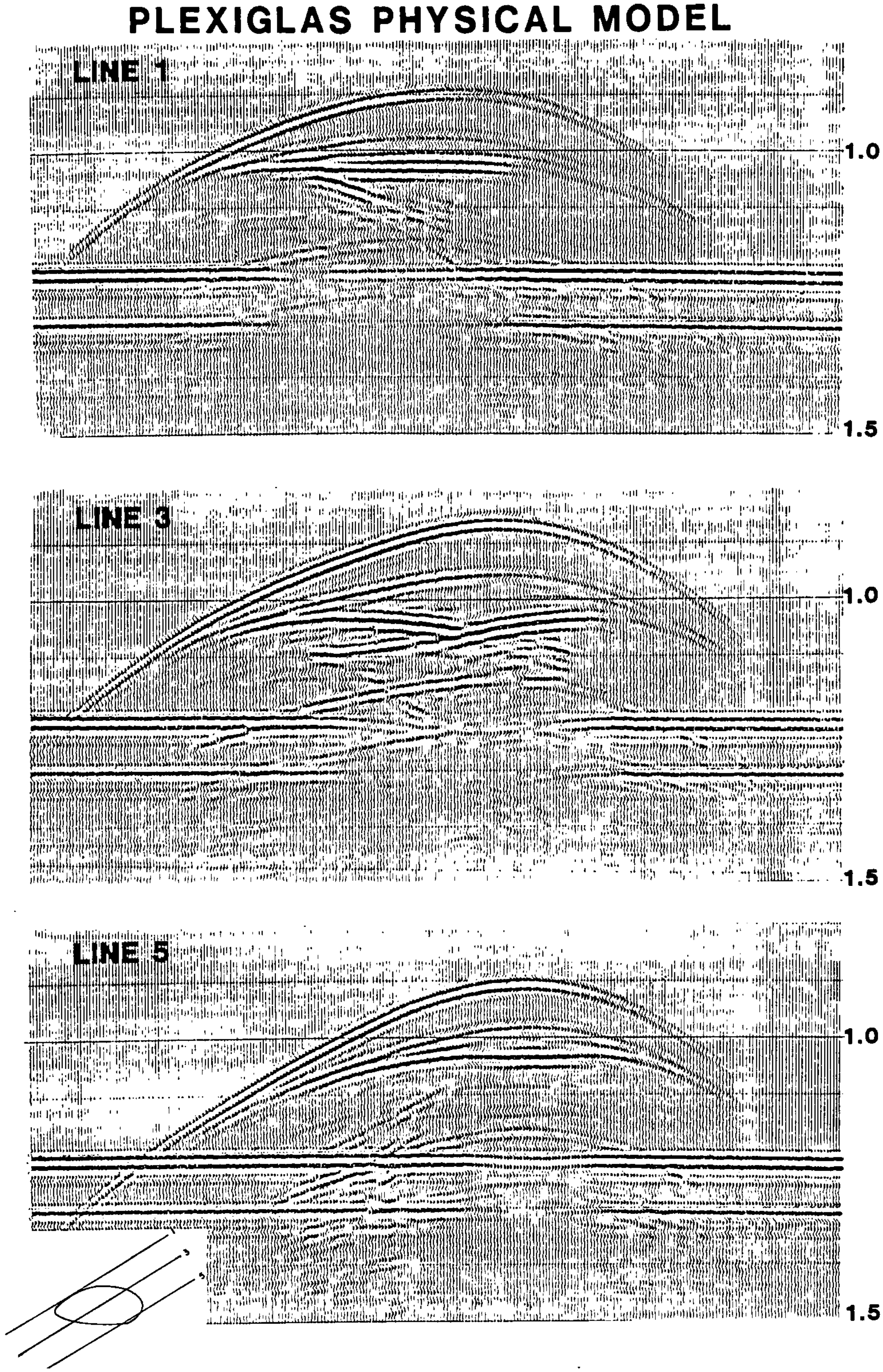

Figure 5-14 Raw sections across physical plexiglas reef -- diagonal lines.

RTV THEORETICAL MODEL

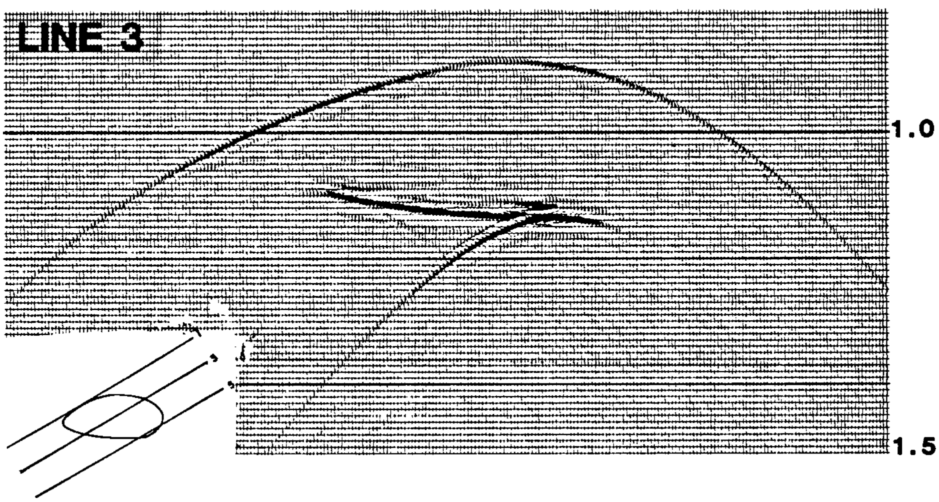

Figure 5-15 Raw sections across theoretical RTV reef
-- diagonal lines.

section.

2. The velocity pushdown zone under the low velocity anticline is better described by wave theory than by ray theory.

3. For a 3-D reef model of tight curvature, physical model results have additional events which Kirchhoff wave theory cannot predict. However, theoretical results do help to aid in the physical data interpretation.
4. The larger the reflection coefficient, the more the physical model results differ from the theoretical model results.

VI. VELOCITY ANALYSIS

6.1 INTRODUCTION

Several 3-D velocity analysis algorithms have been developed recently. A space-frequency domain approach based upon holographic principles to extract 3-D earth parameters was reported by Morgan and Hilterman (1981). Owusu and Gardner (1981) developed a Kirchhoff integral procedure which was based on a logarithmic transformation of the areally collected time data.

A time-domain version which is equivalent to Morgan's space-frequency algorithm is another velocity analysis approach. Like conventional 2-D velocity spectrum analysis (Taner and Koehler, 1969), this 3-D velocity analysis is based on the straight ray geometrical approach and the CMP moveout formula by Levin (1971).

In this chapter, three different time-domain approaches are developed and evaluated for estimating velocity for areal gather data. They are: CDP algorithm, areal CMP algorithm and crooked-line algorithm. Both theoretical and physical model data are used to test the robustness of the algorithms.

6.2 CDP AND AREAL CMP VELOCITY ANALYSIS

A. ALGORITHM

Figure 6-1 is a cartoon of three CDP gathers for a reflection from a dipping interface. The shape of the hyperbolae are almost identical except for a small time shift $\pm \Delta T$ about the center CDP point. In a conventional 2-D velocity analysis without beam steering, the inclusion of all three CDP gathers would not yield a coherent correlation coefficient. However, as several geophysical companies have shown in brochures, by beam steering the CDP gathers along pre-selected dips, not only will the velocity estimate be enhanced but a good estimate of the apparent dip will be obtained.

The 2-D approach basically searches the equation

$$t_x^2 = t_o^2 + x^2/V^2 \tag{6-1}$$

for a suite of velocities at each t_o and the highest correlation velocity is the stacking velocity. If instead we search the equation

$$t_x^2 = t_o^2 + x^2\cos^2\delta/V^2 \tag{6-2}$$

for both δ (apparent dip) and V, then the velocity obtained would be the 3-D migration velocity. Since most of SAL's use for the 2-D velocity analysis is conventional profile lines, the 2-D algorithm is in the stacking velocity mode.

The extension of this approach to 3-D is quite simple. The equation

$$t_x^2 = t_o^2 + x^2(1-\sin^2\delta\cos^2\phi)/V^2 \tag{6-3}$$

is searched as a function of δ, (dip), ϕ (azimuth) and V (migration velocity). The input data is an areal common-midpoint gather. The

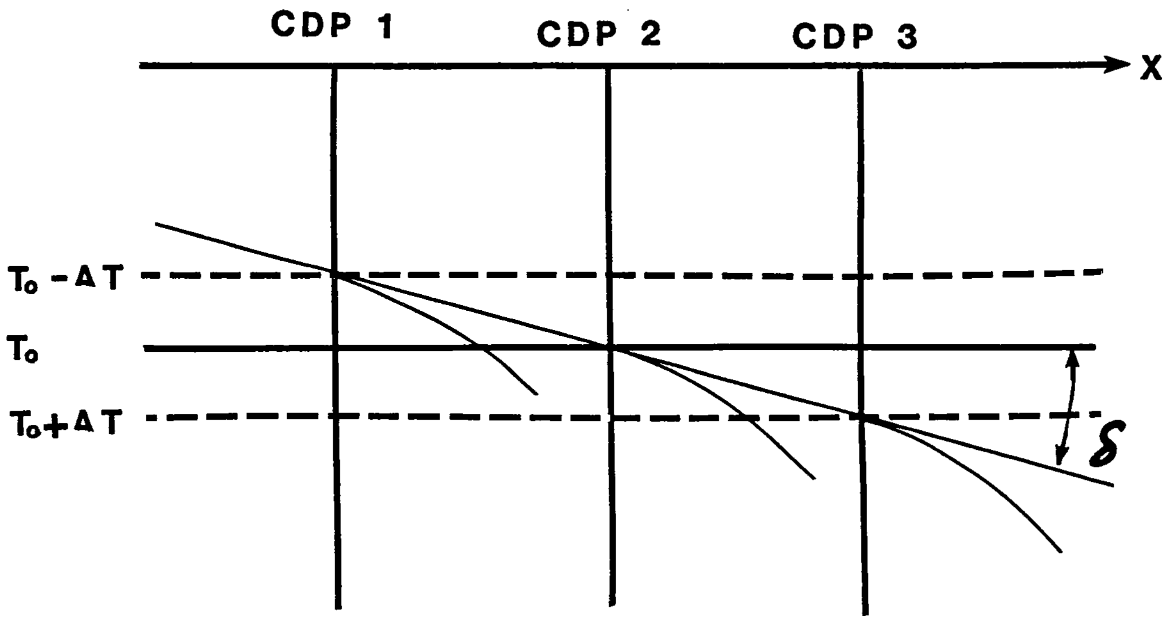

Figure 6-1 Time-distance curves of three CDP gathers from a dipping interface.

assumptiom that the reflection is planar over the "specular" reflection point is made and this assumption is tested with our synthetic data. Because only one areal CMP is employed the reflection times are based on the normal incident travelpath and the dip analysis is ambiguous with respect to sign.

The output displays for the 2-D velocity analysis is an integral part of the 3-D display, so only the 3-D display will be shown. In Figure 6-2, the upper left box is a four-dimensional display with correlation coefficients filling the grid inside the box. This box contains all the coefficients for a specified t_o. For a particular t_o, there are three output displays. For example, the maximum correlation coefficient for a specified velocity plane is found for all dips and strikes and this 2-D correlation chart is plotted as shown on the upper right-hand side. The corresponding search is done for a specified dip in terms of the velocity-strike plane, etc.

B. TEST RESULTS -- THEORETICAL DATA

In all the theoretical results the unnormalized cross-correlation coefficient was used for event detection. Figure 6-3A depicts three 12-fold CDP gathers across a plane dipping at 15^o. Plot B depicts the summary plot where a 15^o dip and a stacking velocity of 10353 ft/s ($10000/\cos 15^o$) are the final results. Plots C, D, and E depict the velocity spectra if a single dip is searched.

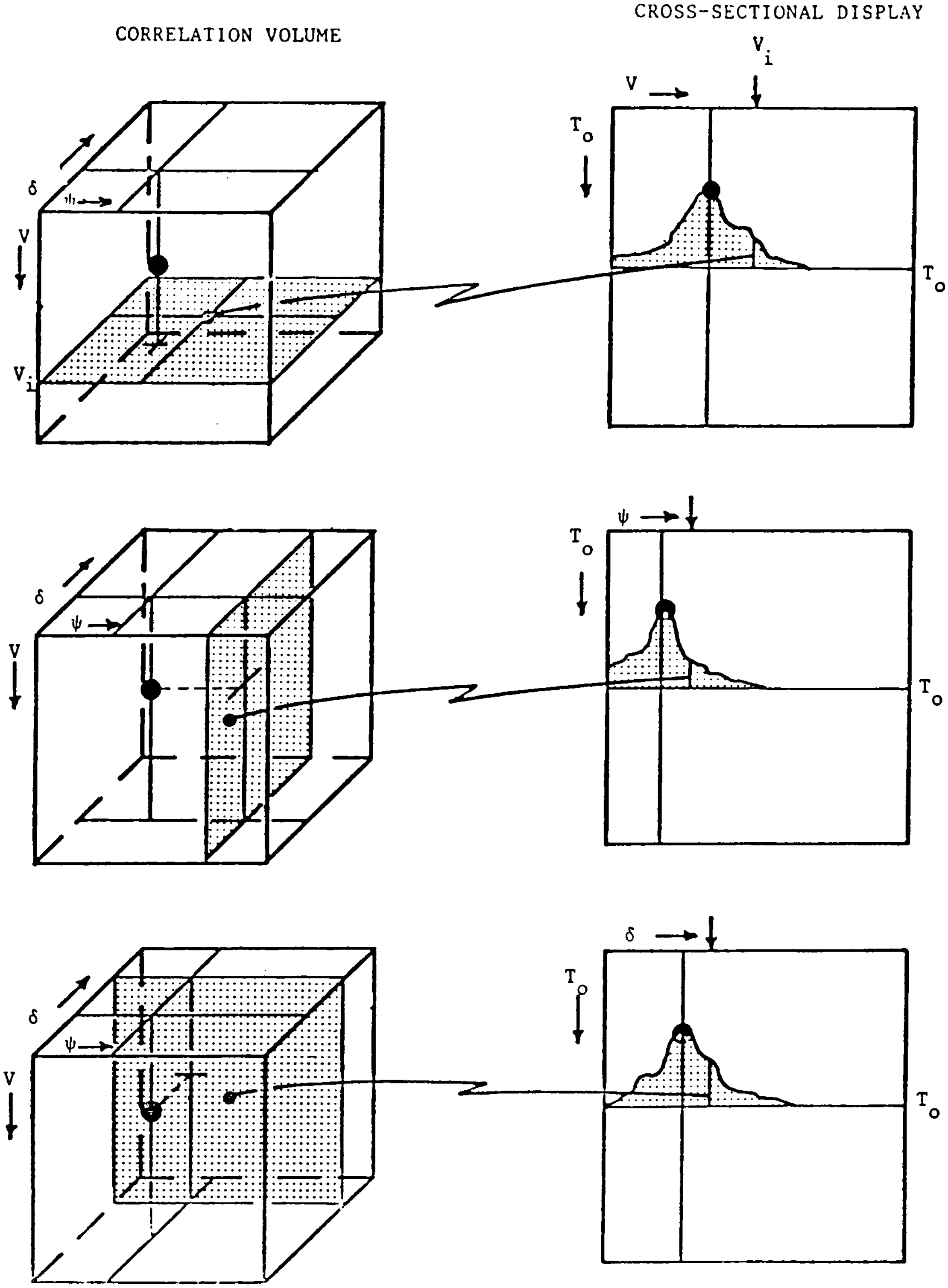

Figure 6-2 Output displays for the 3-D velocity analysis.

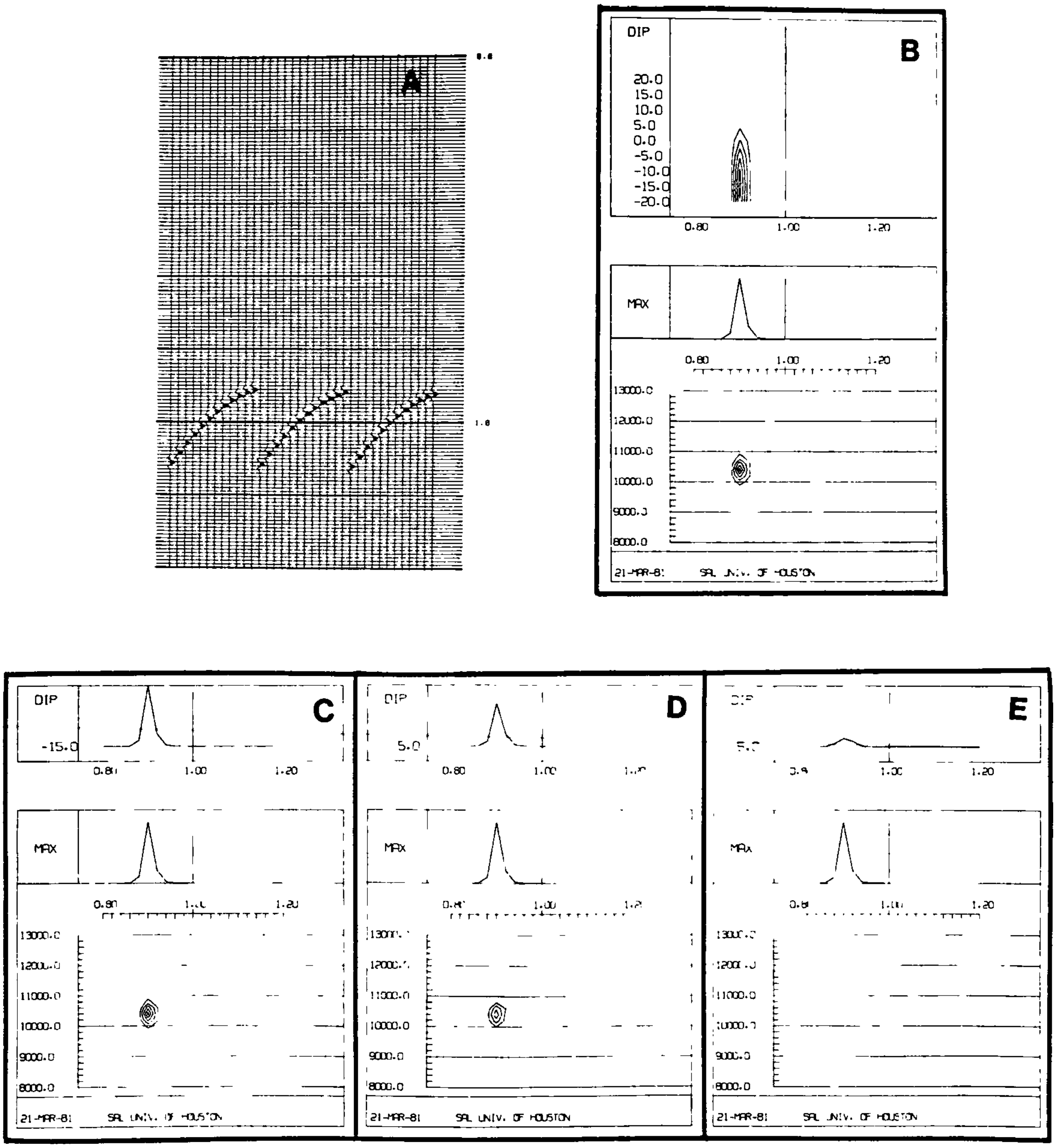

Figure 6-3 Two-D velocity analysis across a plane dipping at 15°.
A. Three 12-fold CDP gathers.
B. Two-D velocity analysis with dip search.
C. Two-D velocity analysis with fixed dip at -15°.
D. Two-D velocity analysis with fixed dip at -5°.
E. Two-D velocity analysis with fixed dip at 5°.

These last plots are optional output to the summary plot.

Figure 6-4 depicts both 2-D and 3-D velocity analyses across three 15^{o} dipping reflectors. The shallow reflector has a NS strike, the middle N 30^{o}E, and the deepest an EW strike. Three different sets of three CDP 12-fold gathers were generated on each profile line and 2-D velocity analyzed. The resulting summary spectra are the plots A, B and C. Each plot accurately depicts the correct stacking velocity as given theoretically by Levin (1971). If the stacking velocities are multiplied by the cosine of the corresponding apparent dip, the true velocity of 10000 ft/s is obtained. The other velocity picks besides the 10000 ft/s and 10353 ft/s correspond to the apparent dip velocities.

The same depth model was then used to generate an areal CMP gather which consisted of four CDP gathers (48 traces) on the EW, NS, N30^{o}E and N45^{o}W profile lines. The velocity 3-D summary plot is F. The strikes, dip and migration velocities, were accurately depicted. Plots D and E are two dip spectra from the dip suite spectra that are optionally called.

Figure 6-5 illustrates 2-D and 3-D velocity analyses across two half-planes where one has a 15^{o} dip. The 2-D spectrum in E and 3-D spectrum in C were taken as indicated in the time section of plot A. From E, a stacking velocity of 12196 ft/s and dip of 10^{o} was

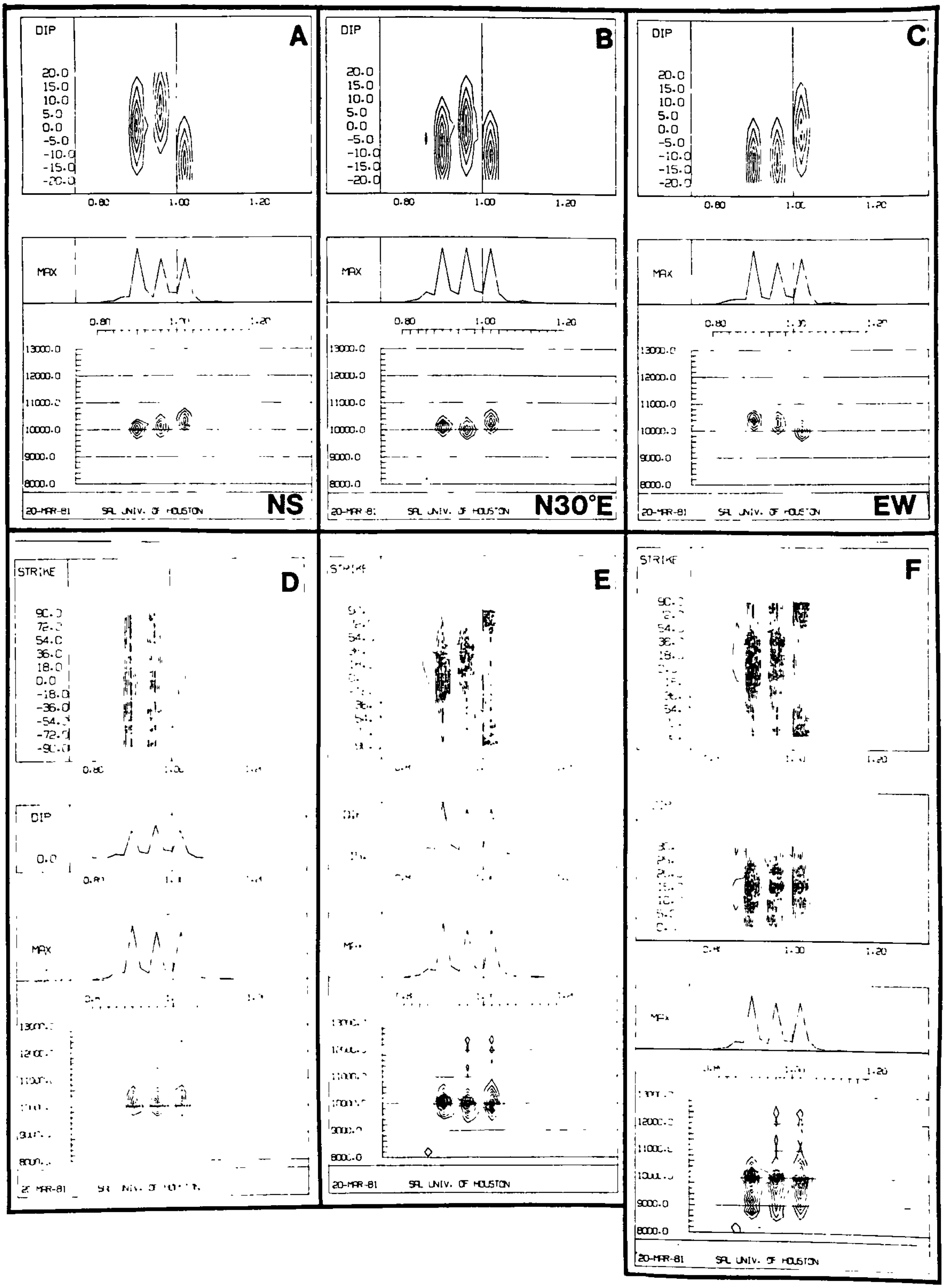

Figure 6-4 Two-D and 3-D velocity analysis across three 15° dipping reflectors. The shallow reflector has a NS strike, the middle a N30°E, and the deepest a EW strike.

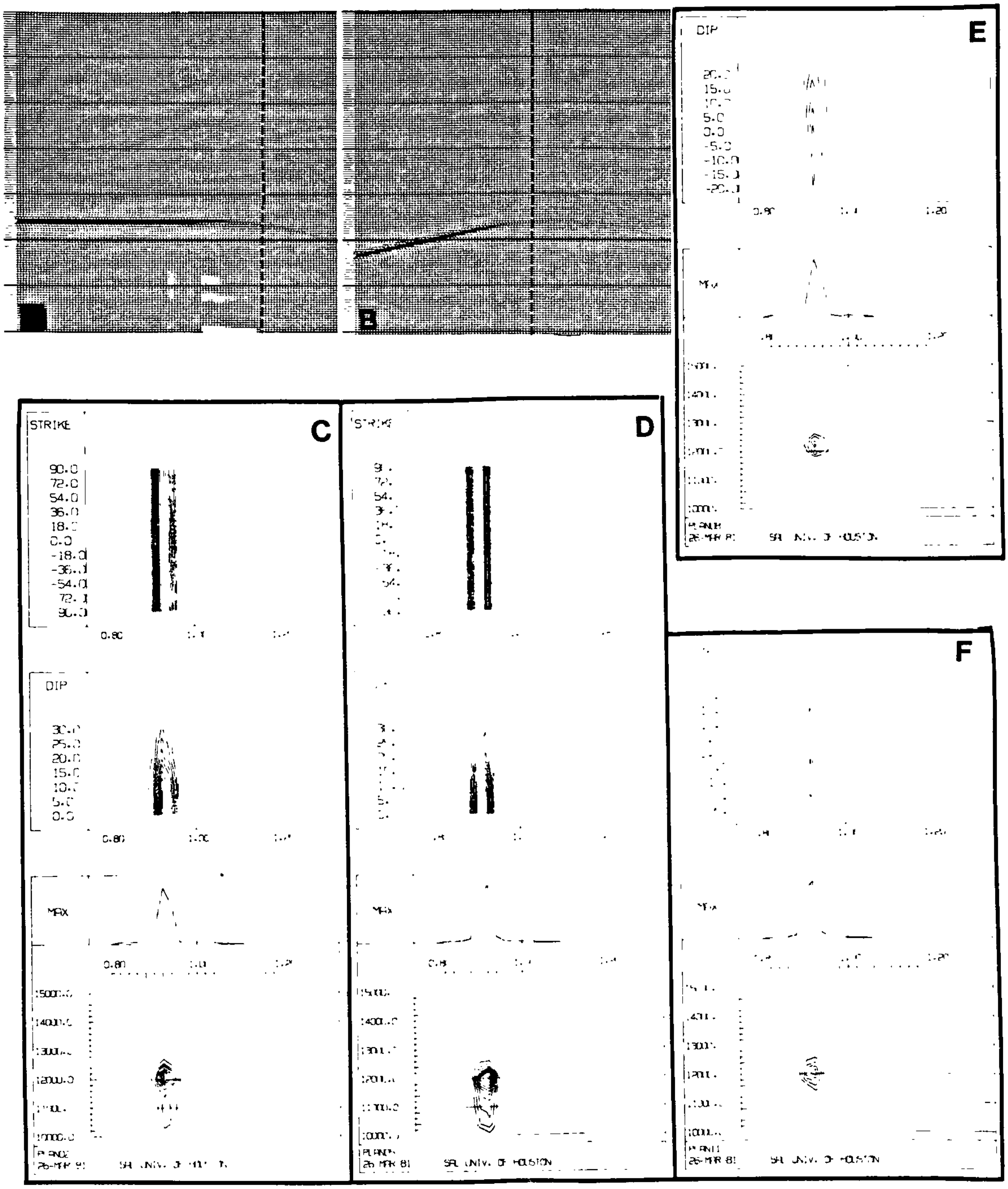

Figure 6-5 Two-D and 3-D velocity analysis across half-planes.
A. Time section of horizontal half-plane.
B. Time section of 15^{o} diping half-plane.
C. Three-D velocity analysis across horizontal half-plane.
D. Three-D velocity analysis across dipping half-plane.
E. Two-D velocity analysis across horizontal half-plane.
F. Two-D velocity analysis across dipping half-plane.

recognized. The 10° dip occurs because the diffractions stack approximately at the migration velocity divided by the cosine of the emergence angle for a ray from the CDP point to the fault edge. This happens to be an emergence angle of 10.3°. Multiplying the 12196 ft/s velocity by cos 10.3° results in the true migration velocity of 12000 ft/s. The corresponding 3-D velocity analysis also shows a dip of 10° but the migration velocity depicted was the medium or migration velocity of 12000 ft/s. For the dipping half-plane in Plot B, the 2-D spectrum is shown in F and the 3-D in D. No dip is indicated on the 3-D spectrum and it has the proper migration velocity of 12000 ft/s. The 2-D stacking velocity at this particular point in plot B happens to be 12000 ft/s also because the effect of the reflection dip has been canceled by the diffraction angle. The small dip shown in the 2-D (Plot F) is insignificant as far as modifying the stacking velocity to yield the migration velocity.

Figure 6-6 illustrates 3-D velocity spectra from two areal CMP gathers. The reflecting model was an irregular plane surface of about the size of a half Fresnel disc (Figure 3-34). The velocity spectra estimates once again are very robust.

The next three Figures (6-7, 6-8 and 6-9) illustrate both 2-D and 3-D spectra across a 2-D syncline, a 3-D basin and a 2-D anticline respectively. The picks are quite good once again and there was insignificant curvature influence on the migration or

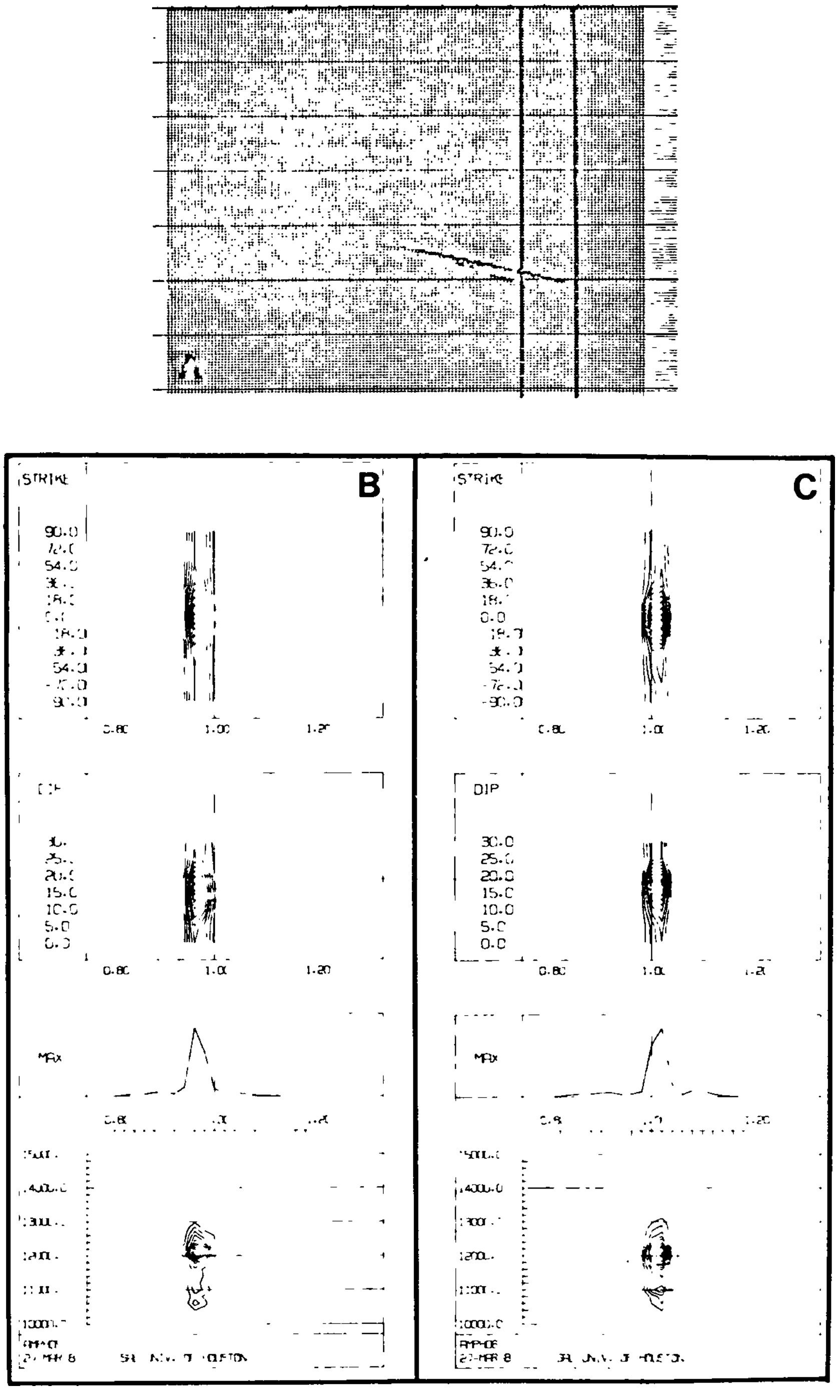

Figure 6-6 Three-D velocity analysis across a partial reflector dipping at 15°.
A. Time section.
B. Velocity analysis on the reflector.
C. Velocity analysis off the reflector.

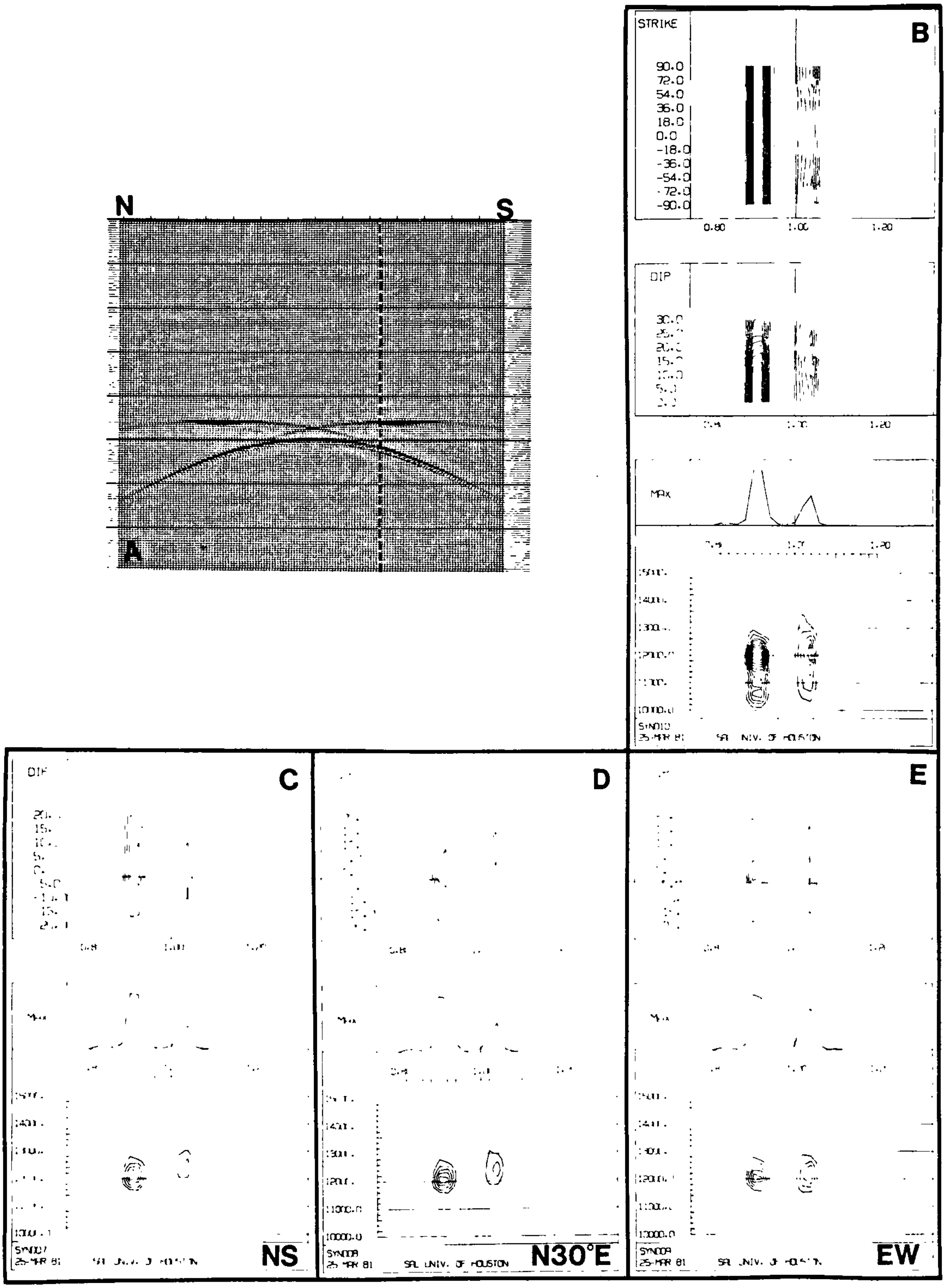

Figure 6-7 Two-D and 3-D velocity analysis across a 2-D syncline.
A. Time section.
B. Three-D velocity analysis.
C. Two-D velocity analysis.
D. Two-D velocity analysis in N30°E direction.
E. Two-D velocity analysis in EW direction.

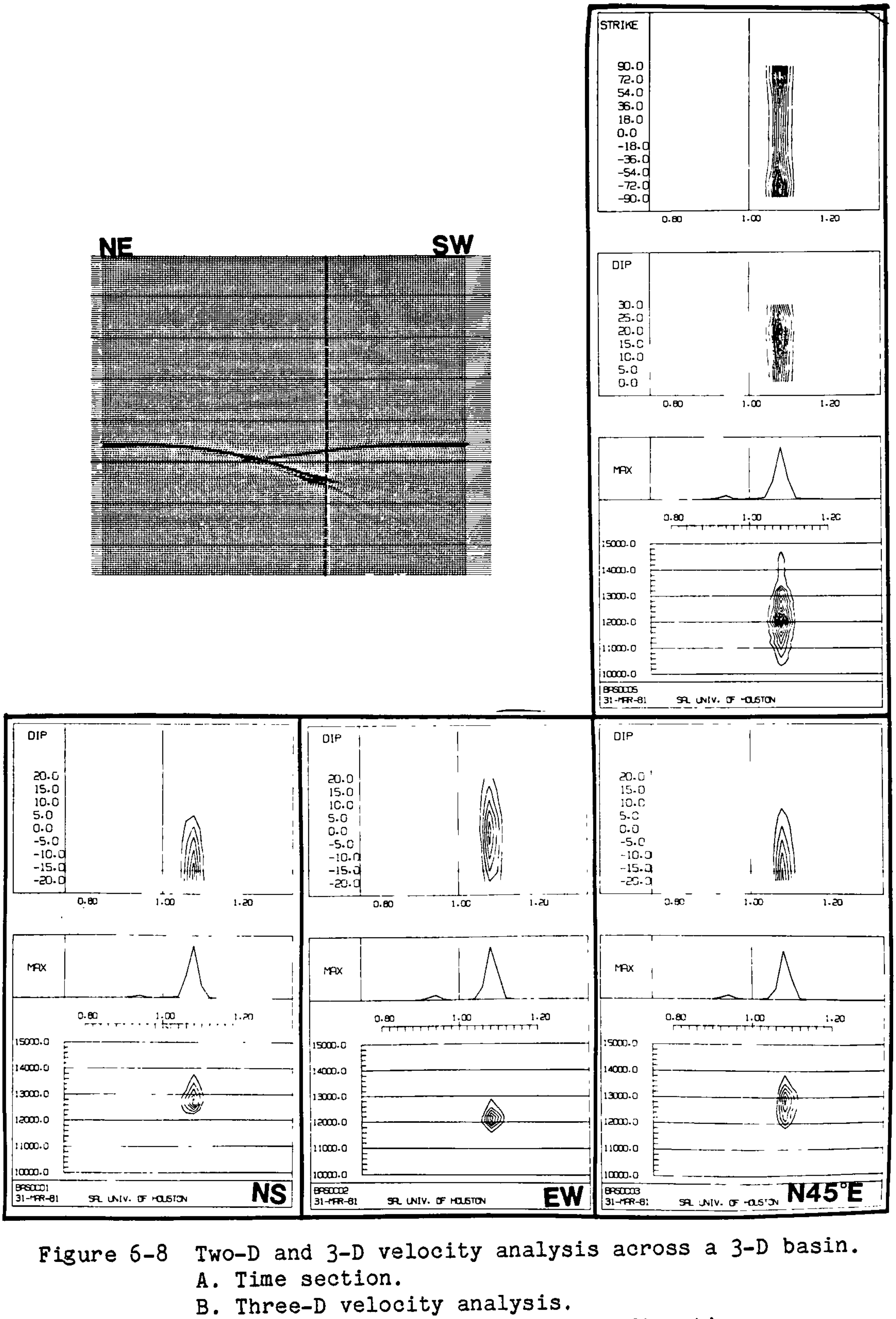

Figure 6-8 Two-D and 3-D velocity analysis across a 3-D basin.
A. Time section.
B. Three-D velocity analysis.
C. Two-D velocity analysis in NS direction.
D. Two-D velocity analysis in EW direction.
E. Two-D velocity analysis in N45°E direction.

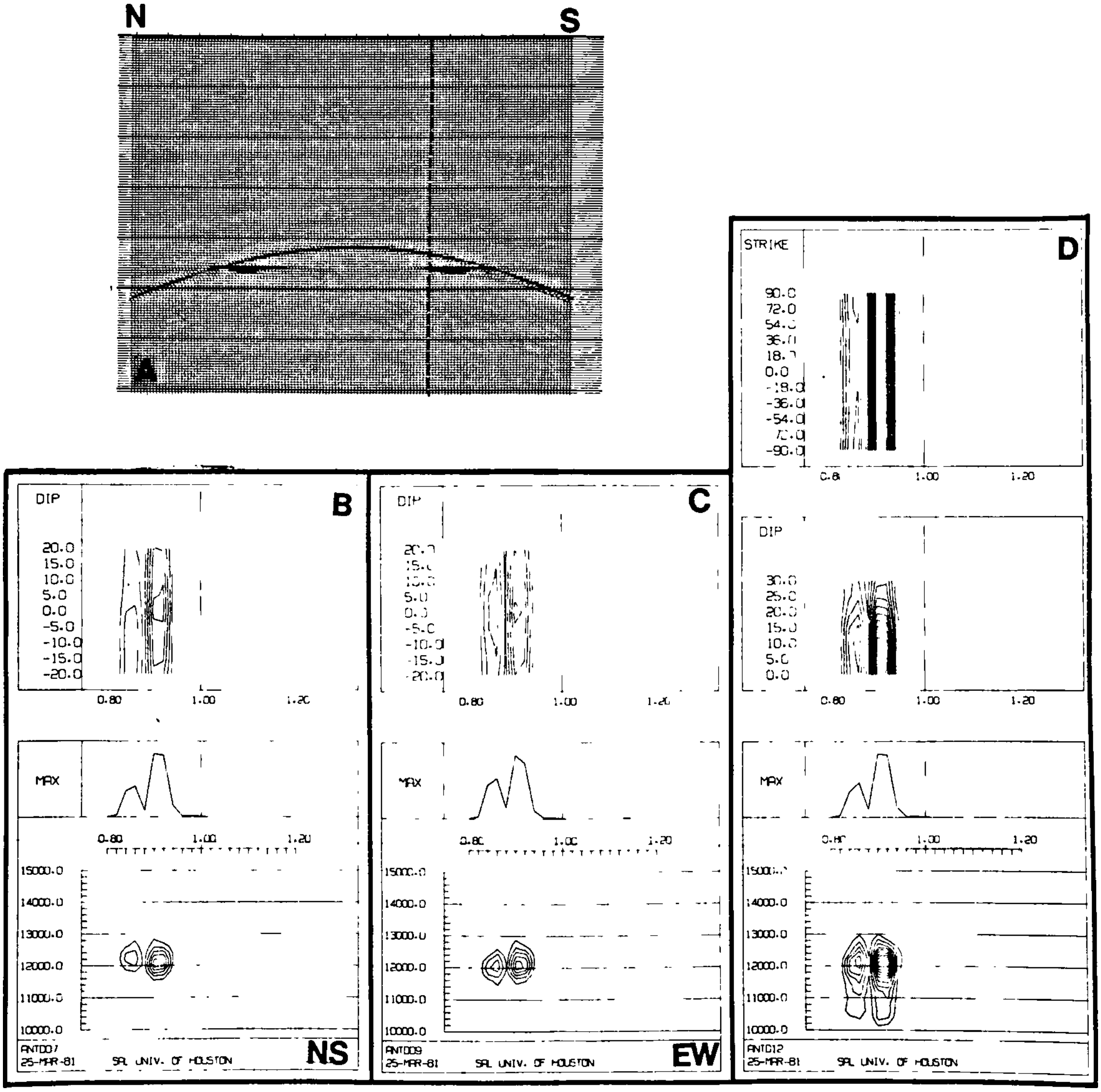

Figure 6-9 Two-D and 3-D velocity analysis across a 2-D anticline.
A. Time section.
B. Two-D velocity analysis in NS direction.
C. Two-D velocity analysis in EW direction.
D. Three-D velocity analysis.

stacking velocity estimates. These results then suggested that we should try the algorithm on physical model data.

C.TEST RESULTS - PHYSICAL DATA

The physical model which was tested for velocity analysis is illustrated along with a constant 1500 ft offset profile line in Figure 6-10. The profile line has an azimuth of 45° with respect to the dip line. The top of the structure was at a depth of 6600 ft and the overburden velocity was 12000 ft/s. All velocity analyses were performed around the portion labeled 2-DVA on both the map view and the time section.

A preliminary test using a conventional 2-D velocity analyses approach was performed first and the results are illustrated in Figure 6-11. An AGC trim with a window length of 0.1 sec was applied to the 12-fold CDP gather and the velocity search parameters had a 20 ms gate window (used on all velocity spectra) and the unnormalized cross-correlation was employed as the correlation coefficient.

The indication of the fault is shown on the velocity spectrum at about 1.22 sec. However, since only one CDP gather was employed, no dip information was available.

Five CDP gathers were then used to carry out a velocity analysis

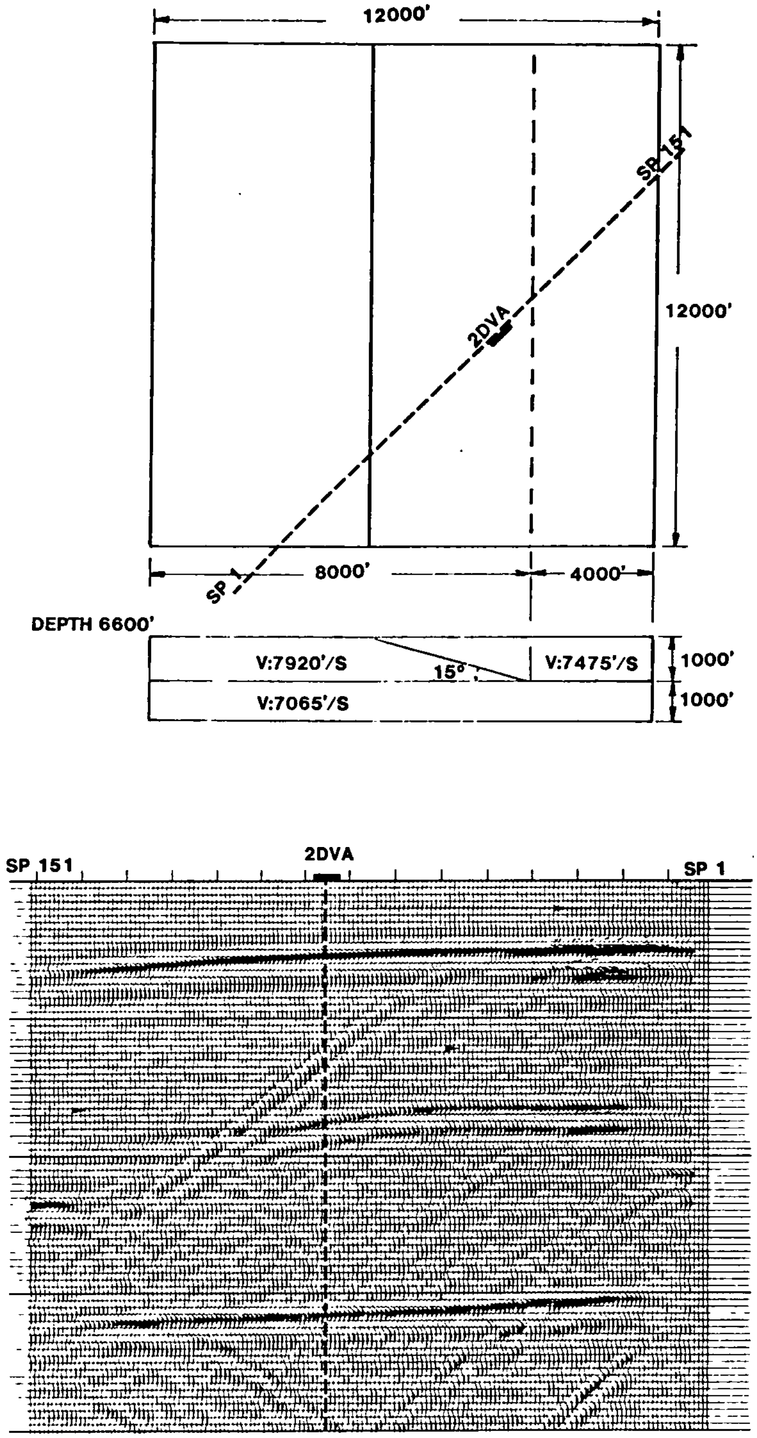

Figure 6-10 Dimensions and time section of physical fault model.

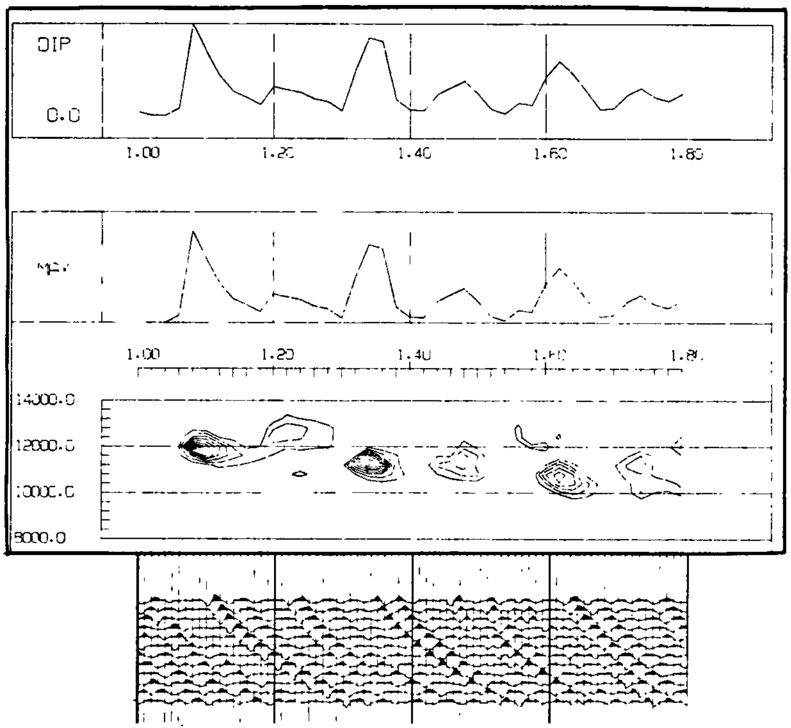

Figure 6-11 Conventional 2-D velocity analysis across fault model.

(Figure 6-12). The processing parameters were the same as those used in Figure 6-11. The velocity resolution for picking the major flat reflectors was definitely improved but since no beem steering was implemented there was no indication of the fault on the spectrum.

A series of velocity parameters and pre-processing gain parameters were then tried and the results are shown in Figure 6-13, 6-14 and 6-15 (deconvolution was not performed). In Figure 6-13, an unnormalized cross-correlation was tested with no AGC on the CDP gathers. Even though beam-steering was used the fault was not seen because of its low reflection amplitude. When the normalized cross-correlation, which is similar to the semblance coefficient (Neidell and Taner, 1971), was applied as shown in Figure 6-14, the fault was found but at the expense of broadening all picks and picking up the tails of the true reflectors. The best pre-processing parameters that we found are shown in Figure 6-15. An unnormalized cross-correlation on CDP gathers that were trimmed with a 0.1 s window yielded the best results. A 20 ms gate window (approximately 1/2 the wavelet period) was optimum. Only the reflectors and inhomogeneities in the physical model were enhanced.

An interesting side note on picking this spectra is shown in Figure 6-15. The shape of the maximum power curve for a single reflector should be similar to the portion of the power curve centered at 1.36 sec. But the inital reflector at time 1.1 sec had a

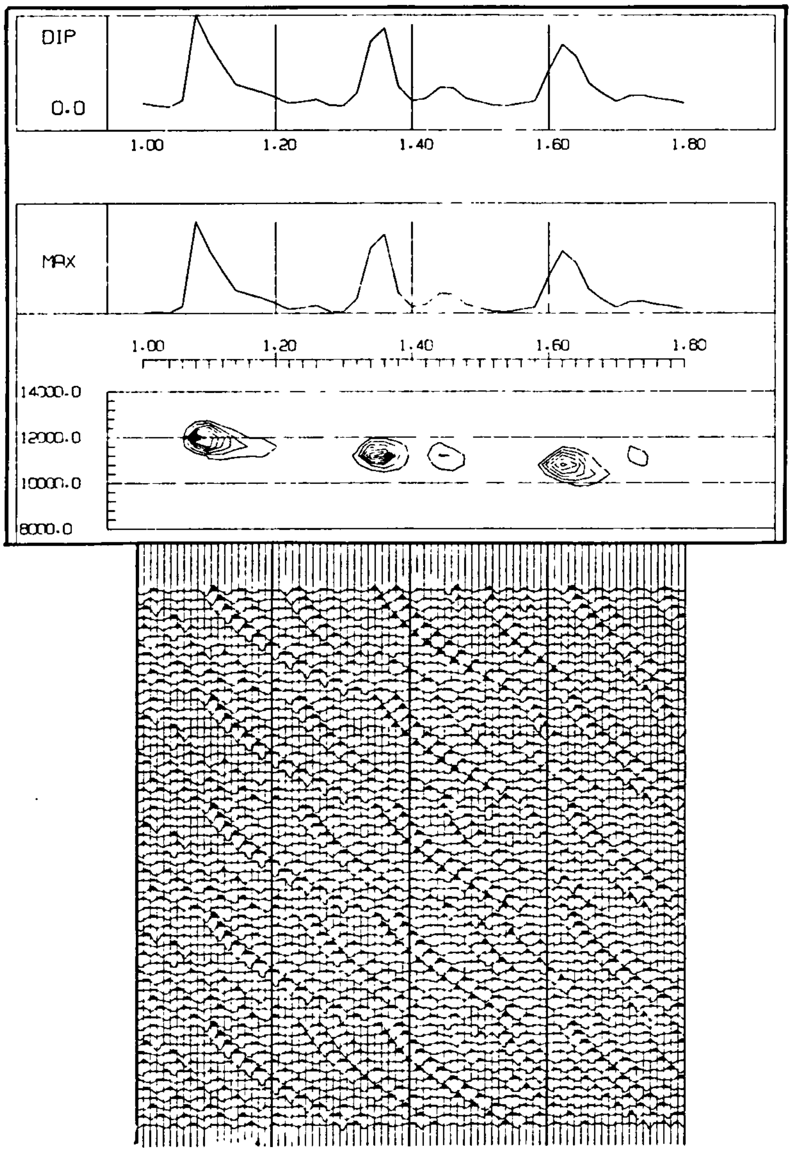

Figure 6-12 Two-D velocity analysis without beam steering across fault model.

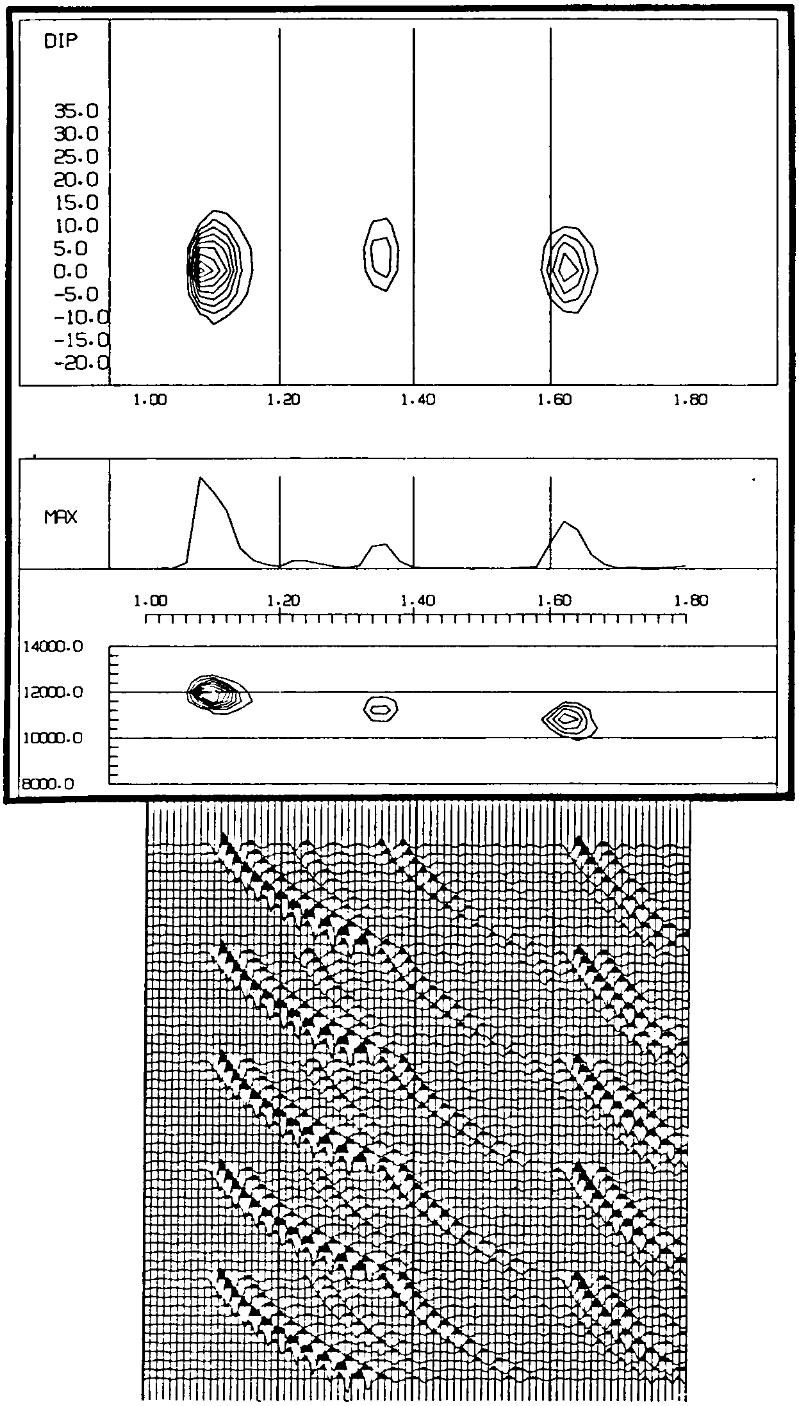

Figure 6-13 Two-D velocity analysis across fault model with dip search and unnormalized cross-correlation. No AGC was applied.

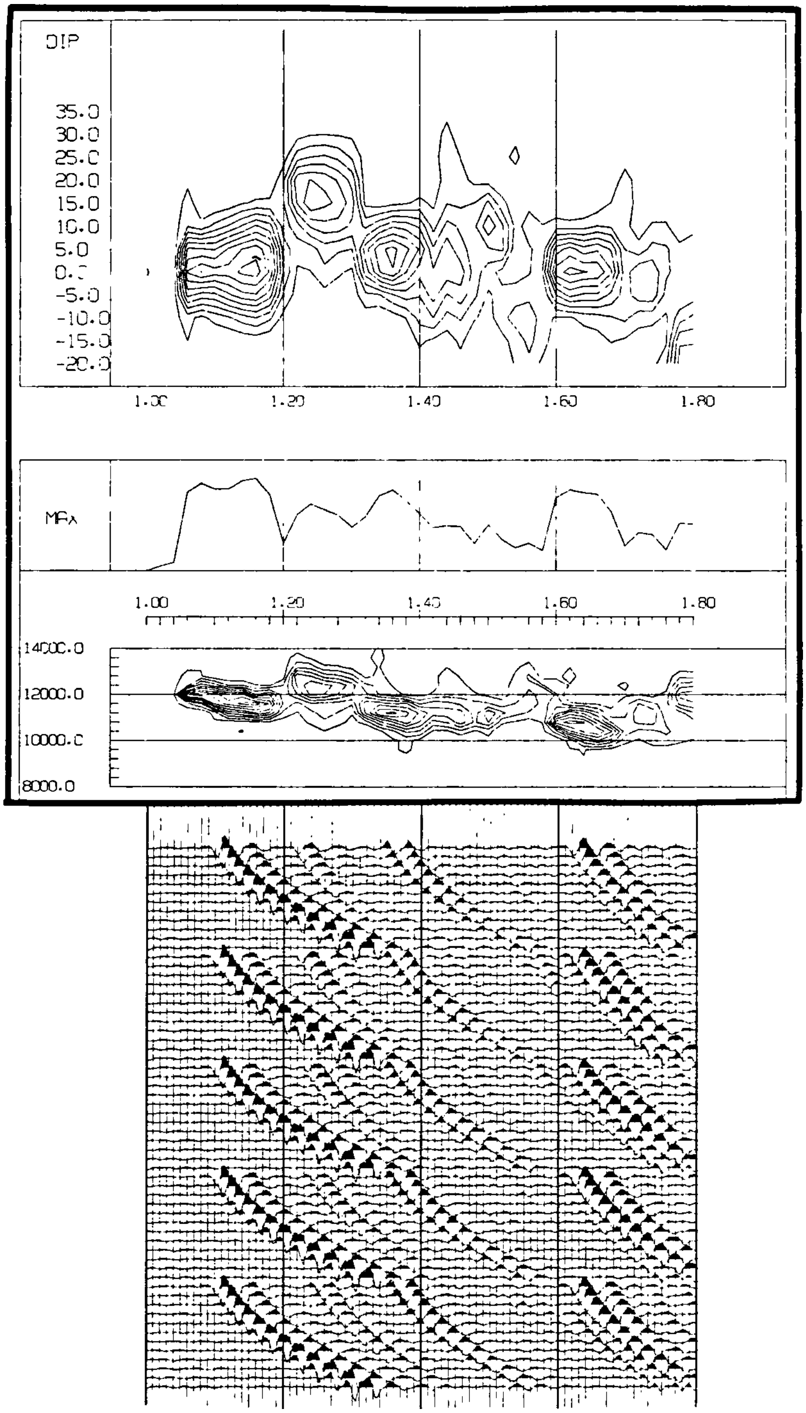

Figure 6-14 Two-D velocity analysis across fault model with dip search and normalized cross-correlation. No AGC was applied.

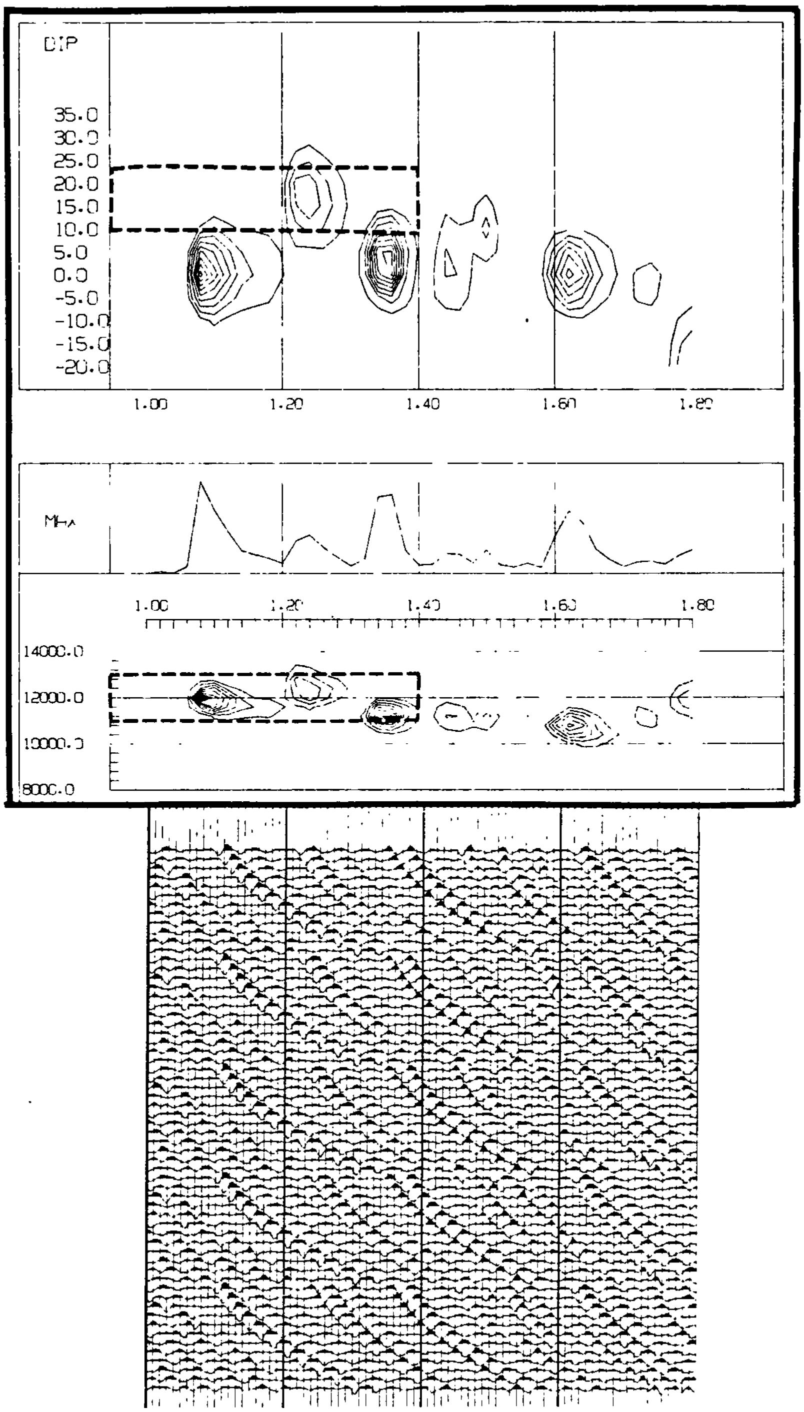

Figure 6-15 Two-D velocity analysis across fault model with dip search and unnormalized cross-correlation. AGC(.1 sec) was applied.

large amplitude and when AGC was employed a "dead zone" appeared before the reflection on the CDP gathers. This gave an erroneous pick (too shallow) for the first velocity analysis. The pick should have been in the middle of the correlation zone, the pulse being basically symmetrical.

After adjusting the velocity picks for the window gate length the following results were obtained:

SECTION TIME	VA TIME	RMS VELOCITY	INTERVAL VELOCITY	INTERVAL THICKNESS
1.110 s	1.105 s	11900 ft/s		
			7617 ft/s	1009 ft
1.368 s	1.370 s	11200 ft/s		
			7608 ft/s	1008 ft
1.633 s	1.635 s	10700 ft/s		

The reflectors picked were the three flat interfaces. The interval thicknesses are quite close to those of the model which has 2 layers each of 1000 ft thickness. Also the true interval velocities are approximately 7475 ft/s and 7065 ft/s. The fault has a VA arrival time of 1.250 sec when adjusted for correlation power curve symmetry. The dotted zones in Figure 6-15 are zones which will be analyzed at a finer sampling rate later.

Figure 6-16 indicates an areal CMP gather that was collected

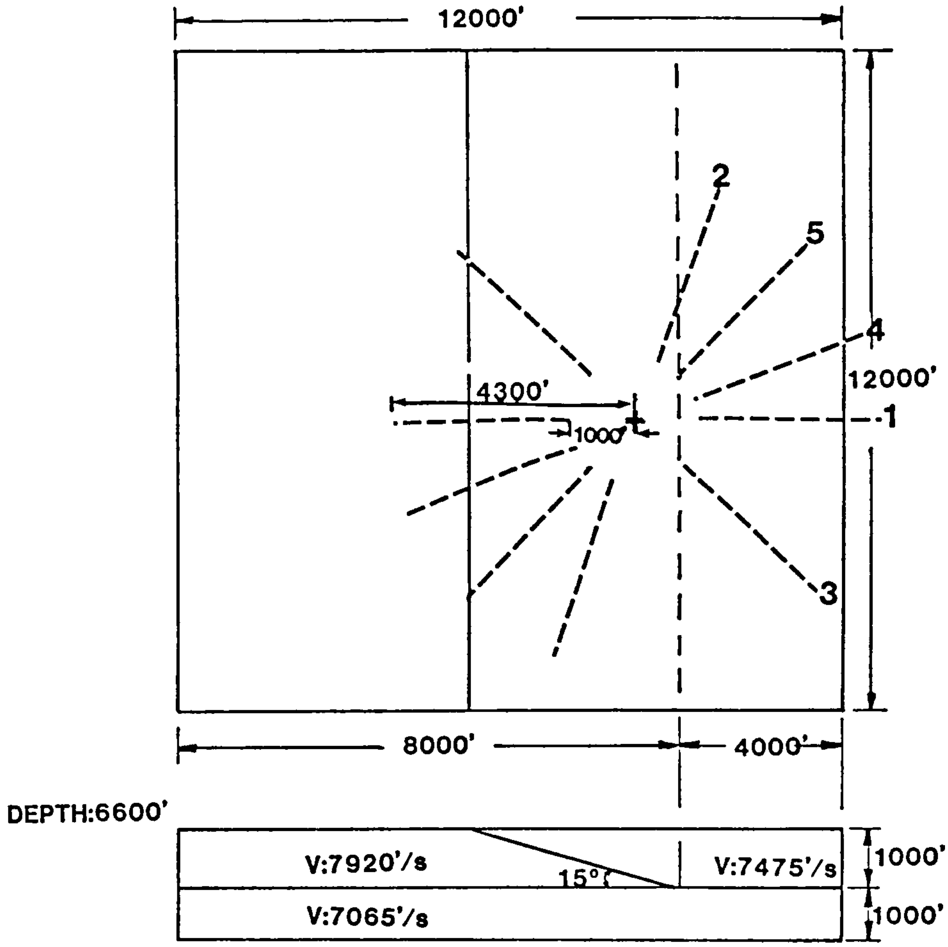

Figure 6-16 Areal CMP gather over fault model.

over the fault model. The corresponding 3-D velocity analyses are shown in Figure 6-17, 6-18 and 6-19; the best of which is Figure 6-19. At first glance this analysis (Figure 6-19) seemed to be discourging because the dip section indicated a 10° dip for the three flat horizons and the strike directions were also incorrect. However we soon realized that the dip and strike estimates are very sensitive to the exact shape of the hyperbolae and cannot be taken as good estimates whereas the velocity estimate is a robust estimate of the migration velocity. The migration velocity for the fault reflection at approximately 1.240 sec (unadjusted) is about 11600 ft/s and this falls on the trend line for the other velocity picks; the similar velocity pick for the 2-D analysis (Figure 6-15) was above the velocity function trend line.

In order to fully understand these VA results, a theoretical model was generated as shown in Figure 6-20. The true physical model in Figure 6-20 was transformed into an equivalent vertical-time model so that the dip changed from 15° to 26.6°. CDP-gathers were generated along the 45° azimuth line to match the physical model data acquisition and an additional set of CDP-gathers were taken on the dip line of the theoretical model.

Figure 6-21 illustrates the VAs from the theoretical model. The dip line has a maximum at 26° which corresponds to the stacking velocity of 13350 ft/s. The 45° line shows an apparent dip of 16°

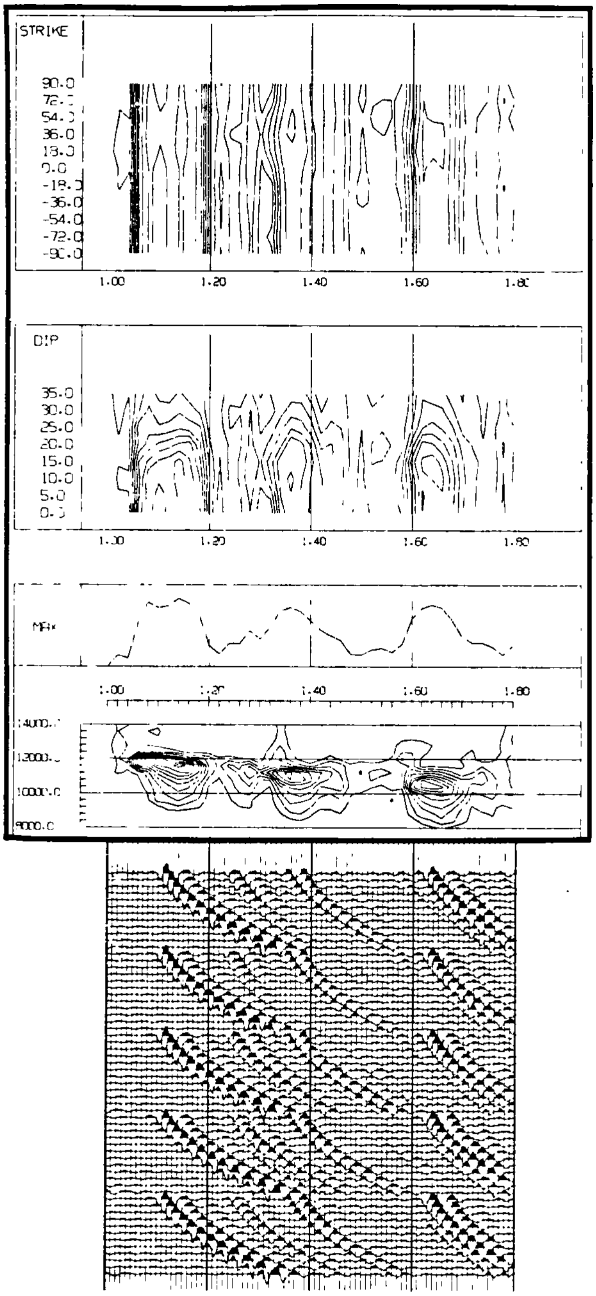

Figure 6-17 Three-D velocity analysis across fault model with normalized cross-correlation. No AGC was applied.

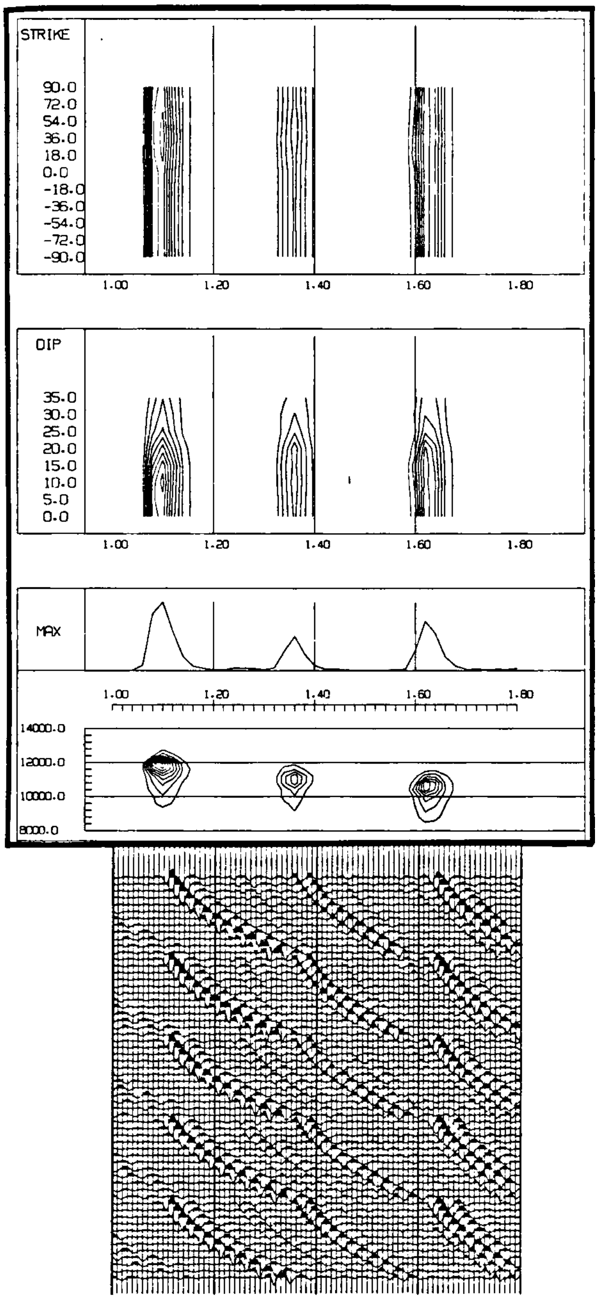

Figure 6-18 Thre-D velocity analysis across fault model with cross-correlation. AGC (.3 sec) was applied.

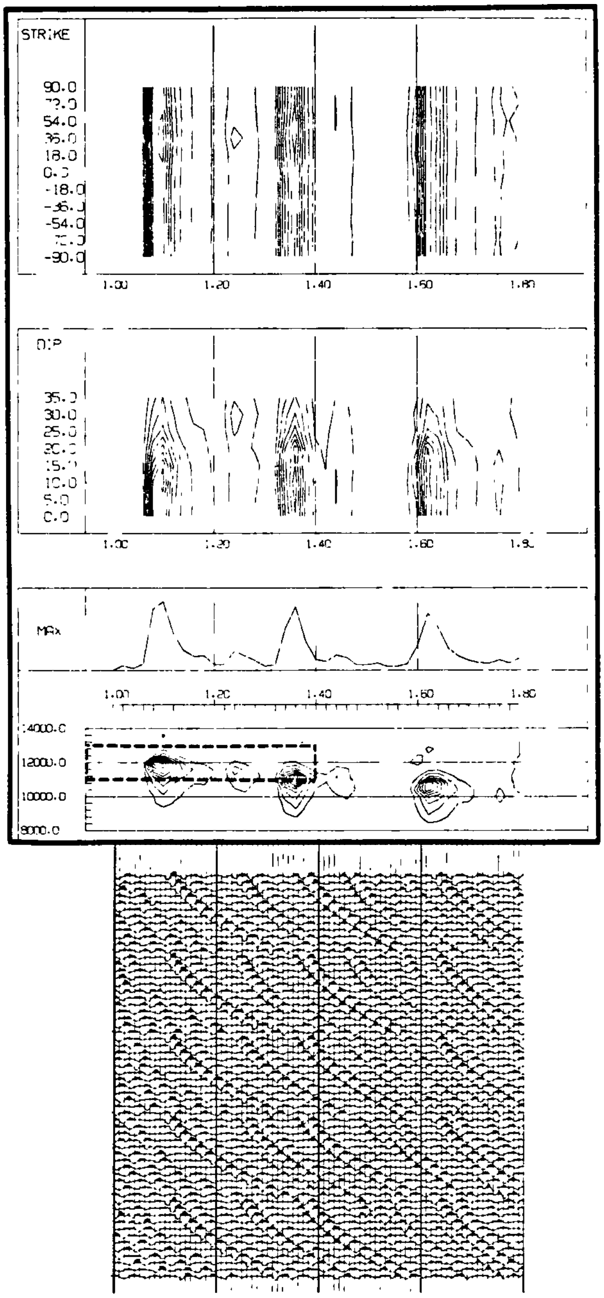

Figure 6-19 Three-D velocity analysis across fault model with cross-correlation. AGC (.1 sec) was applied.

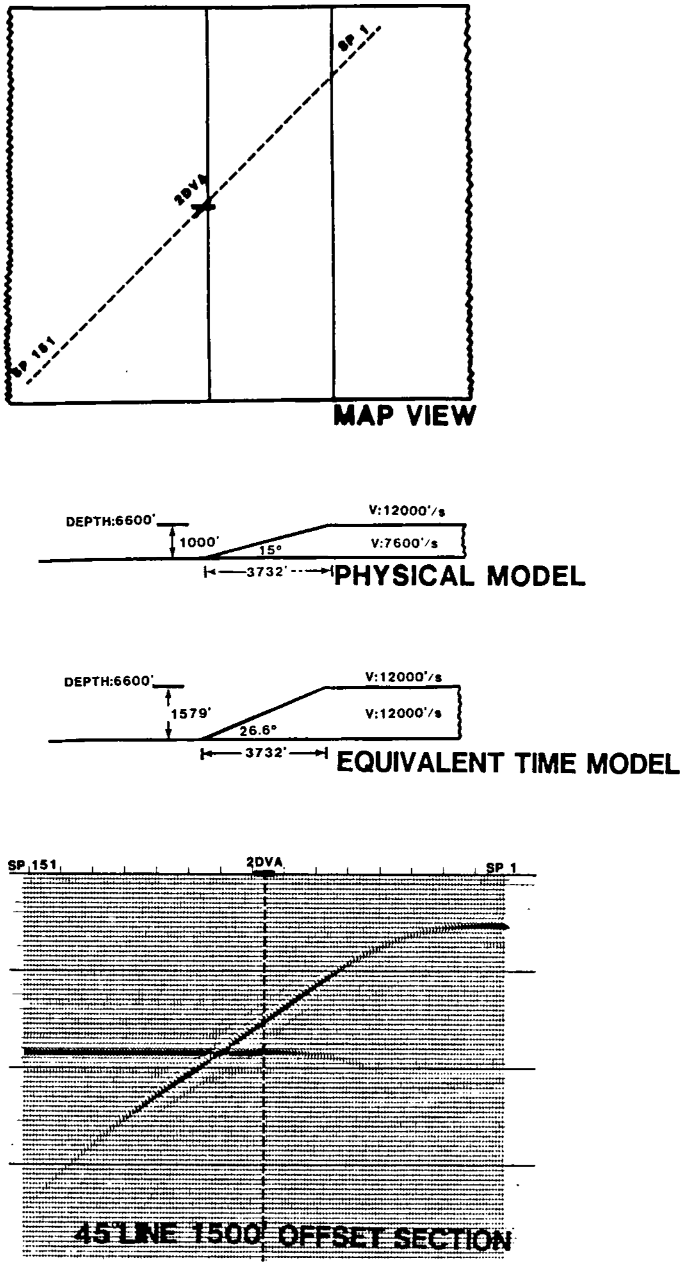

Figure 6-20 Dimensions and time section of theoretical fault model.

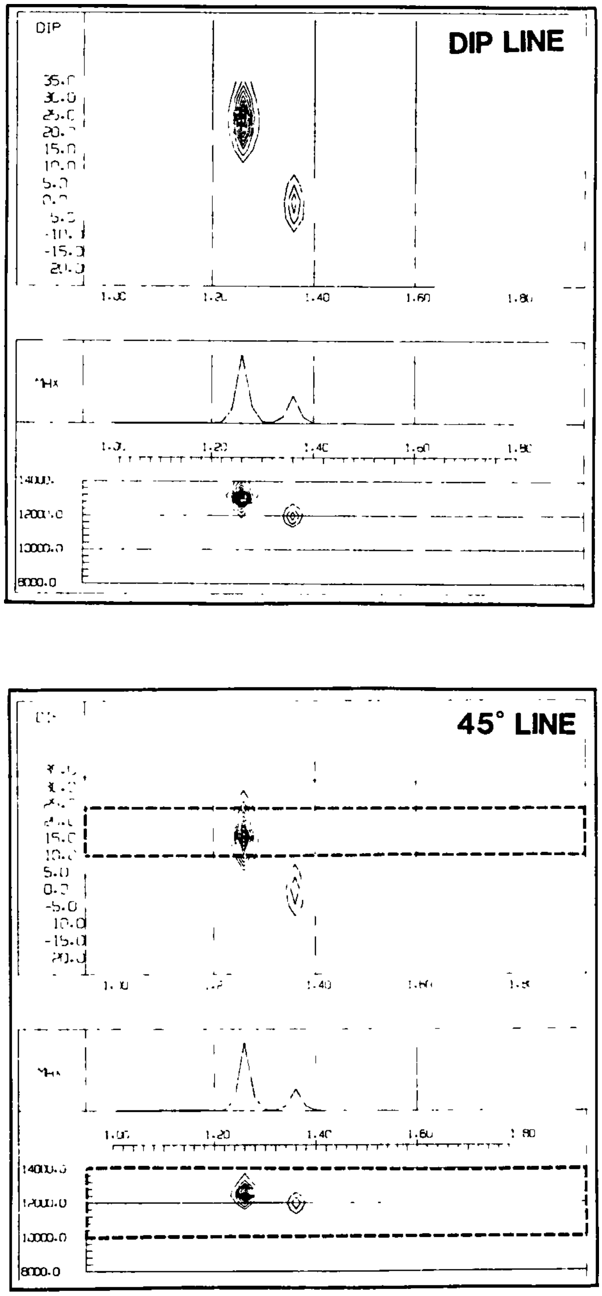

Figure 6-21 Two-D velocity analysis across theoretical fault model.

which corresponds to the stacking velocity of 12500 ft/s. If we multiply cos 16° with 12500 ft/s we approach the true migration velocity of 12000 ft/s. This procedure helped us establish the relationship of the dip to the velocity.

An expanded dip and velocity analysis of the theoretical model is given in Figure 6-22. A similar expanded velocity analysis for the physical model is given in Figure 6-23. The physical model results will not match exactly the theoretical because no low velocity medium was used. From the 2-D VA in Figure 6-23 we find for the fault plane an apparent dip of 18° and a velocity of 12150 ft/s. The 12150 ft/s is the stacking velocity while the migration velocity is $12150(\cos 18^{\circ})=11555$ ft/s at 1.24 sec. The migration velocity from the 3-D velocity analysis indicates 11500 ft/s. To check these results in another manner, the RMS velocity to the fault plane (1.24 sec) was calculated using the flat reflector interval velocities for a result of 11580 ft/s. This provides an excellent comparison.

6.3 CROOKED-LINE VELOCITY ANALYSIS

A. ALGORITHM

This velocity algorithm was designed for multi-midpoint data such as would be gathered in a crooked line survey. It combines both the 2-D beam steering and the 3-D areal CMP velocity analysis. As

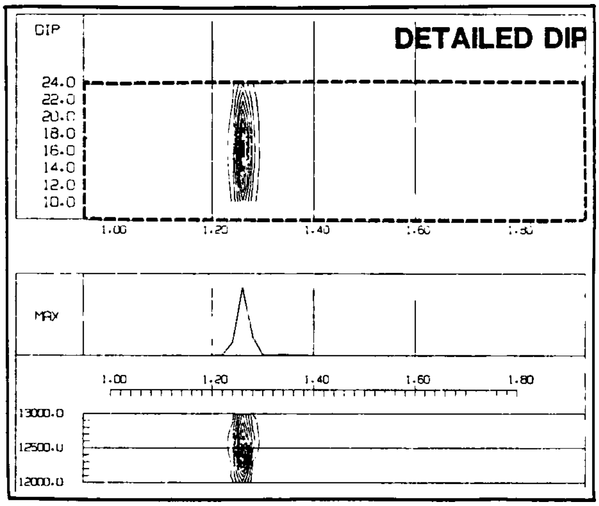

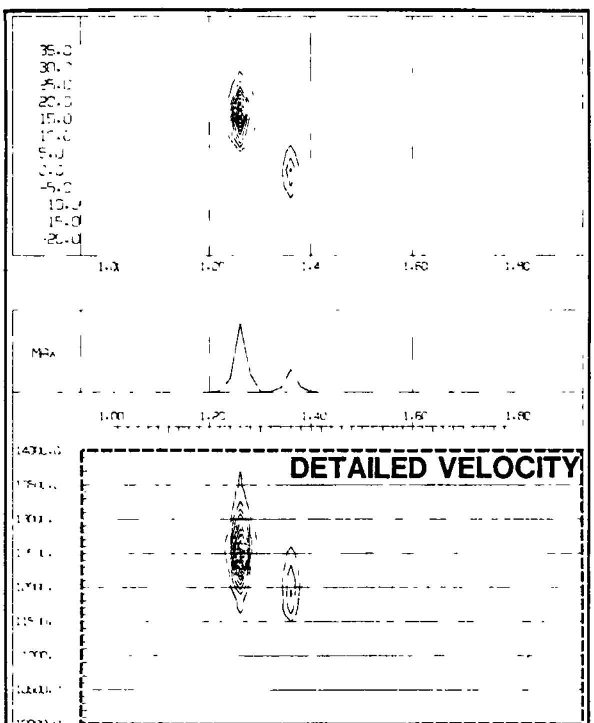

Figure 6-22 Detailed 2-D velocity analysis across theoretical fault model.

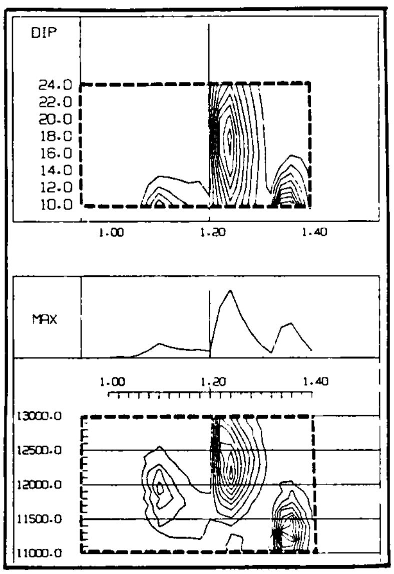

2DVA-XCOR AGC(.1)

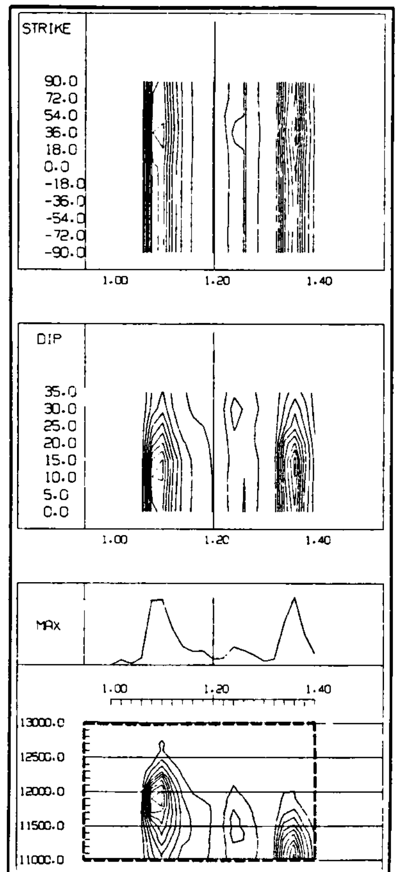

3DVA-XCOR AGC(.1)

Figure 6-23 Detailed 2-D and 3-D velocity analysis across physical fault model.

adjacent CDP gathers are beam steered in the 2-D analysis, the same approach holds for this algorithm, but in 3-D. That is, before equation (6-3) is searched as a function of δ, (dip), ϕ (azimuth) and V (migration velocity), a static adjustment was applied to correct the mislocation of the source-receiver (SR) midpoint with respect to the velocity analysis point. This static adjustment equation is

$$\Delta T = 2\Delta x \cdot \sin\alpha / V, \qquad (6\text{-}4)$$

where α is the apparent dip in the direction from VA point to the SR midpoint. The apparent dip is based on the current dip and strike being searched. Because adjacent areal CMPs can be used there is no ambiguity about the sign of the dip.

Definition of the strike and dip direction is necessary in this algorithm. A strike in the north-south direction is designated as zero strike. Start from the zero strike, + strike is in clockwise direction with a maximum strike of 90°. Minus strike is in counterclockwise direction with a minimum of -90°. Consider the two half planes separated by the strike line, the one containing the north direction was designated as + dip direction when the plane was dipping down in that direction. For zero strike (north), dipping down to the east is the + dip direction.

B. TEST RESULTS -- THEORETICAL DATA

Twelve-fold crooked-line data were collected over a plane which has a N54°E strike and 20° dip as indicated in Figure 6-24A. The CDP spacing is 100 ft along the crooked-line with near offset 800 ft and far offset 9600 ft. Also collected were 4 CMP gathers for comparison to the velocity analysis. The SR midpoint locations are indicated by "+".

As indicated in plot A, data consisting of four CMP areal gathers were first tested (center at point I). Each CMP gather had 36 traces (144 traces for the total 3-D analysis). The 4 CMP's were at the corners of a square with a length of 400 ft. The 3-D velocity analysis for the 4 areal CMP gathers had the ΔT shift evoked and the results shown in plot B depicted accurately the velocity, strike and dip. The second test was conducted over the shaded circular zone covering 65 traces (center at point II). These traces were those generated by the crooked-line survey and the subsequent 3-D velocity analysis in plot C has accurate results.

A crooked-line processing technique to improve the S/N ratio of the stacked data will be illustrated by using the same model data in Figure 6-24A. Shown in Figure 6-25A are the SR midpoint locations (indicated by "+") of ZSR data collected along the crooked-line, and Figure 6-25B are the SR midpoint locations of far (9600 ft) offset data. The dotted line represents the output profile location, which connected the two end points of the crooked-line.

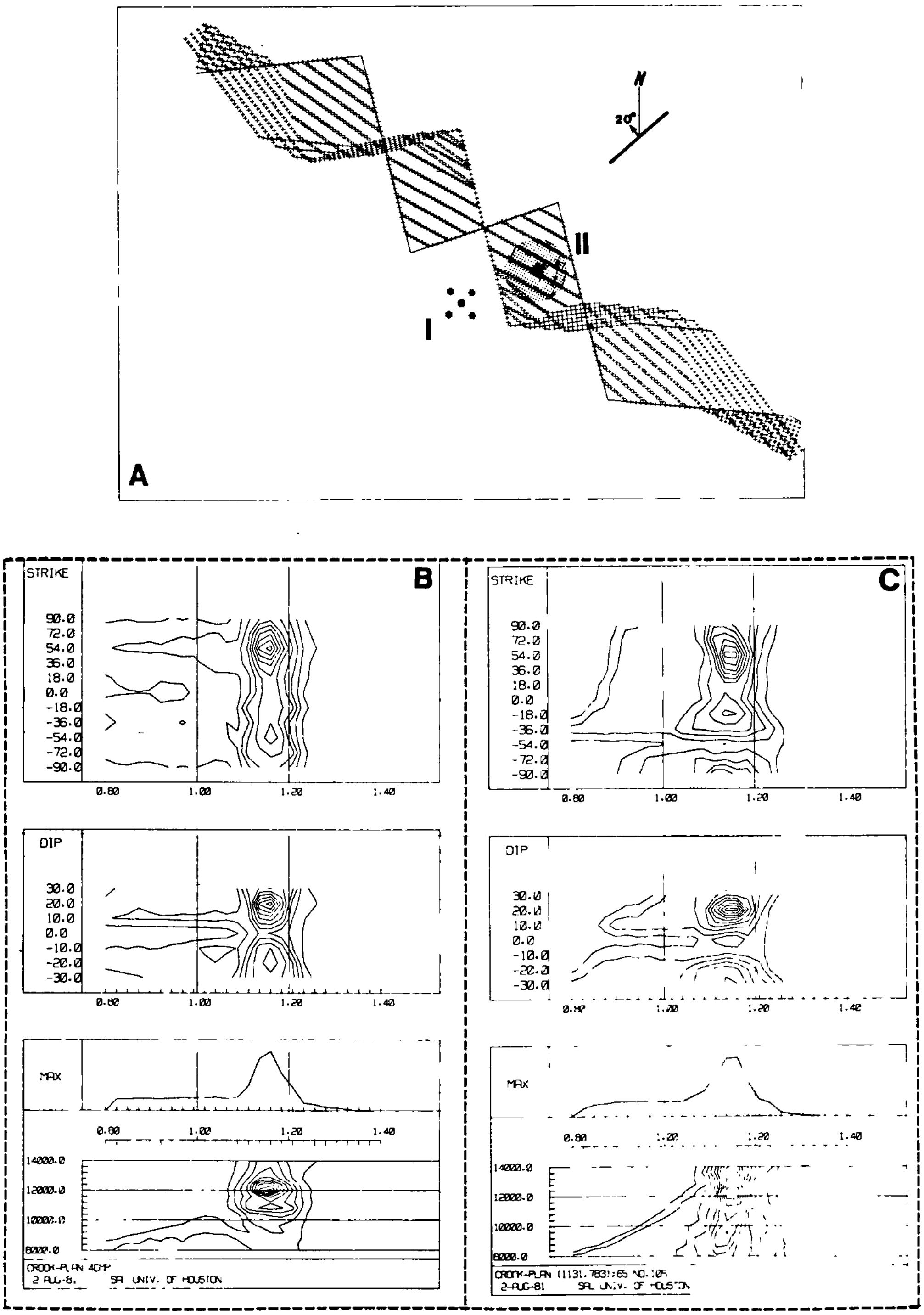

Figure 6-24 Crooked-line velocity analysis across a dipping plane.
A. Source-receiver midpoint locations.
B. Output plot at point I.
C. Output plot at point II.

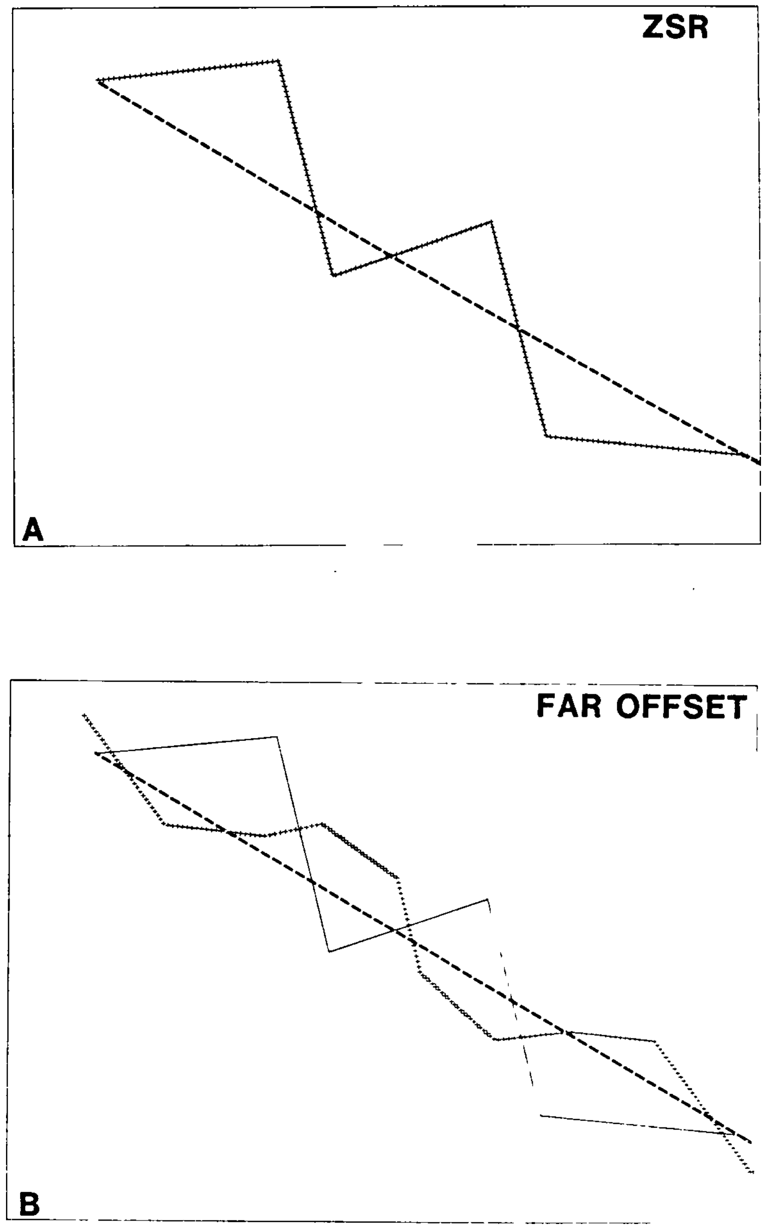

Figure 6-25 Source-receiver midpoint locations.
A. ZSR data.
B. Far offset data.

Section A in Figure 6-26 is the ZSR raw data and the effect of the crooked-line survey over a dipping interface is illustrated by the zigzag event. If the plane is horizontal or the survey line is straight, this event would have been straight. Section B in Figure 6-26 is the projected section (i.e., source-receiver midpoints are projected perpendicularly to the desired output line, the dotted line in Figure 6-25, and the input data are then regrouped by assigning each trace to the nearest output location) and section C is the projected section with a crossdip correction. This crossdip correction is calculated by using equation (6-4) in the VA algorithm. The crossdip effect of the crooked-line survey is removed after this correction is applied. The small gaps in the output line sections occur when no input data are projected to that output location.

Section A in Figure 6-27 is the far offset raw section. If we refer to Figure 6-25, one can see that the midpoint locations of the far offset data are less variant than that of ZSR data. This accounts for the smoother event on the far offset section than that on the ZSR section. Section B in this figure is the projected section and section C is the projected section with the crossdip correction. A smooth event is derived after the crossdip effect is removed as one can see in section C. This is the same section that would be obtained if a 9600 ft constant offset gather were made from a straight profile line.

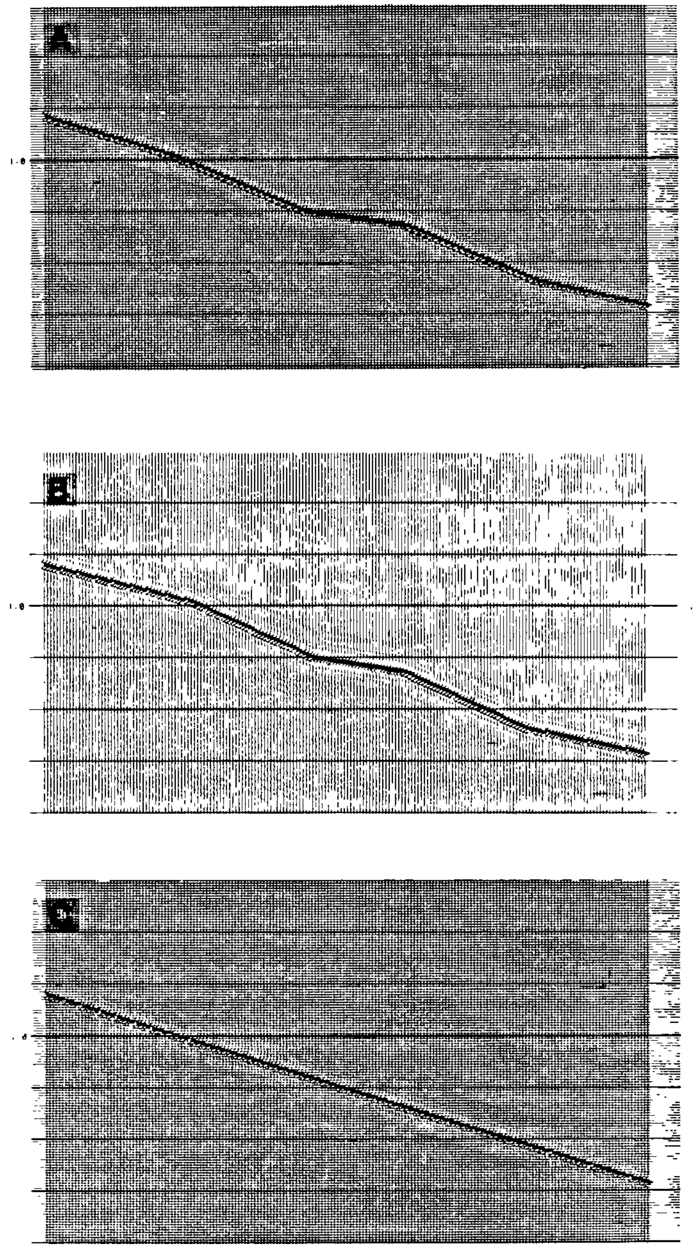

Figure 6-26 Crooked-line ZSR data.
A. Raw section.
B. Projected section.
C. Projected section with the crossdip correction.

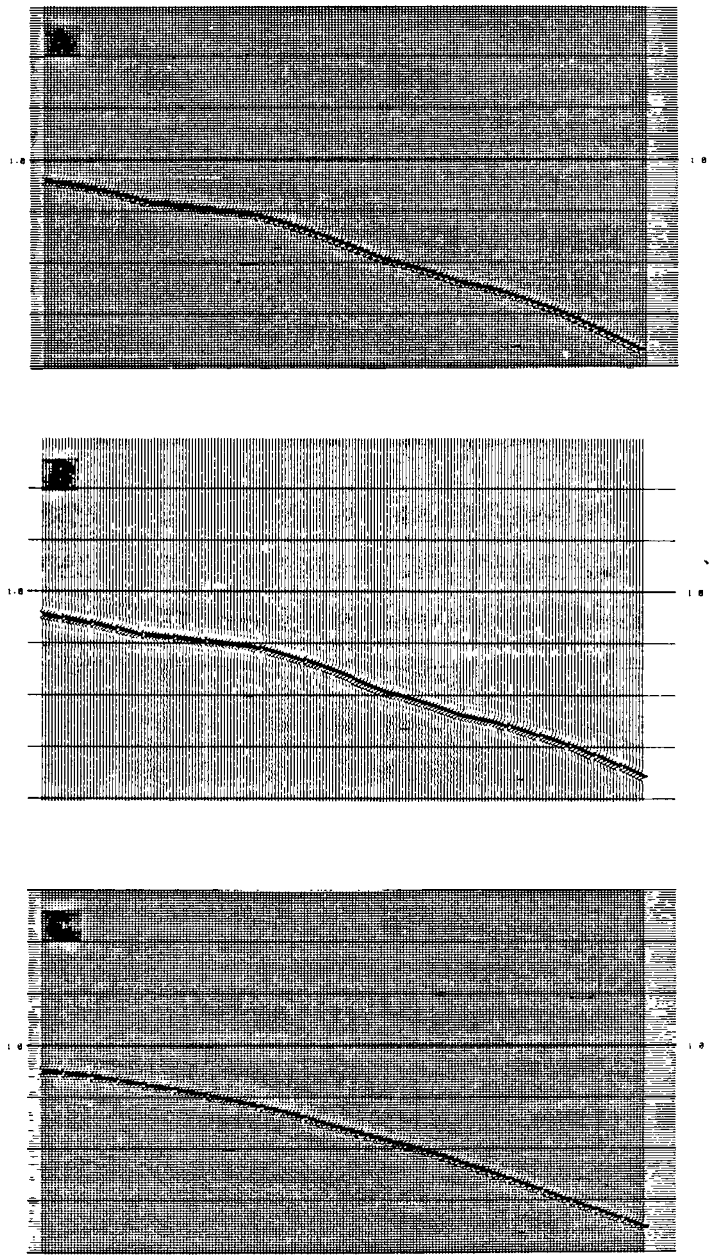

Figure 6-27 Crooked-line far offset data.
A. Raw section.
B. Projected section.
C. Projected section with the crossdip correction.

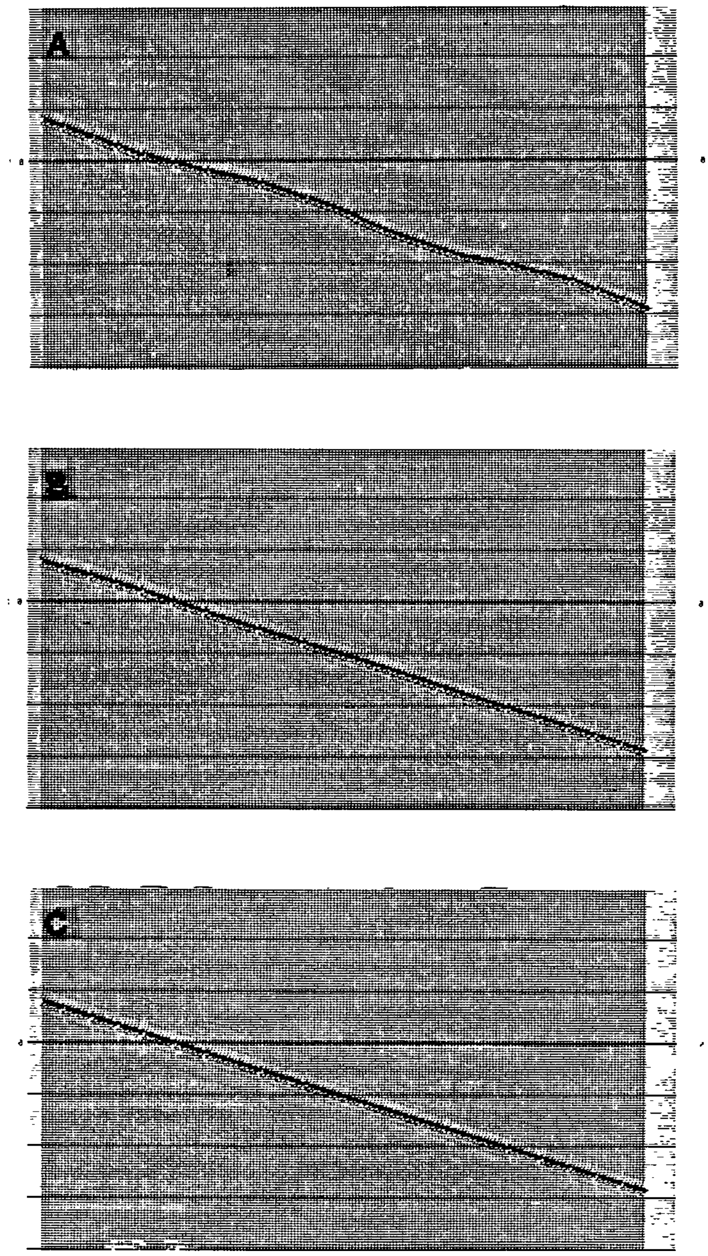

Figure 6-28 Crooked-line far offset data.
A. Projected section with 2-D NMO correction.
B. Projected section with crossdip and 2-D NMO corrections.
C. Projected section with crossdip and 3-D NMO corrections.

Shown in Figure 6-28 are three far offset sections with different processing flows. Section A is the projected section with 2-D NMO correction (i.e., NMO corrected by equation (6-2)). A constant stacking velocity of 12632 (12000/cos18.2°) ft/s was used and will be used later for all 2-D NMO correction. This section is not the same as the projected ZSR section in Figure 6-26B as one might think it should be.

Section B in Figure 6-28 is the projected section with crossdip and 2-D NMO corrections. The crossdip correction has reduced the undulation of the event to an unnoticed amount. Section C in Figure 6-28 is the projected section with crossdip and 3-D NMO corrections (corrected by equation (6-3)). The resulting section shows a straight event which has the same shape as that of section C in Figure 6-26.

The 12-fold stacked sections with different processing flow are shown in Figure 6-29. Section A is the brute stacked section (stacking velocity = 12632 ft/s). Section B is the stacked section with midpoint projection (but no crossdip correction) and 2-D NMO correction. Section C is the stacked section with projection, crossdip and 3-D NMO corrections. Both sections A and B show erroneous events mainly caused by the crossdip variations. The straight event in section C indicates that the crossdip and 3-D NMO corrections are necessary for a satisfactory crooked-line processing

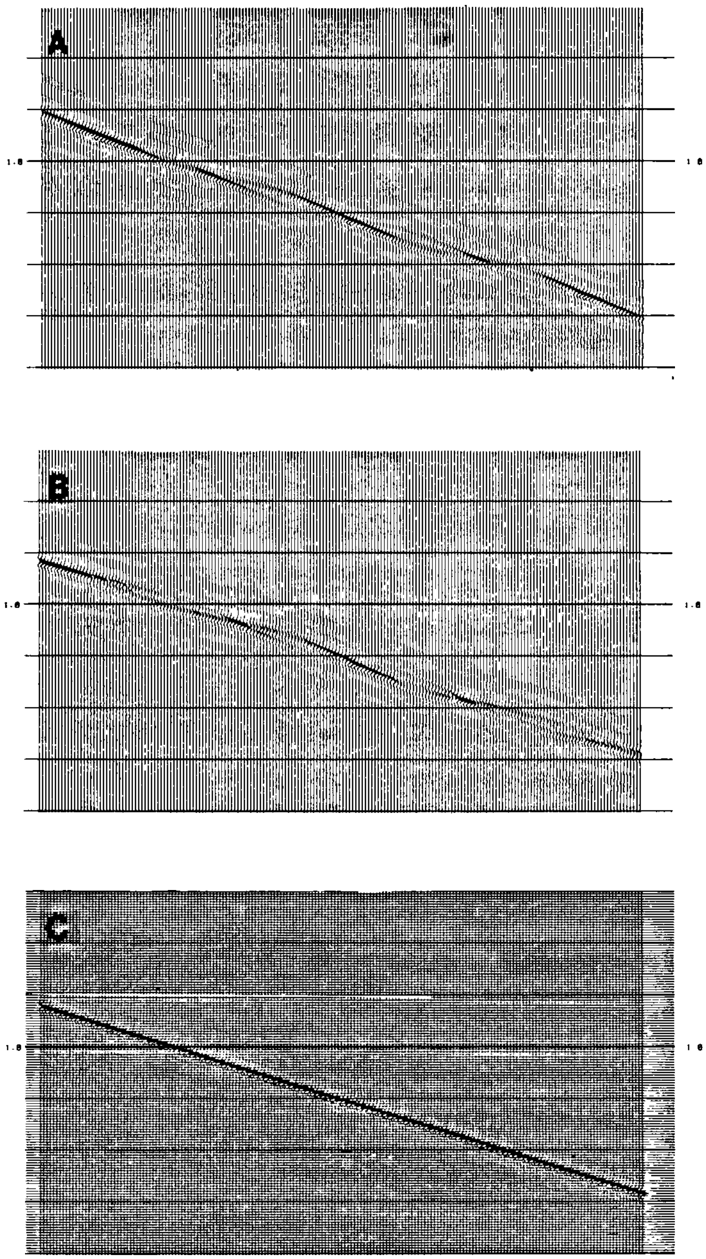

Figure 6-29 Crooked-line 12-fold data.
A. Brute stacked section.
B. Stacked section with projection and 2-D NMO correction.
C. Stacked section with projection, crossdip and 3-D NMO corrections.

result. The main factor however is the crossdip component which requires dip and strike information.

C. TEST RESULT -- PHYSICAL DATA

The physical model which was tested in Section 6.2B is used here to generate four areal CMP gathers as indicated in Figure 6-30A. The diagonal offset between midpoints is 600 ft. Each CMP gather consisted of three CDP gathers (36 traces) on the EW, N45^{o}E and N45^{o}W profile lines with near offset 2000 ft and far offset 8600 ft. The model was at a depth of 6600 ft from the top of the structure.

The output plot is shown in Figure 6-30B. Data were deconvolved and then an AGC trim with a window length of .1 sec was applied. The velocity search parameters had a 20 ms gate window and the unnormalized cross-correlation was employed as the correlation coefficient.

The velocity picks in Figure 6-30B are the same as those in Figure 6-19 and the correct dips and strikes were picked at the three flat horizons. Remember that in Figure 6-19 the dips and strikes were incorrect for these horizons when only one CMP gather was employed. For the fault plane, a N36^{o}E strike with -20^{o} dip was picked. The actual fault plane has a N43^{o}E strike and -26^{o} dip (adjusted dip).

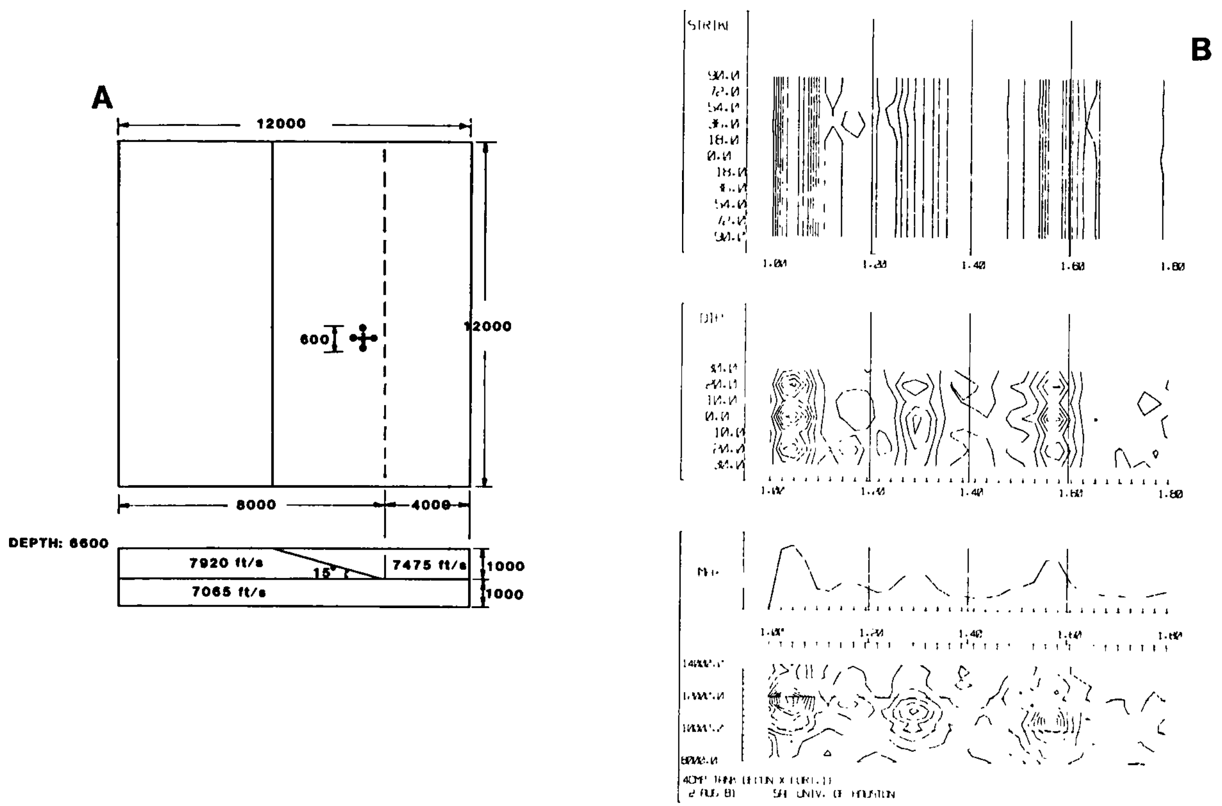

Figure 6-30 Three-D velocity analysis of four CMP gathers.
A. Dimensions of the model.
B. Output plot.

6.4 SUMMARY

Three different time-domain approaches were developed and evaluated for estimating velocity for areally gathered data. The first algorithm was designed for data gathered by closely spaced conventional CDP lines. A 2-D velocity analysis based on several adjacent CDP sets within a profile line yields the optimum stacking velocity along with apparent dip for each profile line. By multiplying the stacking velocity by the cosine of the apparent dip a 3-D migration velocity for application after stack is derived.

The second algorithm was designed for areal common-mid-point data acquisition. Using one CMP gather, a migration velocity is estimated along with strike and dip. This algorithm yields a before stack migration velocity which is usually robust even in the presence of tight curvature boundaries or faulted boundaries.

The third algorithm was designed for areal data gathered as a result of a crooked line survey. This algorithm combines the design philosophy of the first two algorithms to yield an optimum stacking velocity as a function of dip and strike and a final migration velocity.

These three algorithms were tested with theoretical and physical data, and good results were shown. Using the output parameters from the third VA algorithm, a processing technique was derived to correct the mislocated SR midpoints in crooked-line survey. The result shows a good improvement in S/N ratio of stacked crooked-line data.

VII. CONCLUSION

The following conclusions can be drawn from this research:

1. Both theoretical and physical modeling have proven to be a good aid in the area of the seismic interpretation of 3-D structures.

2. Althougth 2-D migration is a powerful tool in defining the shape of the structure, it can produce pitfalls such as pinchouts, grabens, extra layers, cross-stratification, faults, etc. If both 2-D migrated data and unmigrated data are used, such pitfalls can be guarded against although some ambiguity may still remain.

3. In most cases, negative structures produce more interpretational pitfalls than do positive structures. This is because negative structures can have "reflection points" that wander in a direction opposite to the profile direction.

4. For small geological structures first-surface sideswipe effects can generate a low-frequency disturbed zone which one might interpret as a lithology variation. A 3-D migration is recommended to collapse such 3-D edge diffractions.

5. For small geological structures, lateral velocity variations are responsible more for the interpretational pitfalls. For instance,

pitfalls such as dim spots are found to be related to a high velocity lens; bright spots are found to be related to a low velocity lens. Also the "thick lens" effect distorts the lower boundaries more for small structures than for large structures.

6. As for data acquisition schemes, crooked-line data is one of the most difficult to process. To apply a proper processing flow on such data, the earth parameters such as velocity, strike and dip must be searched simultaneously. The easiest data to process would be 2-D multi-fold collected in straight profile lines.

7. Care must be taken in chosing the right processing flow and processing parameters. Using the improper stacking velocity can change the appearance of the seismic section. Non-robust deterministic deconvolution can generate ghosts. For a multi-velocity 3-D structure, it is impossible to do stacking correctly. Therefore, a 3-D migration before stack is needed.

8. The velocity algorithms developed in this research are robust when theoretical and physical model data were tested. The earth parameters of velocity, strike and dip are derived from these algorithms. They also provide a new processing flow which corrects the crooked-line data properly.

REFERENCES AND BIBLIOGRAPHY

Bath, M., 1974, Spectral analysis in geophysics: Elsevier Scientific Publishing Company, Amsterdam.

Baysal, E., and Kosloff, D. D., 1981, Interpretation of physical model results with the aid of forward modeling: Seismic Acoustics Laboratory (University of Houston) Progress Review, v. 7, p. H23-H45.

Bennett, A. D., 1962, Study of multiple reflections using a one-dimensional seismic model: Geophysics, v. 27, p. 61-72.

Berckhemer, H., and Ansorge, J., 1963, Wavefront investigations in model seismology: Geophys. Prosp., v. 11, p. 459-470.

Darby, E. K., and Neidell, N. S., 1966, Application of dynamic programming to the problem of plane wave propagation in a layered medium: Geophysics, v. 31, p. 1037-1047.

Dobecki, T. L., 1973, Three-dimensional seismic modelling for arbitrary velocity distributions: Geophys. Prosp., v. 21, p. 330-339.

Duffy, R. E., 1980, Seismic coal seam modeling constrained by depositional enviroment: Master's thesis, Geology department, University of Houston, Houston, Texas.

Dunkin, J. W., and Levin, F. K., 1971, Isochrons for a 3-D seismic system: Geophysics, v. 36, p. 1099-1137.

French, W. S., 1974, Two-dimensional and three-dimensional migration of model-experiment reflection profiles: Geophysics, v. 39, p.265-277.

Gangi, A. F., and Yang, S. J., 1976, Traveltime curves for reflection in dipping layers: Geophysics, v. 41, p. 425-440.

Goupillaud, P. L., 1961, An approach to inverse filtering of near-surface layer effects from seismic records: Geophysics, v. 26, p. 754-760.

Hall, S. H., 1956, Scale model seismic experiments: Geophys. Prosp., v. 4, p. 349-364.

Hilterman, F. J., 1970, Three-dimensional seismic modeling: Geophysics, v. 35, p. 1020-1037.

__________________, 1976, Interpretative lessons from three-dimensional modeling: 46th annual international SEG meeting, Houston, Texas.

__________________, 1981, Forward 3-D modeling programs: Seismic Acoustics Laboratory (University of Houston) Progress Review, v. 7, p. G1-G16.

Hu, T., and Gardner, G. H. F., 1980, Kirchhoff migration in two steps: Seismic Acoustics Laboratory (University of Houston) Progress Review, v. 5, p. 269-275.

______________________________, 1981, Migration and stacking of sign-bit seismic data: Seismic Acoustics Laboratory (University of Houston) Progress Review, v. 7, p. N1-N37.

Hubbert, M. K., 1937, Theory of Scale Models as Applied to the Study of Geologic structures: Bulletin of the Geological Society of America, v. 48, p. 1459-1520.

Kosloff, D. D., and Baysal, E., 1981, Forward modeling by a Fourier method: Seismic Acoustics Laboratory (University of Houston) Progress Review, v. 7, p. H1-H22.

Levin, F. K., 1971, Apparent velocity from dipping interface reflections: Geophysics, v. 36, p. 510-516.

Levin, F. K., and Hibbard, H. C., 1955, Three-dimensional seismic model studies: Geophysics, v. 20, p. 19-32.

McDonald, J. A., Gardner, G. H. F., and Kotcher, J. S., 1981, Areal seismic methods for determing the extent of acoustic discontinuities: Geophysics, v. 46, p.2-16.

Morgan, T. R., and Hilterman, F. J., 1981, Three dimensional migration velocity analysis in the space-frequency domain: Seismic Acoustics Laboratory (University of Houston) Progress Review, v. 7, p. Q1-Q53.

Neidell, N. S., and Taner, M. T., 1971, Semblance and other coherency measures for multichannel data: Geophysics, v. 36, p. 482-497.

Owusu, J, K., and Gardner, G. H. F., 1981, Velocity estimation from 3-D data, Seismic Acoustics Laboratory (University of Houston) Progress Review, v. 7, p. R1-R75.

Peterson, R. A., Fillippone, W. R., and Coker, F. B., 1955, The synthesis of seismograms from well log data: Geophysics, v. 20, p. 516-538.

Seismic Acoustics Laboratory (University of Houston) Progress Review, Vol. 1, 1978.

Seismic Acoustics Laboratory (University of Houston) Progress Review, Vol. 2, 1978.

Seismic Acoustics Laboratory (University of Houston) Progress Review, Vol. 3, 1979.

Seismic Acoustics Laboratory (University of Houston) Progress Review, Vol. 4, 1979.

Seismic Acoustics Laboratory (University of Houston) Progress Review, Vol. 5, 1980.

Smith, T. A., 1980, Quadrature matched filtering of post-critical reflections: Seismic Acoustics Laboratory (University of Houston) Progress Review, v. 5, p. 108-118.

____________, 1981, 3-D Kirchhoff methods of acoustic modeling and migration: Doctoral dissertation, Geology department, University of Houston, Houston, Texas.

Taner, M. T., Cook, E. E., and Neidell, N. S., 1970, Limitations of the reflection seismic system: Lessons from computer simulations : Geophysics, v. 35, p. 551-573.

Taner, M. T., and Koehler, F., 1969, Velocity spectra-digital computer derivation and applications of velocity functions: Geophysics, v. 34, p. 859-881.

Trorey, A. W., 1962, Theoretical seismograms with frequency and depth dependent absorption: Geophysics, v. 27, p. 766-785.

Weatherby, B. B., 1940, The history and development of seismic prospecting: Geophysics, v.5, p. 215-230.

Widess, M. B., 1973, How thin is a thin bed? : Geophysics, v. 38, p.1176-1180.

Woods, J. P., 1975, A seismic model using sound waves in air: Geophysics, v. 40, p. 593-607.

Wuenschel, P. C., 1960, Seismogram synthesis including multiples and transmission coefficients: Geophysics, v. 25, p. 106-129.

Yu, T. R., and Telford, W. M., 1974, A three-dimensional seismic model for laboratory use: Journal of Geological Education, v. 22-23, p. 43-48.